A Determination of the W Boson Mass near the W-Pair Production Threshold

Christopher John Parkes

Linacre College, Oxford

DELPHI Experiment, CERN

A thesis submitted for the degree of Doctor of Philosophy
at the University of Oxford

Hilary Term, 1998

To Mom and Dad

A Determination of the W Boson Mass
near the W-Pair Production Threshold

Christopher John Parkes
Linacre College, Oxford
Delphi Experiment, Cern

submitted for the degree of Doctor of Philosophy
at the University of Oxford

Hilary Term, 1998

ABSTRACT

In 1996 the Lep Collider operated for the first time at collision energies above the W - pair production threshold. Electron - positron collisions were produced at centre of mass energies of 161 and 172 GeV. An integrated luminosity of approximately 10 pb^{-1} was collected by the Delphi experiment at each of these energies.

These data are used to measure the cross-section for the doubly resonant W^+W^- production.

At $\sqrt{s}$ of 161.31 ±0.06 GeV we obtain:

$$\sigma_{W^+W^-} = 3.82\ ^{+1.06}_{-0.93}\ \text{(stat.)}\ \pm 0.25\ \text{(syst.)}\ \text{pb}$$

At $\sqrt{s}$ of 172.30 ±0.06 GeV we obtain:

$$\sigma_{W^+W^-} = 12.20\ ^{+1.66}_{-1.54}\ \text{(stat.)}\ \pm 0.50\ \text{(syst.)}\ \text{pb}$$

Results on the W boson branching ratios, the CKM matrix element $|V_{cs}|$, and an indirect determination of the W boson width are also provided.

Near the W-pair production threshold, the Standard Model W^+W^- cross-section is sensitive to the W boson mass. We interpret the measured cross-sections, within the Standard Model, as a measurement of M_W.

The W boson mass is also obtained from the method of invariant mass direct reconstruction in the $W^+W^- \to l\overline{\nu}_l q\bar{q}'$ and $W^+W^- \to q\bar{q}'\bar{q}q'$ final states. This method is applied to the data collected at 172 GeV.

Combining the W boson mass measurements made by the direct reconstruction method and the threshold cross-section interpretation, we obtain the value:

$$M_W = 80.14 \pm 0.31\ \text{(stat.)}\ \pm 0.07\ \text{(syst.)}\ \pm 0.02\ \text{(int.)}\ \pm 0.03\ \text{(Lep)}\ \text{GeV/c}^2$$

Preface

" Haben Sie einen gesehen ? "

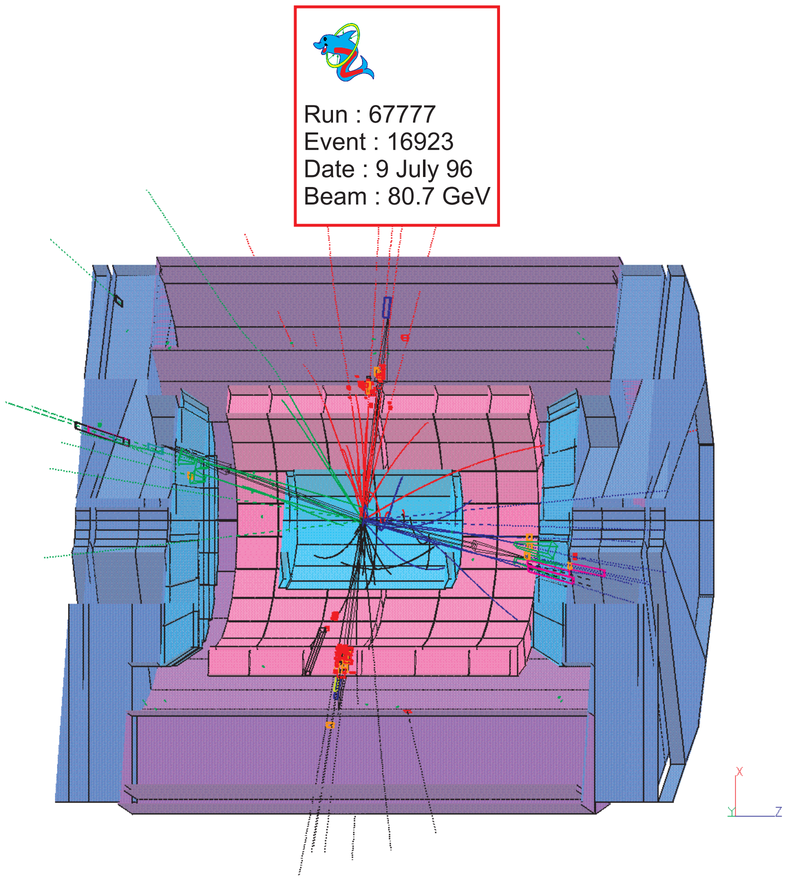

Figure 0.1: The first $e^+e^- \to W^+W^-$ event. Four distinct high momentum jets are observed in the event. The jets can be paired to produce a combination in which the di-jet masses are close to the W boson mass. This event is compatible with the pair production of W bosons and their subsequent decay to hadronic states.

On the 9th July 1996, the first candidate $e^+e^- \to W^+W^-$ event was detected [1] . This event, shown in Figure 0.1, was observed by the DELPHI detector at LEP. This thesis is concerned with the analysis of this event and all the other W^+W^- events obtained by DELPHI in 1996 .

Measurements

The principal measurements made in this thesis are:

- The $e^+e^- \to W^+W^-$ cross-section at $\sqrt{s}$ of 161 and 172 GeV, all Standard Model final states are considered.
- The W boson decay branching ratios.
- The direct measurement of the W boson mass M_W at 172 GeV, from the decay channels $q\bar{q}'\bar{q}q'$ and $l\overline{\nu}_l q\bar{q}'$.

  In addition these results are, subject to additional Standard Model assumptions, interpreted as the following further measurements:
- M_W is obtained from the measured cross-sections.
- The CKM matrix element $|V_{cs}|$ is obtained from the W hadronic branching ratio.
- The W width Γ_W is obtained from the W hadronic branching ratio.

Overview

Chapter One provides a brief introduction to the Standard Model of particle physics. Emphasis is placed upon the areas of Electro-Weak theory most directly relevant to this thesis, and comments are provided on the production and decay mechanisms of W^+W^- bosons. The final section of the chapter reviews W^+W^- interconnection phenomena: an area of the theory which is currently not well understood.

Chapter Two is intended to provide the reader with the relevant background knowledge of the LEP accelerator and particularly of the DELPHI detector required for the analysis chapters that follow. DELPHI is comprised of a significant number of sub-detectors each of which is described. The chapter concludes with a general guide to the DELPHI data read-out and off-line processing structure.

Chapter Three contains a discussion of the reconstruction and selection of charged and neutral tracks in DELPHI. We compare tracks from simulated events with those observed in the data, and present the set of track selection criteria which are used in this analysis. The operational status of the DELPHI detector during the relevant data taking periods is discussed. The LEP Collider beam energy and the integrated luminosity collected for this data are then presented. The role of event generators and detector simulation are summarised in the final sections of the chapter.

Chapter Four presents the selection of $\mathrm{W^+W^-}$ events used in this analysis. We divide the event selection into three primary categories: $\mathrm{W^+W^-}\rightarrow\mathrm{q\bar{q}'\bar{q}q'}$, $\mathrm{W^+W^-}\rightarrow\mathrm{l\overline{\nu}_l q\bar{q}'}$ and $\mathrm{W^+W^-}\rightarrow l\overline{\nu}_l\bar{l}\nu_l$ final states. For each category, we provide the full event selection criteria and compare distributions obtained in data with those expected from simulation events.

Chapter Five concerns the interpretation of the number of selected events in terms of several quantities of physical importance. We obtain the $e^+e^-\rightarrow\mathrm{W^+W^-}$ cross-section and the W branching ratios. From the W hadronic branching ratio measurements we then derive results for the CKM matrix element $|V_{cs}|$ and the W width. The $\mathrm{W^+W^-}$ cross-section is used to obtain a measurement, within the Standard Model, of the W boson mass. The chapter concludes with a study of four-fermion final state interference relevant to the measurement of the $\mathrm{W^+W^-}$ cross-section and the W boson mass.

Chapter Six deals with the invariant mass direct reconstruction method for obtaining $\mathrm{M_W}$. The W mass is extracted from a maximum likelihood fit to the observed mass spectrum of the selected events.

Chapter Seven contains the conclusions. In this chapter we combine the measurements of the W boson mass made in this thesis to provide a final result. The principal measurements made in this thesis are compared with previous determinations of these quantities. Finally, we discuss the future prospects for the M_W measurement during the LEP2 programme.

Appendix A discusses the `WWANA` program. This is the standard DELPHI software used in W physics analyses.

Appendix B provides details of the `PUFITC+` program. This is a kinematic fitting package which is used in the M_W direct reconstruction analysis.

Appendix C contains a list of the members of the DELPHI Collaboration, and of the DELPHI W^+W^- cross-section and W mass working groups.

Acknowledgements

I am very grateful to Guy Wilkinson and Paula Collins for instigating and supporting my early work on Lep2. Guy's guidance at the start of my work on the W^+W^- cross-section measurement was invaluable.

I am very fortunate to have worked alongside such fine collaborators on `WWANA` as Roberto Chierici and Alessandra Tonazzo. Many people in the Delphi W Physics team also have contributed to the work in this analysis: the members of the W team are listed in Appendix C.

I would like to thank Gerald Myatt and Louis Lyons for their help and advice during my time at Oxford. I have also benefited from discussions with my peers Nikolaos Vassilopoulos, Julie Thomas and Jim Libby, and my superiors John Holt and Ainsley Normand.

My supervisor Alan Segar has been very supportive throughout the writing of this thesis and I am grateful for his work on correcting this manuscript.

Finally, I am indebted to Peter Renton without whom this thesis could not have been produced.

In addition, I would like to thank the following people for specific contributions to the work in this thesis.

Chapter One In addition to the specific references made in this chapter, I used several texts extensively in the preparation of this chapter: notably Peter Renton's book [2], Don Perkin's book [3] and the theses of Guy Wilkinson [4] and John Holt [5].

Chapter Two The Delphi Detector Specification Tables (2.1, 2.2, 2.3) are based upon those in the thesis of John Holt [5].

Chapter Three The selection of charged tracks presented here is inspired by the corresponding section in the thesis of Teddy Todorov [6]. I am grateful for the advice of Bill Murray on the operational status of the detector during the data taking.

Chapter Four The W^+W^- event selection developed alongside the work of Roberto Chierici and Alessandra Tonazzo.

Chapter Five Thanks to Tomaz Podobnik for his help with my $|V_{cs}|$ measurement. The study on four-fermion interference was performed with Peter Renton.

Chapter Six The fully-hadronic analysis in this thesis is guided by the work of Niels Kjær and Martijn Mulders.

I would like to acknowledge the financial assistance of PPARC.

Thanks to Zoë Carroll for correcting the grammar and punctuation in this thesis and for putting up with me over the last few months.

This document has been typeset using LaTeX, and is based on a template produced by John Holt. The histograms and Feynman diagrams in this thesis have been produced using `PAW`.

The following detector and accelerator figures are reproduced, with minor amendments, from the WWW service of CERN and DELPHI and the DELPHI detector at LEP paper [7]: 0.1, 2.1, 2.2, 2.3, 2.4, 2.6, 2.7, 2.8, 2.9, 2.10, 2.11. Figure 7.2 is an altered version of that in [8]. All other figures have been produced by the author.

I am very grateful to Robin Devenish and David Ward for sparing the time to read and examine this thesis.

Contents

List of Figures

List of Tables

Chapter 1

The W Boson and the Standard Model

1.1 Introduction

It is anticipated that all contemporary readers will be familiar with the Standard Model (SM) of Particle Physics; hence only the most relevant components of this model are discussed here. The following section provides a few introductory remarks on the SM and then the remainder of this chapter concentrates on the areas of the theory which relate most directly to the W boson.

1.2 Standard Model

The Standard Model of Particle Physics describes the properties of the fundamental particles, and their interactions. The fundamental constituents of the model are the spin $\frac{1}{2}$ fermions, and the integer spin bosons: their properties are summarised in Table 1.1 and 1.2. The theory describes the Electromagnetic, Weak and Strong interactions of the particles, and provides a mechanism for the generation of mass. The model does not include gravitational interactions, the effects of which only become significant at larger scales.

Experimentally the most significant unobserved element of the theory is the Higgs scalar. As discussed below (see 1.3.2), the Higgs mechanism is needed to give masses to the other particles, however it has not been observed directly and the limits on its mass remain weak (see 7.3.1).

Fermion Generation 1	2	3	Quantum Numbers q	t	t_3
Leptons					
$\begin{pmatrix} \nu_e \\ e \end{pmatrix}_L$	$\begin{pmatrix} \nu_\mu \\ \mu \end{pmatrix}_L$	$\begin{pmatrix} \nu_\tau \\ \tau \end{pmatrix}_L$	$\begin{matrix} 0 \\ -1 \end{matrix}$	$\frac{1}{2}$	$\begin{matrix} +\frac{1}{2} \\ -\frac{1}{2} \end{matrix}$
e_R	μ_R	τ_R	-1	0	0
Quarks					
$\begin{pmatrix} u \\ d \end{pmatrix}_L$	$\begin{pmatrix} c \\ s \end{pmatrix}_L$	$\begin{pmatrix} t \\ b \end{pmatrix}_L$	$\begin{matrix} +\frac{2}{3} \\ -\frac{1}{3} \end{matrix}$	$\frac{1}{2}$	$\begin{matrix} +\frac{1}{2} \\ -\frac{1}{2} \end{matrix}$
u_R	c_R	t_R	$+\frac{2}{3}$	0	0
d_R	s_R	b_R	$-\frac{1}{3}$	0	0

Table 1.1: Quantum numbers for the fermions in the Standard Model, where q is the charge, and t and t_3 denote the weak isospin and its third component.

The SM combines the ideas of special relativity and quantum mechanics into a quantised field theory description: where the particles emerge as quanta of the field variables.

Central to the model is the postulate of invariance of the theory under local gauge transformations; that is invariance under a symmetry where the phase at each space-time point is allowed to vary independently. As is known classically, invariance under the global application of symmetries leads to conservation laws (Noether's Theorem). However, the invariance of the SM under local application of the transformations actually leads to the addition of the fields to the theory: this is described further in Section 1.3.1.

Calculations in the Standard Model are expressed as a perturbation expansion in the coupling constant, where the terms are represented by Feynman diagrams containing increasing numbers of vertices. The Standard Model has the property that calculations of physically observable quantities are non-divergent, such a theory is said to be *renormalisable*. It can be shown [9, 10] that gauge theories are automatically renormalisable. However, the need for renormalising particle mass

Boson	q	t	t_3	Mass	Interaction
Vector Boson					
W^+	$+1$		$+1$	80.43 ± 0.08GeV	Weak
Z^0	0	$+1$	0	91.187 ± 0.002GeV	Electro-weak
W^-	-1		-1	80.43 ± 0.08GeV	Weak
γ	0	0	0	0	QED
g	0	0	0	0	QCD
Scalar Boson					
H	0	0	0	115^{+116}_{-66} GeV	Yukawa

Table 1.2: Quantum numbers for the bosons in the Standard Model, where q is the charge, and t and t_3 denote the weak isospin and its third component. The non-zero masses given are the directly measured values from the LEP Electro-weak working group world averages produced for the 1997 European Physical Society Conference (Jerusalem) [8].

and charge implies that the theory cannot predict their values, and these must be taken from experiment.

The gauge group of the Standard Model is $SU(3) \otimes SU(2)_L \otimes SU(1)$, these are respectively the groups corresponding to Strong, Weak, and Electromagnetic interactions. The SU(3) gauge theory is not described further in this thesis, the unification of the Weak and Electromagnetic interactions is discussed in the following sections.

1.3 Electro-Weak Theory

1.3.1 Unification of the Electromagnetic and Weak Forces

The generalised Euler - Lagrange equations of motion are:

$$\partial_\mu\left(\frac{\partial\mathcal{L}}{\partial(\partial_\mu\phi_i)}\right) = \frac{\partial\mathcal{L}}{\partial\phi_i}$$

where $\mathcal{L}$ is the lagrangian[1] energy density (which is conventionally taken as axiomatic), and ϕ_i are the field variables.

If we require that the Lagrangian of our theory is invariant under the transformation of the U(1) (*i.e.* scalar) group wavefunction:

$$\psi \rightarrow e^{-i\frac{g'}{2}y\phi(x)}\psi$$

here the x indicates the local property of the symmetry; the phase ϕ can be changed independently at any point in space-time. The invariance requirement leads to the introduction of a massless neutral field B_μ. The B field couples to the fermions with a strength g' according to the particle's quantum number of Weak hypercharge y, where

$$y = 2(q - t_3)$$

The values of charge q and Weak isospin t_3 of the fermions are given in Table 1.1. For the SU(2) group the condition can be expressed as:

$$\psi \rightarrow e^{-i\frac{g_\mathrm{W}}{2}\alpha(\mathbf{x})\cdot\tau}\psi$$

where α is any real 3-vector, $\tau_{1,2,3}$ are the Pauli matrices and ψ is now a doublet of (left handed chirality) spin $\frac{1}{2}$ fields. This condition results in the need for three new massless fields: two charged fields and one neutral. These $\mathbf{W}_\mu$ fields couple with strength g_W to the left handed chirality states.

The charged W bosons are given by:

$$\mathrm{W}^{\pm}_\mu = \frac{1}{\sqrt{(2)}}(W^1_\mu \mp i\mathrm{W}^2_\mu)$$

Since the Z couples to both left and right-handed fermions it is clear that the fields corresponding to the physical photon and Z are orthogonal linear combinations of the $\mathbf{W}$ and B fields.

$$A_\mu = \sin\theta_\mathrm{W} W^3_\mu + \cos\theta_\mathrm{W} B_\mu$$

$$Z_\mu = \cos\theta_\mathrm{W} W^3_\mu - \sin\theta_\mathrm{W} B_\mu$$

[1] Under the field theory quantisation procedure the Lagrangian does not change, only our interpretation of the field variables.

where θ_w is known as the Weinberg Weak mixing angle. The relationship between the Weak coupling of the W field g_{W}, the g' coupling of the B field, and the photon coupling g_e can be derived from the above:

$$g_W \sin\theta_{\mathrm{W}} = g' \cos\theta_{\mathrm{W}} = g_e$$

1.3.2 Higgs Mechanism

In the section above we described how gauge invariance leads to the introduction of the massless W and B fields. Through the spontaneous symmetry breaking of the Higgs mechanism [11, 12] we can produce a gauge invariant theory in which the gauge bosons have acquired mass.

Gauge Boson masses

We introduce to the model a Weak isospin doublet of complex scalar fields, with hypercharge $y = 1$: the top component thus has $q = 1$, and the lower component is neutral. This is the minimal choice of fields required to generate the boson masses. For simplicity this can be written as four real fields:

$$\phi(x) = \frac{1}{\sqrt{2}} \begin{pmatrix} \sigma_1(x) + i\sigma_2(x) \\ \phi_1(x) + i\phi_2(x) \end{pmatrix}$$

The $SU(2)_L \otimes U(1)$ invariant Lagrangian now contains extra kinetic energy ($\mathcal{T}$) and potential energy ($\mathcal{V}$) type terms (*cf.* with the classical $\mathcal{L} = \mathcal{T} - \mathcal{V}$). The potential energy[2] like terms are:

$$\mathcal{V}(\phi) = \mu^2 |\phi|^2 + \lambda |\phi|^4$$

where the ground state (vacuum) of the system corresponds to a minimum in $\mathcal{V}(\phi)$. Now let us choose the minimum of the $t_3 = +\frac{1}{2}$ component of the ϕ doublet to be zero, and consider the potential in terms of ϕ_1 and ϕ_2. For the choice $\lambda^2 > 0$ and $\mu^2 < 0$ the potential is of the form shown in Figure 1.1. The minimum is now degenerate, lying on a circle, and occurs at the value :

[2]The Higgs potential $\mathcal{V}$ cannot depend upon powers higher than the fourth in the scalar fields since otherwise the theory is unrenormalisable.

$$|\phi|^2 = -\frac{\mu^2}{2\lambda} = \frac{v^2}{2}$$

where v is known as the vacuum expectation value. We can choose to re-define our origin at one of the minima, say the point $\phi_1 = v$, $\phi_2 = 0$, and expand around this point by introducing the fields η_1, η_2 (see Figure 1.1).

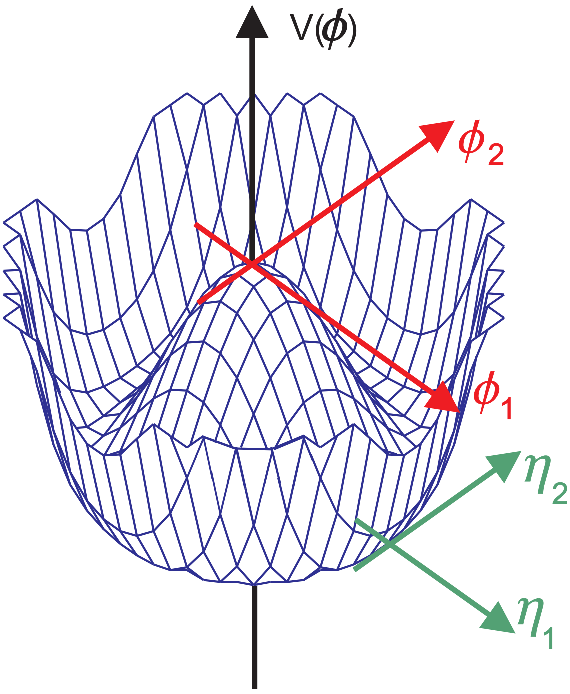

Figure 1.1: The Higgs potential $\mathcal{V}(\phi) = \mu^2 |\phi|^2 + \lambda |\phi|^4$ for a scalar field.

Expressing the Lagrangian in terms of these fields we obtain one massive particle η_1 of mass $\sqrt{2\lambda v^2}$, which we call the Higgs boson (H), and three massless particles η_2, σ_1 and σ_2, known as Goldstone bosons.

Applying a unitary transformation to the field doublet $\phi(x)$ we can obtain :

$$\phi(x) = \frac{1}{\sqrt{2}} \begin{pmatrix} 0 \\ v + H(x) \end{pmatrix}$$

leaving only the real Higgs field.

Our original Electro-Weak Lagrangian contained four massless fields (**W** and B). We mixed these fields to produce the γ, Z and W$^{\pm}$ bosons. Applying the Higgs mechanism to our Electroweak Lagrangian (see [2]), we find the W and Z bosons have now acquired masses $\mathrm{M_W} = g\frac{v}{2}$ and $\mathrm{M_Z} = g\frac{v}{2}\cos\theta_\mathrm{W}$: thus[3]

$$\mathrm{M_W}^2 = \mathrm{M_Z}^2 \cos^2\theta_\mathrm{W}$$

Our four original massless fields each had two possible polarisation states. We have now created three massive bosons ($\mathrm{W}^\pm$ and Z) and the massless γ. The unitary transformation applied above, removed the three Goldstone bosons from the theory; they are transformed into an extra degree of freedom for the $\mathrm{W}^\pm$ and Z bosons. As one expects for a massive spin-1 object, the $\mathrm{W}^\pm$ and Z bosons now have three possible polarisation states $J_Z = 1, 0, -1$.

Fermion masses

We may now construct a set of terms coupling the Higgs doublet to the fermions, invoking a set of arbitrary coupling parameters known as the Yukawa couplings[4].

We then apply the symmetry breaking procedure and obtain mass terms in the Lagrangian for each of the fermions. The masses depend on the Yukawa couplings and hence the SM has no direct predictive power for the fermion masses. The mass terms in the Lagrangian are of the form:

$$\begin{aligned}
\mathcal{L}_{fermion\ mass} &= (m_l)_{jk}\ \bar{l}^j_L\ l^k_R\ (1 + \frac{1}{v}\mathrm{H}(x)) - &(1.1)\\
&[(m_u)_{jk}\ \bar{u}^j_L\ u^k_R + (m_d)_{jk}\ \bar{d}^j_L\ d^k_R]\ [1 + \frac{1}{v}\mathrm{H}(x)] &(1.2)
\end{aligned}$$

Where the j, k indices refer to the 3 fermion generations, the L and R to the left handed doublets and right handed singlets, and the u, d to the three generations of up and down type quarks. Lepton number conservation is assumed in the SM, hence the lepton mass matrix has the diagonal form:

$$m_l = \begin{pmatrix} m_e & 0 & 0 \\ 0 & m_\mu & 0 \\ 0 & 0 & m_\tau \end{pmatrix}$$

[3]This relation holds true if we introduce further Higgs doublets: however in the case of higher Higgs field representations $\mathrm{M_W}^2 = \rho\mathrm{M_Z}^2\cos^2\theta_\mathrm{W}$, where ρ is an adjustable dimensionless parameter.

[4]In the SM neutrinos are given no Yukawa coupling, and hence remain massless.

For the quark sector we must consider the general (non-diagonal) form of the mass matrices. However, we can diagonalise $(m_u)_{jk}$, $(m_d)_{jk}$ using four unitary matrices which we denote by $V_L^u, V_R^u, V_L^d, V_R^d$. We apply these so:

$$V_L^u m_u V_R^{u\,\dagger} = m_u^{diag} = \begin{pmatrix} m_u & 0 & 0 \\ 0 & m_c & 0 \\ 0 & 0 & m_t \end{pmatrix}$$

$$V_L^d m_d V_R^{d\,\dagger} = m_d^{diag} = \begin{pmatrix} m_d & 0 & 0 \\ 0 & m_s & 0 \\ 0 & 0 & m_b \end{pmatrix}$$

hence we can rewrite the quark mass terms in the Lagrangian as

$$\mathcal{L}_{quark\ mass} = [(m_u^{diag})_{jk}\ (\bar{u}_L^{phys})^j\ (u_R^{phys})^k + (m_d^{diag})_{jk}\ (\bar{d}_L^{phys})^j\ (d_R^{phys})^k][1 + \frac{1}{v}\mathrm{H}(x)]$$

where $(u_L^{phys})^j = (V_L^u u_L)^j$ *etc*, these are the physical quark eigenstates.

When we now consider the couplings of the quarks to the Z and γ fields we find that the neutral current terms remain unchanged under the diagonalisation procedure: there are no flavour changing neutral currents at the tree-level in the SM. However for the charged current components the Lagrangian contains the following interaction terms:

$$\mathcal{L}_{quark\ \mathrm{W}^\pm\ interaction} = -\frac{g_w}{2}(\bar{u}_L^{phys})^j \gamma^\mu \mathrm{W}_\mu^\pm (V_{CKM})_{jk} (d_L^{phys})^k$$

where

$$V_{CKM} \equiv V_L^u V_L^{d\,\dagger} \equiv \begin{pmatrix} V_{ud} & V_{us} & V_{ub} \\ V_{cd} & V_{cs} & V_{cb} \\ V_{td} & V_{ts} & V_{tb} \end{pmatrix}$$

V_{CKM} is the Cabibbo-Kobayashi-Maskawa mixing matrix which expresses the coupling strength of up-type quarks to down-type quarks; flavour changing charged currents appear as a consequence of the off-diagonal terms. In general all the elements of the matrix are complex and there are 13 independent terms; however in the SM the matrix is unitary and this implies only four independent parameters.

Hence, we have indicated how the Higgs mechanism is responsible not only for the generation of the masses of the fermions and the gauge bosons, but also for the difference between the physical quark eigenstates and those of their interaction with the W boson.

1.4 W Boson

The original theory of beta-decay was proposed by Fermi in 1933 ([13]). In this theory the process was treated as a contact interaction as illustrated in Figure 1.2(a). This theory (incorporating the V-A coupling form) predicts the total cross-section for neutrino electron scattering

$$\sigma_{total(e\overline{\nu}_e)} = \frac{{G_F}^2 s}{\pi}$$

where in the SM for $s \ll \mathrm{M_W}^2$

$$\frac{G_F}{\sqrt{2}} = \frac{g_W^2}{8\mathrm{M_W}^2}$$

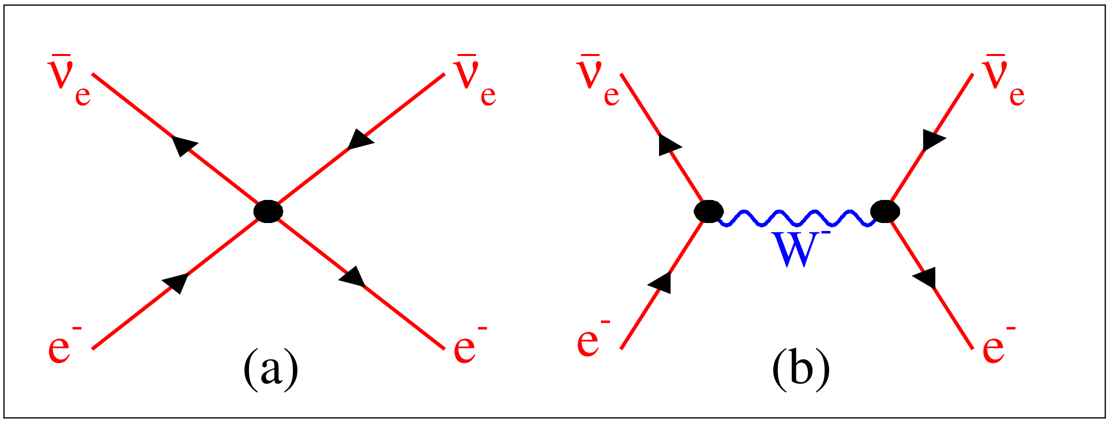

Figure 1.2: Electron neutrino interactions (a) as a contact interaction, (b) with the addition of an intermediate vector boson.

It was recognised at an early stage that the Fermi model was simply a low energy effective theory, as the cross section will violate the partial wave theory (unitarity) limit at high energies: indeed the idea of a Weak mediator, as in Figure 1.2(b), was proposed as early as 1934 by Yukawa in his momentous meson theory paper ([14]). However it was only with the emergence of the Glashow-Salam-Weinberg Electroweak theory [15, 16, 17] (discussed above) that a firm prediction for the mass of the W boson appeared. The existence of the W boson was confirmed in 1983 by the UA1 ([18]) and UA2 ([19]) collaborations on the S$p\overline{p}$S collider at CERN: they have since also been observed by the CDF and D0 collaborations on the TEVATRON Collider at Fermilab.

As both the S$p\overline{p}$S and the TEVATRON are proton anti-proton rings the production mechanism is predominantly of single W production in up and down valence quark collisions. However the observation of W bosons at DELPHI, described in this thesis, was made in e^+e^-collisions at LEP: here the dominant production mode is of W$^+$W$^-$ pairs[5] (see Figure 1.3). The s-channel W$^+$W$^-$ production mechanism provides the first direct evidence at LEP on trilinear vector-boson interactions; previous results have been obtained only by considering loop effects. Equivalently we can say that our direct knowledge of Electro-weak theory was previously largely restricted to vector-boson fermion interactions.

From the SM Lagrangian (see Section 1.3.2) one can obtain the Feynman rules [2], the triple-vertex rules for W's are given in Table 1.3. The W coupling is of Vector - Axial vector form (V-A). This form projects out the left-handed states[6] and it can thus be considered as a vector coupling between left handed states. It is the maximal parity violating form of the interaction. In the following sections we expand on these Feynman rules, noting their implications for W$^+$W$^-$ production and W decay.

Spin-1 Propagator		$\frac{-i(g_{\mu\nu}-\frac{q_\mu q_\nu}{(m)^2})}{q^2-(m)^2}$
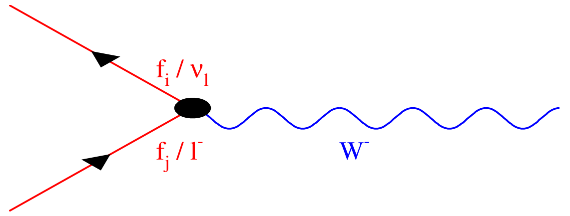	Leptons Quarks	$\frac{-ig_{\mathrm{W}}}{2\sqrt{2}}\gamma^\mu(1-\gamma^5)$ $\frac{-ig_{\mathrm{W}}}{2\sqrt{2}}\gamma^\mu(1-\gamma^5)V_{ij}$
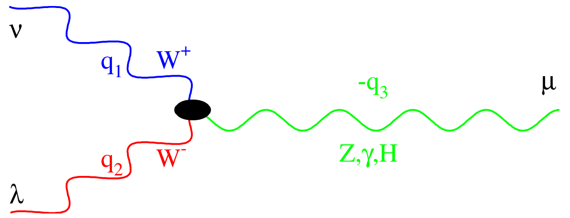	Z γ H	$ig_{\mathrm{W}}\cos\theta_{\mathrm{W}}[g_{\nu\lambda}(q_1-q_2)_\mu+$ $g_{\lambda\mu}(q_2-q_3)_\nu+g_{\mu\nu}(q_3-q_1)_\lambda]$ $ig_{\mathrm{W}}\sin\theta_{\mathrm{W}}[g_{\nu\lambda}(q_1-q_2)_\mu+$ $g_{\lambda\mu}(q_2-q_3)_\nu+g_{\mu\nu}(q_3-q_1)_\lambda]$ $\frac{ig_{\mathrm{W}}}{\sin\theta_{\mathrm{W}}}\mathrm{M_W}g_{\nu\lambda}$

Table 1.3: The Feynman rules for triple-vertex interactions of the W boson, where g_{W} is the Weak coupling constant, and V is the CKM matrix.

[5]Evidence for W pair production has also been claimed by CDF and D0 [20, 21], and for single Ws by L3[22].

[6]Strictly helicity and chirality are only equivalent in the ultra-relativistic negligible mass limit, as the helicity of a massive particle is not a relativistically invariant quantity.

1.4.1 W^+W^- Production

The leading order diagrams for W^+W^- production are given in Figure 1.3. The coupling of the Higgs boson is proportional to mass (see Equation 1.2), thus this diagram is highly suppressed due to the electron Higgs vertex and is neglected in the discussion presented below; however in a full calculation it is needed to avoid unitarity problems at very high energies.

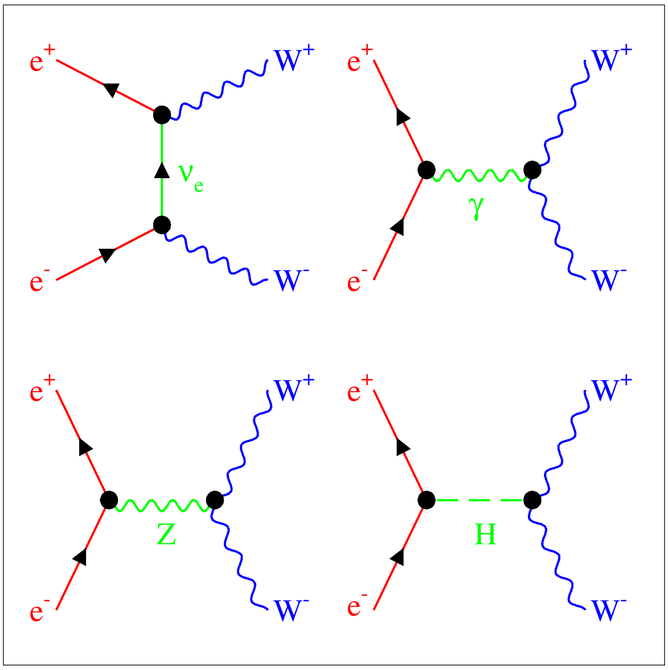

Figure 1.3: The leading order Feynman diagrams for W^+W^- production.

The matrix element for on-shell W^+W^- production at LEP at the Born level can be expressed as [23, 24]:

$$\mathcal{M} = \sqrt{2}e^2[\bar{\mathcal{M}}^\gamma + \bar{\mathcal{M}}^Z + \bar{\mathcal{M}}^\nu(\Theta)]\Delta\sigma(-1)^{\bar{\lambda}} d^{J_0}_{\Delta\sigma,\Delta\lambda}(\Theta) \tag{1.3}$$

$$\bar{\mathcal{M}}^\gamma = -\beta\delta_{|\Delta\sigma|,1}A^\gamma_{\lambda\bar{\lambda}}$$

$$\bar{\mathcal{M}}^Z = \beta[\delta_{|\Delta\sigma|,1} - \frac{1}{2\sin^2\theta_W}\delta_{\Delta\sigma,-1}]\frac{s}{s-{M_Z}^2}A^Z_{\lambda\bar{\lambda}}$$

$$\bar{\mathcal{M}}^\nu = \frac{1}{2\sin^2\theta_W\beta}\delta_{\Delta\sigma,-1}[B^\nu_{\lambda\bar{\lambda}} - \frac{1}{1+\beta^2-2\beta\cos\Theta}C^\nu_{\lambda\bar{\lambda}}]$$

where $\beta \equiv \sqrt{1-(\frac{2m_W}{\sqrt{s}})^2}$ is the velocity of the W bosons, σ ($\bar{\sigma}$)and λ ($\bar{\lambda}$) are the z components of the electron (positron) and W^+ (W^-) spins (*i.e.* their polarisation state), $\Delta\sigma = \sigma - \bar{\sigma}$, $\Delta\lambda = \lambda - \bar{\lambda}$, $J_0 \equiv max(|\Delta\sigma|, \Delta\lambda)$ is the minimum angular momentum of the system, and Θ is the scattering angle of the W$^-$with respect to the e^- in the c.m. frame.

$\Delta\lambda$	$(\lambda\bar{\lambda})$	$A^{\gamma,Z}_{\lambda\bar{\lambda}}$	$B^{\nu}_{\lambda\bar{\lambda}}$	$C^{\nu}_{\lambda\bar{\lambda}}$
± 2	$(+-),(-+)$	0	0	$2\sqrt{2}\beta$
$+1$	$(+0),(0-)$	2γ	2γ	$2(1+\beta)/\gamma$
-1	$(0+),(-0)$	2γ	2γ	$2(1-\beta)/\gamma$
0	$(++),(--)$	1	1	$1/\gamma^2$
0	(00)	$2\gamma^2+1$	$2\gamma^2$	$2/\gamma^2$

Table 1.4: Coefficients for the $e^+e^-\to$W$^+$W$^-$ production matrix element (see text). The γ used in the coefficients is $\sqrt{1-\beta^2}$, while that used in the superscript label represents a photon.

In the SM, Ws only couple to the left-handed chiral components of the electrons ($\sigma = -\frac{1}{2}, \bar{\sigma} = -\frac{1}{2}$) and hence the right handed chiral amplitudes are given entirely by the γ and Z exchange graphs of Figure 1.3 in which the W does not couple directly to the electron.

In general a massive (including virtual photons) spin-1 boson has three polarisation states. However, it can be shown [2] p143 *ff* that in conserved current reactions only transverse polarisations are possible: thus in the s-channel diagrams the γ and Z must have $J_Z = \pm 1$. Angular momentum conservation prevents the case $\lambda = -\bar{\lambda} = \pm 1$ being reached by these diagrams (see Equation 1.3, Table 1.4) and ensures that the electron and positron have σ = -$\bar{\sigma}$.

The terms $\bar{\mathcal{M}}^{\gamma}$ and $\bar{\mathcal{M}}^{Z}$ in eqn 1.3 are proportional to β. At threshold $\beta \to 0$ and hence W$^+$W$^-$ production is dominated by the t-channel neutrino exchange graph of Figure 1.3, this can clearly be seen in Figure 1.4. The phase space factor introduces a further β dependence, thus at threshold the t-channel graph cross-section has a β dependence and the s-channel cross-sections vary as β^3. Since the W bosons are produced at rest in the c.m. frame they can have no orbital angular momentum, and hence the total J of the system must be 0,1 or 2. As 0 is prevented by electron chirality considerations (as above), and 1 by CP invariance, the W helicity amplitudes are simply related by the Clebsch-Gordan coefficients for J=2.

At high energies ($\sqrt{s} \gg \mathrm{M_W}$) $\gamma \rightarrow \infty$ and $\beta \rightarrow 1$ and hence several of the coefficients in Table 1.4 $\rightarrow \infty$. The $\bar{\mathcal{M}}^{\mathrm{Z}}$ component of Equation 1.3 has two terms, the first is a parity conserving ('Electromagnetic' component) and this is cancelled by the $\bar{\mathcal{M}}^{\gamma}$ component. At high energy $A^{\mathrm{Z}}_{\lambda\bar{\lambda}} = B^{\nu}_{\lambda\bar{\lambda}}$ and hence the Weak terms (existing only for left-handed electrons) in $\bar{\mathcal{M}}^{\mathrm{Z}}$ and $\bar{\mathcal{M}}^{\nu}$ also cancel. Considering the $C^{\nu}_{\lambda\bar{\lambda}}$ term components we find they are are all suppressed by γ factors except the $(+-)$ and $(-+)$ amplitudes; due to kinematic factors the $(-+)$ amplitude dominates. The $\mathrm{W^+W^-}$ cross-section is shown in Figure 1.4, although the purely t-channel contribution $\sigma_{\nu\nu}$ grows quickly the total cross-section σ_{total} rapidly reaches its peak as the s and t channel interference terms $\sigma_{\mathrm{Z}\nu}$ and $\sigma_{\gamma\nu}$ are both negative. The well-behaved nature of the $\mathrm{W^+W^-}$ cross-section at high energies is a consequence of these cancellations, and thus of the specific forms of the gauge boson couplings in the SM: in general introducing other couplings (anomalous Trilinear-Gauge Couplings - TGCs) will produce further terms for longitudinally polarised Ws which will have divergent behaviour at high energies.

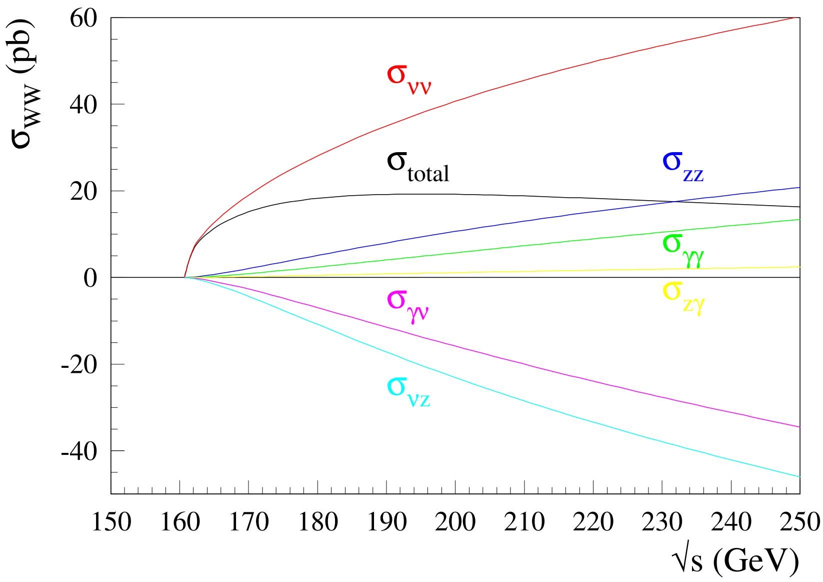

Figure 1.4: The $e^+e^- \rightarrow \mathrm{W^+W^-}$ cross-section in the Born-level approximation, the six individual contributions to the total cross-section are shown. These terms arise, when squaring the matrix element, from the interference of the three component diagrams.

1.4.2 W Decays

From the arguments already presented it is clear that the outgoing fermion and anti-fermion from a $W^{\pm}$ decay are in left and right-handed chiral states respectively. Using the Feynman rules presented in Table 1.3 the matrix element for W decay can be calculated [2] p491: in the W c.m. frame the matrix elements depend upon the angle between the W and the produced fermions, the angular dependence differs for each of the three W polarisation states.

The W bosons are produced and decay with the characteristic Breit-Wigner form of a resonance, this form and the correlations between the two W masses are discussed further in Section 6.3. The total width of the Breit-wigner Γ_{W} is produced by summing the partial decay widths for each of the accessible channels. The width for each decay channel can be obtained from the Matrix element (applying Fermi's golden rule):

$$\Gamma_{\mathrm{W}^{\pm}\to f_i \bar{f}_j} = \frac{g_W^2 \mathrm{M_W}}{48\pi} \left|V_{ij}\right|^2 N_c^f \tag{1.4}$$

where massless fermions have been assumed. For leptonic decays V_{ij} and the colour factor N_c^f are both one; for hadronic decays V_{ij} is the relevant element of the CKM matrix, and (neglecting QCD corrections [25]) N_c^f is three.

1.4.3 Corrections

The principal aim of the LEP2 measurement programme is to obtain $\mathrm{M_W}$ to a precision of approximately 50 MeV [26] or better. Achieving this objective will require accurate theoretical knowledge of the dynamics of the production and decay stages of $\mathrm{W^+W^-} \to 4$ fermions.

The calculations presented above for the $\mathrm{W^+W^-}$cross-section are at the Born level only. A full treatment must include off-shell Ws, radiative corrections, and interconnection phenomena. Brief comments on the readily calculable component of the corrections are provided in this section. For further discussion the reader is recommended to see [27]. The issues of interconnection phenomena are reviewed in the following section.

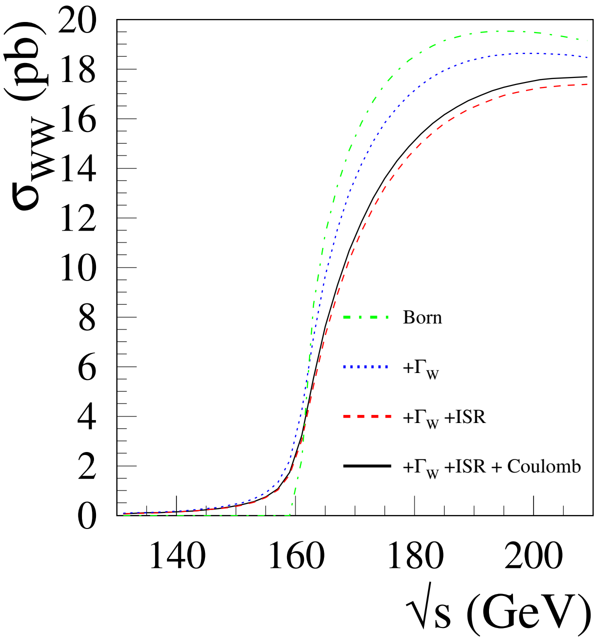

Figure 1.5: The cross-section for $e^+e^- \to W^+W^-$ in various approximations: (i) Born (on-shell) cross-section, (ii) Born (off-shell) cross-section, (iii) with first order Coulomb corrections, and (iv) with initial state radiation.

Finite Width Corrections

The approximation of stable, that is zero-width, W production is particularly bad in the threshold region. This is illustrated in Figure 1.5: on shell production of W^+W^- is obviously not permitted for the region $\sqrt{s} < 2M_W$. Instead we must treat the W s as resonances, which naturally has the effect of smearing out the W^+W^- cross-section. The first step is to generalise from the on-shell cross-section, thus:

$$\begin{aligned}\sigma(\sqrt{s}; m_{W1}, m_{W2}) &= B_{f_1\bar{f}_2}\ B_{f_3\bar{f}_4} \int_0^{\sqrt{s}} dm_{W1}\ \rho_W(m_{W1}) \\ &\quad \int_0^{\sqrt{s}-m_{W1}} dm_{W2}\ \rho_W(m_{W2})\ \ \sigma_0(s; m_{W1}, m_{W2}) \qquad (1.5)\end{aligned}$$

where

$$B_{f_1\bar{f}_2} \equiv \frac{\Gamma_{W\to f_1\bar{f}_2}}{\Gamma_W}$$

is the branching ratio for the W to the final state fermions $f_1\bar{f}_2$: to obtain the total cross-section we sum these branching ratios to 1.

The Breit-Wigner for a particle of mass m is :

$$\rho_W(m;\mathrm{M_W},\Gamma_\mathrm{W}) = \frac{1}{\pi}\frac{\Gamma_\mathrm{W}}{\mathrm{M_W}}\frac{m^2}{(m^2-\mathrm{M_W}^2)^2+m^4(\frac{\Gamma_\mathrm{W}}{\mathrm{M_W}})^2}$$

by analogy with the description used for the Z at LEP1 and as recommended for the W in [26], we use an energy dependent width which is motivated by considering the effect of (non-photonic) radiative corrections. Putting $\sqrt{s}=m$,

$$\Gamma_\mathrm{W}(s) = \frac{s}{\mathrm{M_W}^2}\Gamma_\mathrm{W}(\mathrm{M_W}^2)$$

This result (Equation 1.5) is discussed further in Section 6.3, where it is used to justify the form of the function used in the mass fitting.

Radiative Corrections

The $\mathrm{W^+W^-}$ electroweak corrections have been calculated to sufficient accuracy for this analysis and are discussed in [26]. An important correction near threshold is due to virtual photon exchange between the two W bosons, see also Section 1.5.1. In addition there are corrections due to the radiation of real photons from the initial state, the W bosons, and the final state, as well as interference effects.

At LEP2 energies initial state radiation is significant. At $\sqrt{s}$ of 175 GeV the average energy per event carried by radiated photons is 1.2 GeV [26]. The effect of ISR is to reduce the effective centre of mass energy ($\sqrt{s'}$) of the collision and hence close to threshold this reduces the $\mathrm{W^+W^-}$ cross-section (and the sensitivity to $\mathrm{M_W}$), see Figure 1.5. Since the $\sqrt{s'}$ of each event cannot now be accurately determined, this leads to distortions of the reconstructed W Breit-Wigner distribution.

The leading order (virtual one loop) corrections to the W mass are illustrated in Figure 1.6. Through these diagrams $\mathrm{M_W}$ obtains a dependence upon the top quark and Higgs boson massses. The relevant terms enter essentially as the top quark mass squared and as the logarithm of the Higgs boson mass.

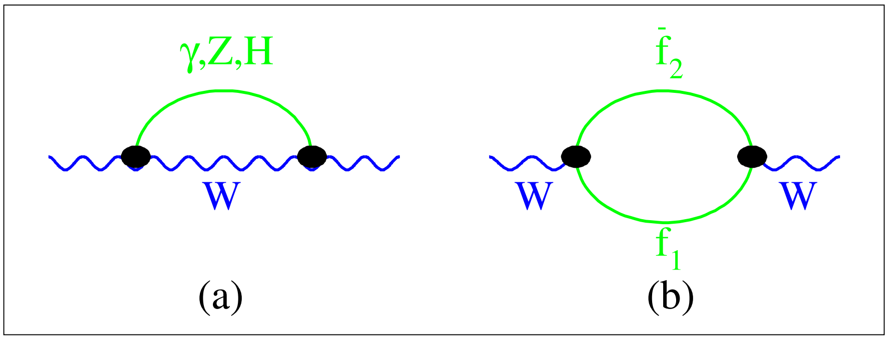

Figure 1.6: Leading order corrections to M_W (a) bosons (b) fermions.

Four Fermion Interference

The final states produced in W^+W^- decays are also accessible through other diagrams (both charged current and neutral current graphs): the effects of these processes are discussed in Section 5.7.

1.5 Interconnection Phenomena

Interconnection phenomena may obscure the separate identity of the two W bosons, so that the final state may no longer be considered as a superposition of two separate W decays. We consider here three such interconnection mechanisms: Coulomb Correction, Colour reconnection, and Bose-Einstein effects; the latter two of these mechanisms are relevant only in the $q\bar{q}'\bar{q}q'$ decay channel.

1.5.1 Coulomb Correction

The dominant $O(\alpha)$ correction (+6%) to the W^+W^- production cross-section at threshold is the Coulomb Correction [26]. The Coulomb correction results from the exchange of a photon between the two almost stationary W bosons. The correction falls rapidly with $\sqrt{s}$, and at 190 GeV it is less than 2% . Naturally, the inclusion of the finite W width also has a significant effect on the value. The threshold cross-section correction from this effect has been calculated to much better than 1% .

1.5.2 Colour Reconnection

Colour reconnection is the most commonly used term for the QCD interconnection effects between the W^+W^- decay products.

At LEP2 energies the average space-time separation between W^+W^- decay vertices is less than 0.1 fm, where this small value is a result of the large W width. However, the typical distance scale of hadronization is 1 fm. Hence, the fragmentation of the W^+ and the W^- may not be independent, and this could influence the reconstructed W mass in the $q\bar{q}'\bar{q}q'$ decay channel.

Only soft gluons (Energy $\lesssim \Gamma_W$) with a wavelength larger than the W^+W^- decay vertex distance, will be affected jointly by the action of all four quark colour charges. Consequently the reconnection effects in the perturbative decay phase are expected to be small [28].

Estimates of the effect on the W mass of the non-perturbative phase rely on Monte-Carlo fragmentation models. The introduction of reconnection effects is likely to affect the general event shape predictions of the model. It must be a pre-requisite that any generator model can be tuned to describe the high statistics LEP1 data, before its influence on the reconstructed W mass can be reliably estimated. The value of the shift on M_W is also found to be sensitive to the mass reconstruction method, and conceivably also to the event selection [26].

Colour reconnection models have been included into the `ARIADNE`, `HERWIG`, and `PYTHIA` fragmentation packages. Applying realistic experimental reconstruction methods to simulation events produced with these models, the M_W shift is found to be $\lesssim$ 50 MeV [29]. The reconstructed mass is generally, but not universally, found to be higher than the generated mass.

A model incorporating hadron formation with a more local space-time structure has been suggested by Geiger and Ellis [30, 31]. This approach to hadron formation has already been shown to improve the description of TEVATRON data [32]. The 'colour-full' Geiger Ellis scenario leads to mass shifts of up to 300 MeV. While noting that this model has not yet been tuned to LEP1 data, these predictions cannot simply be dismissed.

Some Colour reconnection models have experimentally verifiable predictions: these include a reduction of up to 10% in the charged particle multiplicity in W^+W^-

$\rightarrow q\bar{q}'\bar{q}q'$ decays compared with $W^+W^- \rightarrow l\overline{\nu}_l q\bar{q}'$ decays. There is no suggestion in the 1996 LEP data of a multiplicity reduction [33] [34], but the statistical precision is not yet sufficient to rule out any of the models.

We note that while colour reconnection may be a nuisance when we wish to determine M_W, it provides a potentially illuminating environment for learning about non-perturbative QCD.

1.5.3 Bose-Einstein Effect

In hadronic decays large numbers of pions are produced, these bosons must obey Bose statistics. Hence, we expect an enhancement of the production of identical particles at small momentum separations, relative to the hypothetical state of uncorrelated production. As already noted above, the space time regions of the two W bosons are overlapping and Bose-Einstein effects may occur between the two Ws. The Bose-Einstein correlation radius has been measured at LEP1 [35] to be approximately 0.5 fm.

It is unclear whether event charged multiplicities are expected to increase due to this effect, or just that identical bosons will be pulled closer together. Note that any effects on multiplicity are, in practice, at least partially accounted for by the tuning of the generators to the data.

The semi-classical treatment of the Monte-Carlo simulation fragmentation programs are intrinsically unsuited to modelling the quantum mechanical Bose-Einstein effect. The simulation approaches adopted fall into two categories, which we will term 'local' and 'global' [28].

In the global approach the generated particles are re-weighted; the weights are intended to account for all the multiparticle correlations. Models in this class commonly predict mass shifts compatible with zero.

The most developed model is of the local type and is implemented in `JETSET` [36]. In this approach momentum shifts are applied to pairs of generated identical bosons. Energy-momentum conservation is thus violated and non-identical particles must be shifted to compensate. The authors predict shifts of up to 30 MeV at 170 GeV, rising to 50 MeV at higher energies: generally the reconstructed mass is shifted above the true value.

A method has been proposed to assess W^+W^- Bose-Einstein correlations by DELPHI [37] (and also adopted by ALEPH[38]). In this method $W^+W^- \rightarrow q\bar{q}'\bar{q}q'$ events are compared with $W^+W^- \rightarrow l\overline{\nu}_l q\bar{q}'$ events. No enhancement is currently observed, but the current statistics are not capable of discriminating between the models.

Chapter 2

The DELPHI Detector and the LEP Accelerator

2.1 Introduction

This chapter introduces the LEP accelerator and the DELPHI detector. DELPHI is comprised of a significant number of sub-detectors each of which is described. At the end of this chapter, a guide to the DELPHI data read-out and offline processing structure is provided.

The reader is advised to consult the literature for more information on the topics discussed in this chapter, notable starting points are [7, 39] for DELPHI and [40, 41] for LEP.

2.2 The LEP Accelerator

The **L**arge **E**lectron **P**ositron collider (LEP) is located on the French-Swiss border at the European Laboratory for Particle Physics (CERN), as shown in Figure 2.1.

The LEP main ring is 26.7 km in circumference and lies within a stable layer of rock at an average depth of about 100m below the surface. The tunnel was excavated as a sequence of straight sections and arcs; the ring consists of eight lengths of each type. The e^+, e^- beams are bent by around 3000 dipole magnets which are located in the curved sections of the ring. These curved sections contain the full electromagnetic guide field system of LEP: this consists of not only the dipole magnets, but also quadrupoles, sextupoles, and horizontal and vertical dipole

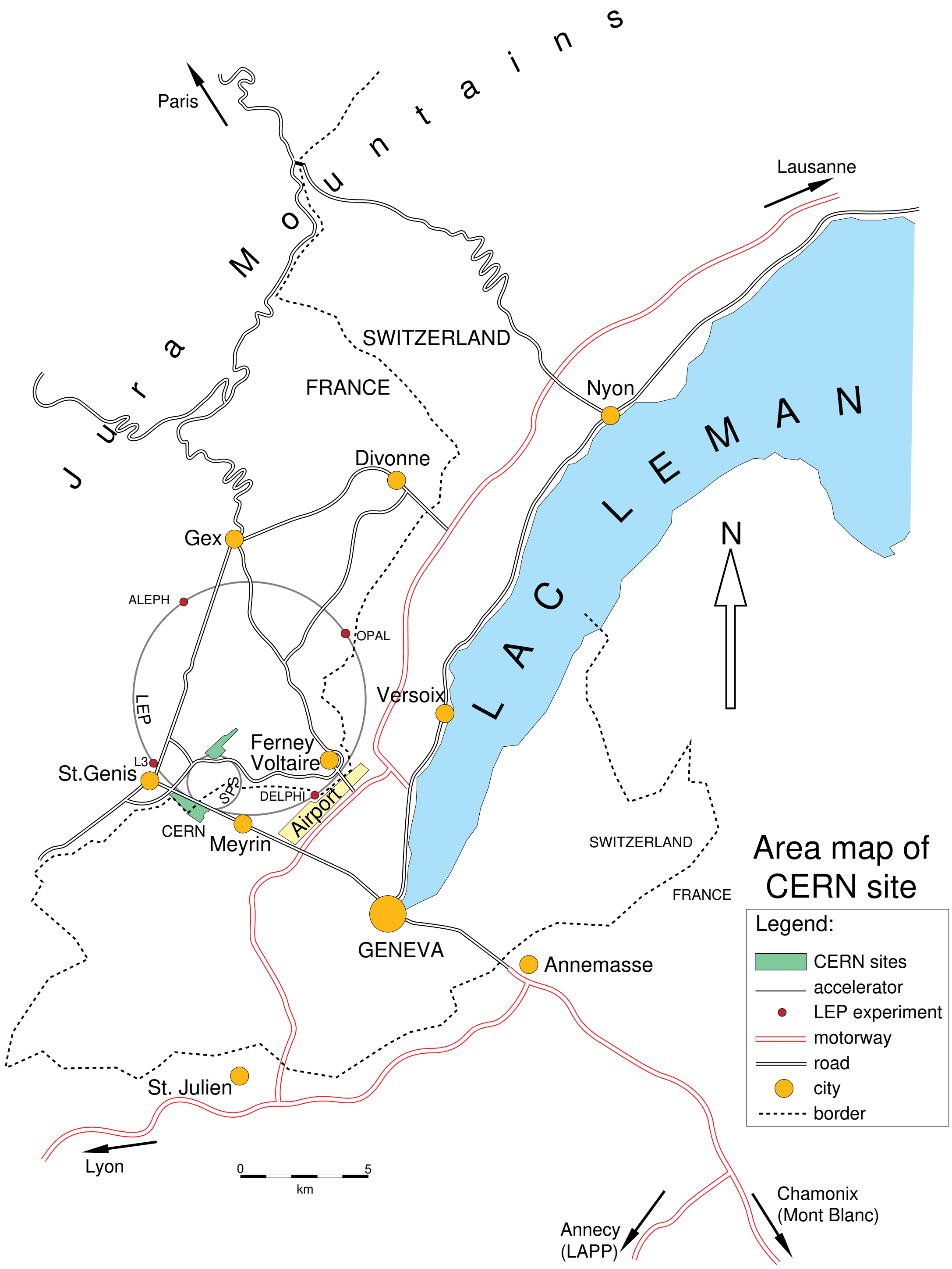

Figure 2.1: The location of the CERN laboratory and the LEP accelerator.

correctors. The quadrupoles act on the beam as focussing lenses, with the sextupole magnets compensating for the dependence of the focussing strength on the beam energy. The horizontal and vertical correctors are used to further guide the beam through its vacuum pipe.

The four multi-purpose detectors (L3, ALEPH, OPAL, DELPHI) are located in alternate straight sections. Positioning the detectors in straight sections protects the experiments from the synchotron radiation of the beams. The centre of each straight section, where the beams are brought to a focus, is known as an interaction point.

The e^+, e^- beams are accelerated using RF cavities located in the straight sections[1] . The cavities are required to increase the beam particle energies from their value at injection into LEP (20 GeV) to the value required at collision. Once the required acceleration has been achieved, LEP is operated as a storage ring, and the cavities are used to replace the energy lost by the particles in synchotron radiation. The energy radiated by a particle in synchotron radiation is proportional to $\frac{E^4}{r}$, where E is the beam energy and r the radius of curvature. The 120 five-cell copper cavities used at LEP1 were supplemented by 170 superconducting (Nb and Nb coated Cu) cavities in 1996. The superconducting cavities increase the accelerating power with the minimal increase in power consumption. It is planned that 272 superconducting cavities will be installed before the accelerator run in 1998; space constraints require the removal of half the copper cavities.

The bunches of each beam must be tightly focussed ('squeezed') in the centre of the detectors in order to increase the luminosity. This is accomplished by a set of superconducting quadrupoles with very strong field gradients that focus the transverse beam dimensions to about 10 μm and 150 μm in the vertical and horizontal planes respectively.

However, we do not always wish the beams to collide every time they cross : the beams are prevented from colliding in the four interaction points (IPs) without detectors, and no collisions are required in the ring during the ramping (*i.e.* accelerating) phase. Electrostatic separators are installed at each of the IPs to vertically deflect the electron and positron beams from each other. The separators are

[1] Only the sections near L3 and OPAL were used during LEP1.

also used to fine tune the beam positions, steering the beams to be head-on when collisions are required.

2.2.1 Injector Chain

The accelerator complex on the CERN site is shown in Figure 2.2. LEP utilises a chain of mostly pre-existing accelerators to accelerate the electron and positron beams before they are injected into the main ring.

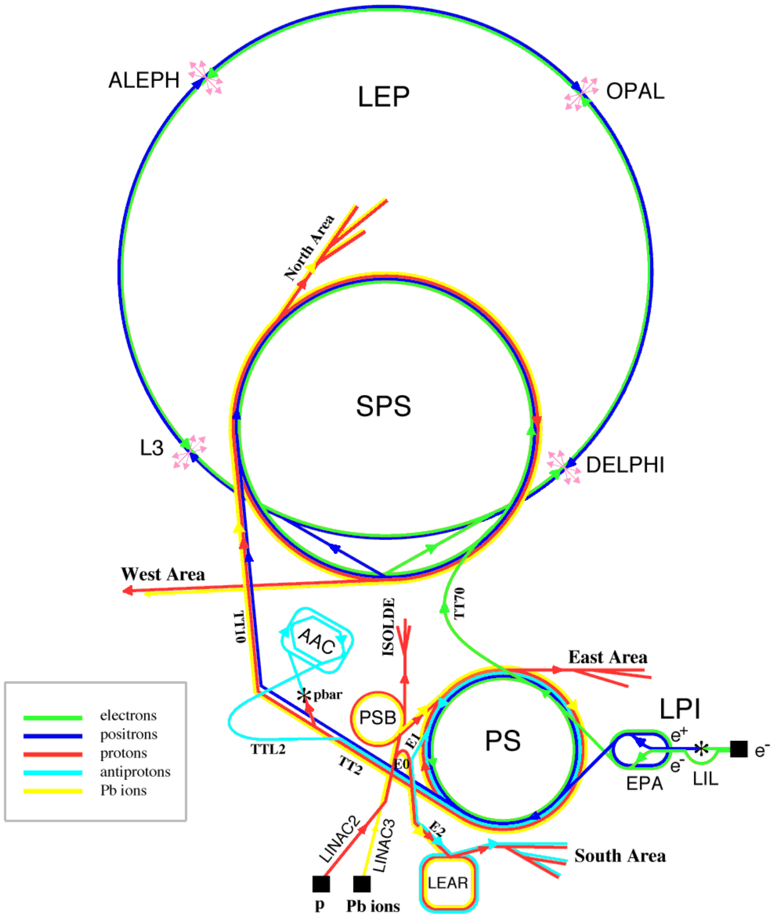

Figure 2.2: The CERN Accelerators. The following key includes only those components used by LEP. LEP: Large Electron Positron collider, SPS: Super Proton Synchrotron, PS : Proton Synchrotron, LPI: LEP Pre-Injector, EPA: Electron Positron Accumulator, LIL: LEP Injector Linac.

- A high intensity electron source and linear accelerator (LINAC) produce a beam of 200 MeV electrons. Positrons are produced by bombarding a tungsten target with this electron beam.

- Electrons are produced by a second lower intensity electron gun.
- A LINAC accelerates both the electron and positron beams to 600 MeV.
- The Electron Positron Accumulator (EPA) is used to store these beams.
- The beams are then injected into the Proton Synchotron (PS), where they are accelerated to 3.5 GeV.
- The Super Proton Synchotron (SPS) further accelerates the beams to 20 GeV, when they are injected into the LEP main ring.

2.2.2 Performance

From 1989 to 1995 LEP accumulated, accelerated, stored and collided electron and positron beams of around 45 GeV energy. Approximately four million Z decays were collected by each of the four multi-purpose experiments. In the autumn of 1995, the energy was increased to around 65 GeV per beam. The LEP2 phase of operation started in 1996 with the beam energy rising first to 81 then 86 GeV: it is the data collected during this period that is used in this thesis; the beam energy in 1996 is discussed further in Section 3.7.

The instantaneous luminosity achieved in 1996 commonly exceeded $10^{31}\mathrm{cm}^{-2}/s$; however, the integrated luminosity delivered by LEP of 24.7 $\mathrm{pb}^{-1}$was lower than had been anticipated. A contributing factor to this low value was the delay in the start of data-taking resulting from obstructions in the beam-pipe[2]. The integrated luminosity collected by DELPHI is discussed further in Section 3.6.

In 1996 LEP was operated with four bunch trains of electrons and four of positrons circulating in the ring. Each bunch train can contain a number of bunch trains or wagons. In 1996 most of the running was performed with one wagon; two wagons were used for the latter part of the 161 GeV running . The time between beam cross-overs (BCOs) was 22 μs, and between wagons was 250 ns.

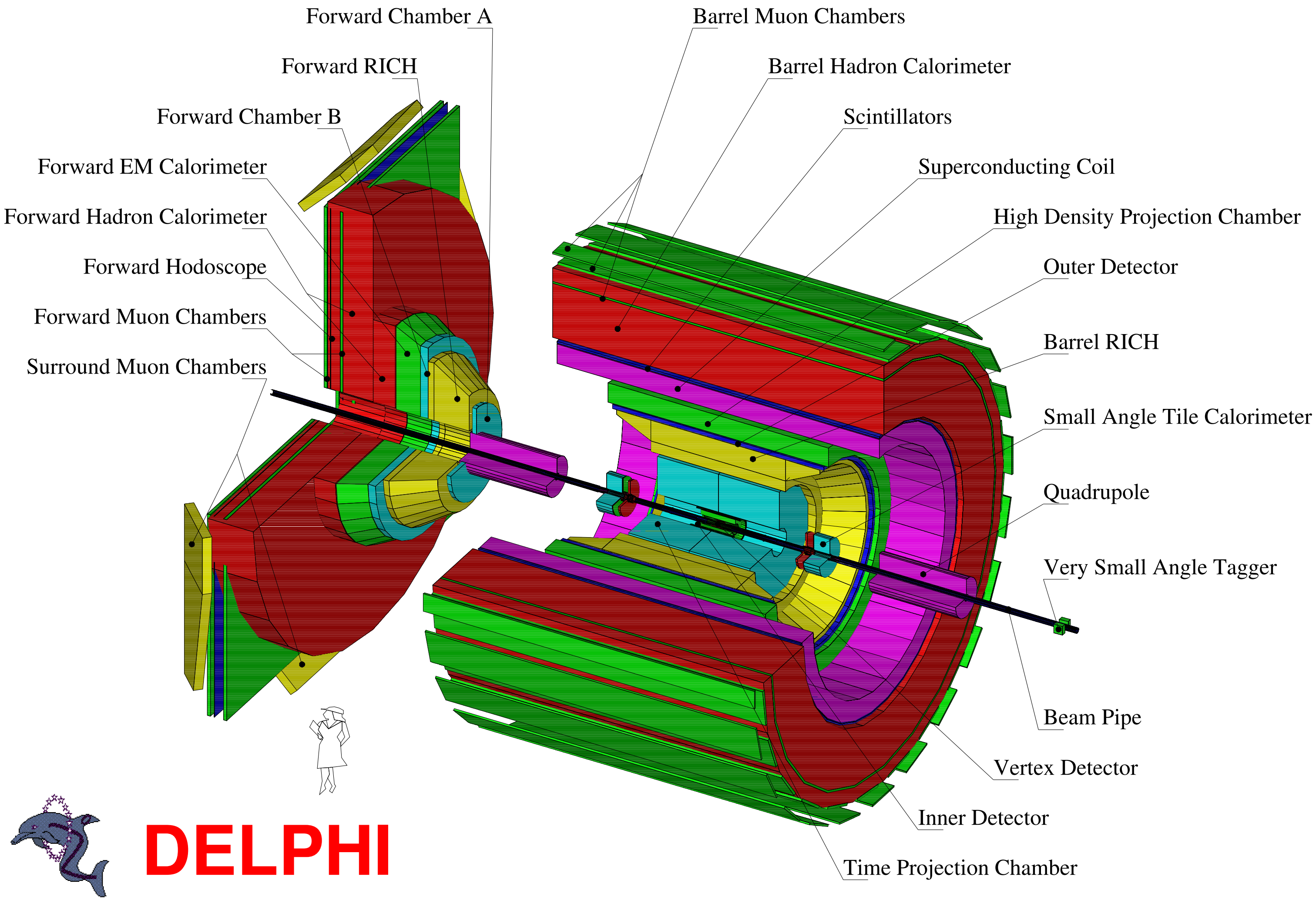

Figure 2.3: A cut-away view of the DELPHI detector.

Figure 2.4: The Delphi Cavern: the four storey structure of cabins contain the detector read-out electronics.

2.3 The DELPHI Detector

The Delphi (**DE**tector with **L**epton, **P**hoton and **H**adron **I**dentification) detector is the most elaborate of the four general purpose Lep experiments. The design aims for high tracking efficiency and good calorimetry performance over nearly the full solid angle. The detector includes both powerful particle identification capacities and precise vertex determination. The sub-detector designs which lead to these capabilities are briefly reviewed below.

As illustrated in Figure 2.3 Delphi consists of a central cylindrical barrel section and two forward endcaps (only one is shown). The endcaps may be retracted to allow access to the inner part of the barrel. A 5.2 cm radius Beryllium beam-pipe runs along the cylinder's axis. The detector has an overall length and diameter of over 10m and weighs 3500 tons. The scale of the detector can be seen in the photograph Figure 2.4.

[2]Heineken reaches the part(icle accelerator)s that other beers cannot.

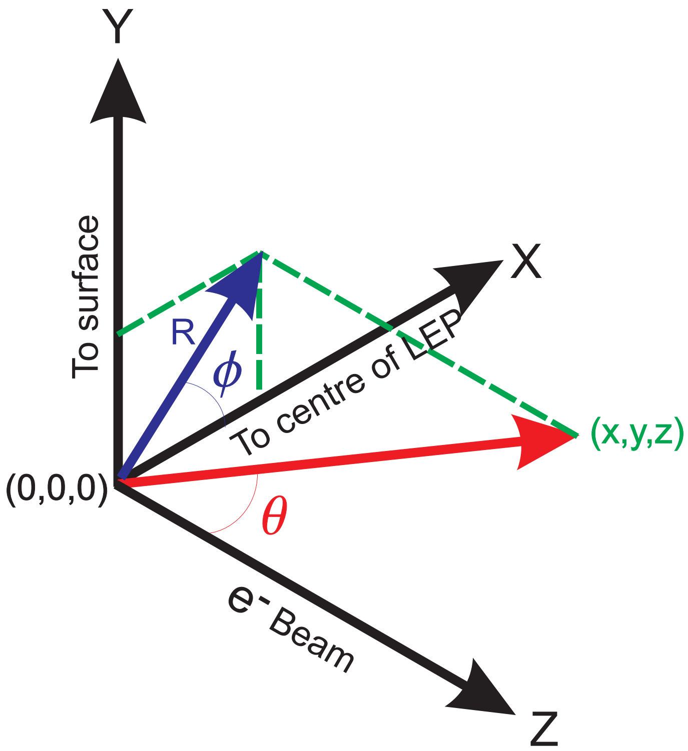

Figure 2.5: The DELPHI co-ordinate systems (x,y,z) and (R,ϕ,θ) are defined with respect to the nominal centre of DELPHI.

The DELPHI co-ordinates system is illustrated in Figure 2.5: both the cartesian axes (x, y, z) and the polar axes (R, θ, ϕ) systems are used in DELPHI.

2.3.1 Tracking Detectors

The trajectory of charged particles produced in collisions is determined from their ionising properties in the tracking detector active volumes through which they pass. The curvature of a particle in the DELPHI magnetic field is used to determine its charge and momentum.

The acceptances and resolutions of the tracking detectors described below are given in Table 2.1. Most charged particles will have space points measured in more than one of these detectors. It is therefore necessary to combine tracking information from all the subdectors: the algorithm used is discussed in Section 3.1.1.

The resolution for a 45 GeV/c muon, where the track contains information from all the barrel tracking detectors (VD,ID,TPC,OD), is discussed in [39]. The

	Position R (cm)	$\|z\|$ (cm)	Acceptance θ(deg) $(+z)$	Max. No. Points along Track	Resolution per point (σ) (mm)
VD	6.6/9.2/10.6	≤ 24	≥ 21	$R\phi$: 3 z: 3	$R\phi$: 0.008 z: 0.010
VFT			$11 - 26$	4	x, y 0.1
ID drift ID straws	$11.8 - 22.3$ $23 - 28$	≤ 62 ≤ 105	≥ 10 ≥ 15	24 5	$R\phi$: 0.085 $R\phi$: 2.4
TPC	$35 - 111$	≤ 134	≥ 20	$R\phi, z : 16$ $R\phi : 192$	$R\phi$: 0.23 z: 0.9
OD	$198 - 206$	≤ 232	≥ 43	$R\phi : 5$ $z : 3$	$R\phi$: 0.11 z: 44
FCA	$30 - 103$	$155 - 165$	$11 - 33$	6	0.3
FCB	$53 - 195$	$267 - 283$	$11 - 35$	12	0.25

Table 2.1: Specifications and performance of the DELPHI tracking detectors. This description applies to the detector that was operated during 1996. The resolution in z is given for tracks which cross the VD at 90°.

mean resolution on the inverse of the momentum $\sigma(1/p)$ is found to be 0.57×10^{-3} $(\mathrm{GeV/c})^{-1}$.

Solenoid

The tracking system is enclosed within the worlds largest superconducting solenoid: it is 7.4 m long and has a radius of 2.6 m. The solenoid generates a highly uniform 1.2 Tesla field; correcting coils at the ends ensure that the field remains parallel to the z-axis. The return yoke of the solenoid incorporates the hadron calorimeter (see below).

Vertex Detector (VD)

A significantly upgraded vertex detector [42] was installed during the spring of 1996, the length of the detector having been doubled to 48 cm. The barrel vertex detector consists of three concentric shells of doped silicon strip detectors at average radii of 6.6, 9.2 and 10.6 cm. The detectors contain strips both parallel and perpendicular to the z-axis: the central sensors of the middle layer are the only part of the silicon tracker which does not supply three dimensional information. The strips parallel to the z-axis are spaced at 25 μm intervals, and every other diode is read out via

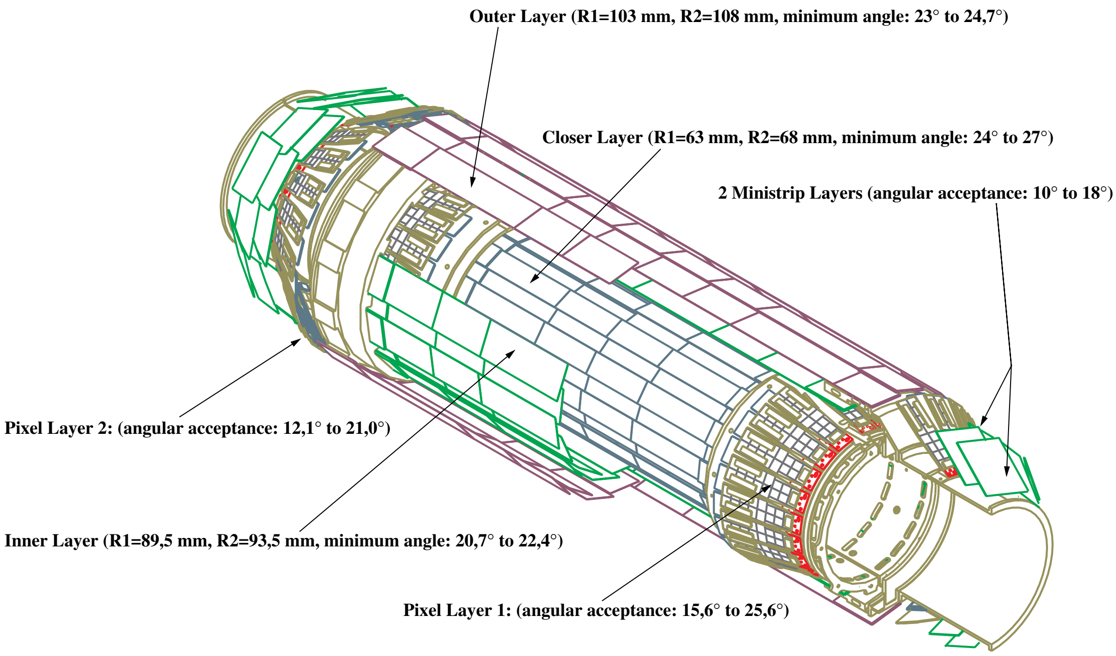

Figure 2.6: The Silicon tracker consists of three concentric cylinders of silicon strips known as the vertex detector, and in the forward region two layers of pixels and two of ministrips referred to as the very forward tracker.

capacitive coupling. A single hit resolution of eight μm is achieved. The strip pitch for the detectors providing Rz information varies from 50 μm to 150 μm, to give the best resolution for tracks of different inclination. The amount of material used is kept to a minimum by the use of double-sided detectors and light mechanics. Over 99% of the detector is operational, and the data were immediately available for use in physics analyses.

Very Forward Tracker (VFT)

The VFT consists of two layers of mini-strip and two layers of pixel detectors: though only 5/8 of the pixel detectors were installed in 1996. The ministrips have a 100 μm pitch and consist of back-to-back strips with an 86° angle between them: the small stereo angle is used to aid pattern recognition. The pixel upgrade was completed in 1997, and contains 1.2 million detector elements each of dimension 330×330 μm^2 . The aim of the detector is to improve the tracking efficiency and resolution in the polar angle region 10° to 25°. The detector has been demonstrated to be performing well (see [42])), an efficiency of over 96% has been achieved. However, compatible data and simulation processings in 1996, including the VFT in tracking, have not yet been produced, and hence this detector is not used in this thesis.

Inner Detector (ID)

The inner detector consists of two concentric sections: an inner drift chamber, surrounded by straw tube detectors.

The high resolution drift chamber is divided into 24 azimuthal sectors. The electric fields are designed so that the drift velocity is proportional to the radius from the DELPHI z-axis. Sense wires lie down the centre of each sector, and from the arrival time of the signals the track may be reconstructed in the $R\phi$ plane, subject to a left-right ambiguity.

Five cylindrical layers of straw tube detectors provide further measurements in the $R\phi$ plane. These layers were introduced in 1995. For the data analysed in this thesis, they were used in the triggering but not in the track reconstruction.

Time Projection Chamber (TPC)

The principal tracking detector of DELPHI is a 2×1.5 m long drift chamber which is illustrated in Figure 2.7. The TPC provides three dimensional spatial information, and measurements of particle $\frac{dE}{dx}$. The chamber is symmetric around the $z = 0$ plane.

A charged particle passing through the detector causes ionisation to occur in the active drift volume: this volume is filled with a mixture of Argon and CH_4 in the proportion 4 : 1 and maintained at atmospheric pressure. The drift field of the chamber, nominal value 150 V/cm, is parallel to the z-axis and gives rise to a drift velocity of 67 m/ms.

The endcaps of the TPC are multi-wire proportional chambers, divided into six sectors. 192 sense wires are strung in the $R\phi$ plane perpendicular to the radial line that runs along the centre of each sector. The charge avalanches near the sense wires induce pulses on the 16 concentric circles of cathode pads which lie on the back plane 4 mm from the wires. The $R\phi$ co-ordinate is determined from the induced charges on the cathode pads. The z position is calculated from the arrival time of the drifted electrons. $\frac{dE}{dx}$ information is obtained from the charges collected on the sense wires.

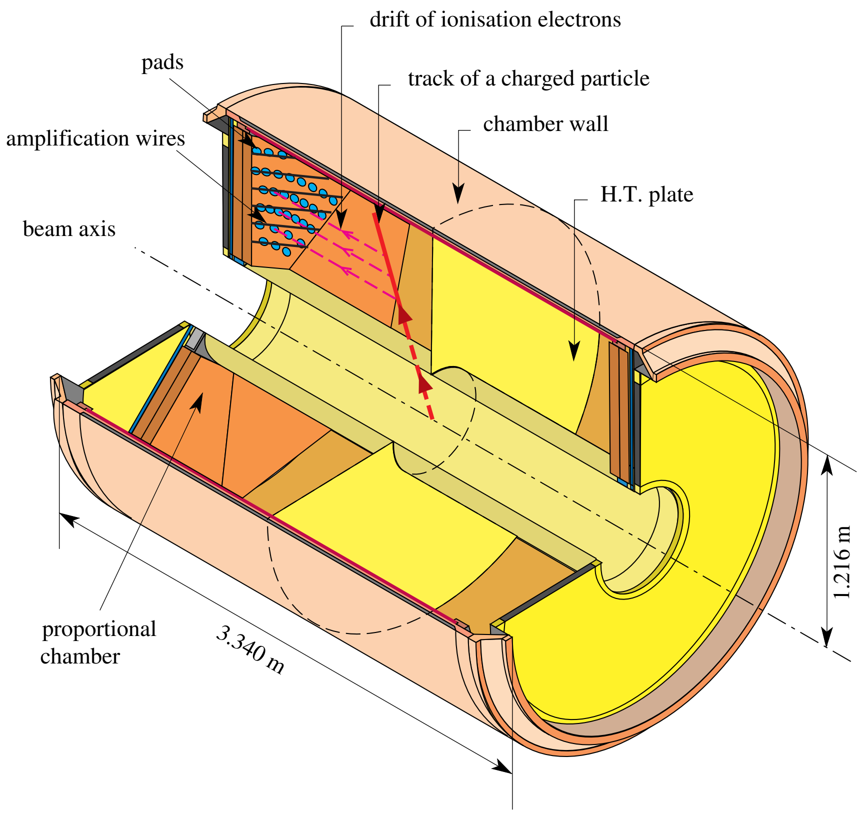

Figure 2.7: The internal structure of the Time Projection Chamber, showing the passage of a charged particle through the detector.

Outer Detector (OD)

The incorporation of the barrel RICH (see below) detector into the DELPHI design constrained the volume available for the TPC. The inclusion of an extra tracking detector at larger radius is essential to improve the momentum resolution of fast particles. The OD lies between the barrel RICH and the electromagnetic calorimeter.

The Outer Detector consists of five layers of drift tubes operated in the limited streamer mode. All layers provide an $R\phi$ co-ordinate measurement, and three also provide z measurements from the relative timing of signals at both ends.

Forward Chamber A (FCA)

The two FCA chambers are positioned on opposite sides of DELPHI next to the endcaps of the TPC. The chambers contain three sets of two staggered layers of drift tubes, operating in limited streamer mode. Each set of drift tubes is rotated by 120° in the $R\phi$ plane with respect to the previous set, thus aiding pattern recognition.

	Position $r(cm)$	$\|z\|\ (cm)$	Acceptance θ (degrees)	Depth
HPC	$208-260$	≤ 254	≥ 43	$18X_0(\sim 0.6\lambda)$
FEMC	$46-240$	$284-340$	$10-36.5$	$20X_0(\sim 1\lambda)$
HCAL barrel	$320-479$	< 380	≥ 43	$\sim 6\lambda(\sim 57X_0)$
HCAL forward	$65-460$	$340-489$	$10-43$	$\sim 6\lambda(\sim 57X_0)$
STIC	$6.4-41$	$218-249$	$1.7-10.6$	$27X_0$

Table 2.2: Specifications of the DELPHI calorimeters.

Forward Chamber B (FCB)

A further tracking chamber (FCB) is included in the DELPHI endcaps between the RICH and electromagnetic calorimeters: a location analogous to that of the OD in the barrel. FCB is a drift chamber with two independent semi-circular modules in each endcap. The modules contain 12 read-out planes of wires. Each plane of wires lies in the $R\phi$ plane but is strung at a 120° angle to the previous layer.

2.3.2 Calorimetry

The DELPHI calorimetry system is used to measure the energy of charged and neutral particles. The acceptances and resolutions of the DELPHI calorimeters are defined in Table 2.2.

Electromagnetic Calorimeters

Electromagnetic calorimeters aim to measure the energy of electrons and photons. e^+e^- pair production and *bremsstrahlung* of photons occur as particles decelerate in the Coulomb fields surrounding nuclei: the combined effect of these processes is the development of electromagnetic showers. We define the radiation length X_0 as the length of material which reduces by *bremsstrahlung* the mean energy of an electron by a factor of e. The DELPHI electromagnetic calorimetry uses two different designs: one for the barrel region and the other in the endcaps.

High Density Projection Chamber (HPC)

The barrel electromagnetic calorimeter is a sampling calorimeter which uses the time projection technique to collect the charge from electromagnetic showers. The detector consists of 144 modules arranged in 6 rings. A typical module (see Figure

2.8) is a trapezoidal box of width 52 to 64 cm, height 47 cm and length 90 cm. Each HPC module is a small TPC with layers of high density material dividing the gas volume. The layers of lead wires act as the conversion material and also provide the electric field cage. As in the TPC a proportional wire chamber is used to read-out the drift volume. Thus, a three dimensional picture of the evolution of an electromagnetic shower is obtained. For fast triggering purposes, a plane of scintillators is inserted into one of the HPC sampling gaps close to the shower maximum.

The energy resolution $\sigma(E)/E$ for 45 GeV electrons is about 6.5% [39].

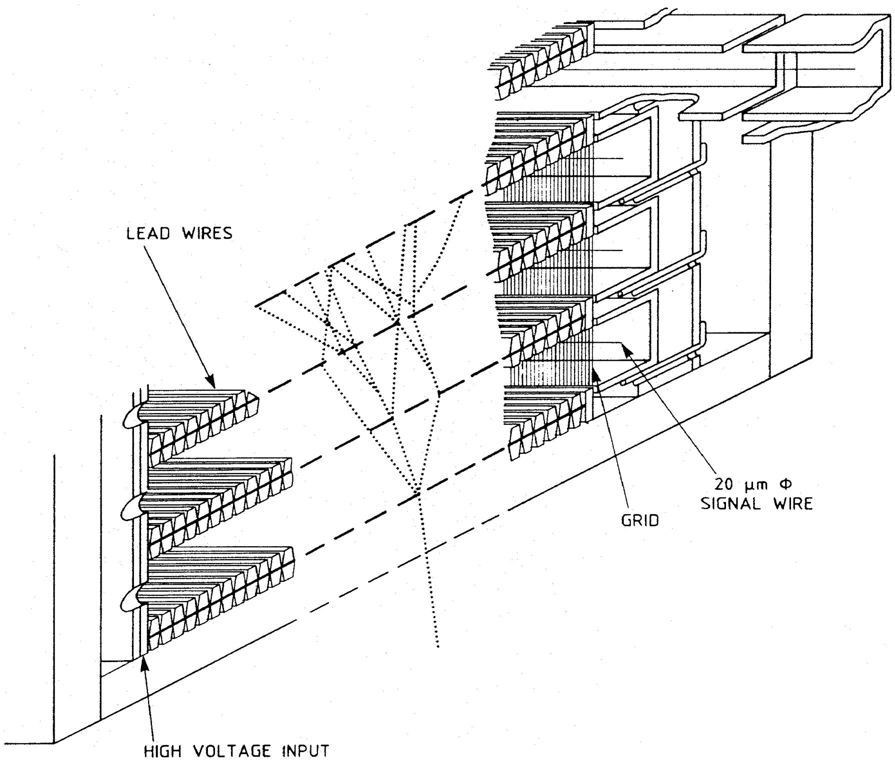

Figure 2.8: The internal structure of a HPC module, showing the development of a typical electron shower.

Forward Electromagnetic Calorimeter (FEMC)

Each endcap contains an array of 4532 lead glass blocks which constitute the forward electromagnetic calorimeter. The blocks are truncated pyramids which are mounted to point near to the interaction point: a small tilt angle ($\approx 1^{\circ}$) prevents particles escaping through the insensitive regions between the blocks. The charged particles of the electromagnetic shower that develops in the blocks emit Čerenkov photons (see RICH below). The Čerenkov photon signal from each block is then read-out by a photomultiplier.

The energy resolution $\sigma(E)/E$ for 45 GeV electrons is about 4.8% [39].

Hadronic Calorimeter (HCAL)

Hadron calorimeters rely on detecting the showers of secondary particles produced by inelastic hadronic interactions with the nucleons of a converter material. We define the interaction length λ in a material as the mean free path of a particle before undergoing an inelastic interaction.

The iron return yoke of the DELPHI solenoid also comprises the conversion material for the hadron calorimeter. The sampling calorimeter consists of layers of limited streamer tubes sandwiched between 5 cm thick iron plates: there are 20 layers in the barrel, and 19 in the endcaps. In the barrel, two end-to-end streamer tubes run the length of DELPHI. The geometry requires that tubes of lengths down to 40 cm are required in some areas of the endcaps. The cathode strips around the streamer tubes are capacitively coupled to copper-clad read-out boards. The read-out pads are shaped to form towers pointing to the intersection point; in the barrel (endcaps) pads of 5 (4 or 7) adjacent layers are combined into a tower. The HCAL read-out geometry is illustrated in Figure 2.9. The standard calorimetry information (as used in this thesis) relies on the information collected on the cathode pads; however, anode read-out information is now also available.

In the barrel region, the energy precision in the hadron calorimeter is found to be $\sigma(E)/E = 0.21 \ \oplus \ 1.12/\sqrt{E}$, where E is in GeV [39].

Small Angle Tile Calorimeter (STIC)

The STIC is a sampling lead-scintillator calorimeter that covers polar angles below that of the FEMC. The calorimeter's measurements are used both in physics analyses (including this thesis), and in determining the luminosity: the luminosity determination is discussed in Section 3.6.

Threaded through the 47 lead-scintillator layers of the calorimeter are 1600 wavelength shifting optical fibres. These read-out fibres run perpendicular to the scintillator plates. This calorimeter geometry is known as the *Shashlik* technique: it

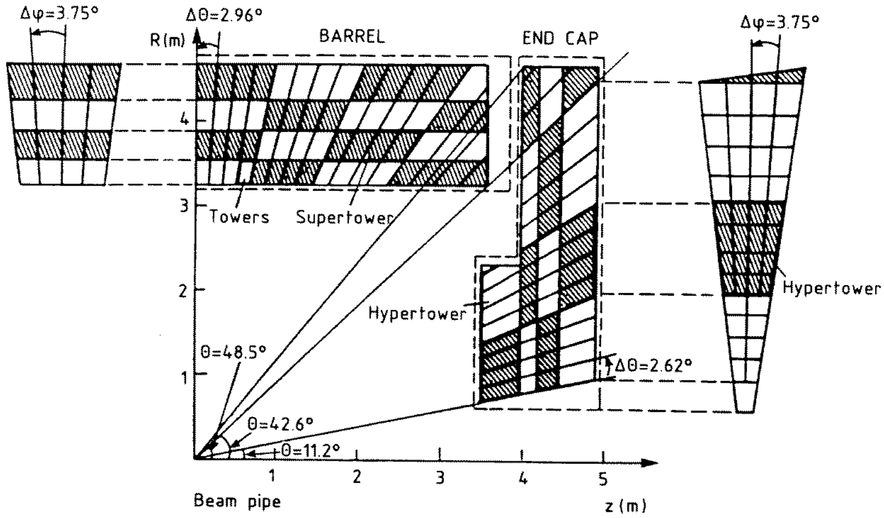

Figure 2.9: The projective readout geometry of the HCAL.

	Position r (cm)	Position $|z|$ (cm)	Acceptance θ(deg)	No. Points along Track	Resolution per point σ (mm)
MUB	~ 445	≤ 385	$52 - 128$	$2 - 6$	$r - \phi$: 1.5 z: 10
MUF	$70 - 460$	463/500	$9 - 43$	$4(x, y)$	x, y: 1.0 z: 10
MUS	550	487	$42 - 53$	2	10×10

Table 2.3: Specifications and performance of the DELPHI muon chambers. The resolution quoted for the MUS is given in the local coordinate system of each chamber.

combines a highly uniform energy resolution with good photon collection, while retaining excellent detector hermeticity.

Two layers of scintillator planes are placed in front of the calorimeter: these are used to separate charged from neutral showers. The reconstruction of the shower direction is aided by two layers of silicon strips embedded in the calorimeter. An acceptance defining tungsten nose, that had been present in one arm of the detector, was removed for the 1996 run.

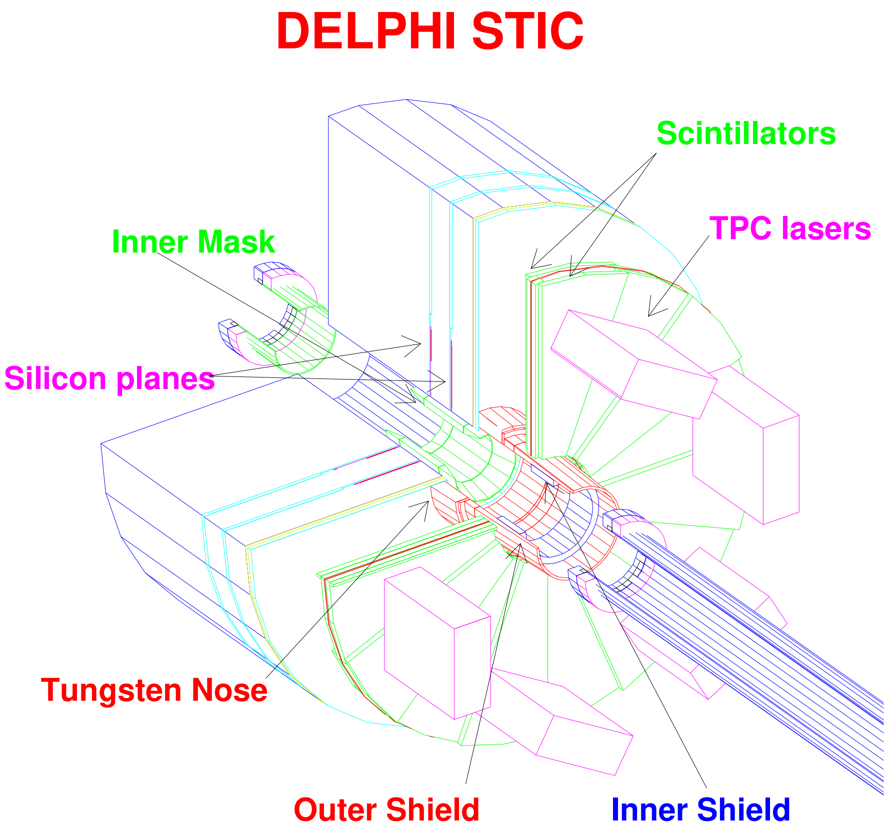

Figure 2.10: A cut-away diagram of the STIC.

2.3.3 Particle Identification

Ring Imaging Čerenkov Detectors (RICH)

Charged particles travelling faster than the local speed of light in a di-electric (radiator) medium, cause the polarized molecules of the medium to emit photons in a cone around the particle trajectory. The opening angle of the cone depends upon the particle's velocity. Hence, when combined with a measurement of the momentum or energy, an estimate of the particle's mass can be obtained. Thus, the RICH detectors can be used for particle identification.

DELPHI has RICH detectors both in the barrel and in the endcap sections. Both the RICH detectors contain two perfluorocarbon radiator media: a liquid radiator is used to identify particles of low momenta (0.7 to 8 GeV/c), and a gas radiator is used from 2.5 to 25 GeV/c. Photo-sensitive TPCs are used to detect the Čerenkov photons.

Muon Chambers

The DELPHI muon detection system consists of three separate sub-detectors : the first system covers the barrel region, the second the forward region, and the final component covers the gap between the barrel and the endcap regions.

Barrel Muon Chambers (MUB)

The barrel muon detector was built and is maintained by the Oxford Group. The detector consists of three layers of muon chamber modules, and is divided into 24 azimuthal sectors. A typical sector of the barrel muon chambers is illustrated in Figure 2.11. The inner modules lie 20 cm inside the iron of the Hadron Calorimeter, and the outer modules outside the iron. The peripheral modules are arranged to cover the gaps not seen by the previous two layers of modules. Each module layer comprises a number of drift chambers arranged in two active layers. The location of the inner modules makes maintenance extremely difficult. In this module layer a third layer of chambers is included; these chambers are used only when adjacent chambers malfunction. The chambers within each module are staggered, thus resolving the inherent left-right ambiguity of drift chambers.

A typical muon drift chamber has a gas volume of $363 \times 20 \times 1.6$ cm^3; the gas used is comprised of 85.5% argon, 8% methane and 6.5% carbon dioxide.

An electric field of nominal value 400 V/cm is produced between the central anode wire and the 13 copper cathode strips which run along the top and bottom inner surfaces of the chamber. The timing of the signal on the anode wire is used to determine the $R\phi$ hit position. One of the central cathode strips is comprised of an insulated copper winding with a signal propagation speed of approximately 0.5 cm/ns. The z co-ordinate of a particle is determined by the relative timing of the signals travelling on this delay line to the ends of the chamber.

Forward Muon Chambers (MUF)

The forward muon detectors consist of two detection planes: the first lies 20cm inside the iron of the forward HCAL, the second outside. Each plane comprises two orthogonal layers of drift chambers. As was described above for MUB, the anode signal timing provides one co-ordinate and the timing of a delay line signal is used to obtain the orthogonal co-ordinate. However, the MUF chamber operation differs from MUB as the forward drift chambers are operated in limited streamer mode.

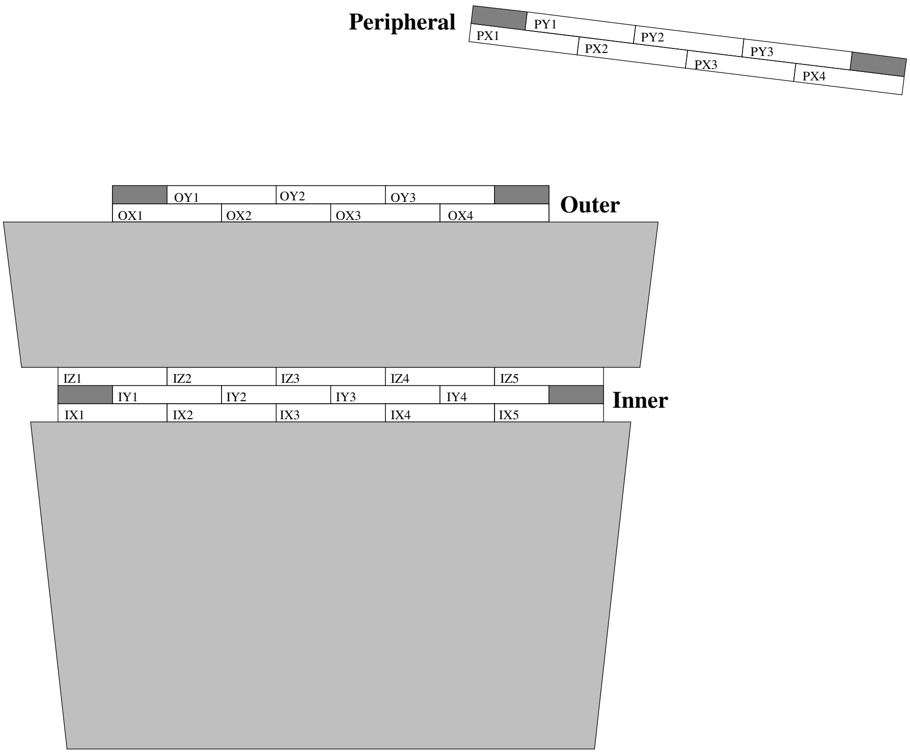

Figure 2.11: A sector of the barrel muon chambers is shown in the $R\phi$ plane.

Surround Muon Chambers (MUS)

The surround muon chambers cover the gap between the MUB and MUF chambers at a polar angle of around 45°. At each end of DELPHI eight chambers are attached in pairs to the edges of the endcaps. The chambers on the top and sides of the endcap are inclined at 45° to obtain the maximum angular coverage. Each module is comprised of two staggered layers of streamer tubes. The tubes are the same as those used in the HCAL.

2.3.4 Other Sub-Detectors

Here we briefly review the other DELPHI detectors which have not been introduced above.

The Very Small Angle Taggers (VSAT) lie at $z = \pm 7.7m$, and are calorimeters covering the polar angle between 5 and 7 mrad: these devices are not used in this analysis.

A cylinder of scintillation counters known as the Time of Flight counters (TOF) lie between the solenoid and its return yoke: they provide a fast event triggering capability. In the endcaps, the forward scintillator Hodoscopes (HOF) perform the same role.

Cracks exist in the electromagnetic calorimetry system of DELPHI between the HPC modules at 90° polar angle, and in the coverage of the HPC and FEMC at 40°. Supplementary photon taggers are installed to cover these gaps. In addition scintillation counters are also placed around the feet of DELPHI directly into the ϕ cracks between the HPC modules. Thus, almost complete hermeticity is obtained.

Radiation monitors are mounted on the support bars of the inner detector ($z \approx$ 1.5 m) on one side of DELPHI. Under extreme beam conditions a beam-dump is automatically triggered. The purpose of the beam-dump is to provide protection for the VD and VFT from prolonged high background radiation levels.

2.4 Data Acquisition System, Triggering, and Offline Processing

The Data Acquisition System (DAS)[3] reads out digitised data from the detector, storing the results for subsequent analysis. The data flow is subject to the DELPHI trigger systems and proceeds according to timing signals from a central trigger control supervisor. Detector operation is monitored and controlled by the Slow Controls system. This section is based on [39].

2.4.1 Trigger

The role of the trigger system is to reduce the rate of beam cross-overs (45,000 Hz) to the desired read-out and storage rate (a few Hz). The DELPHI triggering algorithm is composed of four successive levels of increasing selectivity (T1,T2,T3,T4).

- T1

The T1 decision is taken at 3.5 μs after the BCO. Hence the decision relies only on information from detectors with fast read-out times: ID, TPC($\theta \leq$ 43°), OD, FCA, FCB, TOF, HOF, HPC scintillators, EMF,and MUB are included. The decision taken is based on the individual detector information; correlations are not taken into account. The trigger rate is typically 700 Hz.

[3] In DELPHI the acronym used is DAS, rather than the more common DAQ.

- T2

The signals from the TPC, HPC and MUF, and detector correlation information are now available. A decision is made 39 μs after the BCO. A positive T2 decision triggers the acquisition of the data collected by the front-end electronics. The trigger rate is typically 5Hz.

- T3

The T3 level repeats the T2 logic using more detailed detector information. Signals from tracks, muon chamber hits, and calorimeter deposits are analysed. The decision is taken asynchronously with respect to the BCO. This trigger halves the T2 trigger rate.

- T4

T4 is based on a tailored version of the DELPHI reconstruction program `DELANA` and rejects events without tracks pointing to the interaction region or significant energy deposits in the calorimeters. This final trigger level again roughly halves the trigger rate.

2.4.2 DAS

The detector read-out and triggering is controlled by the DELPHI DAS system. The DAS is based on the FASTBUS standard.

Each detector uses its own front-end electronics. Almost all front-end modules are equipped with a buffer that can hold four events. When a T2 trigger is received, the information is switched to the next buffer (if available). The handling of the trigger and the read-out of the front-end digitizers are handled by the crate processor. The crate processor controls the read-out if T2 is passed and performs the local T3 processing.

If T3 is passed data is transferred via optical fibres to the surface: T4 processing is then performed.

The data is written to disk and then copied to tape (10 Gb Digital Linear Tape) in the CERN central computing centre. The offline data analysis farm of DELPHI is then used to perform the final reconstruction.

2.4.3 Offline System

The raw data is written out by the data acquisition system (see above). The raw data consist of the unprocessed digitized signals from each of the detectors for each triggered event. This data must be processed by the DELPHI offline system to produce data suitable for direct use in physics analyses.

The main component of this processing is performed by the DELPHI central analysis program `DELANA` [43]. `DELANA` performs the required data calibrations, pattern recognition, and track fitting: the track reconstruction algorithm is discussed in Section 3.1.1. `DELANA` also performs basic event classification that can be used to select events of interest to specific classes of analysis. Some standard particle identification algorithms are also performed at this stage. The output of `DELANA` is a Data Summary Tape (DST).

During the high energy running phases of LEP2 a series of specialized event analysis tags have been performed concomitantly with `DELANA`. This DELPHI Analysis For New Events (DAFNE) package [44] allows the identification of potentially interesting new events within two hours of data taking. The analysis tags include the author's W^+W^- tag[4], which was used to identify the first W^+W^- events.

Further forms of DST are produced from the master DST for use in the physics analyses. More sophisticated processing (*e.g.* b quark tagging algorithms) and particle identification algorithms are performed at this stage.

All the DELPHI data storage formats are based on `ZEBRA` [45], the CERN data management system.

A number of standard tools exist in DELPHI for extracting and analysing information from the DST. The analysis documented here relies upon the packages `PHDST` [46], `SKELANA` [47], and `WWANA` [48]. The standard DELPHI W physics analysis package `WWANA` is discussed further in Appendix A.

[4]The W^+W^- tag was co-written with R. Chierici and A. Tonazzo. The author also contributed the original first level pre-identification filter for `DAFNE` and the original two-photon collision tag.

Chapter 3

Track Reconstruction and Data Selection

3.1 Introduction

3.1.1 Tracks

Following these introductory remarks, the standard charged track reconstruction procedure of DELPHI will be outlined. The main text of this chapter will then describe the selection of the reconstructed tracks that are used in the analysis. This track selection is primarily developed for use in hadronic events. For simplicity, however, the selection is used for all the analyses in this thesis: where the selection differs for low multiplicity events it is indicated in the text. However, the author considers further data simulation comparisons are necessary for leptonic final states, and these studies are reviewed in section 3.9.

The data taken in 1996 were the first to include the extended barrel Vertex Detector and the Very Forward Tracker: these are described in Section 2.3.1. The extended barrel vertex detector was used in the tracking for all of the DELPHI physics publications at LEP2. At the time of writing, however, simulation events were not available incorporating the VFT in the tracking, and hence this detector is not included in this analysis. The author's studies suggest that this detector could lead to a 20% increase in reconstructed charged tracks in the polar angle region 10 - 25°.

The principal aim of the track selection procedure is to ensure that, after the selection, the tracks in simulation events provide a reliable description of the types of tracks observed in the data. If an acceptable description of the data at the track level is obtained, a suitable description of the global event properties will then naturally follow. However, we wish to retain the maximum amount of information available for our analysis. Fortunately, the class of tracks in data that are likely to be modelled worst are also the group that contain the least information: these are the tracks which have been badly reconstructed. Other classes of track that we hope to remove by this selection procedure include fake tracks (for example, those produced by electronics noise), and cosmic radiation particles.

The alignment of the detector in previous years relied on the large statistics collected at the Z peak. The reduced statistics available in 1996 necessitated the use of high energy data, cosmic ray muons, and two photon collision events in alignment studies. Given the changes in procedure required for LEP2 running, it is especially important to check the track selection for the 1996 data sample.

3.1.2 Data Selection and Simulation Production

The selection of the data samples to be used in this analysis requires a discussion of the trigger, run quality, luminosity and energy studies that have been performed.

The final section of this chapter provides a brief introduction to the techniques used to obtain the simulation events. Generator and fragmentation programs are discussed, as well as the modelling of the DELPHI detector.

3.1.3 Event Selection

The data and simulation plots that are shown in the following sections were produced on the two event samples taken at the Z peak during 1996. These events were taken directly before both periods of high energy running. These events thus provide us with a reasonably high statistics, high purity event sample that can be compared with the simulation events; they also allow us to check that significant alignment problems did not occur between the two running periods. Naturally, similar checks were also performed on the high energy data.

The standard DELPHI hadronic event selection was applied following [49]. The basis of this selection at the Z peak is :

- Number of Charged Tracks $N_{CH} > 4$
- Charged Track Energy $> 12\%\ \sqrt{s}$
- For N_{CH} <11 we require $\sqrt{E^2_{forward} + E^2_{back}} < 90\%\ E_{beam}$

where the final cut is on the energy deposits observed in the forward electromagnetic calorimeter (FEMC) in both end-caps: this is used to reduce the Bhabha background[1]. This selection has 95% efficiency for Z→$q\bar{q}$ and includes a background of under 1%.

Checks on the high energy $q\bar{q}$ events were performed using similar selection criteria. Note that these cuts will have a high efficiency for W^+W^- events as well as the dominant Z/γ→$q\bar{q}(\gamma)$ contribution. Full details of this selection performance are presented in [50].

- Number of Charged Tracks $N_{CH} > 7$
- Charged Track Energy $> 15\%\ \sqrt{s}$
- $\sqrt{E^2_{forward} + E^2_{back}} < 90\%\ E_{beam}$

The key to the graphs in this section (Figures 3.2 to 3.8) is provided in Figure 3.1. For charged tracks the simulation tracks are divided into two categories: those for which there is an associated track amongst the simulation truth information, and those for which a good match with a generated track was not found. This division into 'good' (associated) and 'fake' (non-associated) categories for the simulation tracks is provided only for the charged track selection plots, not for the neutral energy clusters. The data collected at the Z resonance is divided into two samples: firstly that collected before the 161 GeV data (this is known as Period 1); secondly, that collected two months later before the 172 GeV data (referred to as Period 2).

[1] The reconstructed charged multiplicity in Bhabha events can be high due to the conversion of radiated photons into e^+e^- pairs.

Unless otherwise stated the distributions are shown after all selection cuts have been applied. The distributions are normalised to the integrated luminosity collected (see section 3.6) at the Z peak during period 1: thus absolute normalisation differences are visible as well as differential variations.

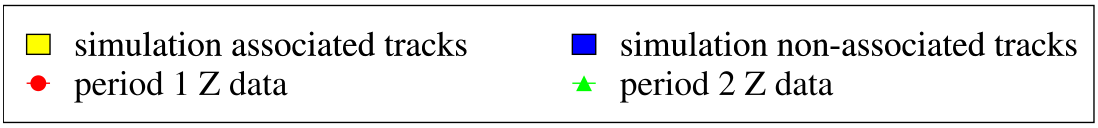

Figure 3.1: Key to the data and simulation track selection comparison plots. For charged tracks the simulation tracks are divided into two categories (see text); for neutral energy clusters this distinction is not available. The collected data at the Z resonance in 1996 is divided into two samples.

3.2 Charged Tracks

3.2.1 Reconstruction of Charged Tracks

The track reconstruction algorithm is implemented within the DELPHI off-line analysis program `DELANA`(for further information see [39]).

The first stage of the reconstruction program is performed by independent routines for each of the sub-detectors. The raw data from each sub-detector is analysed, and calibration procedures applied, in order to form the basic space points or 'hits'. Where possible, local pattern recognition is then performed within the sub-detector. Hits that are consistent with forming part of a track are associated as a track element or T.E. These track elements provide the input to the global DELPHI track search.

The main track search algorithm used in the barrel region starts with the track segments seen in the TPC. These track segments are then extrapolated to the other sub-detectors and compatible track elements are identified. Track searches based on other detector combinations such as VD-ID, ID-OD, and the forward chambers are also used.

All strings of track elements found by the above search techniques are passed through the full track fitting process and any remaining ambiguities are resolved.

The track fitting procedure is based on Kalman filter techniques [51] and accounts for multiple scattering and energy loss in the material between the measurements.

3.2.2 Selection of Charged Tracks

Impact Parameters

Tracks that originate at the primary vertex of the event and are well-reconstructed carry the principal event information. The distance of closest approach of the track to the electron beam collision point provides a suitable way of selecting these tracks; this enables us to reject badly reconstructed tracks, cosmic radiation particles, and also those tracks from secondary interactions of particles with the material in the detector. Here, we cut on the distance of closest approach in the $R\phi$ plane to the beam-spot, and the distance along the Z-axis of this point: these are known as the impact parameters. The impact parameters are also given a sign which may be derived from considering the path of a negatively charged particle travelling from the perigee. If the trajectory encircles the origin, the impact parameter is positive.

The beam spot is calculated for each file sequence of data[2] by fitting the impact parameter distributions of selected tracks [52].

The impact parameter distributions are presented in Figure 3.2. In the lower plots, we show the fraction of tracks which have associated simulation truth tracks as a function of the impact parameters. As anticipated, these quantities are observed to fall as the absolute value of the impact parameter increases; thus demonstrating that these variables discriminate between good and fake tracks. The impact parameter distributions show a good level of agreement between data and simulation. The cuts imposed were :

- $IP_{R\Phi} < 4$ cm
- $IP_Z < 4 \times cosec(\theta)$

where the latter cut varies with the polar angle of the track. This dependence is introduced because the Z distance to the point of closest approach in the $R\phi$ plane is a less reliable indicator of the track's true Z distance of closest approach when the track is travelling in the forward direction.

[2] A file sequence corresponds to a data taking period of typically 30 minutes.

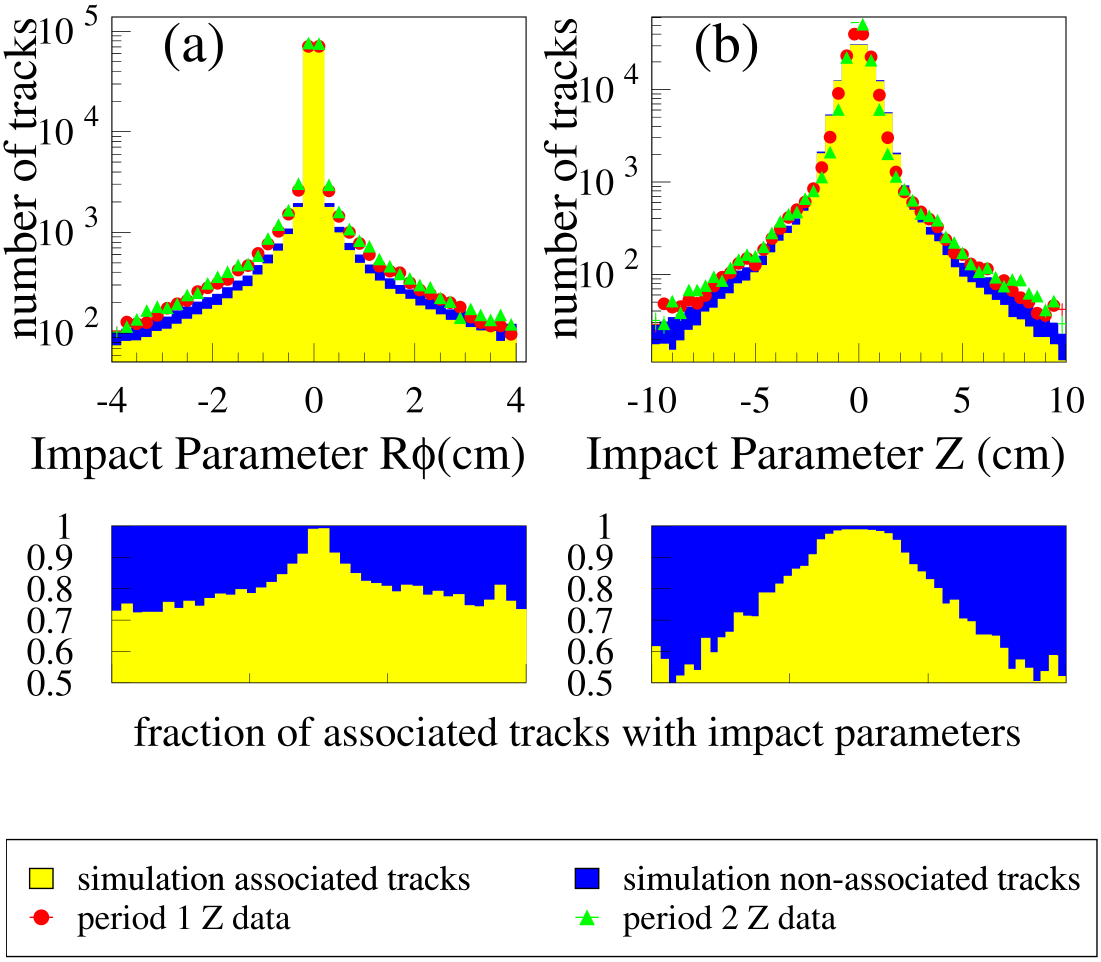

Figure 3.2: Impact parameter distributions with respect to the beam-spot in data and simulation (a)$R\phi$ (b) Z. The upper plots show the number of selected tracks with impact parameters, and the lower the proportion of tracks in the simulation with an associated truth track.

Track Momentum and its Error

The reconstruction of charged tracks is inefficient for particles of very low momentum, due to the small radius of curvature and the more significant effects of multiple scattering. The quality of the reconstructed tracks degrades at low momentum and the fraction of non-associated tracks increases. In this regime ($<$ 400 MeV), it was observed that data simulation agreement is degraded: hence these tracks are rejected. After applying this cut, good agreement is observed over the full momentum range (see Figure 3.3(a)).

Tracks for which the trajectory parameters are badly determined (for example, where the track reconstruction χ^2 was large, or the error on the parameters of the contributing T.E.s are excessive) are removed by imposing an additional cut. This selection is based on the estimated fractional momentum error of the track $\Delta p \;/\; p$. In Figure 3.3(b) the fraction of non-associated tracks can be seen to increase with $\Delta p \;/\; p$: hence, this variable is considered a good criteria for judging the quality of the reconstruction. We reject tracks for which the estimated error on the momentum Δp is larger than the track momentum p.

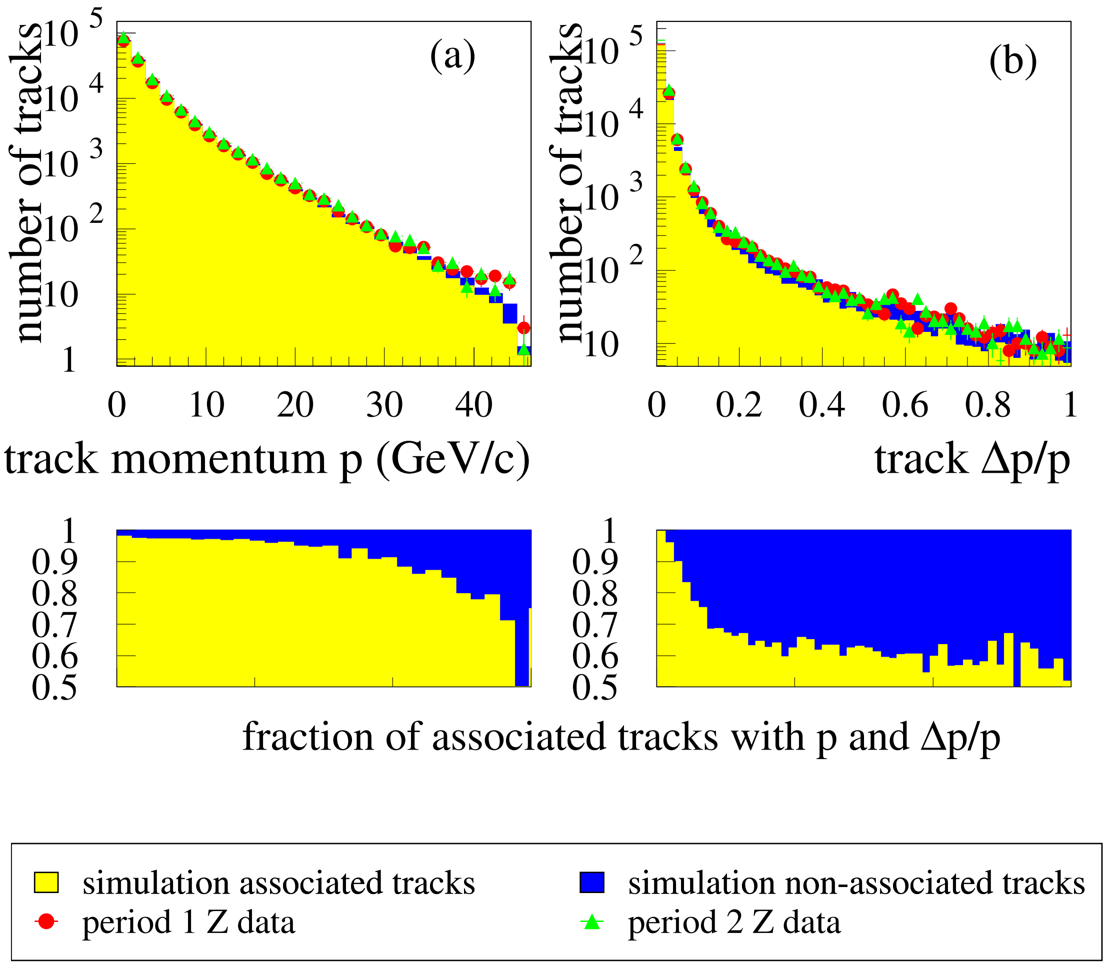

Figure 3.3: The distribution of the number of observed tracks with the track momentum (a) and its relative error (b). The upper plots show the number of selected tracks with impact parameters, and the lower the proportion of tracks in the simulation with an associated truth track.

Tracking Detectors

Figure 3.4 shows the number of track elements observed in each tracking detector. A given selected track is comprised of several T.E.s and thus each reconstructed track has multiple entries in this plot. Good agreement in this distribution is a necessary, but not sufficient, condition of good tracking agreement: disagreements may still occur amongst the large number of tracking detector combinations. From the study of these more detailed plots, the problems apparent in Figure 3.6 were seen.

The track length is defined as the distance along the track between the first and last tracking chamber hits recorded on the track; its distribution is shown in 3.5. Significant disagreement was observed between the data and simulation in the small number of tracks of very low length, these are not shown in the Figure. The cut imposed was :

- Track Length > 20 cm

The two plots 3.4 and 3.5 reveal that even after the event selection has been performed some discrepancies remain. These differences occur mainly between the data and the simulation; however, the two data-taking periods agree well, indicating that detector alignment changes over the data-taking period are not observed. The discrepancies visible in these plots concern the principal DELPHI barrel tracking chambers and could not easily be solved by further track selection. The normalisation of the plots are in reasonable agreement. The simulation has 4% less tracks than the period 1 data. This is not a significant discrepancy: although it is probably too large to be explained by the neglection of backgrounds in the simulation, or by uncertainties on the recorded luminosity. The normalisation of the two data taking periods differ by only 2%. However, the relative proportion of the tracks with an OD point is reduced in the data (at the 10% level) compared with the simulation - leading to a reduction of the peak at 200 cm plus track lengths (see Figure 3.5) and a corresponding increase in the peak at lower track lengths.

Amongst recent amendments to the track reconstruction process, a track search including VD-ID points only, was included [53]. In the central region of the plot (Figure 3.6), the search is found to recover a number of associated tracks in the 90° TPC crack; unfortunately, the data simulation agreement is bad and hence these tracks are rejected. In the polar region between the OD and the forward tracking chambers, the results of this tracking search were very problematic in this

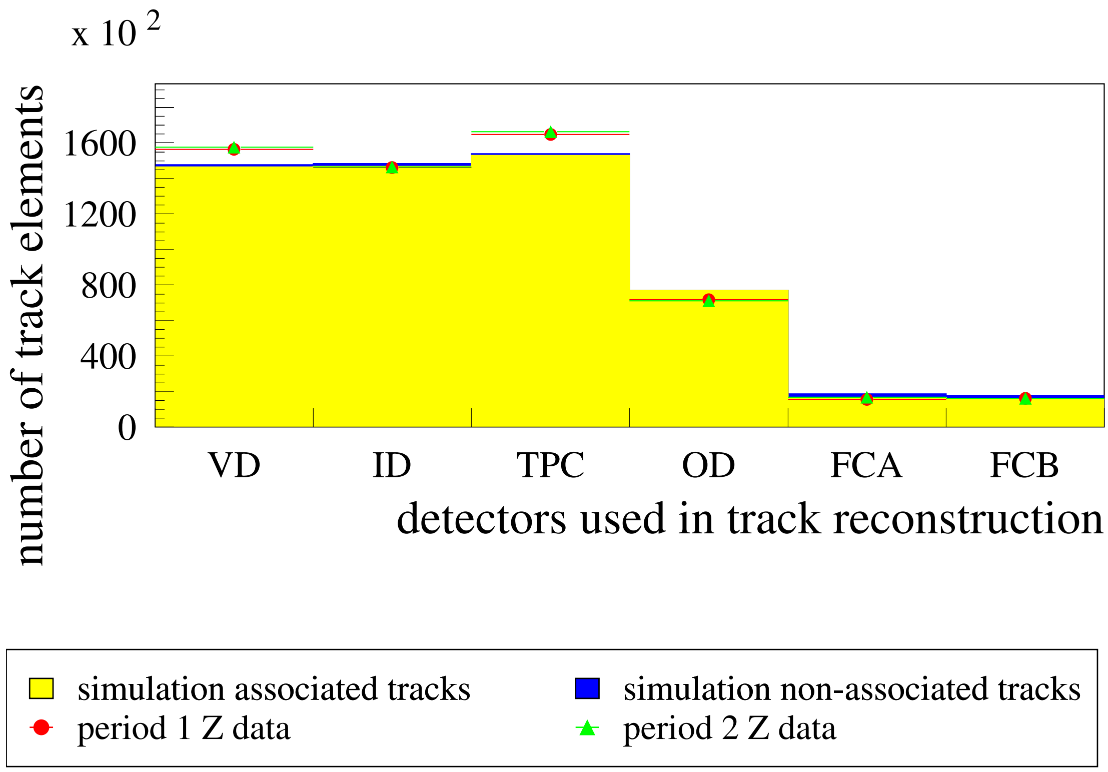

Figure 3.4: Number of track elements on the selected tracks for each tracking chamber. Note each track has multiple entries in this plot.

data processing [3]: large numbers of high momentum fake tracks are produced. The selection imposed was :

- VD-ID track $\theta > 50$
- VD-ID track $\theta < 130$
- VD-ID track $\theta < 85$ OR $\theta > 95$

Unphysical High Momentum Tracks

Unphysical high momentum tracks are an occasional product of the track fitting procedure. In the selected hadronic events, before cuts are applied, tracks of momentum greater than 75% of the beam energy[4] occur at the rate of one in 400.

[3] This was caused by the mis-assignment of VD Z information, and has been solved for future data processings.

[4] Only 1% of leptons from W decays have a true momentum greater than 60 GeV.

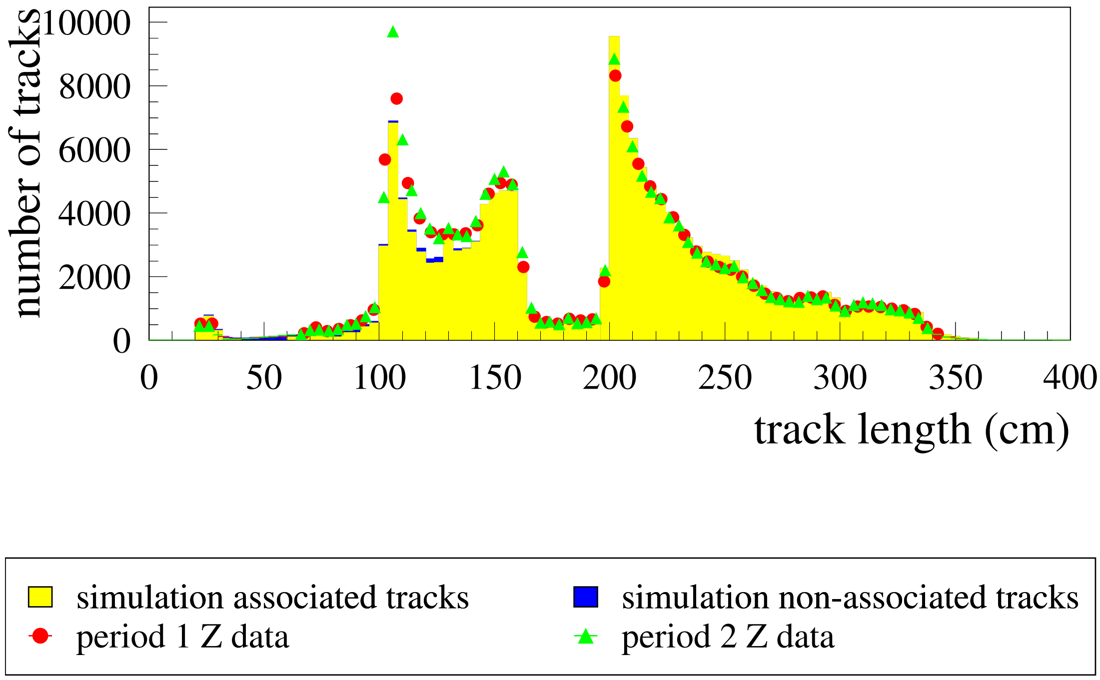

Figure 3.5: The track length for the selected charged tracks.

Although they will affect only one in 25 hadronic events, these tracks if untreated will have a gross biasing effect on the reconstructed jets and will certainly render these events unusable for mass reconstruction. Current statistics do not allow a meaningful study of these tracks and here we adopt a treatment based primarily on LEP1 studies [54]. These studies on $q\bar{q}$ events suggest they are not fake tracks, but rather genuine hadronic tracks of significant momentum. This re-scaling prescription is only applied to events with a charged multiplicity greater than seven; for low multiplicity events, tracks must exceed 125% of the beam energy. The applied rescaling algorithm is as follows :

For $p > 75\%\ E_{Beam}$ (high multiplicity events), or $p > 125\%\ E_{Beam}$ (low multiplicity events).

- rescale momentum to TPC TE

  require : 400MeV $< p_{TPC\ TE} <$ 75% or 125% E_{Beam} and

  $\frac{\Delta p}{p} < 0.5$

ELSE

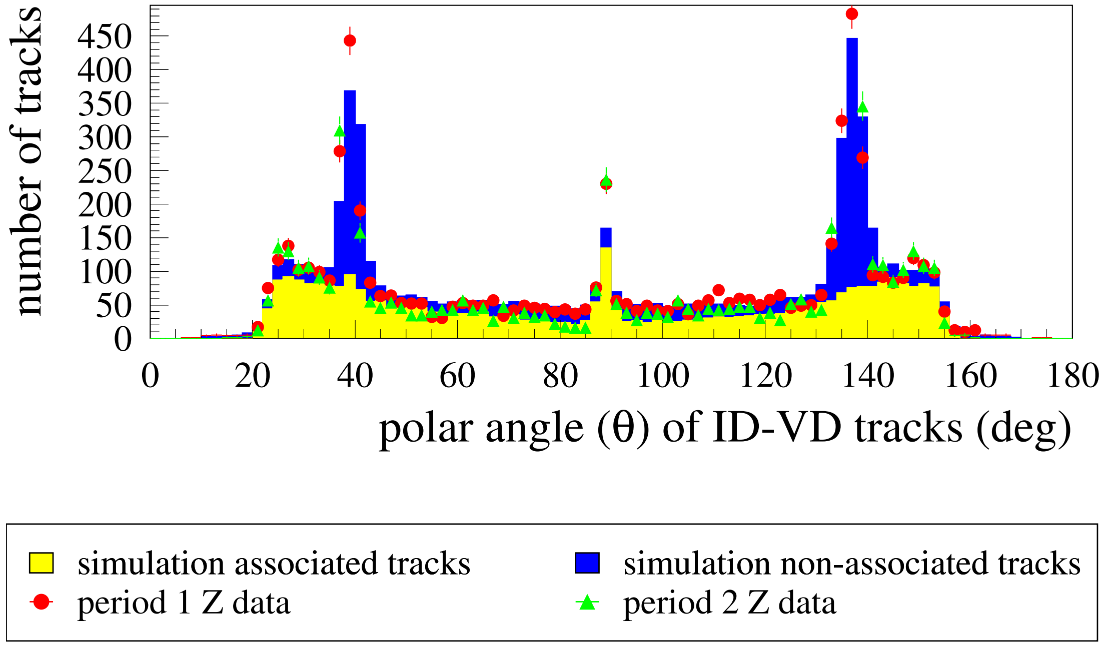

Figure 3.6: Distribution of reconstructed tracks containing only VD and ID points with the polar angle of the track. All selection cuts have been applied except those on ID-VD tracks.

- rescale momentum to sum of Hadronic and Electromagnetic Calorimeter energies.

  A calorimeter deposit is included in the sum only if it exceeds 8 GeV

ELSE

- rescale the track to 15 GeV for high multiplicity or E_{Beam} for low multiplicity events.

Summary

The distributions studied show acceptable agreement between data and simulation after selection cuts have been imposed. Previous DELPHI experience warns of forward tracking disagreements; the tracking efficiency is certainly reduced, but this study did not find major disagreements between data and simulation in this region.

Prior to the selection, non-associated tracks constituted 21% of the total charged track sample in the simulation events. In the final sample, this was reduced to

2% of the selected tracks. The selection removed 40% of the charged tracks from the simulation events, and a similar proportion of the tracks in the data. In the simulation events, 20% of the neutral deposits were rejected by the cuts made (see Section 3.3.1); this number was 30% in the data.

The effect of the remaining discrepancies between data and simulation in the selected track samples are included in the systematic error of the final analysis.

3.3 Neutral Tracks

Approximately one third of all hadronic energy will be carried by neutral particles, and will be deposited in the DELPHI calorimetry system. Clusters of energy are recognised by the calorimeter processing and those that are not associated to charged tracks are used to form neutral tracks. A neutral track is simply a cluster which is assigned a track extrapolated back to the vertex.

3.3.1 Selection of Neutral Tracks

Shower profile selection cuts are made to remove noise clusters during the `DELANA` processing. The only remaining simple quantity on which to base further selection is the recorded energy of the cluster. The error on the energy is calculated directly from the measured calorimeter energy and hence is not an independent quantity. The energy distributions of the calorimeter clusters are shown in Figure 3.7 for the four calorimeters used in this analysis. Significant data-simulation disagreements were observed in the very low energy region, particularly in the HAC, where detector noise is interpreted as low energy clusters. The selection imposed was :

- HPC, FEMC, STIC cluster energy > 500 MeV
- HAC cluster energy > 750 MeV

The total number of observed neutral clusters is shown in Figure 3.8. The deviations observed are of similar magnitude ($\approx 5\%$) to those seen for charged tracks.

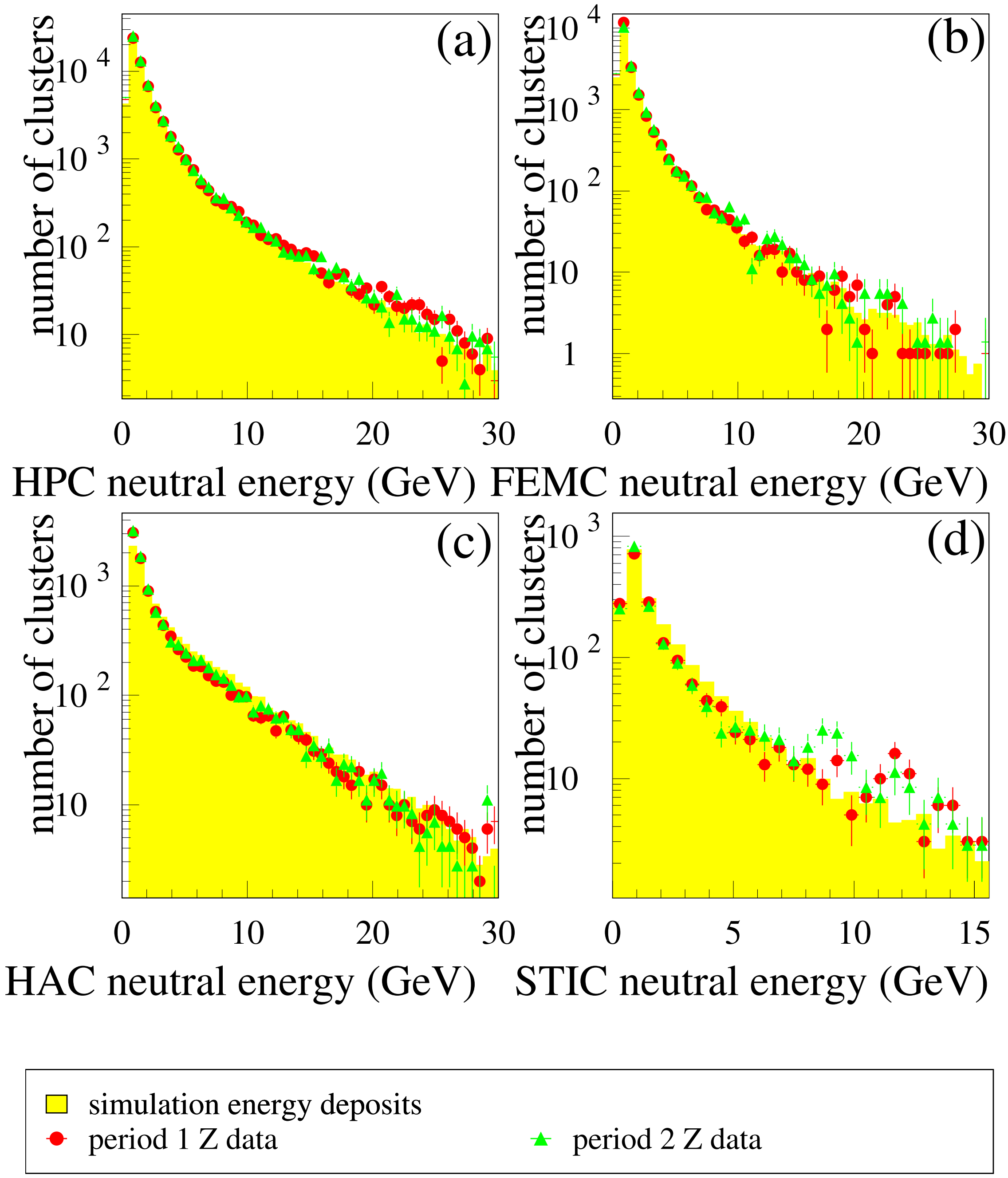

Figure 3.7: Distribution of neutral cluster energy deposits in the four DELPHI calorimeters (a) and (b) are the barrel (HPC) and forward (FEMC) electromagnetic calorimeters, (c) is the hadronic calorimeter (HAC), and (d) is the very forward STIC luminosity monitor calorimeter.

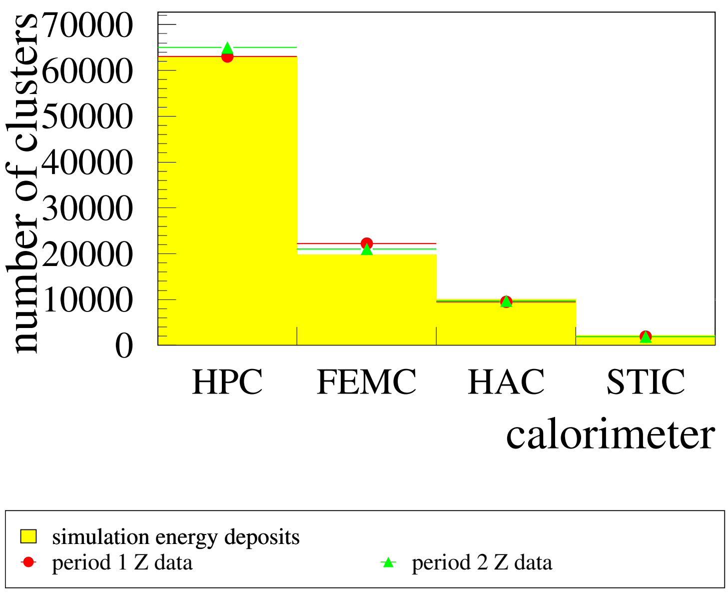

Figure 3.8: Number of selected neutral clusters observed in the calorimeters.

3.4 Trigger Efficiencies

The DELPHI trigger system is described in Section 2.4.1. From trigger efficiencies measured for single charged particles with redundant trigger combinations, the efficiency for two charged particles (which is the worst case for all events of interest in this analysis) was found to exceed 99% [55].

3.5 Run Selection

The analysis described in this thesis uses the data taken at energies above the Z peak during the period July-November 1996. During this period, the data collected by the DELPHI experiment were obtained with a good performance level from all the sub-detectors: over 95% of the collected data were used for this analysis. The data rejected from this analysis were removed based on Quality Checking work[5]. The rejection was performed at the level of individual file sequences. Data were accepted only if :

- TPC data taking efficiency was $> 90\%$

[5]The author compiled the results of general studies performed by Vladimir Nikolaenko and Bill Murray, and Barrel muon chamber work of Guy Wilkinson.

- All other tracking chambers efficiency > 70%
- muon chambers and hadronic and electromagnetic calorimeters operating efficiency > 70%

A small amount of data (0.05 pb^{-1}) was collected at 164.5 GeV: these events are not considered further in this analysis.

Samples of data containing problems with FCA/FCB and the Barrel muon chambers were treated separately (see below).

3.6 Luminosity

[6] The luminosity was measured using the Small Angle Tile Calorimeter (STIC). Events corresponding to Bhabha scattering were selected by requiring a coincidence of two coplanar electromagnetic showers, each with energy larger than 65% of the beam energy. In order to minimise the sensitivity to the position of the interaction point, asymmetric cuts were imposed on the reconstructed radii of the two showers.

The calculation of the accepted cross-section was based on the event generator BHLUMI 4.03 [56], which has a theoretical accuracy of 0.25% at LEP2 energies. The total experimental systematic error on the luminosity amounts to 0.5%, with the main contribution arising from the uncertainty in the radial cuts. A luminosity file was produced with an entry for each file sequence of data recorded.

Using the run selection outlined above, the luminosity of the analysed data samples was obtained. The results are given in Table 3.1

3.7 Beam Energy

The mean LEP beam energy [57] was determined using a model based on the field readings of nuclear magnetic resonance probes installed in the dipole magnets. The model describes the variation of the average beam energy with time from effects such as the earth tides and temperature fluctuations. The probes were calibrated to an energy scale determined by resonant depolarisation measurements. However, the determination of the absolute energy scale is more complicated at LEP2 than at

[6] Paragraph 1 and 2 are reproduced from [55] .

LEP1 because polarisation measurements at the new physics collision energies have not proved possible. The presence of machine imperfections inhibits the build up of transverse polarization at collision energies significantly higher than M_Z. In 1996, the energy scale was established by extrapolation of three polarisation measurements made at beam energies of 45 GeV or 50 GeV. A cross-check of the energy scale was made using flux-loop measurements. The effect of the RF system at the DELPHI interaction point was modelled and an energy file was produced, with an entry for each file sequence of data recorded: the mean correction for DELPHI of 9 MeV at 161 GeV and 8 MeV at 172 GeVwas applied to the centre-of-mass energy.

Using this energy file and the luminosity file and run selection described above, the high energy data were divided into three energy samples and luminosity-weighted average c.m. energies $\bar{E}_{\rm c.m.}$ were produced: the results are given in Table 3.1.

The 161 GeV sample contains 0.192 pb^{-1}, where the barrel muon chambers were off or functioning only at low efficiencies. The 172 GeV sample includes 0.636 pb^{-1}, where chambers FCA and/or FCB were not taking data. Both of these data taking periods require special treatment, and are discussed further below.

label	$\bar{E}_{\rm c.m.}$(GeV)	$\sigma_{E_{\rm c.m.}}$(GeV)	Luminosity (pb^{-1})
Period 1 Z	91.35 ±0.06	0.02	0.343 ± 0.004(stat.) ± 0.002(syst.)
Period 1 LEP2	161.31 ±0.06	0.05	9.560 ± 0.037(stat.) ± 0.053(syst.)
Period 2 Z	91.08 ±0.06	0.02	0.248 ± 0.005(stat.) ± 0.001(syst.)
Period 2 LEP2 170	170.28 ±0.06	0.03	1.038 ± 0.015(stat.) ± 0.006(syst.)
Period 2 LEP2 172	172.30 ±0.06	0.04	8.741 ± 0.043(stat.) ± 0.049(syst.)
Period 2 LEP2 Sum	172.08 ±0.06	0.62	9.779 ± 0.045(stat.) ± 0.055(syst.)

Table 3.1: The luminosity weighted average energy $\bar{E}_{\rm c.m.}$, its weighted standard deviation and the corresponding integrated luminosity are given for the data used in this analysis. Note the final row does not describe an independent data sample: it contains the results for the sum of the Period 2 high energy data.

3.8 Data For Special Treatment

3.8.1 Forward Chamber Problems

As noted above 7% of the data recorded at 172 GeV were obtained with the forward tracking chambers FCA/FCB at a significantly reduced operational efficiency. In

Figure 3.9 we show some charged particle distributions for this data sample. The property shown in Figure 3.9(a) is a variable on which the selection of the $q\bar{q}'\bar{q}q'$ channel relies. This jet multiplicity distribution does not show a statistically significant discrepancy. However, when we consider the total charged multiplicity of all tracks in events (Figure (b)), a different picture emerges. We observe $20 \pm 5\%$ difference in the total number of charged tracks in the FCB acceptance region. No difference was observed for neutral tracks ($1 \pm 5\%$). We correct the simulation by removing charged tracks in the forward region and include the errors as systematic contributions in the analysis.

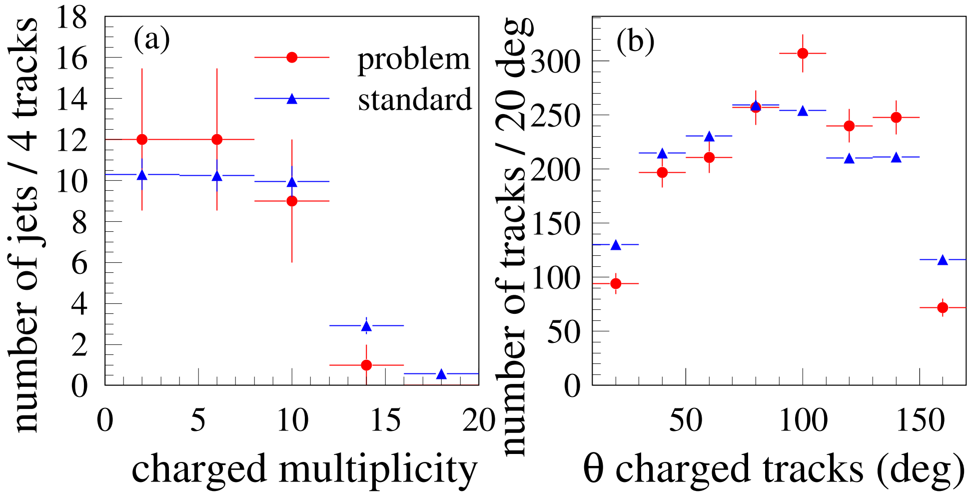

Figure 3.9: Charged track distributions for data with low FCA/FCB chamber efficiency. (a) shows the number of charged tracks per jet for the two leading jets in a selected $q\bar{q}$ event, when the jets lie in the polar angle acceptance of the FCB chamber. (b) gives the total number of charged tracks observed in all selected events as function of the polar angle. The plots are normalised to the number of entries in the 'problem' sample.

3.8.2 Barrel Muon Chamber Problems

As noted above, 2% of the data recorded at 161 GeV were obtained with the barrel muon chambers at a significantly reduced operational efficiency. This affects the procedure adopted for selecting events in the $l\overline{\nu}_l q\bar{q}'$ decay channel. In this data sample the muon tag was not used and the simulation was treated by turning off the muon tag for the same fraction of simulation events: note this is not equivalent to rejecting these events, as events may be recovered by the other selection streams in the $l\overline{\nu}_l q\bar{q}'$ analysis (see Section 4.3.2).

3.9 Additional Lepton Studies

Studies of high momentum tracks have been made by the DELPHI Collaboration [58]. These studies are based on the selection of lepton-pair events and cosmic-ray muons. A study of muon tagging efficiency on the 172 GeV data was performed by the author. Here we summarise the results of most significance to this thesis.

- The track reconstruction efficiency in data and simulation differ by up to 2%.
- The data and simulation agree to within 2% in muon momentum, and 2% for electron energy.
- The lepton tagging efficiency in data and simulation agree to within 5%.

The lepton identification criteria adopted in this analysis, are based upon the DELPHI W^+W^- team standard. The criteria are provided in Section 4.3.3

3.10 Detector Simulation

The DELPHI simulation program `DELSIM` [59] aims to produce simulation events which resemble as closely as possible the real raw data. These simulation data are treated by the reconstruction and analysis programs in an identical manner to the real data. `DELSIM` is based on three main components: an event generator, detector models, and the particle trajectory description.

Event generators are used to describe the primary physics process and are the topic of the next section.

An independent software module is used to describe the interaction of particles inside each active detector component. The routines aim to provide a realistic simulation of the detector response.

As the simulated particles move through the DELPHI detector, their path in the magnetic field must be calculated. The particle tracking description includes the effects of energy loss, multiple scattering and secondary processes such as *bremsstrahlung* and nuclear interactions. A database is used to store a very detailed description of the material layers and the active components in the detector.

In addition to this detailed simulation, a simplified version has been implemented to obtain a much faster detector simulation of DELPHI. This is used in Section 5.7.

3.11 Generators

We use event generators to produce unweighted simulation events. The generator aims to produce a full set of final state particles typical of those that would result from a given physics process. These particles can then be passed through a detector simulation (see above).

An event generator consists of three main stages: the primary hard process, the parton shower, and the hadronisation model. Here we briefly describe the models used in this thesis; we emphasise the features which are required background knowledge for the reader to the $\mathrm{q\bar{q}'\bar{q}q'}$ analysis systematics discussion (Section 4.2.6).

The primary hard process of main relevance to this thesis is $e^+e^- \to \mathrm{W^+W^-} \to f_1\overline{f_2}f_3\overline{f_4}$, where f_{1-4} are fermions. The matrix elements for these processes are calculated, and we mainly rely on the `PYTHIA/JETSET` [60] implementation for the processes in this thesis. In Section 5.7, `PYTHIA` results are compared with the four-fermion approach of the `EXCALIBUR` [61] generator.

Perturbative QCD cannot provide full theoretical insight into the transition of the primary quarks to observable hadrons: the so-called fragmentation or hadronization process. Only the part of the transition where large momentum transfer occurs (mainly the radiation of hard gluons) is calculable perturbatively. The final formation of hadrons is hidden due to the increase of the strong coupling constant α_s at small momentum transfers and hence the failure of perturbation theory. This process must be described by QCD inspired phenomenological models. These models include a number of tunable parameters (`JETSET` has approximately 15) which must be determined empirically. The parameter values are chosen such that an optimal description of the observed LEP1 hadronic event shape and inclusive charged particle distributions is obtained. The simulation used in this thesis relies upon the tuning described in [62].

The `JETSET` parton shower algorithm is the most commonly used description of the perturbative phase. The algorithm describes the parton division mechanism, thus producing parton showers. The shower evolution is stopped at a fixed mass scale, when fragmentation takes over. Alternatively, the parton shower simulation can be replaced by the `JETSET` matrix element. This is an exact second order matrix element calculation which provides up to four partons. `ARIADNE` [63] is based on the Colour Dipole Model. In this description the emission of a gluon from a colour dipole, *i.e.* the initial $q\bar{q}$ pair, creates two new dipoles - one stretched from the quark to the gluon and one from the antiquark to the gluon. Both the new dipoles can radiate further gluons. Again, a cut-off scale is imposed for the transition to the hadronisation stage.

The fragmentation model used here is that in `JETSET`, which is based on the Lund string scheme. A colour string is stretched between oppositely coloured quark and anti-quark. As the string expands, its energy increases to a point where the string may snap, and a quark anti-quark pair are created on the new ends of the string.

Chapter 4

Event Selection

4.1 Introduction

We distinguish three basic topologies of W^+W^- decay:

- $e^+e^- \rightarrow W^+W^- \rightarrow q\bar{q}'\bar{q}q'$ (Fully - Hadronic decays)
- $e^+e^- \rightarrow W^+W^- \rightarrow l\overline{\nu}_l q\bar{q}'$ (Semi - Leptonic decays)
- $e^+e^- \rightarrow W^+W^- \rightarrow l\overline{\nu}_l \bar{l}\nu_l$ (Fully - Leptonic decays)

In Figure 4.1 we show the distribution of these three classes of W^+W^- event as a function of charged multiplicity. The fully-hadronic decay channel has the highest multiplicity and the primary share of the branching ratio: in the Standard Model we expect to have produced about 16 events in this class at 161 GeV and 50 at 172 GeV. We expect to have produced a similar number of events in the semi-leptonic decay class. These events will have about half the multiplicity of the fully-hadronic decay events. Fully-leptonic channel events occur at the rate of only about one in ten W^+W^- events: hence we expect production of only 3 events at 161 GeVand 11 events at 172 GeV. The peak in the multiplicity distribution occurs at 2 charged tracks, with the tail to higher values comprising of multi-prong tau decays and electrons that have showered within the tracking detectors. The numbers given here, and throughout this chapter, on W^+W^- production assume the Standard Model branching ratios and the current world average value of M_W of 80.43 [8].

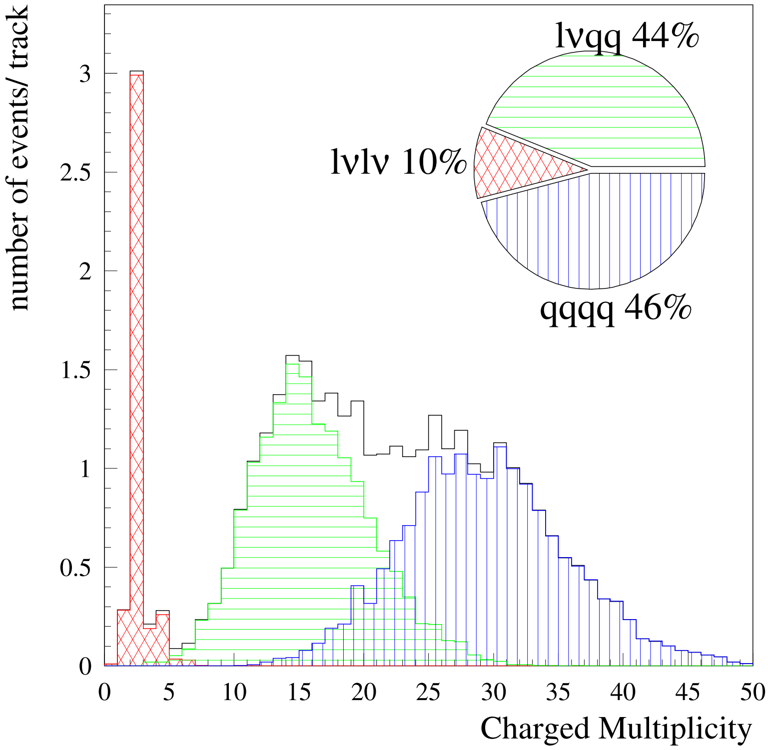

Figure 4.1: The reconstructed charged track multiplicity distribution of simulated $\mathrm{W^+W^-}$ events. The events have been separated into the three identification categories used in this analysis. The inset pie chart indicates the relative Standard Model branching ratios of the three decay types. The plot is normalised to 10 $\mathrm{pb^{-1}}$at 161 GeV.

The $\mathrm{W^+W^-}$ production Feynman diagrams have been discussed previously (see Section 1.4.1). Between 161 and 172 GeV, the cross-section for $\mathrm{W^+W^-}$ production increases threefold, and the s-channel diagrams begin to make a significant contribution (see Figure 1.4). As we move away from threshold, the velocity of the W bosons also increases.

The principal background to $\mathrm{W^+W^-}$ decays is $e^+e^- \rightarrow \mathrm{Z}/\gamma \rightarrow f\bar{f}$ events. As illustrated in Figure 4.2, these events can be subdivided into two major categories: *(i)* non-radiative events and *(ii)* radiative return events mediated by an on-shell Z boson. These events are discussed further in this chapter, most notably in section 4.2.4. The cross-section for these events decreases by 15% between 161 and 172 GeV.

The other major backgrounds are from (non-$\mathrm{W^+W^-}$) four-fermion final state production. The Feynman diagrams for the relevant processes and a study of four-fermion interference effects is provided in the following chapter.

Two photon collisions and Bhabha events must also be considered when selecting the $W^+W^- \rightarrow l\overline{\nu}_l\overline{l}\nu_l$ decay channel.

In this chapter, we present the event selection criteria imposed for each of the three decay channels in turn; the interpretation of the selected events is deferred to the following chapters. The event selection is tuned at both energies to minimise the statistical error. In general, looser cuts are imposed at 172 GeV than at 161 GeV: as the collision energy increases we have adapted the selection criteria to the regime of an increased signal to background ratio. We treat the data taken at 170 GeV in the same manner as that recorded at 172 GeV.

The following event selection description is illustrated with figures showing data and simulation distributions for the most important selection variables. These plots are shown after the final selection criteria have been imposed, and when only looser pre-selection cuts have been applied. Throughout this chapter, the signal events in the simulation are normalised using the cross-sections measured in that decay channel. The errors marked on the number N of selected data events in each bin of the plots are simply $\pm\sqrt{N}$; for small N this is an underestimate of the true statistical error.

In the final section of this chapter, we provide a study of which jet reconstruction algorithm is optimum for the W^+W^- event analyses.

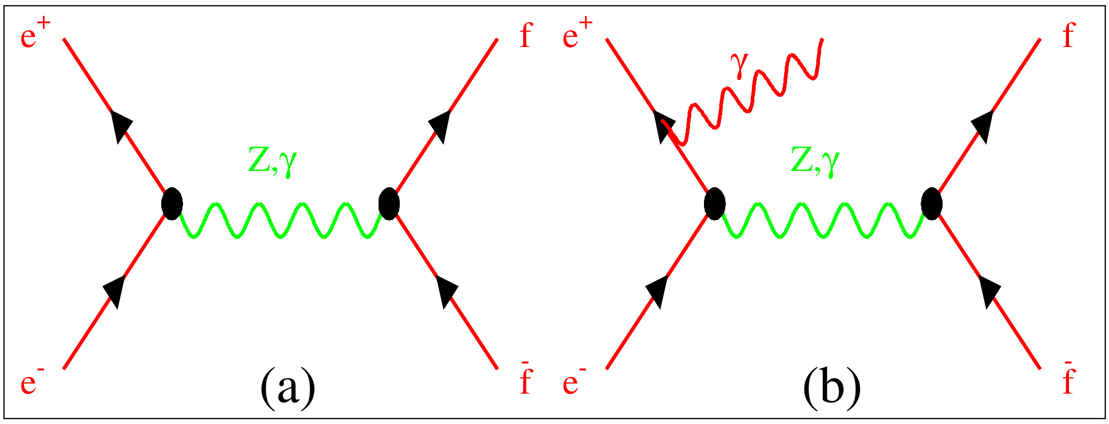

Figure 4.2: Feynman diagrams for the production of a fermion anti-fermion pair final state. In (b) the production is accompanied by an emitted ISR photon.

4.2 $q\bar{q}'\bar{q}q'$ Decay Channel

4.2.1 Introduction

In Figure 4.3, we present a good example of a $W^+W^- \to q\bar{q}'\bar{q}q'$ decay. In the lower polar view of the Figure the four-jet structure of the W^+W^- decay is particularly visible. However, in a fraction of these events, approximately equal to α_s, a gluon of significant momentum is emitted. That is, we expect roughly 10% of the events to have a fifth jet.

For this example event (Figure 4.3), we observe that the jets are well-spaced, and that energy is deposited throughout the 4π detector. Unlike the two-jet collinear structure of Z physics at LEP1, the class of decays studied here use the full detector space in each event. The events have high sphericity and the analysis of W^+W^- decays is only possible due to the excellent angular acceptance and hermeticity of the DELPHI detector.

The total observed energy in the detector should be high - close to the collision energy. The only missing energy in the events will be due to the neutrinos produced during the fragmentation process, or to particles escaping through cracks in the detector and along the beam-pipe.

If we can identify the correct pairings of the four jets, corresponding to a parent W (this problem is discussed further in Section 6.6.1), then the di-jet invariant masses should be large. However, we wish to avoid biasing the analysis towards a particular mass range. Where possible, we will try to avoid selection cuts based on, or highly correlated with, the value of the W mass. Clearly, this is a valuable general procedure, but here it is of particular importance as this analysis utilises the first data on the $e^+e^- \to W^+W^-$ process.

The total cross-sections for the principal backgrounds to this channel are given in Table 4.1. The cross-section for di-quark production is two orders of magnitude larger than that for the W^+W^- process. The cross-section for four-jet events produced by hard gluon emission in the '$q\bar{q}$' events is similar to that of the W^+W^- process[1]. The process denoted ZZ represents the neutral current processes (known

[1] In fact the effect of colour factors leads to an enhancement in the triple gluon vertex over the quark-quark-gluon vertex: *i.e.* if you already have one gluon it is easier to produce another. Indeed the relative background fraction in 5-jet reconstructed events is expected to be larger than in 4-jet events.

as `NC08` [64]) which include contributions where either or both of the bosons are photons: in fact only in 1997 has LEP reached the threshold energy for producing two real Z bosons. For a massless fermion treatment the cross-section is divergent, peaking with the production of photons with a virtuality close to zero. The quoted cross-section is that for bosons of mass greater than 10 GeV/c^2.

Process	σ161GeV		σ172GeV	
	$\sqrt{s'}/\sqrt{s} > 10\%$	$\sqrt{s'}/\sqrt{s} > 85\%$	$\sqrt{s'}/\sqrt{s} > 10\%$	$\sqrt{s'}/\sqrt{s} > 85\%$
$Z/\gamma \rightarrow q\bar{q}(\gamma)$	147.1 pb	34.9 pb	123.0 pb	29.0 pb
ZZ	0.4 pb		0.5pb	

Table 4.1: Total cross-sections of important background processes, before the W^+W^- selection is imposed. These values are obtained from the programs `ZFITTER` for Z/γ and `PYTHIA` for ZZ. The ZZ cross-section is that for production of two neutral current bosons each of mass greater than 10 GeV/c^2. $\sqrt{s'}$ is the effective centre of mass energy of the electron - positron collision.

4.2.2 Four-Jet Topology

The primary background rejection cut imposed in the analysis is the requirement of a four-jet like topology. A comparison of a range of different jet algorithms is provided in Section 4.5. We use the `LUCLUS` algorithm [60] to cluster the selected charged and neutral tracks into four jets. The d_{join} clusterisation measure is increased until two of these jets are combined, and the event is re-clustered as three jets: we refer to this variable below as $d_{join}3 \rightarrow 4$.

$W^+W^- \rightarrow q\bar{q}'\bar{q}q'$ events have four or more natural jets: thus they have a high value of $d_{join}3 \rightarrow 4$. However, $q\bar{q}$ events typically have two hard jets and other softer jets created by gluon emission. These $q\bar{q}$ events will re-cluster at smaller values of d_{join} than the $q\bar{q}'\bar{q}q'$ events.

In Figure 4.4 (a) - (c) we show the distributions of data and simulation for three event samples. Figure (a) shows the distribution of the events at 161 GeV where only a loose pre-selection of hadronic events has been applied: the imposed selection is as in Section 3.1.3. Figures (b) and (c) show the distribution of the events remaining after cuts have been applied on the jet quality and the effective c.m. energy ($\sqrt{s'}$). These plots show the differential three-jet rate, that is the number of events changing from four to three jets, as a function of the d_{join} variable.

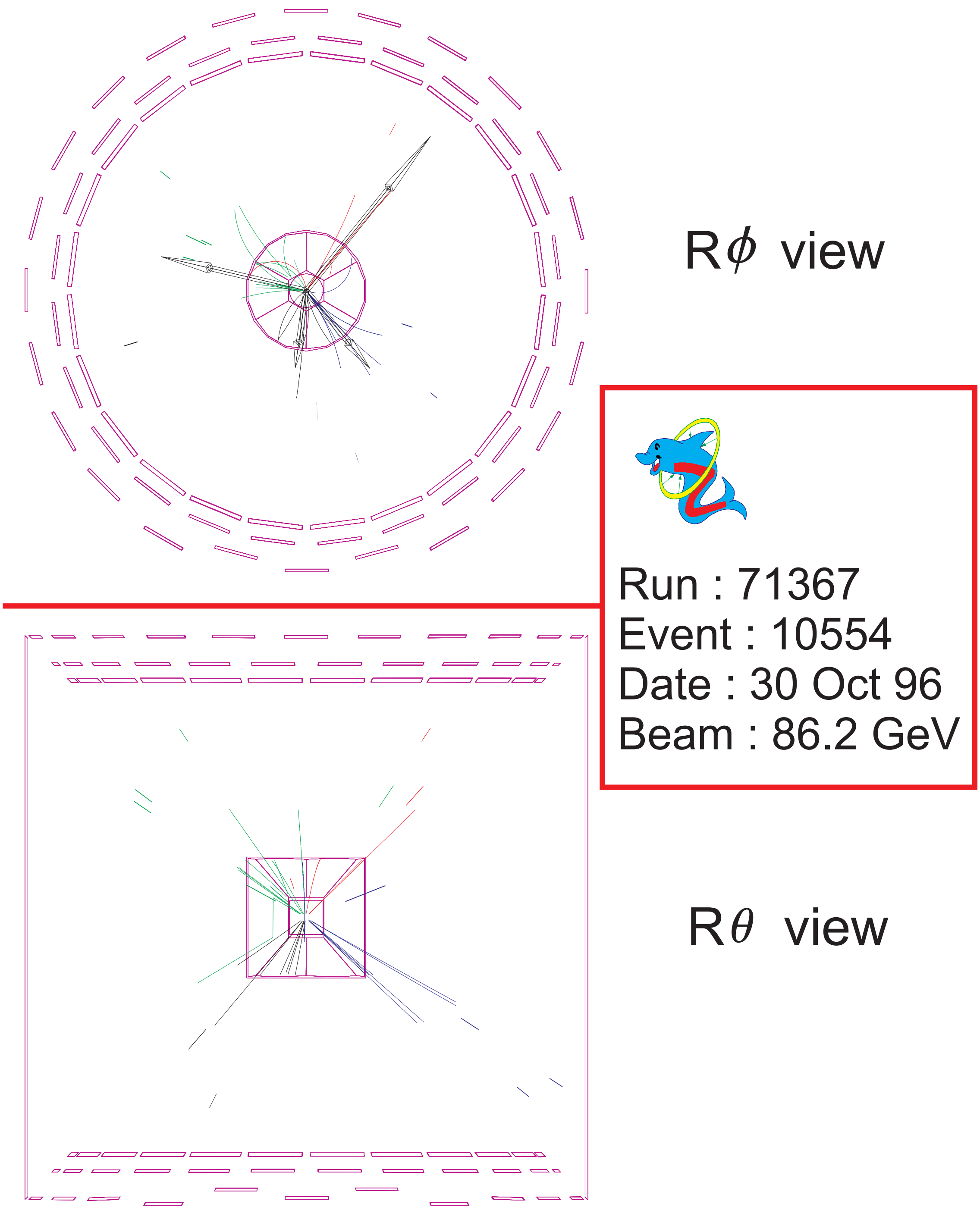

Figure 4.3: Example of a $W^+W^- \rightarrow q\bar{q}'\bar{q}q'$ decay. The barrel muon chambers and TPC are shown. In the upper section of the plot the reconstructed jet directions are indicated with arrows.

In Figure (d) we show a plot of the$W^+W^-\rightarrow q\bar{q}'\bar{q}q'$ selection efficiency × purity as a function of the imposed cut on the d_{join} variable: all other selection cuts have been applied. As discussed in Section 5.2, maximising the quantity $\epsilon \times P$ minimises the statistical error of the analysis. The values of the $d_{join} 3 \rightarrow 4$ selection cut are indicated on Figures (b) and (c), and are listed in Section 4.2.7.

4.2.3 Jet Quality

Having clustered the events to a four-jet like topology, we impose a selection based on the quality of these jets. Studies showed that an important discriminator for jets is their track multiplicity. Jets originating from quark fragmentation are characterised by a large number of tracks (charged + neutral), while the softer gluon jets or 'artificial' jets have a lower multiplicity. We choose to select our events based on the number of tracks in the jet of lowest multiplicity. In Figure 4.5, we present the same range of plots for this variable as was presented for the d_{join} variable above.

4.2.4 Radiative Events

The $q\bar{q}$ background events can be separated into two classes, those with and those without significant initial state radiation. ISR emission by the incoming beam electrons leads to the effective centre of mass energy ($\sqrt{s'}$) of the collision being reduced. About three quarters of the $q\bar{q}$ events are accompanied by an ISR photon of significant momentum (see Table 4.1). The dominant contribution to these events comes from the process of radiative return to the Z peak; for the collision energies considered in this thesis, the typical photon energy is 60 GeV.

In this analysis we use the Sprime algorithm described in [65] to determine the effective centre of mass energy of the collision; this algorithm is outlined below.

Sprime

If a photon (or several collinear photons) are emitted with total energy E_γ and momentum p_γ then the effective centre of mass energy is :

$$\sqrt{s'} = \sqrt{(\sqrt{s} - E_\gamma)^2 - E_\gamma^2} \tag{4.1}$$

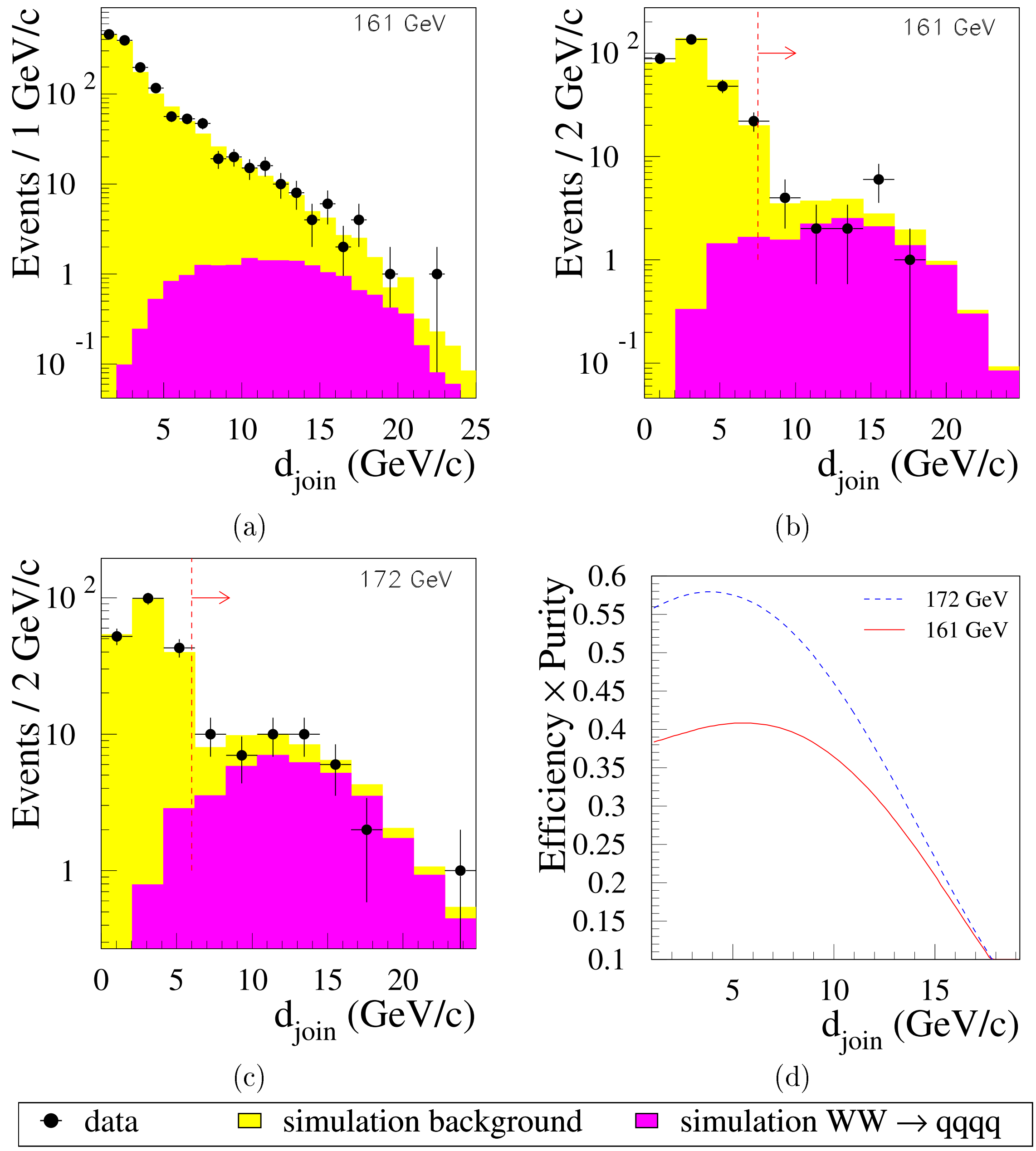

Figure 4.4: A selection of distributions for the $d_{join}3 \rightarrow 4$ variable. The differential three jet rate is shown in (a) at 161 GeV for a hadronic event selection in data and simulation. After the effective centre of mass and jet quality selections (see text) have been imposed, the distributions shown in (b) (161 GeV) and (c) (172 GeV) are obtained. The dashed line indicates the value of the imposed cut. The key to plots (a) to (c) is provided at the foot of the graphs. (d) shows the variation of $\epsilon \times \mathcal{P}$ in simulation as a function of the selection cut.

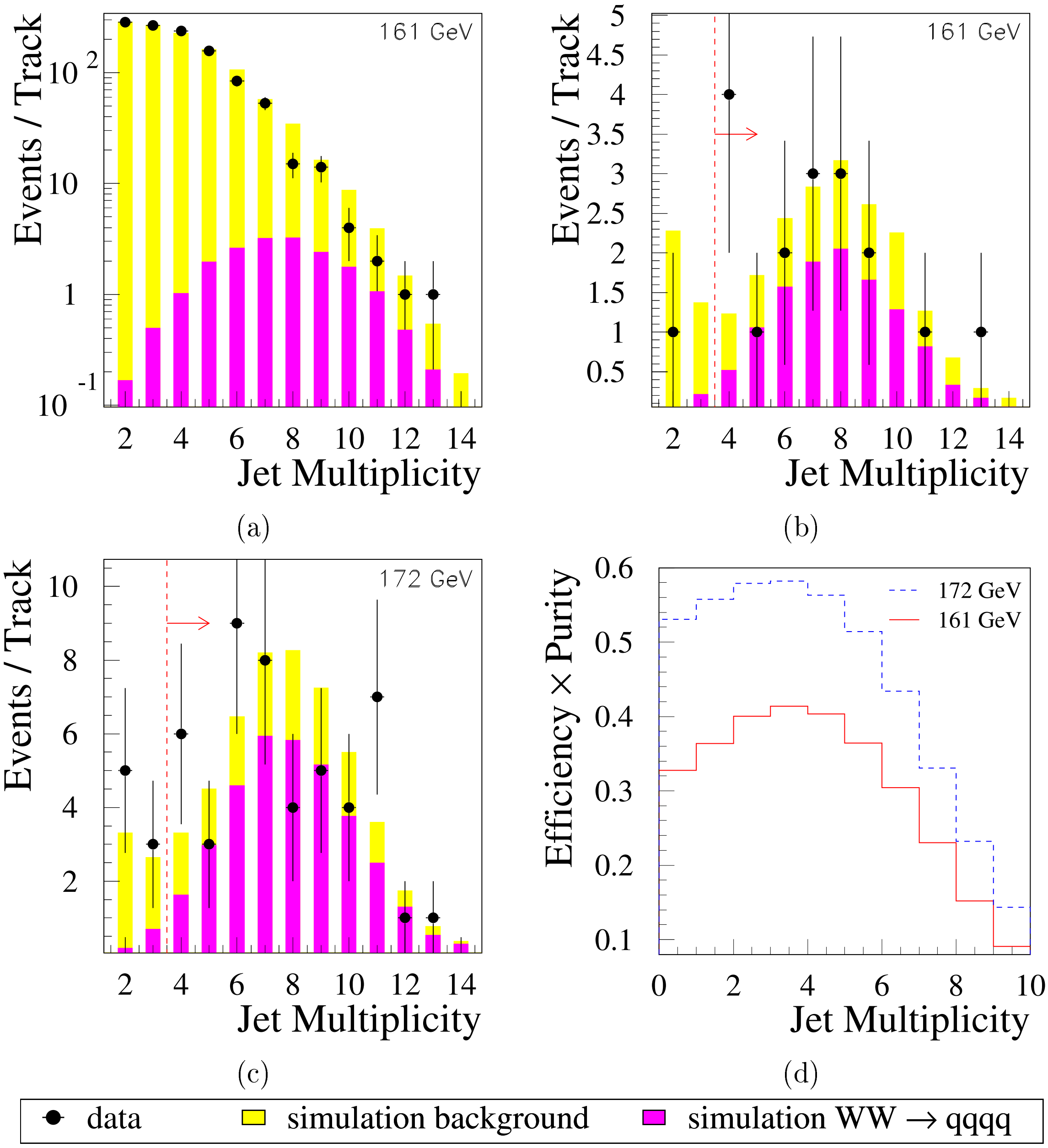

Figure 4.5: A selection of distributions for the minimum jet track multiplicity of the four forced jets in an event. The differential three jet rate is shown in (a) at 161 GeV for a hadronic event selection in data and simulation. After all other cuts have been imposed, the distributions shown in (b) (161 GeV) and (c) (172 GeV) are obtained. The dashed line indicates the value of the imposed cut. The key to plots (a) to (c) is provided at the foot of the graphs. (d) shows the variation of $\epsilon \times \mathcal{P}$ in simulation as a function of the selection cut.

The algorithm applied in this analysis determines the energy of the emitted photon and calculates the $\sqrt{s}$ using Equation 4.1.

Where a large energy neutral cluster is observed in the detector, this is identified as a photon. The ISR photon is generally emitted at low polar angles, and hence this identification relies on the FEMC and the STIC calorimeters. Photon candidates have

- Energy $>$ 10 GeV
- Isolation from charged tracks of over 1 GeV $>$ 0.3 rad.

The remaining tracks in the event are then clustered into two jets. The direction of a jet (or a photon) is generally well measured, while its measured energy is typically 20% lower than its true value. Hence, we choose to rely upon the inter-jet and photon angles in our $\sqrt{s'}$ measurement rather than the jet energies. We use the angles between the three measured jet directions, assuming that the two jets and the photon lie in a plane. The photon energy is determined by applying the sine rule to the triangle of objects in the plane.

Often the ISR photon is lost down the beam-pipe. In this case, we find that our events have significant missing energy and the missing momentum vector has a small polar angle. When the photon is not observed in the detector, we assume that it was emitted collinear with the electron or positron beam and thus lost down the beam pipe. We then calculate the energy of the photon by the same method as we described above. Energy and momentum conservation requires that the three objects (two jets and a photon) will lie in a plane.

When a photon is found in the detector, but it is not coplanar with the two jets, an additional lost γ is postulated when calculating the $\sqrt{s'}$.

The reconstructed $\sqrt{s'}$ is plotted against the true $\sqrt{s'}$ for a sample of simulation events in Figure 4.6. From these $e^+e^-\rightarrow q\bar{q}(\gamma)$ events at 161 GeV we determine that high energy events ($>$85% $E_{\mathrm{c.m.}}$) are selected by this algorithm with 92% efficiency and 86% purity.

The same four types of plot presented for the other variables in this analysis are presented for the reconstructed $\sqrt{s'}$ in Figure 4.7

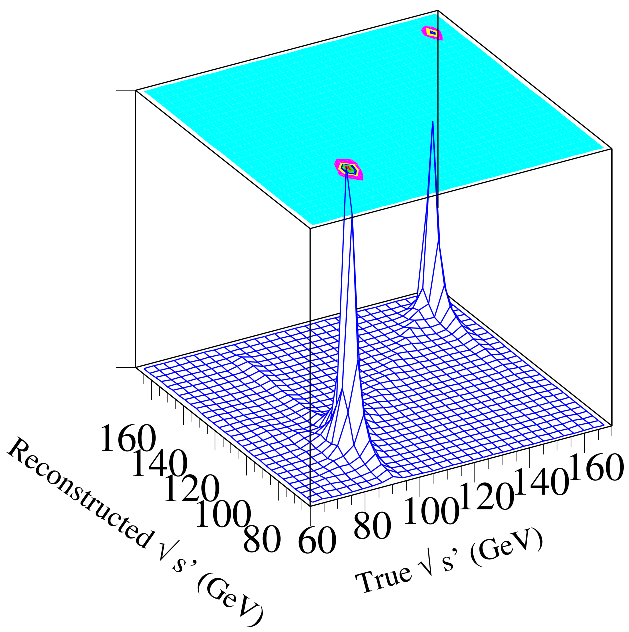

Figure 4.6: The reconstructed effective centre of mass energy $\sqrt{s'}$ is plotted against the true value of this quantity, for a sample of $e^+e^-\to q\bar{q}(\gamma)$ simulation events at 161 GeV.

4.2.5 Gluon Jet

Finally, we require a selection cut to further discriminate quark jets from gluon jets. Jets produced by gluon radiation will typically be at low angle to their parent quarks and have a low energy.

Having clustered the event to a four-jet topology using the `LUCLUS` algorithm, we use a kinematic fit including the constraints of energy and momentum. This technique (discussed in Section 6.4) produces a marked improvement in the jet energy resolution. The energy of the minimum energy jet (E_{min}), after the kinematic fit, is then a useful discriminant variable between the higher energy quark jets and the lower energy gluon jets.

We now wish to exploit the expected small angular separation of the quark and gluon jets. The minimum inter-jet angle is a natural variable to use. However, we find this angle is highly correlated with the $d_{join}3 \to 4$ clusterisation cut that has already been imposed. Better discriminative power can be obtained using the QCD

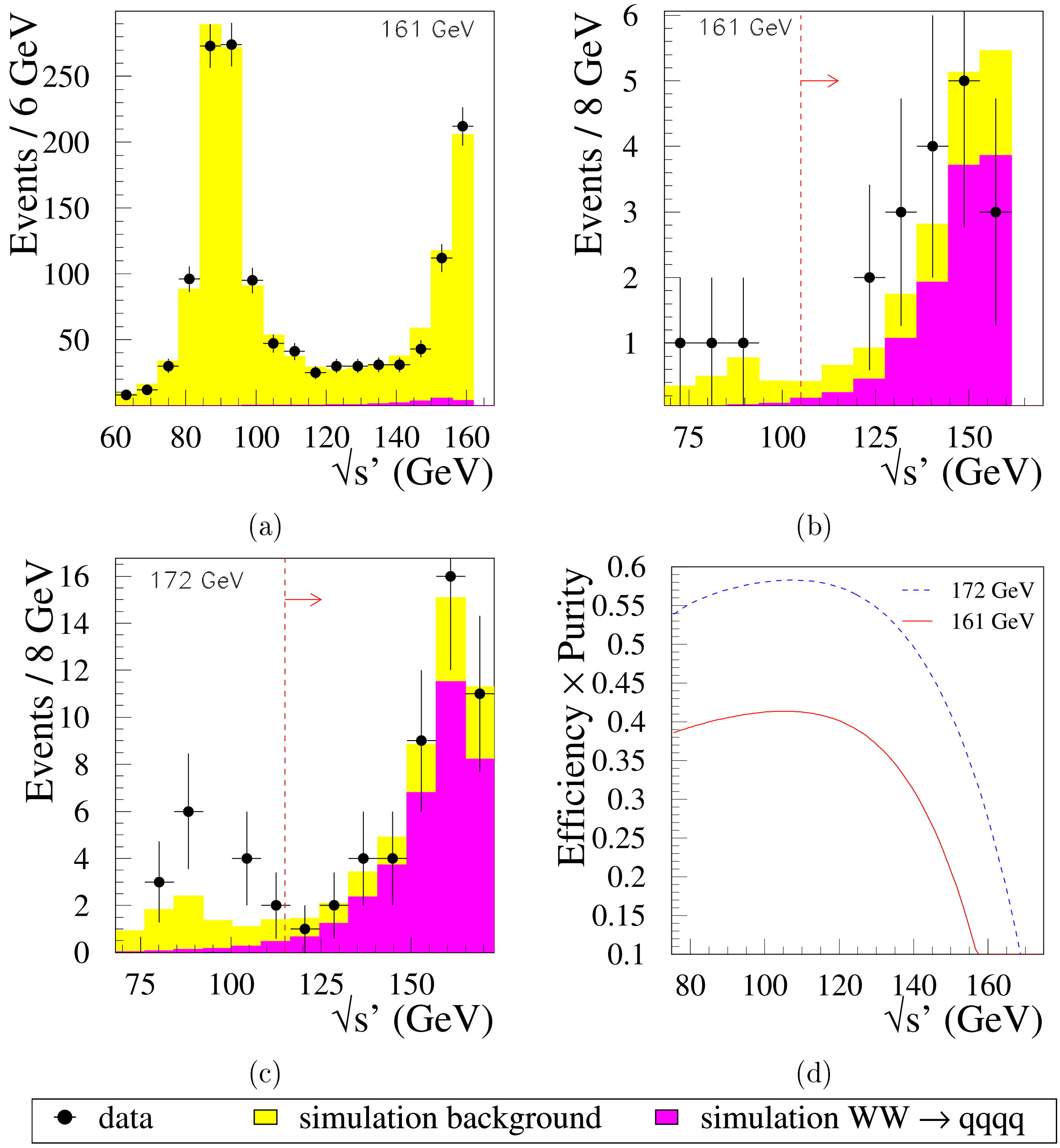

Figure 4.7: A selection of distributions for the effective centre of mass energy of an event ($\sqrt{s'}$). The $\sqrt{s'}$ is shown in (a) at 161 GeV for a hadronic event selection in data and simulation. After all other cuts have been imposed, the distributions shown in (b) (161 GeV) and (c) (172 GeV) are obtained. The dashed line indicates the value of the imposed cut. The key to plots (a) to (c) is provided at the foot of the graphs. (d) shows the variation of $\epsilon \times \mathcal{P}$ in simulation as a function of the selection cut.

variable narrow jet breadth (j_b). This is a momentum weighted angle and is defined by :

$$j_{b\pm} = \sum_{i \in S_\pm} \frac{|\mathbf{p_i} \times \hat{\eta_\mathbf{T}}|}{\sum_i |\mathbf{p_i}|}$$

$$j_b = min(j_{b+}, j_{b-})$$

where the event is divided into two hemispheres, $S_\pm$, by the plane orthogonal to the thrust axis $\hat{\eta_\mathbf{T}}$. True four-jet events will have tracks distributed throughout each hemisphere, and thus have a large narrow jet breadth; while the tracks in two jet events will be at small angle to the thrust axis and hence have a small j_b.

In Figure 4.8 we plot the narrow jet breadth against the minimum jet energy; the signal events are clustered in the top-right of the diagram. We choose to select events contained within the hyperbola indicated by the solid line, that is we define a new variable:

$$D_{gluon} = E_{min} \times j_b$$

D_{gluon} is thus the jet breadth weighted minimum jet energy. The standard range of plots are provided in Figure 4.9.

4.2.6 Systematic Error

A significant component of the systematic error is due to uncertainties in the level of the $e^+e^- \rightarrow q\bar{q}(\gamma)$ background. The variables used in this analysis have all been previously used in analyses at LEP1 and are known to have agreement in their bulk distributions. We have observed the properties of these distributions for the standard $q\bar{q}$ selection at LEP2: these are shown in Figures 4.4, 4.5, 4.7, 4.9. This agreement is a necessary but not a sufficient requirement to demonstrate that the data and simulation agree for the selected events. We require that the simulation provide an accurate representation not only of the full $e^+e^- \rightarrow q\bar{q}(\gamma)$ distributions, but in the selected sample of only 0.35% of these events. The statistics currently accumulated are not sufficient to facilitate a meaningful data/simulation comparison in the selected sample.

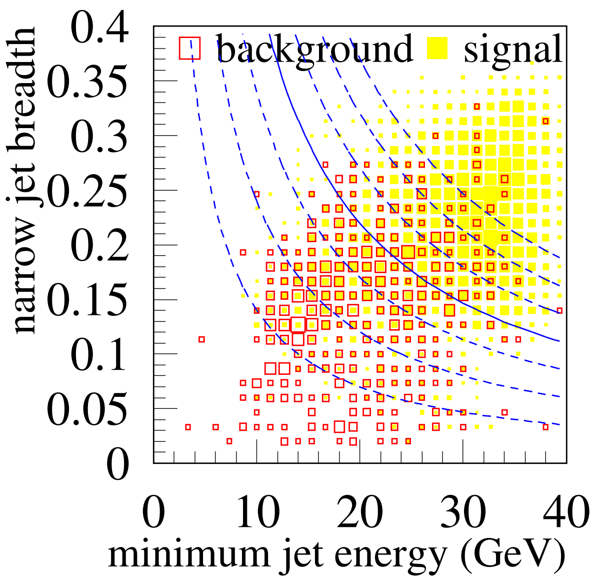

Figure 4.8: The energy of the lowest energy jet is plotted against the narrow jet breadth. The Figure shows the distribution of $W^+W^- \rightarrow q\bar{q}'\bar{q}q'$ and $q\bar{q}(\gamma)$ simulation events at 161 GeV after all other selection cuts have been applied. The hyperbola indicated by the constant line indicates the cut value applied in the analysis; a range of other values of the compound variable D_{gluon} are indicated by the dashed hyperbolae.

A detailed study of the QCD background in this channel was performed by my DELPHI Colleagues [66]. I report here on two comparisons that were performed for this study. Results from this study are given in Table 4.2. The values quoted are for a comparison based on the event selection described in [55, 67], to which the selection adopted here is very similar. Furthermore, during the studies the event selection was varied and the results obtained were compatible with those reported here.

A comparison of data and simulation was performed using large statistic samples recorded by the DELPHI experiment at the Z peak. The selection cuts applied were down-scaled such that the distributions obtained and the proportion of selected events matched that at LEP2 . For this study, the simulation events were generated with `PYTHIA` and the parton shower and fragmentation was performed by `JETSET`

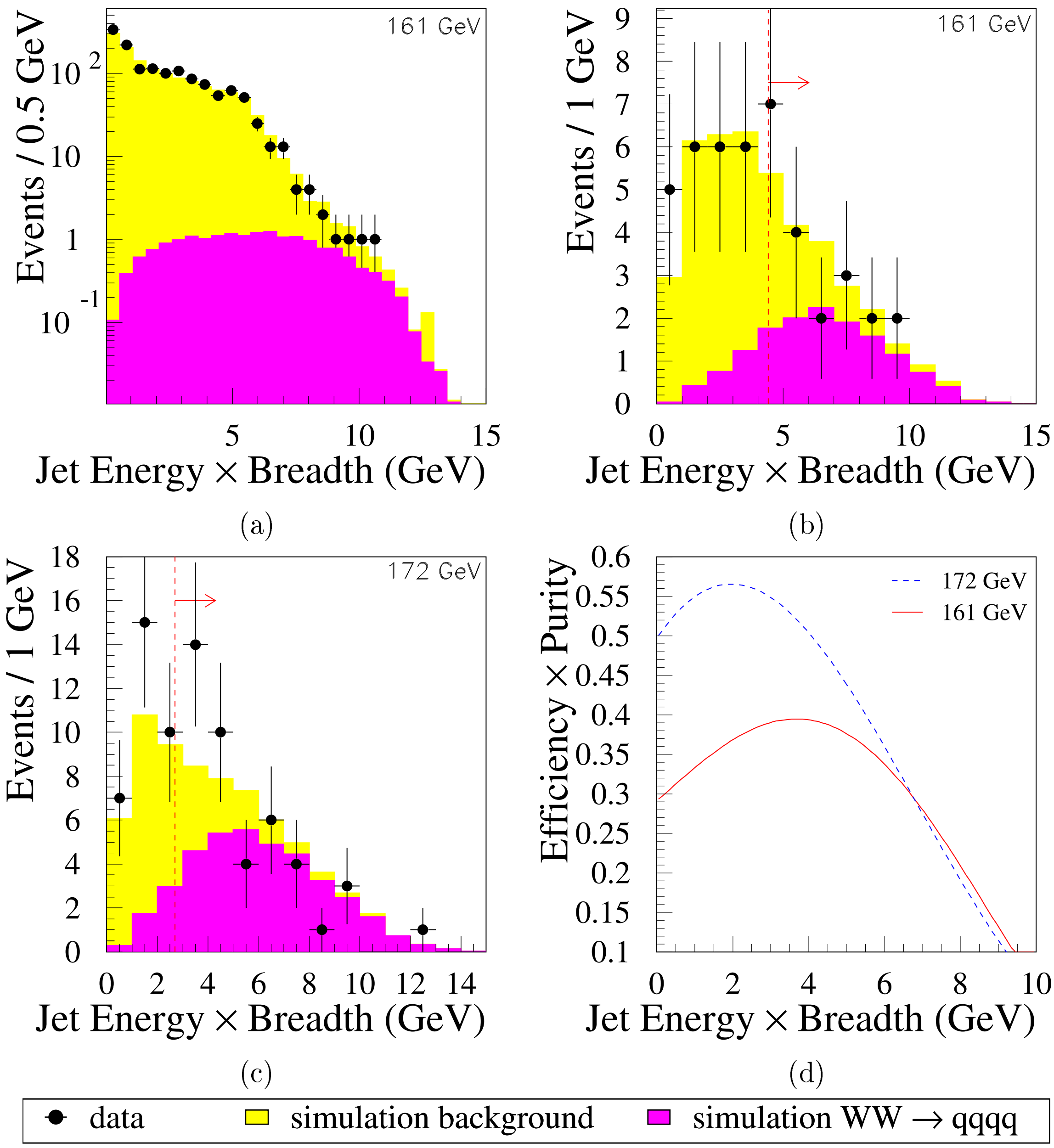

Figure 4.9: A selection of distributions for the d_{gluon} (see text) variable. The jet $energy \times breadth$ is shown in (a) at 161 GeV for a hadronic event selection in data and simulation. After all other cuts have been imposed, the distributions shown in (b) (161 GeV) and (c) (172 GeV) are obtained. The dashed line indicates the value of the imposed cut. The key to plots (a) to (c) is provided at the foot of the graphs. (d) shows the variation of $\epsilon \times \mathcal{P}$ in simulation as a function of the selection cut.

Selection Energy	DELSIM 91 GeV Data	DELSIM ARIADNE	FASTSIM ARIADNE	FASTSIM JETSET M.E.	FASTSIM JETSET 7.3
161 GeV	$+3.0 \pm 0.7\%$		$+6.8 \pm 2.4\%$	$+13.5 \pm 2.4\%$	
172 GeV	$+5.1 \pm 0.3\%$	$+8.3 \pm 0.06\%$	$+4.4 \pm 1.1\%$	$+6.5 \pm 1.1\%$	$-0.8 \pm 1.1\%$

Table 4.2: The table shows results from a DELPHI Collaboration study of the $e^+e^- \to q\bar{q}(\gamma)$ process based on event selections at 161 and 172 GeV for $W^+W^- \to q\bar{q}'\bar{q}q'$. The results are given relative to the accepted cross-section of events produced with PYTHIA and JETSET 7.4. Only statistical errors are given . The columns give results based on a rescaled data study performed at 91 GeV, full DELSIM results using the ARIADNE parton shower routine, and a FASTSIM study. In the FASTSIM study, results are given using the ARIADNE model and the JETSET matrix element formulation. These routines are used to replace the standard JETSET parton shower approach. The final column gives results with version 7.3 of JETSET.

7.4.

Two sets of simulation events were generated at 172 GeV with the PYTHIA generator, the first used the JETSET parton shower algorithm and the second used ARIADNE. The fragmentation was then performed with JETSET 7.4. The results shown in Table 4.2 are those obtained on application of this analysis to these simulation samples. In addition, a comprehensive study using large statistic samples was performed by my colleagues in DELPHI using the FASTSIM tool; the results from this study are also provided in the Table. To assist the reader, a discussion of simulation generators and parton shower algorithms is provided in Section 3.11.

The conclusion of this study was that, in the region of phase-space we are interested in for this analysis, the samples generated with the JETSET parton shower algorithm under-estimate the $q\bar{q}$ background. We choose to re-scale the PYTHIA/ JETSET accepted cross-section by $7.0 \pm 7.0\%$ at 161 GeV and $4.5 \pm 4.5\%$ at 172 GeV.

The contribution to the systematic error from uncertainties in the track reconstruction in simulation was calculated. This was split into two components, varying the track reconstruction efficiency ($\pm 4\%$), and the track energies: charged track momenta were varied by $\pm 2\%$ and neutral cluster energies by $\pm 5\%$. The results were checked by varying the selection variables by their estimated resolution. The major contribution to the systematic error due to the accuracy of the simulation events comes from the D_{gluon} variable. Small variations in the value of this cut lead to a significant change in the selection efficiencies of both signal and background.

	$\epsilon_{W^+W^-\to q\bar{q}'\bar{q}q'}$		$\sigma'_{background}$	
	161 GeV	172 GeV	161 GeV	172 GeV
Central Value	60.8%	75.9%	0.59pb	1.55pb
Simulation Statistics	±0.7%	±0.4%	±0.04 pb	±0.05 pb
Simulation Accuracy	±3.0%	±3.0%	±0.06 pb	±0.10 pb
Background Studies			±0.04 pb	±0.07 pb
TOTAL	±3.0%	±3.0%	±0.08 pb	±0.13 pb
	$\sigma_{W^+W^-\to q\bar{q}'\bar{q}q'}$			
	161 GeV		172 GeV	
`CC03` Correction Factor	±1.5%		±1.5%	
Luminosity	±0.7%		±0.8%	

Table 4.3: Contributions to the systematic error in the $W^+W^-\to q\bar{q}'\bar{q}q'$ channel analysis. The contributions are given separately for the $W^+W^-\to q\bar{q}'\bar{q}q'$selection efficiency ($\epsilon_{W^+W^-\to q\bar{q}'\bar{q}q'}$), and the estimated selected background cross-section ($\sigma'_{background}$). For completeness additional systematics applied to the calculated W^+W^- cross-sections are also listed.

Although some overlap in the error on the background events from this source with that in the background study is inevitable, we conservatively take the two errors as uncorrelated. The full list of contributions to the systematic error are provided in Table 4.3.

The simulation events were generated at 161.0 GeVand 172.0 GeV; the difference in energy from the data (161.3, 172.3) is found to have a negligible effect for both the signal and background. For the data recorded at 170.3 GeV an additional systematic error of 0.6% on the signal efficiency and 0.03pb on the background is included; these values were assessed by applying appropriately rescaled selection cuts to the 172 GeV simulation samples. The signal selection efficiencies are found not to be strongly dependent on the W mass.

4.2.7 Results

The selection criteria imposed in the $W^+W^- \to q\bar{q}'\bar{q}q'$ analysis are listed in Table 4.4.

In Table 4.5 we summarise the results of applying these selection cuts to the data and simulation samples.

Selection Cut		161	172
$d_{join}3 \rightarrow 4$	$>$	7.5 GeV/c	6.5 GeV/c
Jet Multiplicity	$\geq$	4	4
Sprime	$>$	105 GeV	115 GeV
D_{gluon}	$>$	4.4 GeV	2.7 GeV

Table 4.4: Summary table of the applied selection criteria in the analysis of $W^+W^- \rightarrow q\bar{q}'\bar{q}q'$: see the text for further details.

		161 GeV	172 GeV	170 GeV
Efficiency	$W^+W^- \rightarrow q\bar{q}'\bar{q}q'$	$60.8 \pm 3\%$	$75.9 \pm 3\%$	$75.9\ \% \pm 3\%$
Background	$q\bar{q}$	0.56 pb	1.39 pb	1.43 pb
	4f	0.02 pb	0.08 pb	0.08 pb
	Other W^+W^-	0.01 pb	0.07 pb	0.06 pb
	TOTAL	0.59 $\pm$0.08 pb	1.55 $\pm$0.13 pb	1.58 $\pm$0.14 pb
Selected	Events	17	48	4

Table 4.5: Summary of the results of the $q\bar{q}'\bar{q}q'$ decay channel analysis. Where errors are given, they represent the total systematic error on that quantity.

4.3 $l\overline{\nu}_l q\bar{q}'$ Decay Channel

4.3.1 Introduction

Within two days of LEP running at the W^+W^- threshold, the beautiful semi-leptonic W^+W^- decay event shown in Figure 4.10 was observed at DELPHI. Events from this channel are characterised by two hadronic jets and one charged lepton. The jets and the lepton arise from the fermions produced by a W decay, and hence have a momentum distribution peaked around roughly $\frac{1}{2}$ the mass of the decaying W. The fourth fermion from the W decay, the neutrino, is not observed in the detector: the near 4π steradian coverage of the detector means that the missing momentum in the event can be used to determine the neutrino energy and direction (see Section 6.4).

The primary source of background is hadronically decaying Z/γ events, in which one identifies a lepton candidate. The properties of the lepton candidate provide the principal discrimination against this background. True leptons are produced in the cascade decays of heavy quarks; these leptons will generally have lower momentum than true leptons from the W decay. Fake leptons are hadrons that have been mis-identified as electrons or muons, or are selected by the tau analysis stream (see below). Both the true and fake leptons in the background will generally be adjacent to the hadronic activity of the jet from which they originate: a measure of the isolation of the lepton is invaluable in the selection criteria.

Additional sources of background arise from other (non-WW) four-fermion final states. These include ZZ events, and t-channel boson exchange graphs such as the Ze^+e^- and $We\nu_e$ processes.

4.3.2 Analysis Structure

In this analysis, the class of semi-leptonic W^+W^- decays is divided into three sub-categories. This division is made on the basis of the lepton identification :

- tagged as muon candidate
- tagged as electron candidate

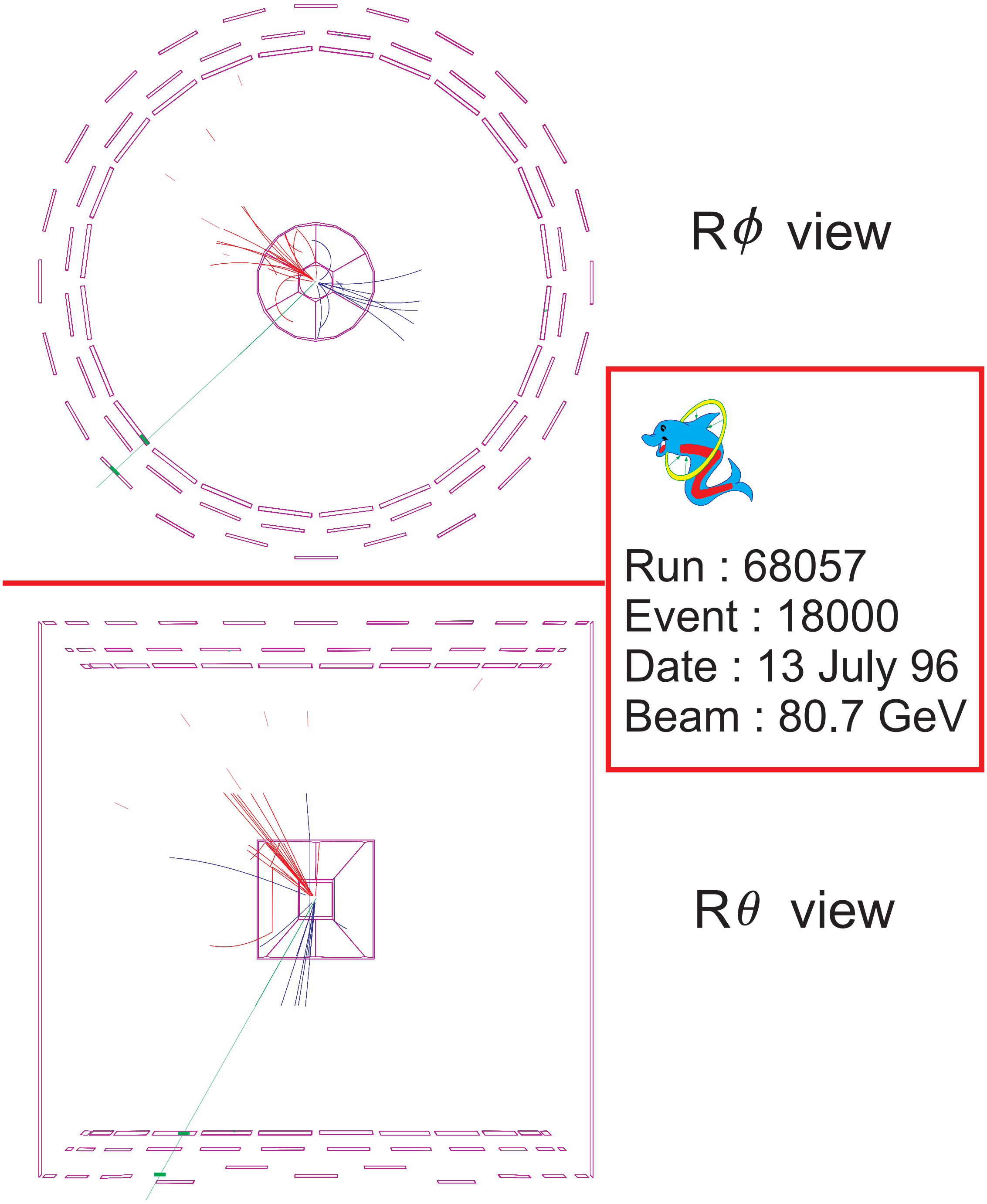

Figure 4.10: Example of a $W^+W^- \rightarrow \mu\overline{\nu}_\mu q\bar{q}'$ decay. The barrel muon chambers and TPC are shown. In both views hits in two layers of the muon chambers are clearly observed for the muon candidate.

- narrow jet (including un-identified single charged tracks)- referred to as the tau analysis stream

Events from the $\mu\overline{\nu}_\mu \mathrm{q\bar{q}'}$ channel will principally be identified by the muon candidate analysis stream; a fraction of the events in which the identification of the muon is not made are recovered using the tau tag. Similarly, in the $\mathrm{e\overline{\nu}_e q\bar{q}'}$ channel the electron candidate analysis selects the primary fraction of these events. The electron identification efficiency is lower than that of muons, and hence the number of true electron events regained through the tau analysis stream is correspondingly larger than that for true muons events. Electrons may undergo *bremsstrahlung* early in the detector (*e.g.* on entering the TPC) and the photons can then convert to e^+e^- pairs. This electromagnetic shower is not always identified as originating from an electron, and can instead be tagged by the tau stream narrow jet algorithm.

Events in the $\tau\overline{\nu}_\tau \mathrm{q\bar{q}'}$ decay channel are more difficult to isolate from the $q\bar{q}$ background. The high momentum of the lepton candidate is one of the principal selection criteria in the $\mathrm{l\overline{\nu}_l q\bar{q}'}$ analysis. However, the tau lepton will decay through a virtual W boson emitting a ν_τ and the momentum of the measured lepton will thus be less than in the other channels. 18% of taus will decay into muons, and the same fraction into electrons; these events may be tagged by the electron or muon analysis streams. Unfortunately, the efficiency for this cross-tagging proves to be low as the decay is accompanied by the emission of a further neutrino: thus the final lepton momentum is further reduced. The tau tag is based on the identification of a narrow jet of one to five particles. This attempts to identify the 13% of taus that decay into one charged hadron (principally pions), and events from tau to multi-prong decays (51%).

The selection variables applied are similar for all three of the lepton identification streams of the analysis. These selection cuts can be divided into several categories : lepton identification, jet quality, cuts against radiative background events, missing momentum, and an anti four-fermion background selection. In the following sections we discuss each of these categories in turn and provide figures illustrating the principal selection variables. The values of the applied selection cuts differ between the three identification streams, the c.m. energy (161 or 172 GeV), and in some cases between different lepton momentum regions. The values of all the applied cuts are provided at the end of this section in Table 4.7.

4.3.3 Lepton

A candidate lepton (for each analysis stream) is the lepton which passes both the momentum and isolation requirements of that analysis. When two leptons candidates pass the isolation requirement for a given analysis stream, the candidate with the higher momentum is retained. The known level of data/simulation agreements for leptons are given in Section 3.9.

Electron Identification

The electron identification is performed on charged tracks in the polar angle range between 20°and 160°. We identify electrons from their characteristic energy deposition in the electromagnetic calorimeters. The following simple criteria are adopted:

- $E_{HPC} + E_{FEMC} > 10\ GeV$
- $E_{FEMC} < 50\ GeV$

The second criterion is imposed to prevent the selection of forward photons, in Z boson radiative return events, that have been erroneously connected to a charged track. The selection efficiency for high energy electrons was found to be $\approx$ 77%.

Muon Identification

Muons are identified simply by requiring that the track has an

- associated hit in the muon chambers (MUB, MUS, MUF)

This tag has a high efficiency ($\approx$ 92%) for true muons of high momentum. The efficiency of the muon tag can be further increased by selecting muons based on their deposits in the Hadron Calorimeter: these deposits are required to be compatible with minimum ionising particles. However, this selection also increases the proportion of selected pions. In the $\mu\overline{\nu}_\mu q\bar{q}'$ decay channel, 'punch-through' pions that have reached the muon chambers are a significant component of the background. Hence, hadron calorimeter identification of muons is not applied in this analysis. Good agreement was found between data and simulation for high momentum muons in $Z \to \mu\mu$ decays, and for low momentum pairs produced in $\gamma\gamma$ reactions.

Tau Identification

A natural jet clusterisation is performed on the event using the `LUCLUS` algorithm with a d_{join} of 6.5 GeV/c. A candidate narrow jet lepton is then identified from the jets formed by :

- Charged Multiplicity ≥ 1 and ≤ 3
- Total Multiplicity ≤ 5
- Neutral Energy in the Jet $<$ 80% Total Jet energy
- Jet Breadth $< \sin 10°$

The multiplicity cuts select one prong and multi-prong tau decays, while providing some discrimination from hadronic jets. Jets that originate from badly reconstructed photons are rejected with the neutral energy requirement. The jet is required to be relatively narrow using the jet breadth requirement, where the jet breadth is defined as in Section 4.2.5.

Momentum

In Figure 4.11, we show the momentum of the selected lepton candidates. The $W^+W^- \to l\overline{\nu}_l q\bar{q}'$ signal events in simulation are shown with the events selected by the three analysis streams indicated separately. The momentum of the lepton candidate from true tau events is generally lower than that in the electron or muon channels as an extra neutrino is emitted.

The most accurate determination of the electron energy is obtained from its calorimeter deposits, rather than the momentum obtained from the tracking detectors. Hence, throughout this analysis, electron candidates have their direction taken from the tracking detectors measurements, but their momentum is rescaled to their energy deposited in the electromagnetic calorimeters. Based on comparisons of Bhabha events in data and simulation, fixing routines [68] have been developed for the 1996 data to recalibrate the observed energy deposits in the electromagnetic calorimeters.

For the tau analysis stream, we use the total energy of the narrow jet: this is computed in the standard manner from the sum of the momenta of the charged tracks and the calorimeter energy deposits of the neutral clusters.

In Figure 4.11 (a), a pre-selection has been imposed where only the lepton identification, a loose isolation cut and the jet quality selections have been applied. The peak of fake lepton candidates in the background at low momenta is clearly visible.

Isolation

In $W^+W^- \to l\overline{\nu}_l q\bar{q}'$ events the selected lepton candidate will, in general, be spatially well separated from the products of quark fragmentation and decay. Both the hadronic products of fragmentation and leptons from heavy quark decay will lie within jets of relatively narrow angular spread. We demand that the selected lepton candidate should be well separated from the remaining tracks in the event.

We define the isolation angle (θ_{iso}) as the full-space angle between the lepton candidate and the nearest charged track of over 1 GeV. We rely on charged particles as they are reconstructed and simulated more accurately than neutral clusters. The minimum momentum requirement makes the variable less sensitive to the parton shower and hadronization algorithms used in the simulation.

This variable is illustrated in Figure 4.12. A sharp peak is visible in the preselection plot (a), where lepton candidates have been selected at small isolation angles: these lepton candidates are thus likely to be products of jet fragmentation.

4.3.4 Jets

If a candidate lepton is selected in a given analysis stream, we proceed with the analysis of the jets in that event. Removing the lepton candidate, we cluster the remaining tracks in the event into two jets using the `LUCLUS` algorithm.

We then make a selection based on the quality of the reconstructed jets. As in the $q\bar{q}'\bar{q}q'$ channel analysis, each jet is required to have a total multiplicity of four

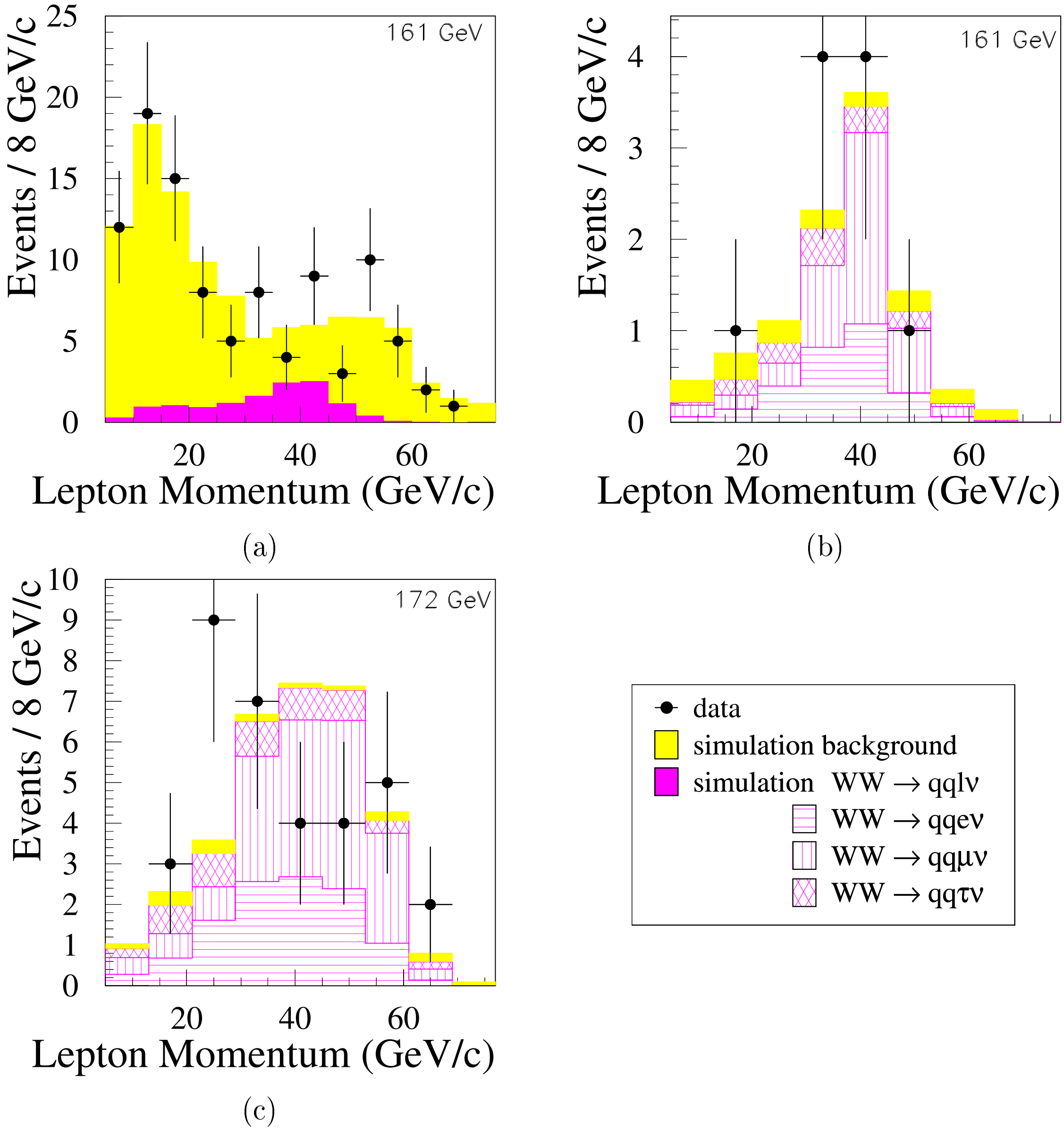

Figure 4.11: The momentum of the selected lepton candidate is shown in (a) at 161 GeV for a loose event pre-selection in data and simulation. After all other cuts have been imposed the distributions shown in (b) (161 GeV) and (c) (172 GeV) are obtained. The key to plots (a) to (c) is provided, the signal simulation is divided into the events selected by the three analysis streams.

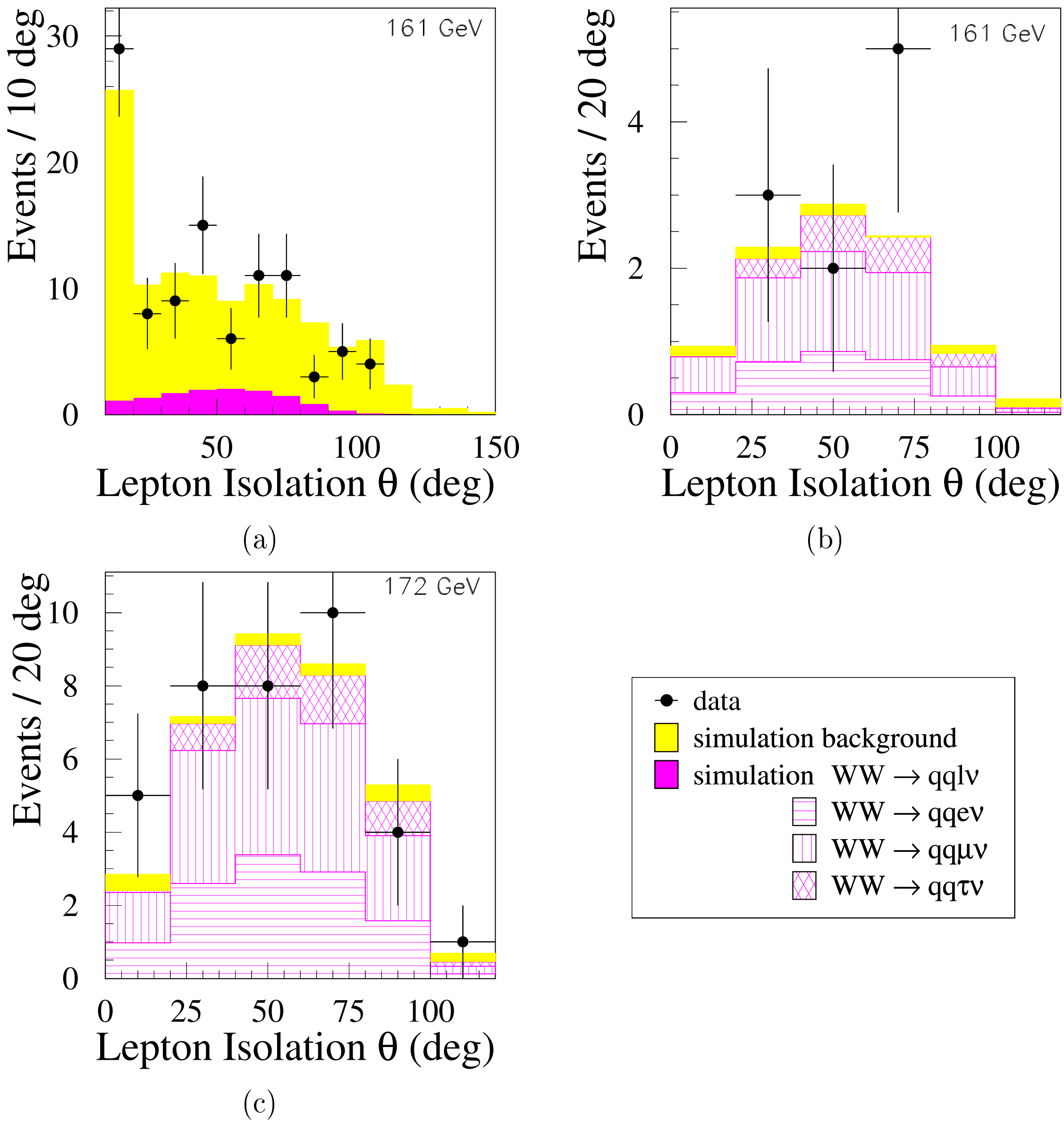

Figure 4.12: The angle between the selected lepton candidate and the nearest charged track of momentum greater than 1 GeV/c is shown in the Figure. Distributions are given at 161 GeV for a loose event pre-selection in data and simulation (a), and after all other cuts have been imposed (b) (161 GeV) and (c) (172 GeV). The key to plots (a) to (c) is provided; the signal simulation is divided into the events selected by the three analysis streams.

or more tracks. Furthermore, we demand that each jet contain at least one charged particle.

The non-W^+W^- four-fermion background processes are simulated using the `PYTHIA` generator. This generator is not considered reliable in simulating neutral bosons with a virtuality close to zero. An explicit cut is therefore imposed on the the invariant mass of the two jets. As the cut is imposed at 30 GeV it does not have a significant biasing effect on the W mass measurement.

In the narrow jet analysis stream we perform a natural jet clusterisation. Only events that are reconstructed as containing three jets are retained for further analysis. This selection requirement reduces the background from the $W^+W^- \to q\overline{q}'\overline{q}q'$ decay channel, as well as from $q\bar{q}$ events.

4.3.5 Radiative Events

$q\bar{q}(\gamma)$ background events in which a large momentum ISR photon is emitted are the major component of the background in this analysis. However, the sprime algorithm discussed in section 4.2.4 is of limited use in this analysis: the missing neutrino in $l\overline{\nu}_l q\overline{q}'$ events is interpreted as indicative of a missed ISR photon and this leads to the reconstructed $\sqrt{s'}$ of these events forming a broad distribution.

Seen Photons

Photon identification is performed by considering the neutral energy clusters in the event: *i.e.* those which are unassociated with a charged track. Events containing large electromagnetic calorimeter energy clusters are rejected.

Unseen Photons

From the imbalance of the reconstructed track momenta in an event, we define a missing momentum vector. We then make a selection based upon the polar angle of this vector: this is illustrated in Figure 4.13. In the $q\bar{q}(\gamma)$ background events, the distribution is observed to be sharply forward peaked: this is indicative of an undetected photon having been produced collinear with the beam pipe.

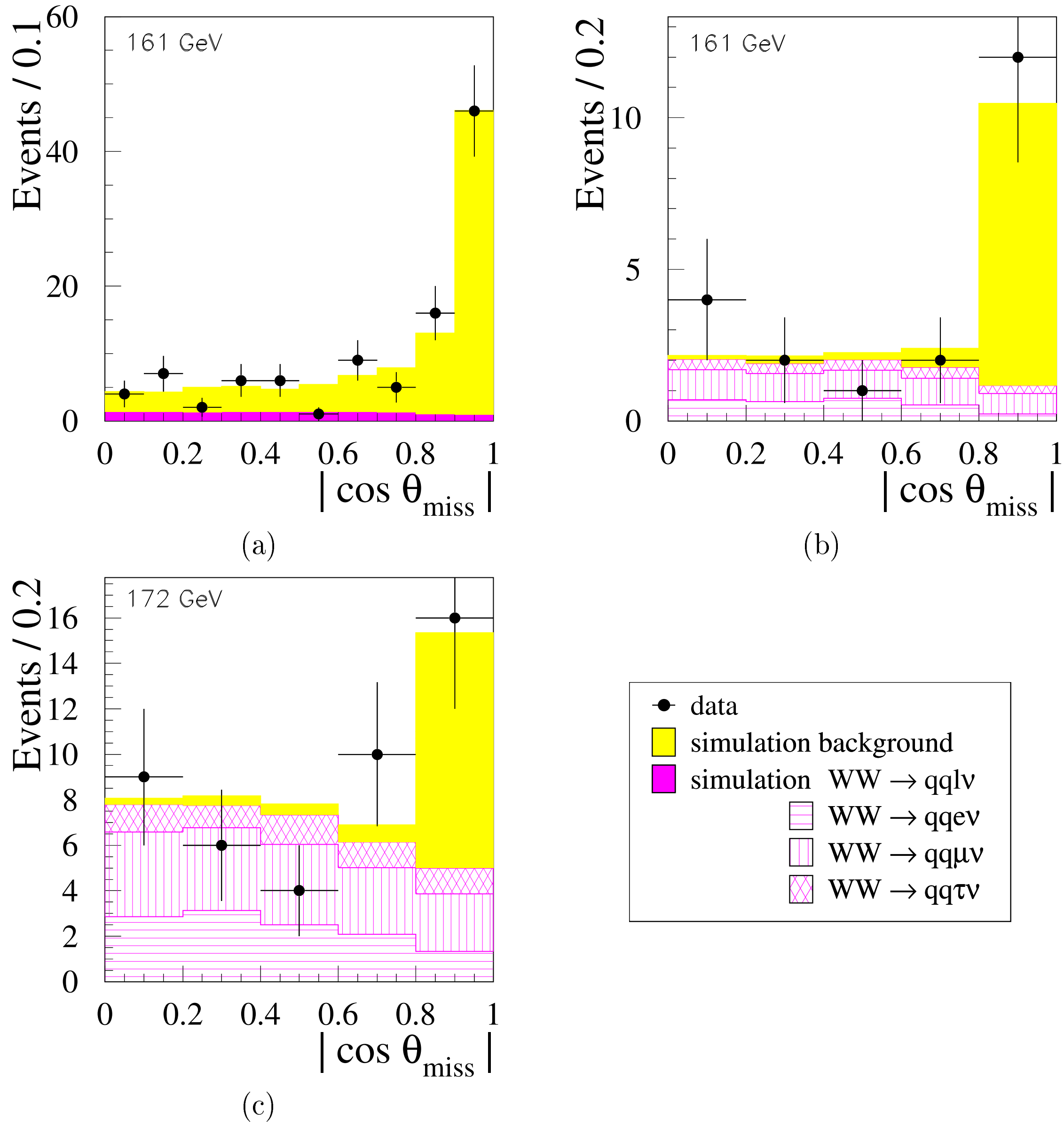

Figure 4.13: The cosine of the polar angle of the missing momentum in the event is shown in (a) at 161 GeV for a loose event pre-selection in data and simulation. After all other cuts have been imposed the distributions shown in (b) (161 GeV) and (c) (172 GeV) are obtained. The key to plots (a) to (c) is provided; the signal simulation is divided into the events selected by the three analysis streams.

4.3.6 Missing Momentum

In the previous sections, we have discussed the suppression of radiative $q\bar{q}$ events. However, we must also attempt to reject non-radiative $q\bar{q}$ events. As the leptonically decaying Ws will produce a high momentum neutrino, we expect our signal events to be accompanied by a large missing momentum. We impose a selection cut on the magnitude of the missing momentum vector.

When particles are missed in the DELPHI detector, this can lead to both an artificial increase in the isolation of a lepton candidate and the feigning of missing momentum in the event. The angle between the lepton and the missing momentum vector can thus be used to reject these events. This variable is used in all the analysis streams and is illustrated in Figure 4.15. In the tau analysis stream, a cut is also applied to the angle between the momentum of the jets in the event and the missing momentum vector.

The W^+W^- production studied in this analysis occurs close to the nominal W^+W^- production energy threshold. The boost of the W bosons is thus low compared with their mass, and hence the lepton and neutrino produced in a decay will be at high angles. The imposed cut on the angle between the lepton and the missing momentum vector is roughly equivalent to requiring an invariant mass of greater than 40 GeV. This value is sufficiently low that the W mass bias introduced into the analysis can safely be neglected.

4.3.7 Second Lepton

Four-fermion neutral current backgrounds ($q\bar{q}\ l^+l^-$) were reduced by applying an additional cut to events in which a second lepton candidate was found. In the rejected events, this lepton was required to be of the same flavour as the first selected lepton, and the charge of the second lepton candidate was required to be of opposite sign to that of the first selected lepton. This selection was not imposed in the narrow jet analysis stream.

In true di-lepton four-fermion backgrounds, the second lepton will also be isolated from the jets, whereas in semi-leptonic W^+W^- events only one isolated lepton is produced. Hence events are rejected only if the second lepton candidate passes an isolation cut.

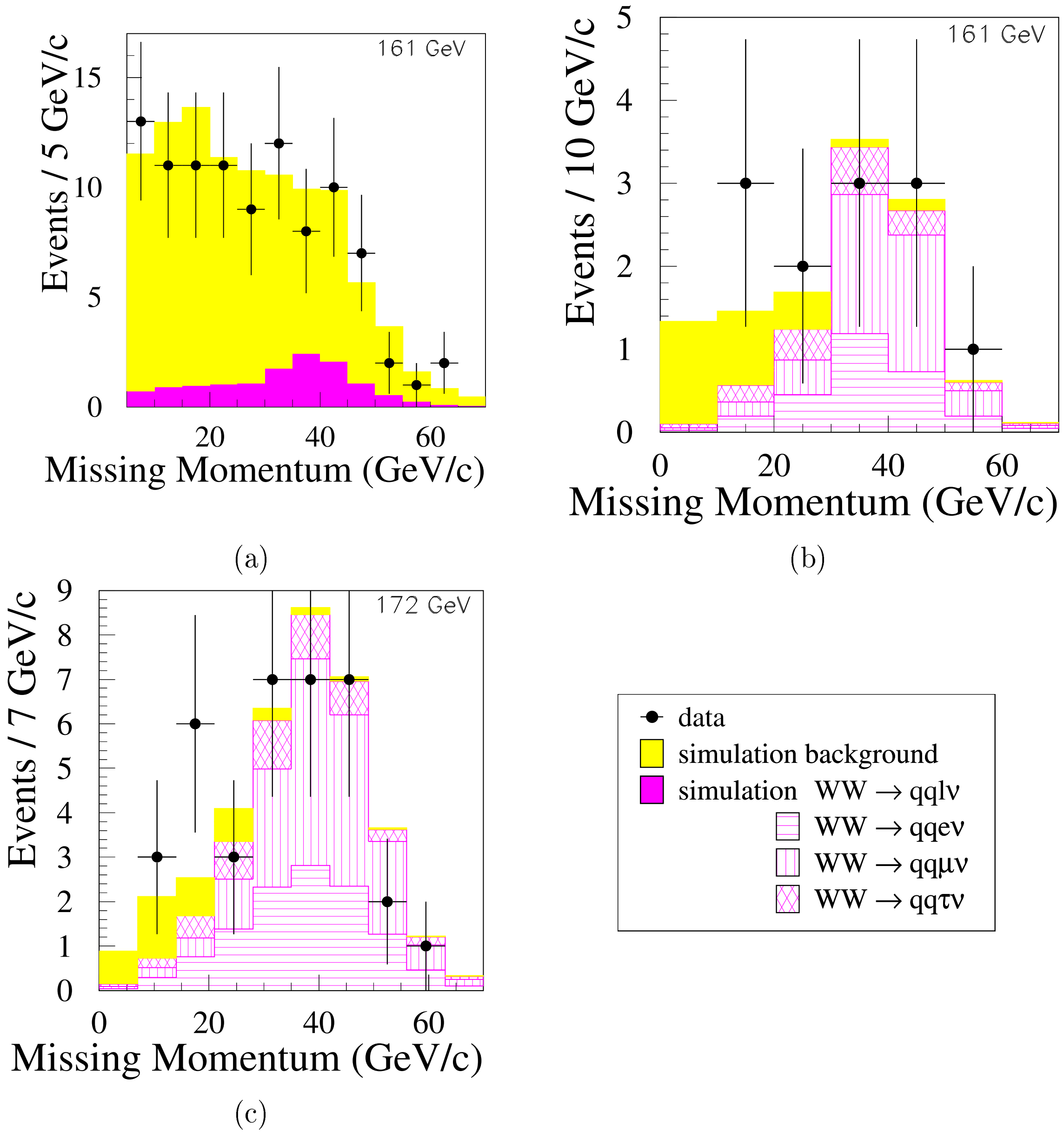

Figure 4.14: The magnitude of the missing momentum observed in an event is shown in (a) at 161 GeV for a loose event pre-selection in data and simulation. After all other cuts have been imposed the distributions shown in (b) (161 GeV) and (c) (172 GeV) are obtained. The key to plots (a) to (c) is provided; the signal simulation is divided into the events selected by the three analysis streams.

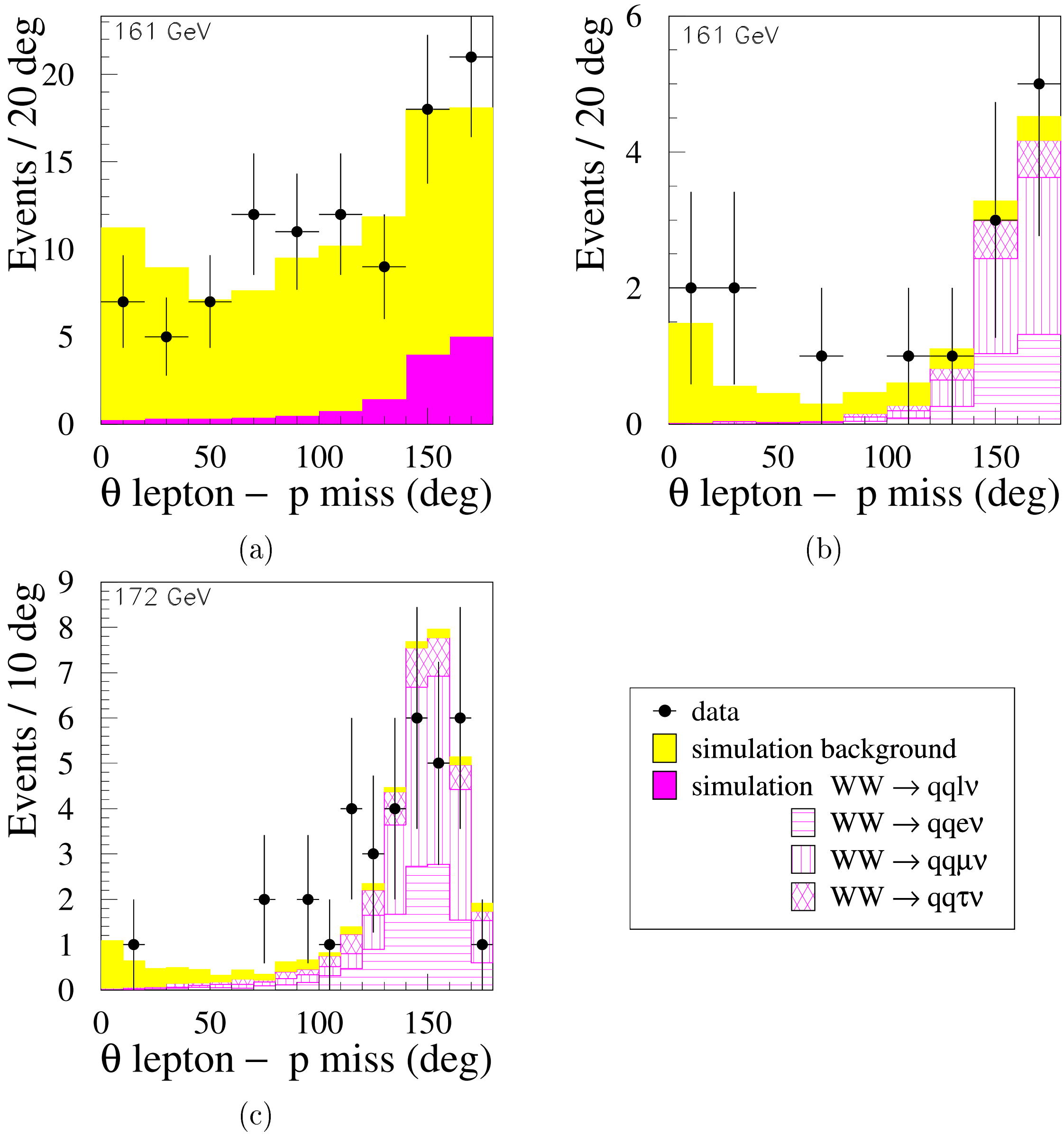

Figure 4.15: The angle between the selected lepton candidate and the missing momentum vector is shown in (a) at 161 GeV for a loose event pre-selection in data and simulation. After all other cuts have been imposed the distributions shown in (b) (161 GeV) and (c) (172 GeV) are obtained. The key to plots (a) to (c) is provided; the signal simulation is divided into the events selected by the three analysis streams.

4.3.8 Systematic Error

The dominant components of the systematic error in the $l\overline{\nu}_l q\bar{q}'$ channel result from the selection of the lepton candidate, rather than of the di-jet system.

The dominant component of the background is due to the mis-identification of isolated high momentum hadronic jet components as lepton candidates. Simulation $q\bar{q}$ background events were produced with both the PYTHIA Parton Shower algorithm and the ARIADNE model. The author (in agreement with other DELPHI studies) observed no significant differences in the accepted background in this analysis between the two samples, though the study was statistically limited at the 10% level. We conservatively quote the statistical error of ±10% as the systematic error on the background cross-section due to this source.

DELPHI collaboration studies of samples of e^+e^- and $\mu^+\mu^-$ events at LEP1 energies report overestimates of the track reconstruction efficiency in simulation of up to 2% [58]. The tracking reconstruction systematic was assessed applying this variation, in simulation events, for high momentum tracks (> 10 GeV). As in Section 4.2.6, a 4% variation in tracking efficiency was applied to the remaining tracks in the event and the track energies were also allowed to vary. The resulting error is provided in Table 4.6, where it is indicated as 'simulation accuracy'.

The errors due to data/simulation differences in muon and electron identification are reduced in the combined $l\overline{\nu}_l q\bar{q}'$ analysis by the cross-tagging possibilities between the analysis streams. True electron or muon events that are untagged can be recovered in the tau analysis stream. For example, the 2% of data at 161 GeV with muon chamber problems (see section 3.8.2) produces a correction to the combined efficiency of the analysis of only 0.3%. Lepton mis-identification probabilities have been studied at LEP1, and here we rely on these results [69] to estimate the uncertainty in the background from this source.

The statistical error on the estimation of the background efficiency is a major component of the systematic error. At 161 GeV, only 0.1% of $Z/\gamma \rightarrow q\bar{q}(\gamma)$ events pass the selection criteria: hence we required large samples of simulation events. We inevitably obtain small numbers of selected simulated background events once the full analysis is applied. These small statistics require careful use to prevent introducing a bias to the final result: both when positioning the analysis cuts and studying the systematics, extensive use was made of looser pre-selections of the background events.

	$\epsilon_{W^+W^-\to l\overline{\nu}_l q\bar{q}'}$		$\sigma'_{background}$	
	161 GeV	172 GeV	161 GeV	172 GeV
Central Value	54.7%	59.5%	0.18 pb	0.29 pb
Simulation Statistics	±0.7%	±0.5%	±0.03 pb	±0.02 pb
Simulation Accuracy	±4.5%	±4.5%	±0.02 pb	±0.03 pb
Lepton Identification	±1.5%	±1.5%	±0.01 pb	±0.02 pb
Background Studies			±0.02 pb	±0.03 pb
TOTAL	±4.8%	±4.8%	±0.04 pb	±0.05 pb
	$\sigma_{W^+W^-\to l\overline{\nu}_l q\bar{q}'}$			
	161 GeV		172 GeV	
`CC03` Correction Factor	±1.5%		±1.5%	
Luminosity	±0.7%		±0.8%	

Table 4.6: Contributions to the systematic error in the $W^+W^-\to l\overline{\nu}_l q\bar{q}'$ channel analysis. The contributions are given separately for the combined $W^+W^-\to l\overline{\nu}_l q\bar{q}'$ selection efficiency ($\epsilon_{W^+W^-\to l\overline{\nu}_l q\bar{q}'}$), and the estimated selected background cross-section ($\sigma'_{background}$). For completeness additional systematics applied to the calculated W^+W^- cross-sections are also listed.

4.3.9 Results

Table 4.7 summarises the applied selection values in this analysis. The Table is divided into three result columns, one for each of the analysis streams; each of these columns is then further divided by c.m. energy. In the muon and electron streams, a low momentum lepton selection is included. The standard selection in these channels selects high momentum (> 20 GeV) leptons with a relatively loose isolation criteria. The low momentum selection improves the efficiency of the analysis by lowering the momentum threshold (> 10 GeV). In order that a low level of background is obtained, the lepton isolation criterion and the missing momentum polar angle cut are tightened.

Several selection cuts are loosened at 172 GeV compared with their 161 GeV values: notably, the low energy electron selection is introduced at 172 GeV which is absent at 161 GeV. While adapting slightly to the regime of an increased signal to background ratio, the 172 GeV selection is intended to retain the character of the

161 GeV selection: insofar as a high purity analysis is retained in all channels. The optimal point of statistical sensitivity in the tau channel at 172 GeV would double the accepted background cross-section.

In Table 4.8 the selections' efficiencies of this analysis at 161 GeV are shown for the four analysis streams. We include this table to illustrate further that the off-diagonal elements in the selection are non-negligible: particularly the label 'tau stream' while providing a convenient nomenclature, should not be interpreted too literally by the reader. The pattern of values in Table 4.8 does not change significantly at 172 GeV; although the electron selection efficiency increases by 15% of its 161 GeV value. The rise in the electron stream efficiency is due to the inclusion of a low momentum selection in the 172 GeVanalysis.

Occasionally events can be tagged by more than one of the identification streams. We solve this ambiguity such that we obtain the smallest off-diagonal elements in Table 4.8: the imposed hierarchy gives presidence to the muon stream analysis, followed by the electron stream, and finally the tau stream. In Table 4.8 and all the quoted results, each event has only one entry.

The results for the combined $\mathrm{l}\overline{\nu}_{\mathrm{l}}\mathrm{q}\bar{\mathrm{q}}'$ channel analysis are provided in Table 4.9. The major background contribution is from radiative Z $\rightarrow q\bar{q}\,\gamma$ events, though (non-$\mathrm{W}^+\mathrm{W}^-$) four-fermion events must also be considered. The principle component of the four-fermion final state backgrounds is from the electron analysis stream, where the process $e^+e^-\rightarrow \mathrm{Z}e^+e^-\rightarrow q\bar{q}\ e^+e^-$contributes.

Selection Cut		Electron Stream 161	Electron Stream 172	Muon Stream 161	Muon Stream 172	Tau Stream 161	Tau Stream 172
Lepton Momentum (GeV/c)	>	20	20 — 10	20 — 10	20 — 10	10	10
Lepton Isolation ∠	>	10 °	10 ° — 30 °	10 ° — 30 °	10 ° — 30 °	10 °	10 °
Jet Quality		mass > 30 GeV, ≥ 4 tracks including ≥ 1 charged per jet					
Photon Energy (GeV)	>	20	30	20	30	30	40
$\theta_{p_{miss}}$	<	25 °	25 ° — 30 °	20 ° — 30 °	20 ° — 30 °	35 °	35 °
Missing Momentum (GeV/c)	>	15	15	10	10	20	15
∠ Lepton — p_{miss}	>	90 °	70 °	80 °	60 °	100 °	80 °
∠ Jet — p_{miss}	>	15 °	10 °	—	—	25 °	25 °
2^{nd} Lepton Isolation ∠	<	20 °	20 °	20 °	20 °	—	—

Table 4.7: Summary table of the applied selection criteria in the analysis of $W^+W^- \rightarrow l\overline{\nu}_l q\bar{q}'$: see the text for further details. Where two sets of values appear in a single column, they show the standard selection and the tighter cuts that were imposed on low momentum leptons.

Decay Channel	Electron Stream	Muon Stream	Tau Stream	All Streams
$e\overline{\nu}_e q\bar{q}'$	52%	0%	3%	55%
$\mu\overline{\nu}_\mu q\bar{q}'$	0%	78%	7%	85%
$\tau\overline{\nu}_\tau q\bar{q}'$	9%	4%	14%	27%
$l\overline{\nu}_l q\bar{q}'$	20%	27%	8%	55%

Table 4.8: Selection efficiencies at 161 GeV for the $l\overline{\nu}_l q\bar{q}'$ analysis by true lepton type and analysis stream

		161 GeV	172 GeV	170 GeV
Efficiency	$W^+W^- \rightarrow l\overline{\nu}_l q\bar{q}'$	$54.7 \pm 4.8\%$	$59.5 \pm 4.8\%$	$59.5\% \pm 4.8\%$
Background	$q\bar{q}$	0.14 pb	0.19 pb	0.19 pb
	4f	0.04 pb	0.10 pb	0.10 pb
	TOTAL	0.18 $\pm$0.04 pb	0.29 $\pm$0.05 pb	0.29 $\pm$0.05 pb
Selected Events	$e\overline{\nu}_e q\bar{q}'$ Stream	1	15	0
	$\mu\overline{\nu}_\mu q\bar{q}'$ Stream	5	13	1
	$\tau\overline{\nu}_\tau q\bar{q}'$ Stream	4	6	0
	TOTAL	10	34	1

Table 4.9: Summary of the results of the $l\overline{\nu}_l q\bar{q}'$ decay channel analysis. Where errors are given they represent the total systematic error on that quantity.

4.4 $l\overline{\nu}_l\bar{l}\nu_l$ Decay Channel

4.4.1 Introduction

The fully-leptonic W$^+$W$^-$ decay channel can be sub-divided into six categories by lepton type :

Decay Channel	Relative Branching Fraction
W$^+$W$^-$$\rightarrow e\overline{\nu}_e\overline{e}\nu_e$	$\frac{1}{9}$
W$^+$W$^-$$\rightarrow \mu\overline{\nu}_\mu\overline{\mu}\nu_\mu$	$\frac{1}{9}$
W$^+$W$^-$$\rightarrow \tau\overline{\nu}_\tau\overline{\tau}\nu_\tau$	$\frac{1}{9}$
W$^+$W$^-$$\rightarrow e\overline{\nu}_e\overline{\mu}\nu_\mu$	$\frac{2}{9}$
W$^+$W$^-$$\rightarrow e\overline{\nu}_e\overline{\tau}\nu_\tau$	$\frac{2}{9}$
W$^+$W$^-$$\rightarrow \mu\overline{\nu}_\mu\overline{\tau}\nu_\tau$	$\frac{2}{9}$

However, the basis of the selection presented here is a flavour blind $l\overline{\nu}_l\bar{l}\nu_l$ selection, in which we do not attempt to identify the individual lepton species; rather we identify these events on the basis of characteristics common to all these six decay categories.

The example event shown in Figure 4.16 clearly demonstrates many of these common characteristics. We observe one isolated charged track which has hits in the barrel muon chamber. The other lepton is a tau candidate and consists of a cluster of charged and neutral particles. In order to include multi-prong tau decays we select low multiplicity jets as lepton candidates, rather than only allowing single high energy charged tracks. Two high momentum neutrinos are produced in each event. Thus the events may appear highly unbalanced: the two jets are both highly acollinear and acoplanar.

The Z/γ background is still significant in this W$^+$W$^-$ decay channel but does not dominate over all other sources. The significant backgrounds are s-channel Z/$\gamma\rightarrow l^+l^-$, Bhabhas, two-photon collision events and four-fermion processes. The Bhabha and Z/γ events contribute when they are accompanied by undetected initial or final state radiation: these photons produce missing momentum in the reconstructed events. All the important sources of background contain two leptons of the same flavour, while only $\frac{1}{3}$ of the signal events do. Thus, one might imagine, the flavour blind selection described above can be improved upon by modifying the selection criteria when good lepton identification is obtained. However, in practice lepton identification cannot be performed with sufficiently high efficiency to achieve significant gains from this procedure: neither the data nor simulation statistics currently available justify the adoption of a more complex analysis approach.

In the following sections, the selection cuts imposed are described; the values of the imposed cuts are summarised in Table 4.11. The most important selection cuts are illustrated with figures. Pre-selection plots are provided at 161 GeV, and final selection plots at 172 GeV. In producing the pre-selection plots, the acollinearity, missing momentum polar angle and p_{tr} (see Section 4.4.4) cuts were relaxed appropriately. The low data and simulation statistics inevitably mean that we must rely heavily on pre-selection plots, as the final selection plots contain little information. We note that the two event candidates selected at 161 GeV are the same as in [55], where final selection plots can be found.

4.4.2 Jets

Two-Jet Topology

The tracks in the event are clustered using the `LUCLUS` algorithm with a d_{join} value of 6.5 GeV/c. Only events which cluster to two jets are retained. In the case of electrons or muons the jet is likely to contain only one track; however, for multi-prong tau decays the tracks will be clustered to form a jet.

Jet Quality

Each of the jets is required to contain one charged particle, and the total number of charged particles in the event is required to be less than six. These cuts render the background from hadronic decays negligible compared with that from leptonic states. However, the criteria are sufficently loose that the majority of signal events containing tau decays are retained.

The polar angle of the reconstructed jet axis is required to be above 20°. This cut was imposed during the generation of some of the two-photon collision simulation samples; it is thus necessary to impose this selection when using these samples.

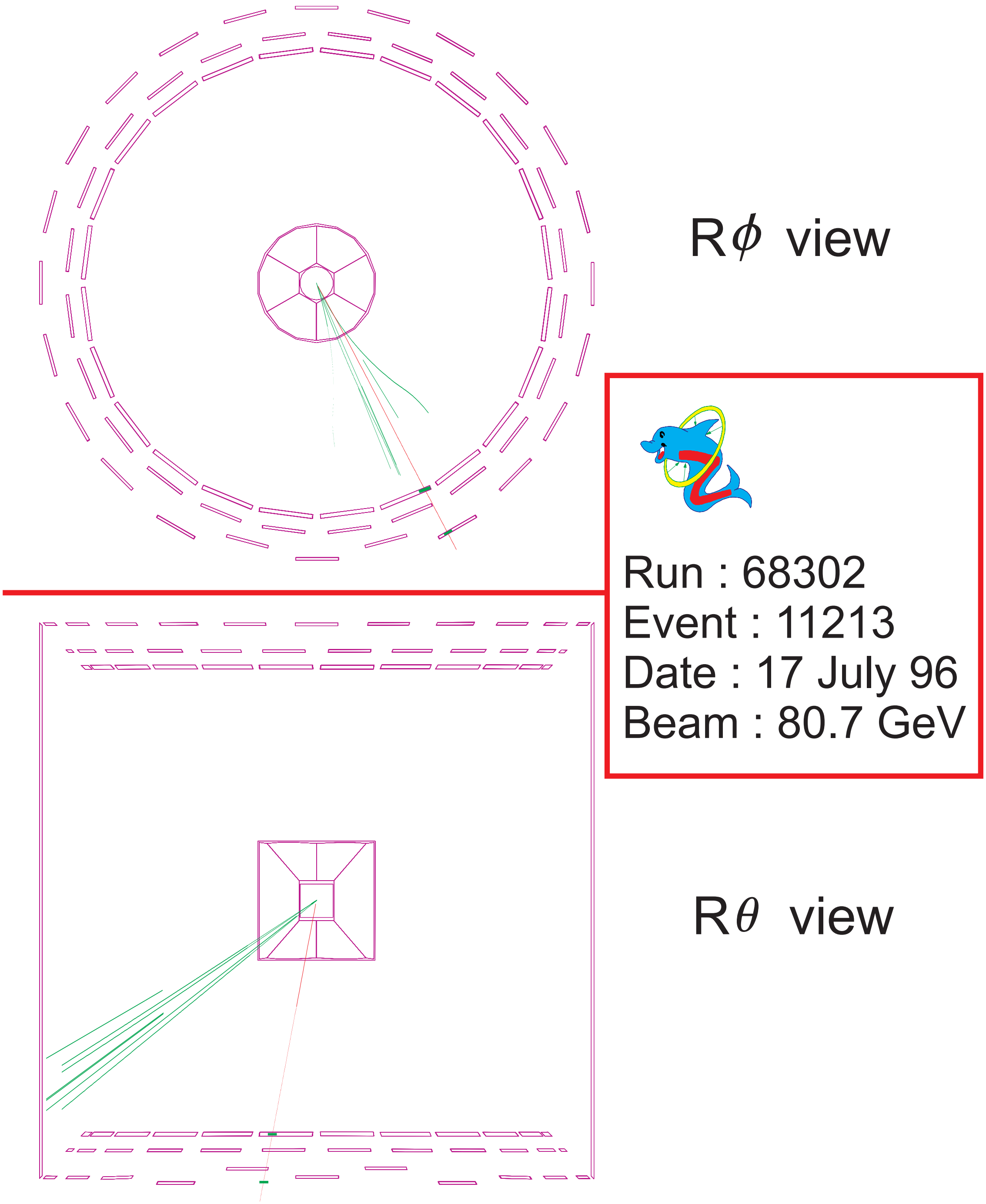

Figure 4.16: Example of a $W^+W^- \to \mu\overline{\nu}_\mu\overline{\tau}\nu_\tau$ decay. The DELPHI TPC and barrel muon chambers are shown on the plot. One 30 GeV track is identified by the barrel muon chambers, the hits are shown. The other tracks cluster into a narrow low multiplicity jet of 35 GeV momentum and are considered as a tau candidate.

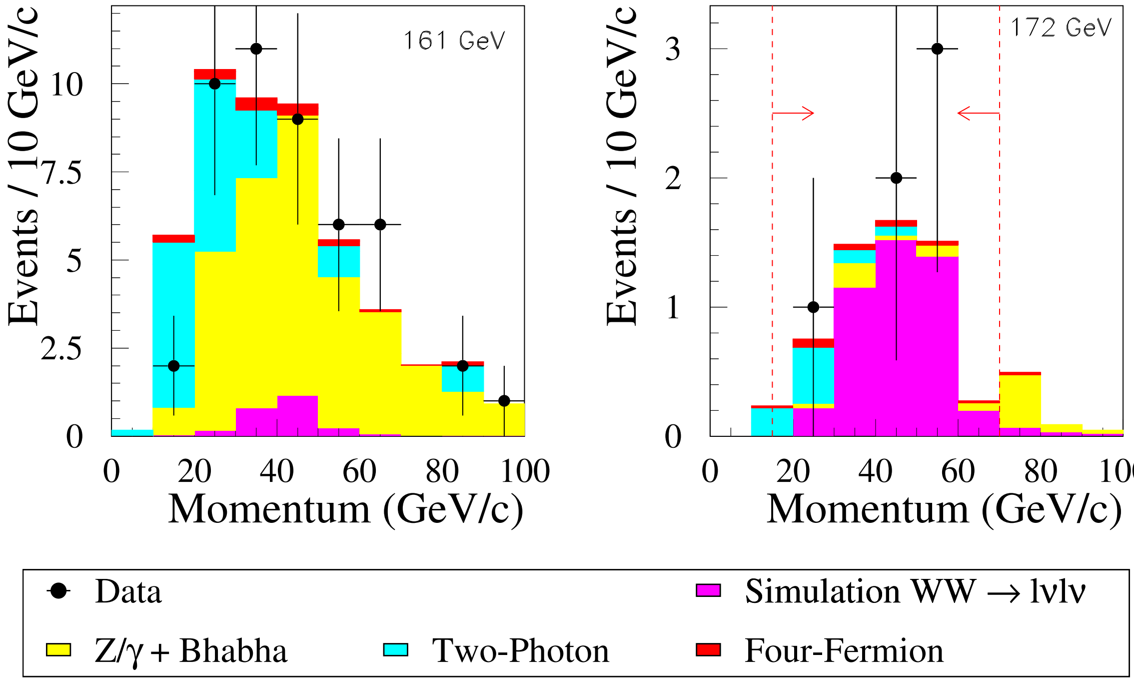

Figure 4.17: The momentum of the leading lepton jet is shown in (a) at 161 GeV for a loose event pre-selection in data and simulation. After all other cuts have been imposed the distribution shown in (b) is obtained at 172 GeV.

However, the cut also has significant value in the selection procedure: the cross-sections of two-photon collision events and Bhabha events are both sharply peaked in the beam direction.

Momenta

In Figure 4.17 the momentum of the highest momentum jet in the event is plotted. The signal events and the radiative return Z/γ events are both clustered in the centre of the plot. The signal events have a somewhat broader momentum distribution at 172 GeV than at 161 GeV, due to the larger W velocity. A selection is imposed both on a minimum and a maximum allowed lepton momentum: the lower limit momentum suppresses two-photon collision events, while the upper limit protects against remaining non-radiative Z/γ and Bhabha events.

4.4.3 $\sqrt{s'} = \sqrt{s}$

One class of possible background events results in back-to-back di-lepton production. Here we impose two cuts which reduce the background from these events.

Acollinearity

We define the acollinearity of the event as :

$$acol = 180^\circ - \cos^{-1}(\hat{\mathbf{p}}_\mathbf{1} \cdot \hat{\mathbf{p}}_\mathbf{2})$$

where $\hat{p_1}, \hat{p_2}$ are the unit normalised momenta of the two lepton jets.

Events of the non-radiative Z/γ $\rightarrow l^+l^-$ type and Bhabhas will have a small acollinearity, while the distribution of signal events is approximately isotropic. This is illustrated in Figure 4.18. The disagreement apparent in the first bin of plot (b) is believed to be of low significance. In fact both the selected events lie at $< 1^\circ$, and thus far from the applied cut. The simulation statistics in this plot are also very low. Furthermore, we remind the reader that the errors indicated on the plot are underestimated, being derived from Gaussian rather than Poisson statistics.

Missing Momentum

The signal events contain two (or more) neutrinos, and thus in general a significant resulting missing momentum. The non-radiative background is sharply peaked at low missing momentum values; we require 15 GeV of missing momentum.

4.4.4 $\sqrt{s'} \neq \sqrt{s}$

Seen Photons and Forward Electrons

As in the previous analysis (Section 4.3.5), events are rejected where a photon candidate (an unassociated electromagnetic energy cluster) is observed in the detector.

As the cross-section for Bhabha and two-photon production is strongly forward peaked, energy may be deposited at low polar angles in these events. Radiative Z/γ events are accompanied by photons at a small-angle to the beam pipe. A selection cut is imposed on the sum of the energy observed in the STIC and FEMC calorimeters within a 15° cone around the beam-pipe.

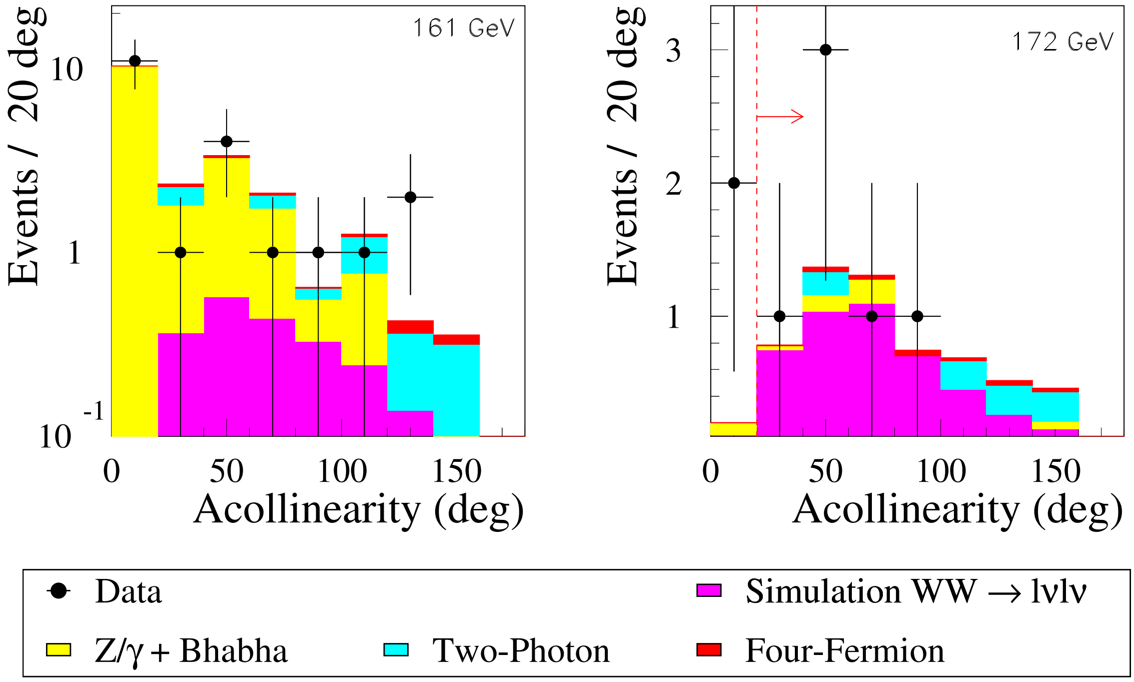

Figure 4.18: The acollinearity of the two lepton jet candidates is shown in (a) at 161 GeV for a loose event pre-selection in data and simulation. After all other cuts have been imposed the distribution shown in (b) is obtained at 172 GeV.

Missing Momentum

In radiative Z/γ events and two-photon collision events, the missing momentum in the event is expected to lie at low polar angles. We use the polar angle of the missing momentum as a selection variable; this is illustrated in Figure 4.19

An additional discriminator used is the variable denoted p_{tr}. This variable is related to the event's acoplanarity and is illustrated in the diagram 4.20. The momenta of the two jets are projected onto the plane perpendicular to the beam pipe, that is the $R\phi$ plane. The two-dimensional thrust axis in this plane is then formed. p_{tr} is then the sum of the absolute values of the $R\phi$ plane components of the jet momenta transverse to the thrust axis. If we denote the normalised 2d thrust axis $\hat{\eta}_{2d}$, and the 2d $R\phi$ plane jet momenta vectors p_1, p_2 then :

$$p_{tr} = \Sigma_{i=1,2} \, |\hat{\eta}_{\mathbf{2d}} \times \mathbf{p_i}|$$

Events which contain missing momentum, but where the direction of this momenta is along the beam pipe (*i.e.* perpendicular to the $R\phi$ plane) will have low

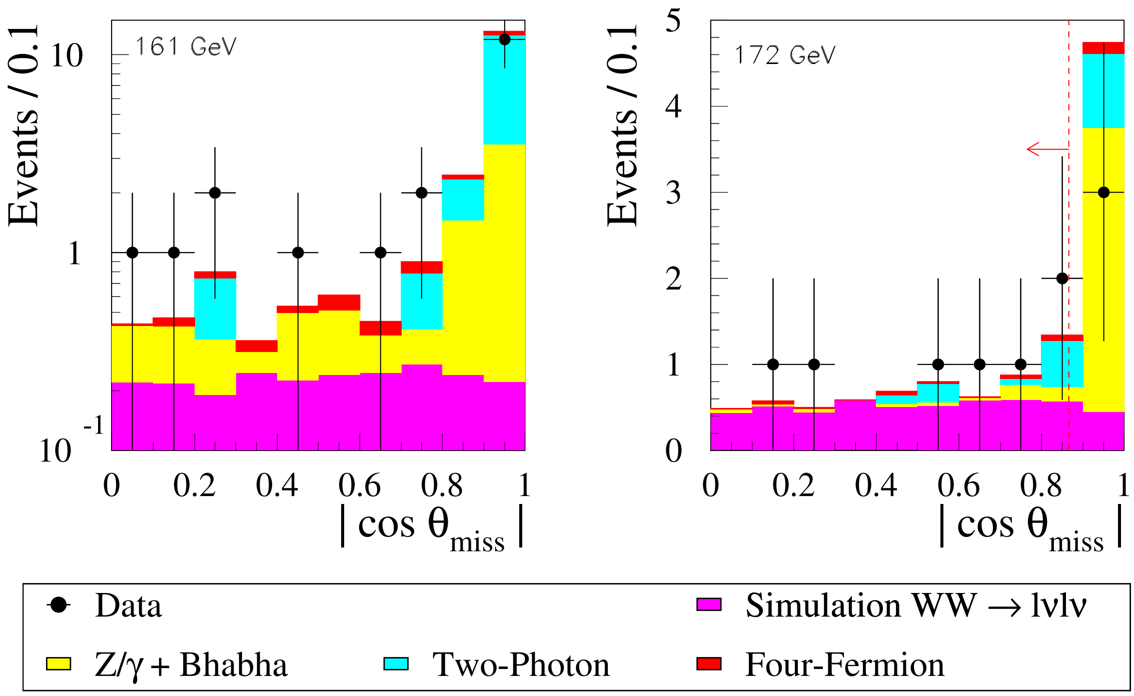

Figure 4.19: The cosine of the polar angle of the missing momentum in the event is shown in (a) at 161 GeV for a loose event pre-selection in data and simulation. After all other cuts have been imposed the distribution shown in (b) is obtained at 172 GeV.

values of p_{tr} , as illustrated in Figure 4.20 (a). In the $l\overline{\nu}_l\bar{l}\nu_l$ signal events the missing momentum direction is essentially random (it is the sum of the missing momenta of the two neutrinos), and thus these events will in general have large p_{tr} values as in Figure 4.20 (b).

This variable is effective against di-lepton events from on-shell Zs and production from two-photon collisions. Naturally, this cut also suppresses non-radiative background events. Data and simulation distributions are given in Figure4.21

4.4.5 Bhabha Suppression

The final cut imposed is principally motivated by suppressing Bhabha events. In addition to the cut (see Section 4.4.2) on the momentum of the jets, we impose an upper bound on the electromagnetic energy of the jet. If an electron is incident upon the DELPHI detector, the majority of its energy will be deposited in the electromagnetic calorimeter. A Bhabha event will typically have an energy of 80 GeV per electron; while an energy cluster of around half this value is anticipated from an

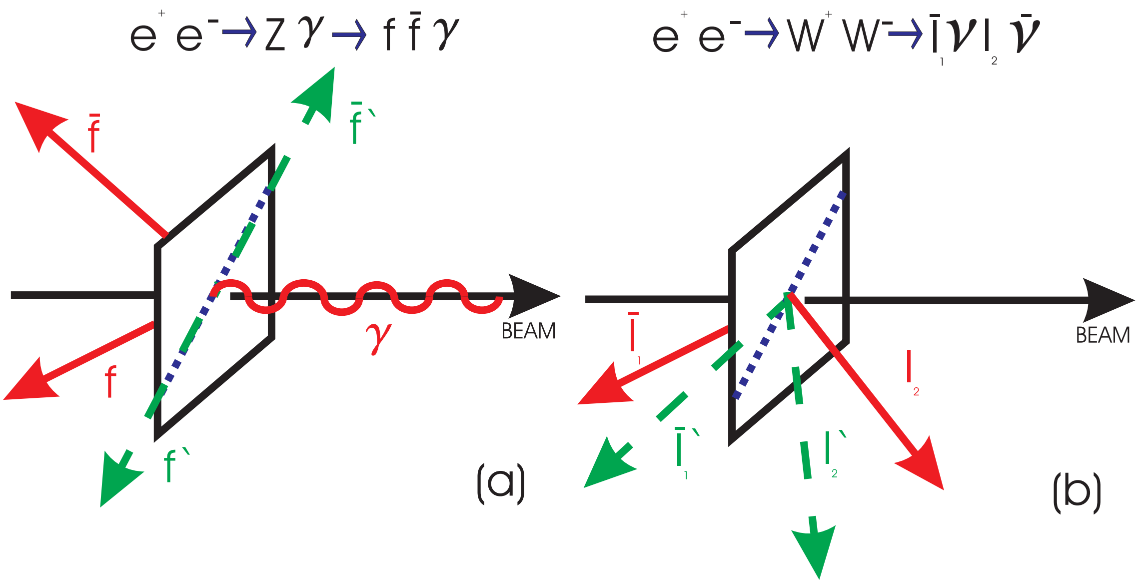

Figure 4.20: The $l\overline{\nu}_l\bar{l}\nu_l$ decay channel selection variable p_{tr} (see text) is illustrated. The final state fermions are indicated with solid lines, and their projection onto the $R\phi$ plane are shown with dashed lines. The dotted line indicates the $R\phi$ plane 2d thrust axis. In diagram (a) a background event is shown where the final state fermions are acoplanar. In the signal event of diagram (b) the final state leptons have significant momentum components in the $R\phi$ plane transverse to the thrust axis.

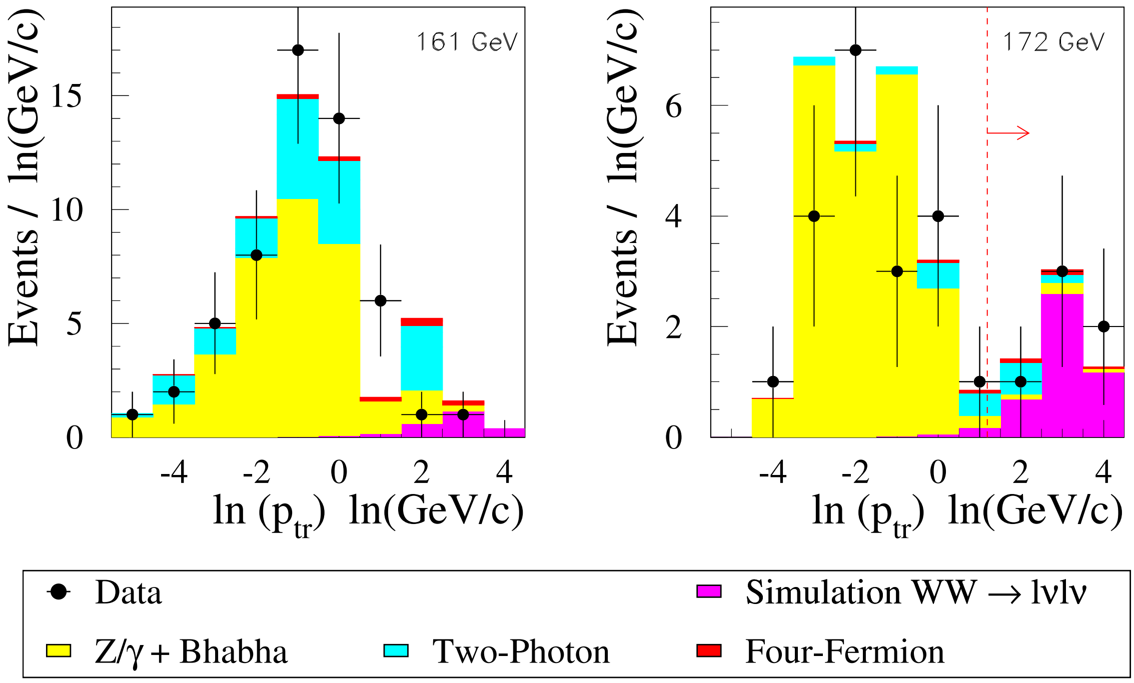

Figure 4.21: The 2d thrust axis relative transverse momentum p_{tr} (see text) is shown in (a) at 161 GeV for a loose event pre-selection in data and simulation. After all other cuts have been imposed the distribution shown in (b) is obtained at 172 GeV.

electron produced in a W decay.

4.4.6 Systematic Error

The major component of the systematic error on the background is due to the available simulation statistics. The statistics prevent us from obtaining an accurate estimation of the systematic error due to the modelling of the selection variables; however, from the use of pre-selection plots one can ascertain that this error is negligible compared with the simulation statistics.

Previous experience with two-photon simulation events counsels that difficulties are encountered with obtaining accurate simulation of the rates of high momentum events. Hence we cautiously ascribe a 50% uncertainty to the accepted two-photon event cross-section: this error is of similar size to the statistical error on these simulation events.

As reported in Section 4.3.8, studies of high momentum leptons report discrepancies of up to 2% in high momentum track reconstruction efficiency between data and simulation. This error was determined to be the major source of systematic error on the selection efficiency of the signal events.

	$\epsilon_{\mathrm{W^+W^-}\to l\overline{\nu}_l\overline{l}\nu_l}$		$\sigma'_{background}$	
	161 GeV	172 GeV	161 GeV	172 GeV
Central Value	53.0%	51.0%	0.12 pb	0.17 pb
Simulation Statistics	±1.5%	±1.0%	±0.05 pb	±0.04 pb
Simulation Accuracy	±3%	±3%	±0.03 pb	±0.05 pb
TOTAL	±3%	±3%	±0.05 pb	±0.06 pb
	$\sigma_{\mathrm{W^+W^-}\to l\overline{\nu}_l\overline{l}\nu_l}$			
	161 GeV		172 GeV	
CC03 Correction Factor	±1.5%		±1.5%	
Luminosity	±0.7%		±0.8%	

Table 4.10: Contributions to the systematic error in the $\mathrm{W^+W^-}\to l\overline{\nu}_l\overline{l}\nu_l$ channel analysis. The contributions are given separately for the combined $\mathrm{W^+W^-}\to l\overline{\nu}_l\overline{l}\nu_l$ selection efficiency ($\epsilon_{\mathrm{W^+W^-}\to l\overline{\nu}_l\overline{l}\nu_l}$), and the estimated selected background cross-section ($\sigma'_{background}$). For completeness, additional systematics applied to the calculated $\mathrm{W^+W^-}$ cross-sections are also listed.

4.4.7 Results

Table 4.11 summarises the applied selection values in this analysis. The selection values were changed between the two energy regimes to account for the change in the lepton momentum distributions. The background simulation statistics were insufficient to justify significant re-tuning of the selection values between the two energy points.

In Table 4.12 the selection efficiencies for the signal events are given by true lepton type. The selection efficiencies are similar across all the categories, although they tend to confirm the expected hierarchy of precedence of muon, followed by electron, then by tau events.

The results of the $l\overline{\nu}_l\bar{l}\nu_l$ decay channel analysis are provided in Table 4.13. Similar contributions to the accepted background cross-section are obtained from two-photon collision events and from the combined s and t channel Z/γ events. Two charged leptons and two neutrinos can be produced in a range of (non-W$^+$W$^-$) four-fermion processes: the processes commonly denoted Ze^+e^-, ZZ, and W$e\overline{\nu}_e$ all contribute. However, the production cross-section for these processes is relatively low and thus the combined background from all these four-fermion states is still not as large as that from the Z/γ process or from the two-photon collisions.

Selection Cut		161	172
Lepton Momentum: leading, other jet (GeV/c)	$>$	20,5	15,5
	$<$	60,50	70,60
Jets with d_{join} of 6.5 GeV/c	$=$	2	2
Charged Multiplicity per Jet	$>$	1	1
Total Charged Multiplicity	$<$	6	6
Jet Polar Angle	$>$	20 °	20 °
Photon Energy (GeV)	$>$	30	30
$\theta_{p_{miss}}$	$<$	30 °	30 °
Missing Momentum (GeV/c)	$>$	15	15
Acollinearity	$>$	20 °	20 °
p_{tr} (GeV/c)	$>$	3.0	3.3
Jet Electromagnetic Energy (GeV)	$<$	50	50
15°Cone Energy	$<$	10	10

Table 4.11: Summary table of the applied selection criteria in the analysis of W$^+$W$^-\to l\overline{\nu}_l\bar{l}\nu_l$: see the text for further details.

Lepton type	$e\overline{\nu}_e$	$\mu\overline{\nu}_\mu$	$\tau\overline{\nu}_\tau$	$l\overline{\nu}_l$
$e\overline{\nu}_e$	$49 \pm 5\%$	$55 \pm 3\%$	$47 \pm 3\%$	$51 \pm 2\%$
$\mu\overline{\nu}_\mu$		$58 \pm 5\%$	$58 \pm 3\%$	$56 \pm 2\%$
$\tau\overline{\nu}_\tau$			$42 \pm 5\%$	$51 \pm 2\%$
$l\overline{\nu}_l$				$53 \pm 2\%$

Table 4.12: Selection efficiencies at 161 GeV for the $l\overline{\nu}_l\bar{l}\nu_l$ analysis by true lepton types in the decay $W^+W^- \rightarrow l\overline{\nu}_l\bar{l}\nu_l$; only the statistical errors are given.

		161 GeV	172 GeV	170 GeV
Efficiency	$W^+W^- \rightarrow l\overline{\nu}_l\bar{l}\nu_l$	$53.0 \pm 3\%$	$51.0 \pm 3\%$	$51.0 \pm 3\%$
Background	Z/γ+ Bhabha	0.04 ± 0.02 pb	0.05 ± 0.02 pb	0.05 ± 0.02 pb
	Two-Photon	0.06 ± 0.05 pb	0.09 ± 0.05 pb	0.09 ± 0.05 pb
	Four-Fermion	0.02 ± 0.005 pb	0.02 ± 0.003 pb	0.02 ± 0.003 pb
	TOTAL	0.12 ± 0.05 pb	0.17 ± 0.06 pb	0.17 ± 0.06 pb
Selected	Events	2	6	1

Table 4.13: Summary of the results of the $l\overline{\nu}_l\bar{l}\nu_l$ decay channel analysis. Where errors are given they represent the total systematic error on that quantity.

4.5 Jet Studies

4.5.1 Introduction

Jet clustering algorithms are an indispensable tool in the analysis of hadronic final states. In this analysis, the algorithms are employed to attempt to reconstruct the primary quarks originating from hadronic decays of the W boson. From the full set of tracks observed in the event, we wish to obtain the number of primary quarks and their directions and energies. A large number of jet clusterisation algorithms have been suggested (see for example [70]) and a range of those that have been most generally used in experimental analyses are considered below.

We restrict this study to considering the $W^+W^- \to q\bar{q}'\bar{q}q'$ decays, as this is the channel in which jet reconstruction is most critical. The results of this study are also applied in the $l\overline{\nu}_l q\bar{q}'$ channel.

4.5.2 Jet Algorithms

We start with the full set of observed tracks or 'objects' . A generic binary combination algorithm then proceeds in the following stages[2]:

- take the pair of objects (ij) with minimum y_{ij}
- IF $y_{ij} < y_{cut}$

  combine objects (ij) (using a combination scheme) to form a new particle
- repeat until $y_{ij} > y_{cut}$

The jet clusterisation measure (y_{ij}), for a number of common algorithms are given in Table 4.14, and the standard combination schemes in Table 4.15. In the studies below, we consider all three combination schemes of the `DURHAM` and `JADE` algorithms, `LUCLUS` E-scheme with and without track re-assignment, and `CAMBRIDGE` E-scheme. In addition, we include one algorithm which is not of the binary form - the `CONE` algorithm[3]. This algorithm has been applied to accurately reconstruct

[2] The `CAMBRIDGE` algorithm uses different variables for selecting the objects and choosing the combination: see [71].

[3] This jet clusterisation method collects tracks in cones around the leading tracks in the event, the half angle of the cone playing an analogous role to y_{ij} of the binary algorithms. A minimum jet energy cut-off is also required; a range of values were considered, and the results given here are for a value of 5 GeV.

jet directions at LEP1 in $\Gamma_{b\bar{b}}$ studies [72] and is extensively used at the TEVATRON. The re-assignment algorithm [60] of `LUCLUS` checks after each stage of the clusterisation procedure that each track is still assigned to its nearest jet and performs any necessary track transfers between jets.

Algorithm Name	y_{ij}	Remarks
`LUCLUS`	$\frac{2\lvert\mathbf{p_i}\rvert\lvert\mathbf{p_j}\rvert\sin\left(\frac{\theta_{ij}}{2}\right)}{\lvert\mathbf{p_i}\rvert+\lvert\mathbf{p_j}\rvert}$	≈ transverse momentum of both objects
`JADE`	$\frac{2E_iE_j(1-\cos\theta_{ij})}{s}$	≈ invariant-mass
`DURHAM`	$\frac{2min(E_i^2,E_j^2)(1-\cos\theta_{ij})}{s}$	≈ p_t of soft object or modified mass
`CAMBRIDGE`	As `DURHAM` with angular ordering and jet freezing	
`CONE`	$\theta_{\frac{1}{2}}$	jets are cones around leading tracks

Table 4.14: The jet clusterisation measure (y_{ij}) for a number of common algorithms. Often the `JADE` and `DURHAM` y_{ij} measures are divided by E_{vis} to give dimensionless quantities.

scheme	combination	remarks
E	$p_{ij} = p_i + p_j$	four momenta sum, conserves $\Sigma\ E$, $\Sigma\ \mathbf{p}$
E0	$E_{ij} = E_i + E_j$ $\mathbf{p_{ij}} = \frac{\mathbf{E_{ij}}}{\lvert\mathbf{p_i}+\mathbf{p_j}\rvert}(\mathbf{p_i}+\mathbf{p_j})$	massless jets, conserves $\Sigma\ E$, violates $\Sigma\ \mathbf{p}$
P	$\mathbf{p_{ij}} = \mathbf{p_i} + \mathbf{p_j}$ $E_{ij} = \lvert\mathbf{p_{ij}}\rvert$	massless jets, conserves $\Sigma\ \mathbf{p}$, violates $\Sigma\ E$

Table 4.15: The commonly used jet algorithm combination schemes.

Note that for the `LUCLUS` algorithm the jet clusterisation measure is conventionally denoted d_{ij} or d_{join} .

4.5.3 Comparison

There are two critical points in the analysis where jet algorithms are used: *(i)* selecting the signal events from the background and *(ii)* forming the invariant mass of the W boson. The first of these is within the scope of this chapter, while the latter is primarily used in Chapter 6. However, for clarity, we provide studies on both these topics in this section.

Event Selection

The primary event selection criterion in the $\mathrm{q\bar{q}'\bar{q}q'}$ channel is the value of the jet clusterisation parameter which moves from 4 to 3 jets, denoted $y_{3\to4}$. Here we compare the performance of our range of jet algorithms at selecting $\mathrm{W^+W^-\to q\bar{q}'\bar{q}q'}$ events from the $\mathrm{Z}/\gamma\to q\bar{q}(\gamma)$ background. This comparison is performed at c.m. energies of 161 GeV. The initial purity of the sample, before the $y_{3\to4}$ cut is applied, is 1%.

In Figure 4.22 we show the efficiency versus purity plots for the jet algorithms studied.

$$Efficiency = \frac{number\ of\ events\ with\ y_{3\to4} > y_{cut}}{total\ number\ of\ events}$$

$$Purity = \frac{Eff_{\mathrm{W^+W^-\to q\bar{q}'\bar{q}q'}} \times \sigma_{WW\to\mathrm{q\bar{q}'\bar{q}q'}}}{Eff_{\mathrm{W^+W^-\to q\bar{q}'\bar{q}q'}} \times \sigma_{WW\to\mathrm{q\bar{q}'\bar{q}q'}} + Eff_{\mathrm{Z}/\gamma\to q\bar{q}(\gamma)} \times \sigma_{\mathrm{Z}/\gamma\to q\bar{q}(\gamma)}}$$

The choice of combination scheme was found to have negligible effect upon the performance of the jet algorithm, and hence we show only the E-scheme combinations on the Figure. `LUCLUS` performs marginally better in its standard mode (with the re-assignment) than without re-assignment.

From this study we conclude that `LUCLUS` is the optimum algorithm to use in the event selection stage of the analysis. Here, we have neglected the effects of correlations with the other variables on which the selection is based. The author's studies suggest the difference between `DURHAM` and `LUCLUS` can be reduced by the careful choice and tuning of the other selection variables.

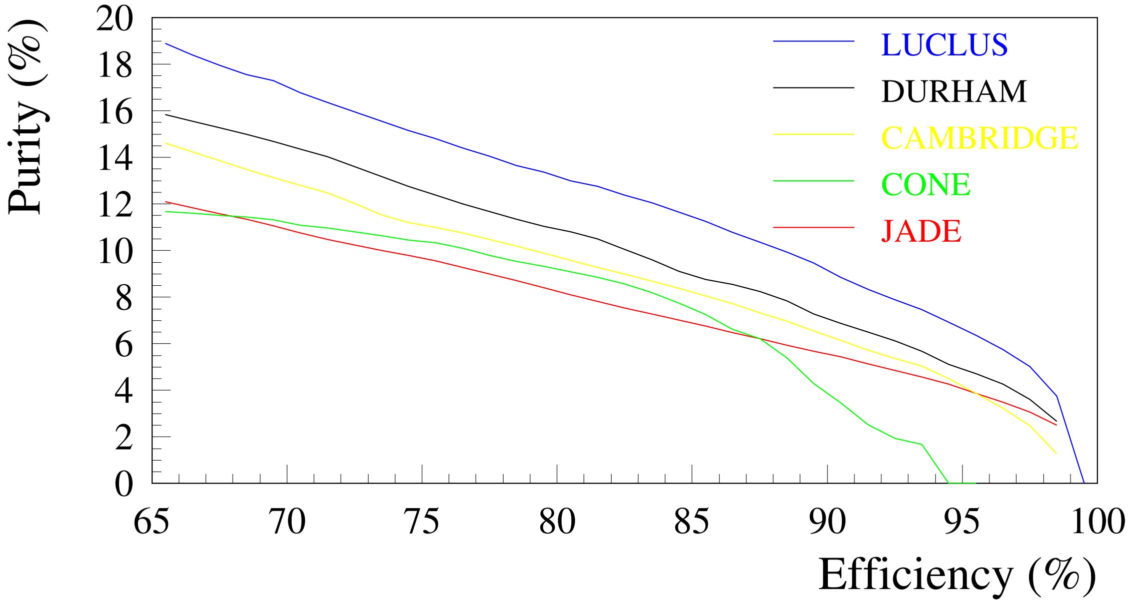

Figure 4.22: Efficiency against purity for selecting $\mathrm{W^+W^-}\rightarrow \mathrm{q\bar{q}'\bar{q}q'}$ events against the $\mathrm{Z}/\gamma\rightarrow q\bar{q}(\gamma)$ background. A range of jet algorithms are shown (see text), the labelling follows the vertical order of the lines at the centre of the plot.

Invariant Mass

The invariant mass of the W boson is obtained, after a kinematic fit, from the energies and directions of the jets. That is, we treat the jets as reconstructions of the primary quarks produced in the W decays. The principal source of information is the jet direction; the jet energy plays only a secondary role since typically 20% of the jet energy is missed in the detector.

Each algorithm is used to force four jets in the simulated $\mathrm{W^+W^-} \rightarrow \mathrm{q\bar{q}'\bar{q}q'}$ events. We then select the reconstructed jet which is closest to a generated quark direction. From these pairings we can calculate the angular and energy resolutions of each jet in a simulation event. Events were considered in the study only when unambiguous pairings of quarks and jets could be obtained.

It was immediately clear that the `CONE` algorithm was not suited to this Four-jet application; in 40% of events we were unable to obtain unambiguous pairings of the generated quarks and the reconstructed jets. The other algorithms all reconstructed similar number of events ($\approx$ 80%), with a 5% difference between the best (`LUCLUS`), and the worst (`JADE` E-scheme).

The jet energy resolution is defined for each of the four jets by

$$E_{res} = E_{quark} - E_{jet}$$

We are interested both in the mean of this distribution, a measure of how much energy is missed, and the r.m.s. which gives us the accuracy with which the energy is determined. The performance of the algorithms in both these measures differed negligibly, Figure 4.23(a) shows the distribution obtained for the `LUCLUS` algorithm: the distribution is skewed to a mean missed energy of 7.4 GeV, and has an r.m.s. of 12.3 GeV. The only notable difference in the study was that the energy conservation violating p-schemes had mean energies skewed by an additional 1.5 GeV.

The angular resolution is the full space angle between the primary generated quark and the corresponding reconstructed jet direction. The distributions obtained for all the algorithms studied were very similar, with a peak around $1.5°$ and long tails. In Figure 4.23(b), the distribution observed with the `LUCLUS` algorithm is presented.

The conclusion of this jet reconstruction study is that all the binary algorithms studied show similar properties in the variables considered. However, the `LUCLUS` algorithm was found to perform best in the event selection comparison. In the absence of other evidence we choose for simplicity, to also adopt the `LUCLUS` algorithm for the direct reconstruction of the W mass.

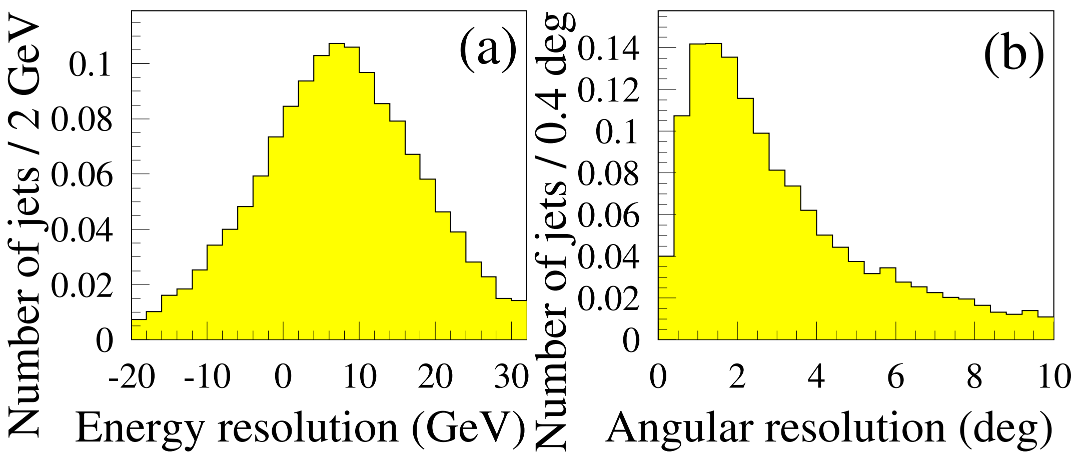

Figure 4.23: The LUCLUS algorithm for $W^+W^- \to q\bar{q}'\bar{q}q'$ events. (a) shows the energy resolution distribution, and (b) the angular resolution distribution. Each event has four entries in these plots, one for each jet. The plot is normalised to 10 pb^{-1} at 161 GeV.

Chapter 5

Interpretation of Selected Events

5.1 Introduction

In the previous chapter, we selected W^+W^- event candidates from the data samples at both 161 GeV and 172 GeV. In this chapter, we use the number of selected events to determine several parameters of physical importance. The direct reconstruction of the invariant mass of the W boson is presented in the following chapter.

In the next section, we derive a result for the expected statistical error on the cross-section determination. The majority of the chapter describes how the $e^+e^- \rightarrow W^+W^-$ cross-section and W branching ratios are determined. The hadronic branching ratio result is then interpreted as a measurement of the CKM matrix element $|V_{cs}|$ and the W width. The cross-section results are re-interpreted in Section 5.6 as a measurement, within the Standard Model, of the W mass.

At the end of this chapter we provide a detailed study on the effect of interference between four-fermion final states in W^+W^- processes. This study includes the effects on the W^+W^- cross-section and also on direct reconstruction of M_W. The quoted W^+W^- cross-sections and branching ratios in this chapter have been corrected for the effects of four-fermion interference. The cross-sections given here are determinations of the so-called W^+W^- `CC03` cross-sections: that is, the cross-sections for the diagrams depicted in Figure 1.3, in the absence of interference from all other processes leading to the same final states.

5.2 Accuracy of Cross-Section Determination

[1] For a given W^+W^- decay channel (i) we observe N_{total} events, made up of the expected background of N_{bck}, and $N_{W^+W^-}$ W^+W^- events.

$$N_{total} = N_{W^+W^-} + N_{bck}$$

The statistical error on the cross-section ($\sigma_{W^+W^-}$) is given by :

$$\Delta\sigma_{W^+W^-} = \sigma_{W^+W^-} \times \frac{\Delta N_{W^+W^-}}{N_{W^+W^-}}$$

Calculating the error on the number of W^+W^- events, allowing for the background, and inserting this we find:

$$\Delta\sigma_{W^+W^-} = \sigma_{W^+W^-} \times \frac{\sqrt{N_{W^+W^-} + N_{bck}}}{N_{W^+W^-}} \tag{5.1}$$

Here we have assumed a Gaussian rather than Poisson error distribution; thus this relation is strictly valid only in the regime of large $N_{W^+W^-}$

Defining the efficiency (ϵ_i) and purity ($\mathcal{P}_i$):

$$N_{W^+W^-} = \mathcal{L}\epsilon_i\sigma_{W^+W^-} \qquad\qquad P_i = \frac{N_{W^+W^-}}{N_{W^+W^-} + N_{bck}}$$

where $\mathcal{L}$ is the integrated luminosity of the collected data sample. We can rewrite equation 5.1 as:

$$\Delta\sigma_{W^+W^-} = \sqrt{\frac{\sigma_{W^+W^-}}{\mathcal{L}}} \times \frac{1}{\sqrt{\epsilon_i P_i}} \tag{5.2}$$

i.e. the statistical error on the W mass is inversely proportional to the square root of the product of the selection efficiency and purity. With the presently available statistics the analysis described here is entirely statistically dominated. Hence the procedure adopted in the previous chapter was to minimise the statistical error by maximising the quantity $\epsilon_i \times P_i$ for each of the decay channels ($q\bar{q}'\bar{q}q'$, $l\overline{\nu}_l q\bar{q}'$, $l\overline{\nu}_l\bar{l}\nu_l$): parts (d) of Figures 4.4, 4.5,4.7,4.9 illustrate the application of this principle in the $q\bar{q}'\bar{q}q'$ channel.

[1] This section is based on the discussion [26].

5.3 Cross-Sections and Branching Ratios

In the following sections the maximum likelihood procedure is applied to calculate the W^+W^- Cross-Section and W branching ratios.

5.3.1 Maximum Likelihood Expression

The probability of obtaining N_{obs} events when the expected number is λ is given by the Poisson distribution:

$$P(N_{obs};\lambda) = \frac{e^{-\lambda}\lambda^{N_{obs}}}{N_{obs}!}$$

Thus we can form a likelihood *prob* for all the decay channels:

$$prob = \Pi_i P_i \tag{5.3}$$

and then maximise this likelihood in terms of the required parameters.

The expected number of events for decay channel i, is given by :

$$\lambda_i = \mathcal{L} \times (\sigma_{tot} \times BR_i \times \epsilon_i + \sigma'_{bck}) \tag{5.4}$$

where $\mathcal{L}$ is the integrated luminosity, σ_{tot} is the total $e^+e^- \to W^+W^-$ cross-section obtained before correcting for interference effects, BR_i is the branching ratio for W^+W^- to the final states of decay channel i, ϵ_i is the efficiency (as assessed from the simulation) for selecting signal events in decay channel i, and σ'_{bck} is the estimated selected background cross-section.

Correction Factors

As mentioned in the introduction to this chapter and discussed in detail in Section 5.7 the measured W^+W^- cross-section and the true CC03 diagram cross-sections may differ due to interference effects. We define the correction factor CF_i by:

$$\sigma_{\mathtt{CC03}} = \sigma_{tot} \times CF_i$$

where $\sigma_{\mathtt{CC03}}$ is the final result we wish to obtain, and σ_{tot} is the quantity that appears in Equation 5.4. The correction factors have been applied to all the results quoted in this document. The correction factors are listed in Table 5.1.

Decay Channel	161 GeV	172 GeV
$\mathrm{q\bar{q}'\bar{q}q'}$	1.004	0.980
$\mathrm{e\overline{\nu}_e q\bar{q}'}$	1.087	1.019
$\mu\overline{\nu}_\mu \mathrm{q\bar{q}'}/\tau\overline{\nu}_\tau \mathrm{q\bar{q}'}$	1.006	0.996
$l\overline{\nu}_l \bar{l}\nu_l$	1.049	0.980

Table 5.1: Four-fermion interference correction factors (see text) at 161.3 GeVand 172.3 GeV.

5.3.2 Lepton Universality

Procedure

The universality of the W to lepton coupling constants can be tested using Equation 5.3 and using as the 'channels' the three sections of the semi-leptonic analysis (see section 4.3.1) :

$$prob = P_{e\ stream} \times P_{\mu\ stream} \times P_{\tau\ stream}$$

The expected number of events (in stream i) is then included in the form of Equation 5.4. However, as previously discussed (see section 4.3.9), the three streams of the semi-leptonic analysis do not each select pure e, μ or τ semi-leptonic event samples. For example 10%, of the selected events from the muon search are actually W to tau decays. Hence we express the number of expected events for each of the three search streams in the expanded form :

$$\begin{aligned}\lambda_i &= \mathcal{L}\sigma_{tot} \times 2\ BR_{\mathrm{W}\to\bar{q}q'} \\ &\times \left(BR_{\mathrm{W}\to e\overline{\nu}_e}\ \epsilon_{\mathrm{e\overline{\nu}_e q\bar{q}'},i} + BR_{\mathrm{W}\to\mu\overline{\nu}_\mu}\ \epsilon_{\mu\overline{\nu}_\mu \mathrm{q\bar{q}'},i} + BR_{\mathrm{W}\to\tau\overline{\nu}_\tau}\ \epsilon_{\tau\overline{\nu}_\tau \mathrm{q\bar{q}'},i}\right) \\ &+\mathcal{L}\sigma'_{bck,i}\end{aligned} \tag{5.5}$$

There are nine selection efficiencies required in this determination: these are $\epsilon_{x,i}$, where x represents the true event category ($\mathrm{e\overline{\nu}_e q\bar{q}'}$, $\mu\overline{\nu}_\mu\mathrm{q\bar{q}'}$or $\tau\overline{\nu}_\tau\mathrm{q\bar{q}'}$) and i represents the analysis search stream (electron, muon or tau). These values are extracted from the simulation and are provided in Table 4.8.

In Equation 5.5 we have expressed the $\mathrm{W^+W^-}$ Branching Ratios $BR_{\mathrm{W^+W^-}\to \mathrm{l\overline{\nu}_l q\bar{q}'}}$, where l is e, μ or τ, in terms of two independent single W branching ratios, writing:

$$BR_{\mathrm{W^+W^-\to l\overline{\nu}_l q\bar{q}'}} = 2 \times BR_{\bar{q}q'} \times BR_{l\overline{\nu}_l}$$

The terms of Equation 5.5 have contributions at each of the c.m. energies where data was taken. Hence we use (in obvious notation) :

$$\lambda_i = \lambda_i^{161} + \lambda_i^{170} + \lambda_i^{172} \qquad (5.6)$$

In principle, for the combined data sample we then have three free independent cross-section values at 161, 170 and 172 GeV. However we choose to assume the Standard Model values of $\sigma_{\mathrm{W^+W^-}}$ with $\sqrt{s}$, for $\mathrm{M_W}$ of 80.43 ± 0.08 GeV.

Furthermore, we assume the W $\to \bar{q}q'$ branching ratio $BR_{\mathrm{W}\to\bar{q}q'}$ is left fixed at its S.M. (unitary CKM) value of 0.677. Both of these assumptions will be justified by measurements later in this chapter.

We wish to extract three parameters from our maximum likelihood fit: the fractions of Ws decaying to each lepton generation ($BR_{\mathrm{W}\to e\overline{\nu}_e}, BR_{\mathrm{W}\to\mu\overline{\nu}_\mu}, BR_{\mathrm{W}\to\tau\overline{\nu}_\tau}$).

Trivially,

$$1 - BR_{qq} = BR_{\mathrm{W}\to e\overline{\nu}_e} + BR_{\mathrm{W}\to\mu\overline{\nu}_\mu} + BR_{\mathrm{W}\to\tau\overline{\nu}_\tau}$$

and hence the likelihood expression is maximised with only two independent parameters: note that the structure of the 3×3 search stream vs. true lepton type efficiency matrix (*i.e.* Table 4.8) introduces correlations between all three extracted parameters.

Results

Contributions to the systematic error were calculated using the values provided in Table 4.6. In addition, we assume a ±5% variation in the electron and muon search tagging efficiencies, allowing for the corresponding anti-correlated change in the tau search efficiency. Contributions to the systematic error were considered from the tagging efficiencies, selected background cross-sections, luminosities, and correction factors; the dominant components were the efficiencies and background uncertainties. The systematic error also includes a (negligible) contribution for the variation in the cross-section ratios due to changing M_W within its current experimental errors.

The results of the W leptonic branching ratio determination are given in Table 5.2. Clearly, the values obtained are compatible with lepton universality in W decays.

	$BR_{W\to e\overline{\nu}_e}$	$BR_{W\to\mu\overline{\nu}_\mu}$	$BR_{W\to\tau\overline{\nu}_\tau}$
S.M.	0.108 ± 0.001	0.108 ± 0.001	0.108 ± 0.001
Result	$0.109^{+0.039}_{-0.031} \pm 0.01$	$0.096^{+0.029}_{-0.026} \pm 0.009$	$0.118^{+0.046}_{-0.051} \pm 0.015$

Table 5.2: The determination of the W leptonic branching ratios, and a comparison with their SM values. The first errors given are statistical, the second systematic.

5.3.3 Cross-Sections and Hadronic Branching Ratio

In the following section we assume lepton universality, as required in the Standard Model and tested in the previous section.

Procedure

We recall that W^+W^- events in three primary decay channel classes were tagged in this analysis: $\mathrm{q\bar{q}'\bar{q}q'}$, $\mathrm{l\overline{\nu}_l q\bar{q}'}$, $l\overline{\nu}_l\bar{l}\nu_l$. The separate cross-sections for production of each of these final states, via the CC03 W^+W^- diagrams, can be extracted without assumptions on the W^+W^- branching ratios. These values can be obtained directly from Equation 5.4, setting the number of expected events (λ) equal to the observed number (N_{obs}). These results are provided at 161 GeV and 172 GeV at the end of this section in Table 5.3.

The measurements made in these three distinct decay channels can be combined; the corresponding expression for the likelihood is given by:

$$prob = P_{\mathrm{q\bar{q}'\bar{q}q'}} \times P_{\mathrm{l\overline{\nu}_l q\bar{q}'}} \times P_{l\overline{\nu}_l\bar{l}\nu_l}$$

Equation 5.4 is applied to calculate the number of expected events: hence we require the W^+W^- branching ratios (BR_i) for each decay channel. Assuming two independent W bosons we parameterise BR_i as:

$$BR_{\mathrm{q\bar{q}'\bar{q}q'}} = (BR_{W^\pm\to\bar{q}q'})^2$$

$$BR_{\mathrm{l\overline{\nu}_l q\bar{q}'}} = 2(BR_{\mathrm{W^\pm}\to\bar{q}q'})(1 - BR_{\mathrm{W^\pm}\to\bar{q}q'}) \tag{5.7}$$

$$BR_{l\overline{\nu}_l\bar{l}\nu_l} = (1 - BR_{\mathrm{W^\pm}\to\bar{q}q'})^2$$

The resulting maximum likelihood expression now has two free parameters: the W boson hadronic branching ratio, and the total $e^+e^-\to\mathrm{W^+W^-}$ cross-section. The values obtained by fitting both of these parameters simultaneously are provided in Table 5.3. In addition, we fix the W hadronic branching ratio at its Standard Model (unitary CKM) value, and extract only the total $\mathrm{W^+W^-}$ cross-section; the results of these fits are also provided in Table 5.3. In Section 5.6, we interpret these cross-section values, within the Standard Model, as measurements of $\mathrm{M_W}$.

Measurements of the W boson hadronic branching ratio are obtained at all three energy points. These three results can be combined to provide a single determination of the branching ratio using the same procedure as described in Section 5.3.2. In each decay channel, the total number of expected events, summed over all three energies, is obtained using Equation 5.6. In this determination, the Standard Model values of the $e^+e^-\to\mathrm{W^+W^-}$ cross-sections are assumed. In the sections below, this combined value of the W hadronic branching ratio is re-interpreted as a measurement of $|V_{cs}|$ and of Γ_{W}.

Results

The results of the maximum likelihood fits at both 161 GeV and 172 GeV are provided in Table 5.3. The systematic errors have been calculated incorporating all the uncertainties described in the previous chapter. Contributions to the systematic errors from efficiencies, backgrounds, luminosities and correction factors were included. The efficiency and background errors for a given channel i were assumed to be fully correlated across the three energy points. Where appropriate, correlations between efficiencies and backgrounds between channels were also considered. The dominant components of the systematic errors are a consequence of the background and efficiency uncertainties.

The lower limit on the result marked † is unphysical, indicating that the number of observed events is compatible with background fluctuations alone. W identification in previous experiments (at $p\overline{p}$ colliders) has only been performed through

	161 GeV	170 GeV	172 GeV
	without branching ratio assumptions		
$\sigma_{\mathrm{W^+W^-\to q\bar{q}'\bar{q}q'}}$ (pb) $\sigma_{\mathrm{W^+W^-\to l\bar{\nu}_l q\bar{q}'}}$ (pb) $\sigma_{\mathrm{W^+W^-\to l\bar{\nu}_l \bar{l}\nu_l}}$ (pb) $\sigma_{\mathrm{W^+W^-}}$ (pb)	$1.96^{+0.77}_{-0.66} \pm 0.17$ $1.64^{+0.69}_{-0.56} \pm 0.17$ $^{\dagger}0.18^{+0.37}_{-0.23} \pm 0.10$ $3.78^{+1.10}_{-0.90} \pm 0.24$	$2.94^{+2.92}_{-2.09} \pm 0.16$ $1.14^{+2.21}_{-1.14} \pm 0.06$ $1.52^{+2.51}_{-1.29} \pm 0.20$ $5.60^{+4.44}_{-2.71} \pm 0.26$	$5.09^{+1.07}_{-0.97} \pm 0.28$ $6.08^{+1.19}_{-1.06} \pm 0.32$ $0.99^{+0.61}_{-0.47} \pm 0.13$ $12.16^{+1.71}_{-1.51} \pm 0.44$
	$\sigma_{\mathrm{W^+W^-}}$ and $BR_{\mathrm{W}\to\bar{q}q'}$ fit		
$\sigma_{\mathrm{W^+W^-}}$ $BR_{\mathrm{W}\to\bar{q}q'}$	$3.82^{+1.05}_{-0.93} \pm 0.25$ $0.729^{+0.080}_{-0.089} \pm 0.012$	$5.20^{+4.03}_{-3.03} \pm 0.21$ $0.647^{+0.267}_{-0.351} \pm 0.015$	$12.24^{+1.67}_{-1.55} \pm 0.50$ $0.663^{+0.044}_{-0.046} \pm 0.015$
	$\sigma_{\mathrm{W^+W^-}}$ fit, fixed $BR_{\mathrm{W}\to\bar{q}q'}$		
$\sigma_{\mathrm{W^+W^-}}$	$3.82^{+1.06}_{-0.93} \pm 0.25$	$5.19^{+3.99}_{-2.99} \pm 0.21$	$12.20^{+1.66}_{-1.54} \pm 0.50$
	$BR_{\mathrm{W}\to\bar{q}q'}$ all energies combined fit, $\sigma_{\mathrm{W^+W^-}}$ fixed		
$BR_{\mathrm{W}\to\bar{q}q'}$	$0.676^{+0.039}_{-0.040} \pm 0.013$		

Table 5.3: The results of the determination of the cross-section for the process $e^+e^- \to \mathrm{W^+W^-}$ in the CC03 approximation, and the W boson hadronic branching ratio. The major assumptions made when deriving these results are indicated in the table headings, and described further in the text. The lower limit on the result marked † is unphysical.

lepton identification: thus the branching ratios can be determined only through the highly indirect method of assuming the total production cross-section. Thus the branching ratio determination from LEP2 constitutes the first direct measurements of this quantity. The measurement of the branching ratio of $\mathrm{W}\to\bar{q}q'$ are compatible with the Standard Model (unitary CKM) value of 0.677 ± 0.001.

Cross-section values were obtained by three procedures: no branching ratio assumptions, two-parameter $\sigma_{\mathrm{W^+W^-}}$ and $BR_{\mathrm{W}\to\bar{q}q'}$ fit, and a fixed branching ratio fit. In each of the three channels, the three total cross-section values obtained are compatible. The statistical error on the cross-section is progressively reduced by the introduction of the successive branching ratio assumptions.

In Figure 5.1, we show the Standard Model prediction for the $\mathrm{W^+W^-}$ cross-section as a function of $\sqrt{s}$. The three measured cross-sections, from the fixed branching ratio determination, are shown on the plot. The components of the Standard Model prediction are discussed in Section 1.4.1). At 161 GeV, the W^+W^- production cross-section is dominated entirely by the Born-level t-channel neutrino exchange diagram: neither the existence of the triple gauge boson WWV vertex (where W is Z,γ) nor the finite W width are required to explain this measurement. However, the 172 GeV point contradicts the hypothesis that only the Born-level neutrino diagram is present at the level of 10^{-5}%, and that only the Born level total cross-section is required at less than 2% . The three measured points are in good agreement with the Standard Model prediction for $M_W = 80.43$; they have a χ^2/dof of 2.5/3.

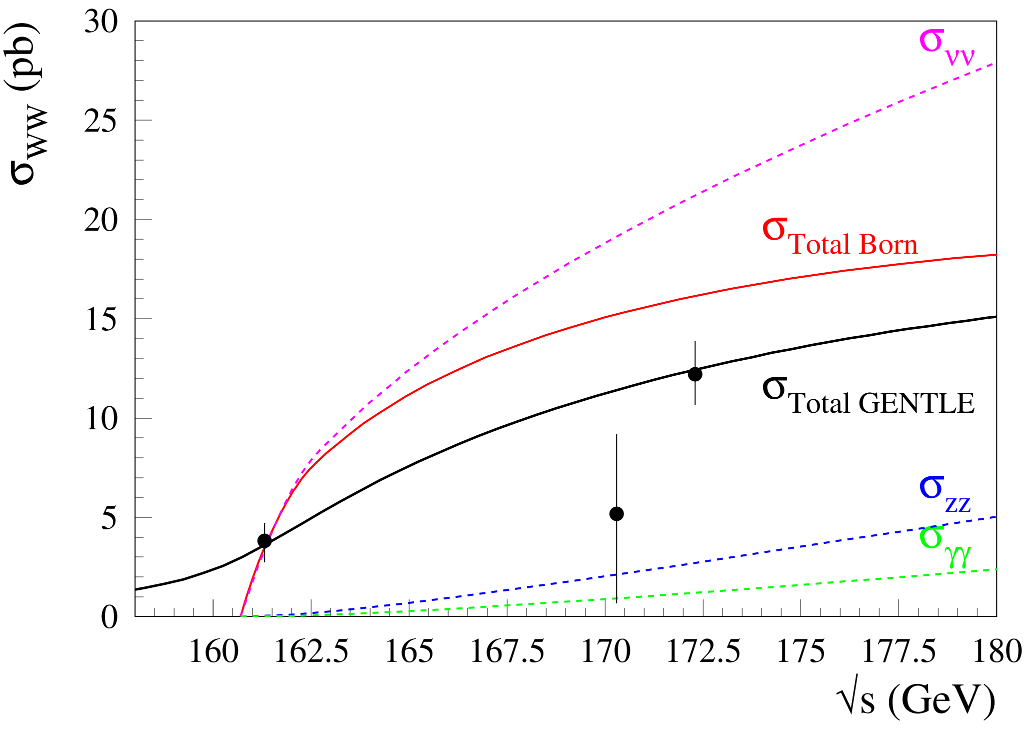

Figure 5.1: The three measured cross-section values are plotted against $\sqrt{s}$. In addition, the total (Born level) on-shell cross-section is shown, with the contributions from the t-channel neutrino diagram ($\sigma_{\nu\nu}$), the s-channel photon graph ($\sigma_{\gamma\gamma}$) and the s-channel Z graph (σ_{ZZ}) indicated; the interference terms are not shown. Including all major corrections the cross-section labelled σ_{Total} GENTLE is obtained.

5.4 $|V_{cs}|$

The role of the CKM matrix in the Standard Model is discussed in Section 1.3.2 . Other than the elements describing the interactions of the top quark, the value of the element relating the quarks of the second generation is known with the lowest precision.

Previous measurements of the CKM matrix element $|V_{cs}|$ were made in semi-leptonic decays of D mesons, where the 18% error is dominated by the poorly known hadronic form factors [25].

In the decays $\mathrm{W}^{\pm} \rightarrow q_1\overline{q}_2$ the coupling of the W to the quarks q_1, q_2 is proportional to the square of the appropriate CKM matrix element: this is illustrated in Figure 5.2

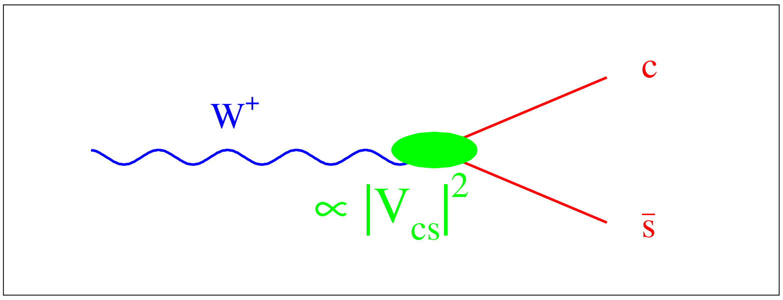

Figure 5.2: The partial decay width of the W boson is proportional to the relevant CKM matrix element squared.

The total W width is given by

$$\Gamma_{\mathrm{W}} = \Gamma_{c\overline{s}} + \Sigma_i \Gamma_i \tag{5.8}$$

where the sum runs over all the other W decay channels, and the partial decay widths are given by Equation 1.4.

In Figure 5.3, we show that the total cross-section has only a weak dependence on $|V_{cs}|$. This result can be explained using the formalism of Section 1.4.3. In Equation 1.5 the $\mathrm{W}^+\mathrm{W}^-$ production cross-section is given in terms of normalised Breit Wigner integrals over the Born level $\mathrm{W}^+\mathrm{W}^-$ cross-section. In this terminology, the Born level cross-section is that for on-shell W bosons only and hence trivially has no width dependence. Neglecting s-dependent width and phase-space effects this will also be true for the integrated off-shell cross-section. In fact, the total cross-section varies by only 4.5% over the full range of Figure 5.3.

However, it can be seen from Figure 5.3 that the relative proportion of $q\bar{q}'\bar{q}q'$ $l\overline{\nu}_l q\bar{q}'$ and $l\overline{\nu}_l\bar{l}\nu_l$ events shows a marked $|V_{cs}|$ dependence. Equivalently considerable information is carried by the measured value of $BR_{W\to\bar{q}q'}$, since

$$BR_{W\to\bar{q}q'} = \frac{\Gamma_{\bar{q}q'}(|V_{cs}|)}{\Gamma_W(|V_{cs}|)} \tag{5.9}$$

where the total W width is given by Equation 5.8, and $\Gamma_{\bar{q}q'}$ is the same quantity where the sum runs only over the hadronic W decay modes.

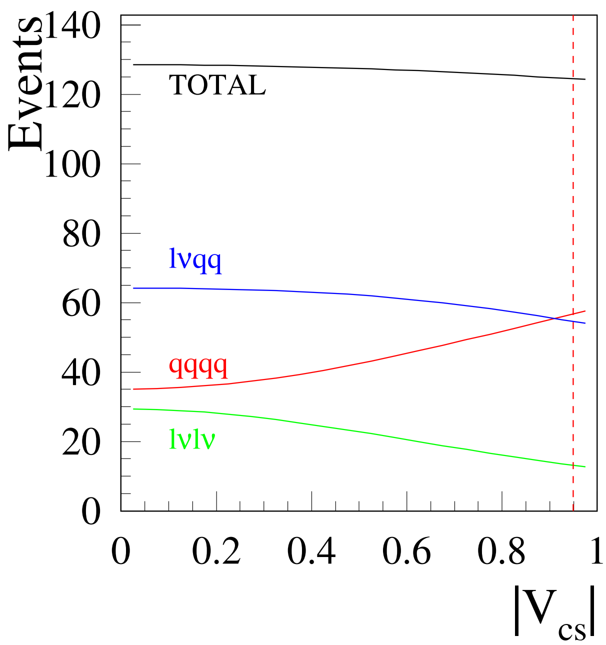

Figure 5.3: The variation of the the $e^+e^-\to W^+W^-$ cross-section as a function of $|V_{cs}|$. The total number of events expected and the number in the decay channels $q\bar{q}'\bar{q}q'$ $l\overline{\nu}_l q\bar{q}'$ and $l\overline{\nu}_l\bar{l}\nu_l$ are indicated. The dashed line shows the Standard Model value of $|V_{cs}|$ when unitarity is imposed on the CKM matrix. The total cross-section was calculated using the program GENTLE. The plot is normalised to 10 pb^{-1}, with $\sqrt{s}$ of 172.3 GeV and M_W of 80.43 GeV/c^2

The measured branching ratio was converted into a $|V_{cs}|$ measurement by assuming all other parameters of the SM to be fixed at their presently measured values.

The errors on the SM parameters (e.g. uncertainties on the other CKM matrix elements, QCD corrections) were included in the systematic error, they contribute only a 1% error. The systematic error (which is small compared with the statistical error) is dominated by signal efficiency and background cross-section uncertainties. The dependence of $|V_{cs}|$ on the $BR_{\mathrm{W}\to\bar{q}q'}$ is shown in Figure 5.4, where the measured value is indicated on the plot. The measured value is:

$$|V_{cs}| = 0.98 \pm 0.19(stat) \pm 0.06(syst)$$

In this result, no unitarity constraints have been applied. On application of unitarity constraints to the CKM matrix in three generations, this element is already determined to high precision: $|V_{cs}| = 0.9743 \pm 0.0004$ [25]. However, we may apply the monadic constraints of an n-dimensional CKM matrix, where $n \geq 3$. This assumption allows us to constrain the upper limit of the measurement since

$$|V_{cs}|^2 \leq \; 1 - {V_{cd}}^2 - {V_{cb}}^2$$

$$|V_{cs}|^2 \leq \; 1 - {V_{us}}^2 - {V_{ts}}^2$$

The first of these is currently the more stringent; using the values in [25], this provides a one s.d. upper limit of 0.974 ± 0.004.

The reader is recommended to consult the DELPHI collaboration published result [73]; in this analysis, the result obtained from the hadronic W branching ratio is improved slightly by using jet flavour tagging techniques.

5.5 W **Width**

The CDF and D0 collaborations at the TEVATRON produce an indirect determination of the W width [74], by introducing two significant assumptions: the total production cross-section σ_{W}, and the partial width $\Gamma_{\mathrm{W}\to l\overline{\nu}_l}$. These quantities are calculated within the Standard Model; the result is systematically limited by structure function uncertainties in the calculation of σ_{W}. The reader is reminded that only the leptonic W final states are observed at the TEVATRON.

At LEP2, an analogous method may be used for the determination of the W width. In this analysis, we have measured W decays for all Standard Model final

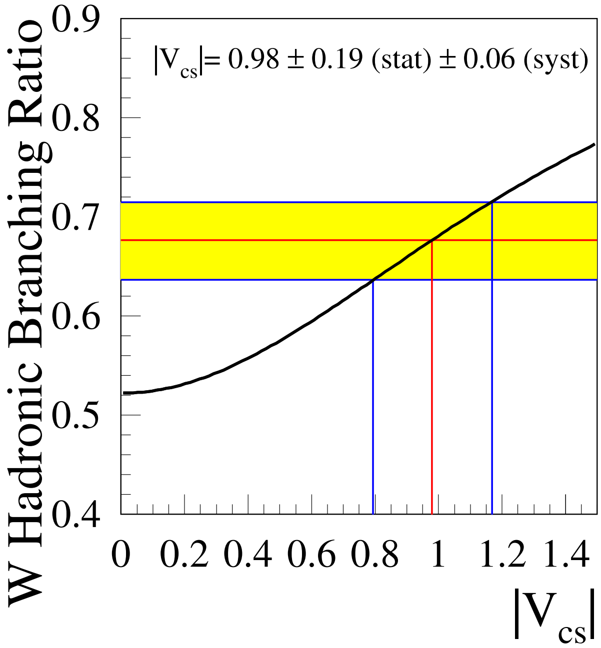

Figure 5.4: The dependence of the CKM matrix element $|V_{cs}|$ is shown against the branching ratio W $\to \bar{q}q'$. The measured value of the branching ratio and its one s.d. errors are indicated by the shaded band, the corresponding values of $|V_{cs}|$ are indicated by the vertical lines.

states, and thus have obtained a direct determination of the W branching ratio. In the section above we used this value to obtain $|V_{cs}|$; rearranging Equations 5.8 and 5.9, we can use this to determine Γ_{W}.

$$\Gamma_{\mathrm{W}} = \frac{\Gamma_{\mathrm{W}\to l\overline{\nu}_l}}{(1 - BR_{\bar{q}q'})}$$

Assuming [25]

$$\Gamma_{\mathrm{W}\to l\overline{\nu}_l} = 676 \pm 3 \text{ MeV}$$

where the error on this partial width is due to the uncertainty on $\mathrm{M_W}$.

We obtain

$$\Gamma_{\mathrm{W}} = 2.09^{+0.28}_{-0.23}(stat) \pm 0.09(syst) \text{ GeV}$$

to compare with the SM (unitary CKM) value of 2.08 ± 0.01 GeV. While this determination is admittedly still highly indirect, it relies on only one major assumption and thus represents a significant improvement on the Tevatron method.

5.6 Mass Determination

5.6.1 Interpreting the Cross-Section as the W mass

The measured W^+W^- cross-section can be interpreted, within the Standard Model, as a measurement of the W Boson mass [75]. In the Born-level on-shell approximation, W^+W^- production starts at $\sqrt{s} = 2M_w$. After finite W-width and correction effects are included (see Section 1.4.3), a steep rise is still observed in the W pair production cross-section close to the nominal threshold energy. Moreover, at a given $\sqrt{s}$, $\sigma_{W^+W^-}$ is dependent on the value of M_W, this dependence naturally being most marked near threshold energies.

The variation of the W^+W^- cross-section with M_W is illustrated in Figure 5.5. The dashed lines are seen to converge with the solid line as the gradient of the curve reduces, this is visible on the left and right edges of the plot: in these regions the sensitivity of $\sigma_{W^+W^-}$ to M_W is reduced.

Quantitatively the error on M_W is given by the following relation:

$$\Delta M_W = \Delta\sigma_{W^+W^-} \times \left| \frac{dM_W}{d\sigma_{W^+W^-}} \right|$$

Earlier (Section 5.2), we obtained an expression for $\Delta\sigma_{W^+W^-}$: the error on the cross-section measurement (Equation 5.2).

Assuming that the selection efficiency and purity of the analyses are not a strong function of $\sqrt{s}$ (reference to the previous chapter will reassure the reader that this is valid), we define a statistical sensitivity factor for unit integrated luminosity:

$$\Delta M_W \propto \sqrt{\sigma_{W^+W^-}} \times \left| \frac{dM_W}{d\sigma_{W^+W^-}} \right|$$

In Figure 5.6, we plot this statistical sensitivity factor as a function of $\sqrt{s}$. The plot is seen to have a broad minimum in the region of $2M_W$. M_W was already sufficiently well measured from $p\overline{p}$ experiments, before the LEP2 data taking phase started, to determine the optimum LEP collision energy with sufficient precision. The minimum is found to lie at $\approx 2M_W + 0.5$ GeV; thus the delivered c.m. energy at DELPHI of 161.3 GeV is near optimal.

The determination of M_W by this method at higher $\sqrt{s}$ rapidly loses precision. The statistical sensitivity factor (and thus the error on M_W) at $\sqrt{s}$ of 172 GeV is more than four times higher than that at the minimum.

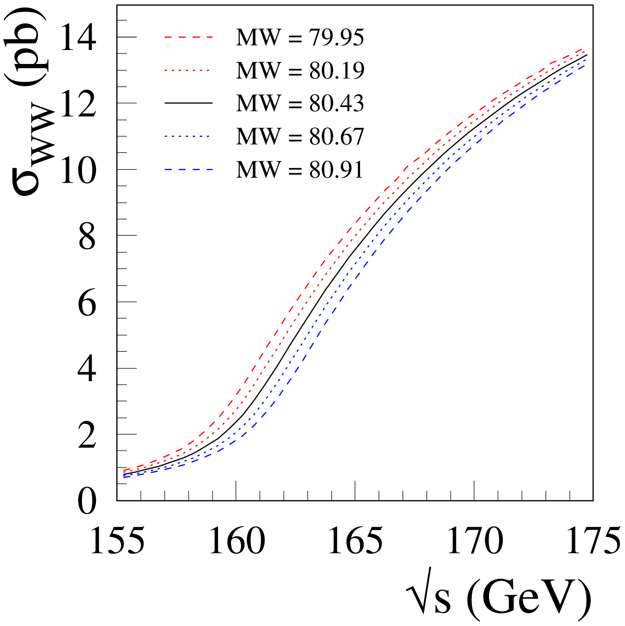

Figure 5.5: The $e^+e^- \to W^+W^-$ cross-section as a function of the centre-of-mass energy using the program GENTLE. The distribution is shown for the current world average value of M_W and values three and six s.d. higher and lower.

5.6.2 Procedure and Results

The indirect determination of M_W is implemented using the program GENTLE ([76]) to perform a semi-analytic calculation of the W^+W^- cross-section in the CC03 approximation; all the previously discussed corrections (see Section 1.4.3) are included in this calculation. The results of the GENTLE program have been cross-checked with those of an independent implementation of this calculation [75]. The cross-section results were found to agree to within 1% [64, 77]: a theoretical error on these calculations of 2% is estimated by the authors of these programs.

The mean value and its errors are estimated from the measured cross-section values (σ_{meas}) using a simple χ^2 procedure:

$$\chi^2(M_W) = \sum_E \frac{\sigma_{\texttt{GENTLE}}^{\sqrt{s}\,=\,E}(M_W) - \sigma_{meas.}^{\sqrt{s}\,=\,E}}{\Delta\sigma_{meas}^{\sqrt{s}\,=\,E}}$$

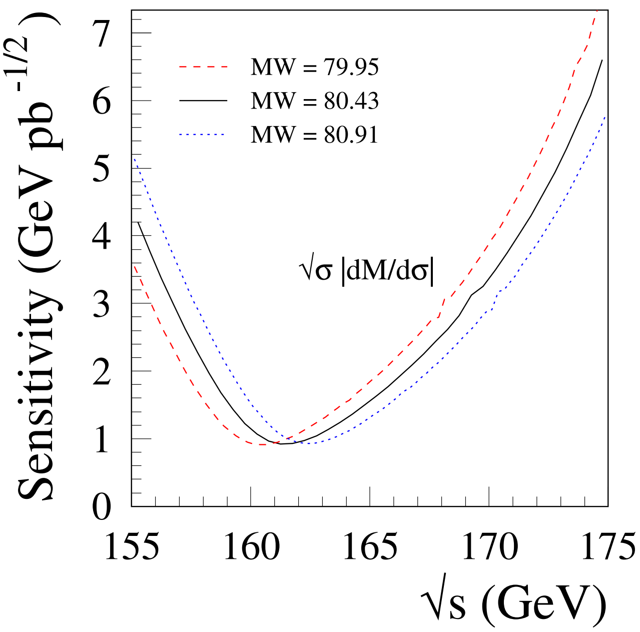

Figure 5.6: The M_W sensitivity factor as a function of the centre-of-mass energy using the program `GENTLE`. The factor gives the expected error on M_W for one pb^{-1} of data, neglecting backgrounds and assuming 100% selection efficiency.

where the sum runs over the energy points we wish to include in the M_W determination. We use the values of the W^+W^- cross-sections obtained in Section 5.3.3, assuming the Standard Model value of the W hadronic branching ratio.

The systematic error is dominated by the systematic errors on the input cross-section values. The LEP beam energy determination gives rise to an additional source of systematic error: this is labelled (LEP) in the results table. The beam energy determination is described in Section 3.7: $\sqrt{s}$ is measured to an accuracy of 60 MeV [57]. It should be noted that Figure 5.3 demonstrates that the total W^+W^- cross-section depends only weakly on the W width. Hence the contribution to the systematic error on the M_W determination of varying the W width is negligible.

M_W was determined separately for the measured cross-sections at 161 GeV and 172 GeV. In addition, a further fit was performed where the cross-section was calculated at each of the the three energy points as M_W was varied. The systematic errors were taken to be fully correlated between all three energy points. The results of the fits are provided in Table 5.4, and illustrated in Figure 5.7 .

	Separate Energies Results	
	161.31 GeV	172.30 GeV
M_W (GeV/c^2)	$80.33 \pm 0.47 \pm 0.12 \pm 0.03$	$80.73^{+1.55}_{-2.99}\ ^{+0.57}_{-0.67} \pm 0.04$
	Combined Energies Results (161,170,172 GeV)	
M_W (GeV/c^2) χ^2/dof	$80.41 \pm 0.46(stat) \pm 0.13(syst) \pm 0.03$(LEP) 2.5/2	

Table 5.4: The determination of M_W from the measured $e^+e^- \to W^+W^-$ cross-sections. The quoted systematic error is divided into two components, the second component being the error due to the LEP beam energy determination.

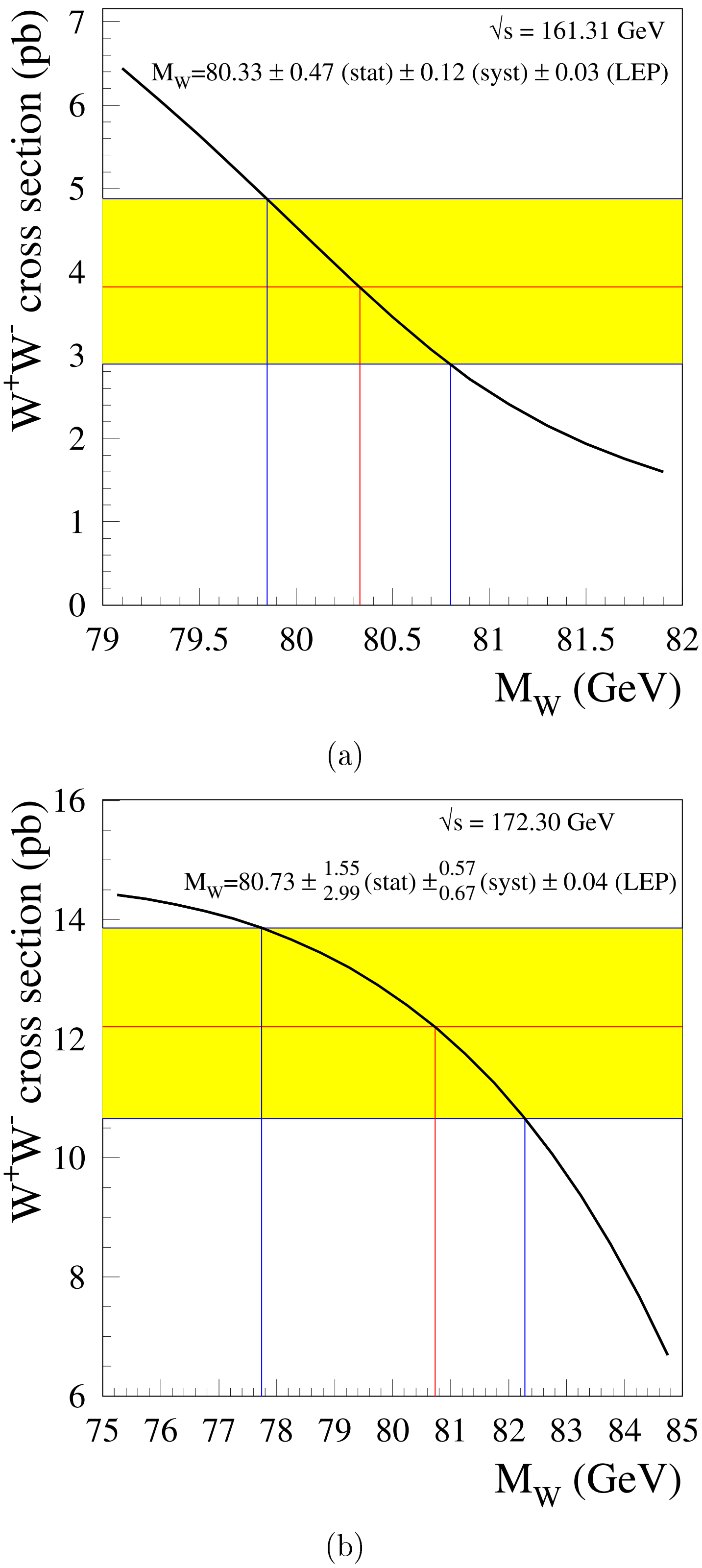

Figure 5.7: The cross-section for $e^+e^- \to W^+W^-$ in the `CC03` approximation is shown at fixed $\sqrt{s}$ against the pole W mass M_W, as calculated by the program `GENTLE` . The shaded band indicates the measured cross-section values and their one s.d errors; the corresponding values of M_W are indicated by the vertical lines.

5.7 A Study of Four-Fermion Final State Interference

The following section is a modified version of the DELPHI note [78]. The generator level study was performed by P.B. Renton and support with the EXCALIBUR generator was provided by H.T.Phillips. An abridged version of this report also appears in [29].

Synopsis

When extracting the W^+W^- cross-section, it is necessary to take account of the interference terms between the Feynman diagrams responsible for this process (the CC03 or doubly resonant production), and those other diagrams that lead to the same final states. This note presents a generator and FASTSIM level study of these effects, in all the W^+W^- decay topologies, over the full range of energies expected at LEP2. The event selection applied is compatible with that used in the DELPHI W mass paper.

The interference terms and background treatment used for the 161 GeV W mass measurement are found to produce significant effects in the $e\overline{\nu}_e q\bar{q}'$ decay channel and the $l\overline{\nu}_l\bar{l}\nu_l$ decay channel. These effects are shown to be relatively insensitive to the event selection and to decrease at higher centre of mass energies.

This note also considers the possible effects on the direct reconstruction of the W mass at 172 GeV. Again, the only significant effect is observed in the $e\overline{\nu}_e q\bar{q}'$ channel, where the studies shows a shift of $\approx$ 50 MeV/c^2.

5.7.1 Introduction

The measurement of the W^+W^- cross-section at DELPHI is the measurement of the cross-section for the process : $e^+e^- \rightarrow W^+W^- \rightarrow f_1 + f_2 + f_3 + f_4$

This involves the production of two resonant W bosons and proceeds at lowest order through the Feynman graphs shown in Figure 5.8. However, the identical final states can be produced through different intermediate states: Table 5.5 shows the number of diagrams corresponding to specific charged current (CC) final states.

Examples of these extra diagrams are provided in Figures 5.9 and 5.10. Singly resonant W production contributes to all decay channels and is shown in Figure 5.9(a). For final states containing particle and anti-particle pairs, neutral current diagrams containing an off-shell γ or Z can contribute; Figure 5.9(b) shows an example Neutral Current process. Figure 5.10 gives examples of t-channel gauge boson graphs for the semi-leptonic decay channel: similar diagrams can also contribute in the fully-leptonic channel. QCD diagrams, involving intermediate gluons, contribute to the $q\bar{q}q\bar{q}$ final states. Note that the diagrams contributing to the muon semi-leptonic final state and the tau semi-leptonic channel are identical.

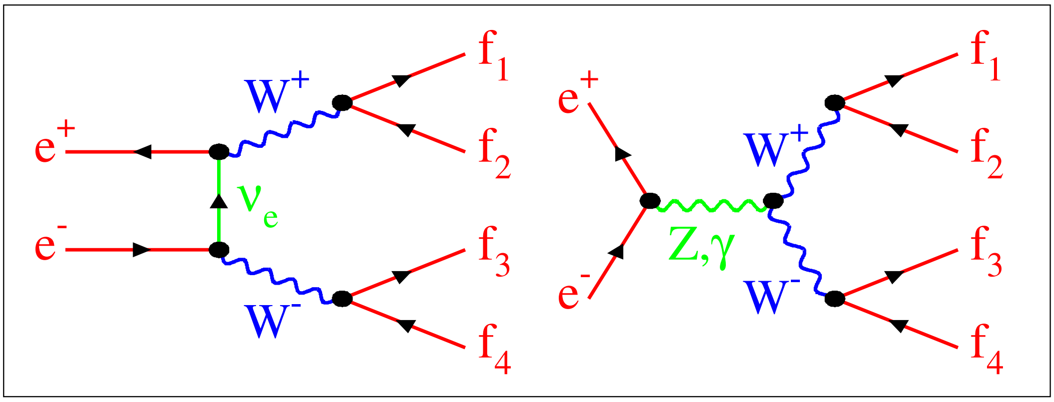

Figure 5.8: The CC03 set of Feynman diagrams for doubly resonant W production.

All these extra diagrams contribute not only as a background[2] but, since the final state is identical to that obtained through the CC03 diagrams, there is also interference *between* these processes: we must sum the matrix element amplitudes, not just consider the squares of the amplitudes.

Clearly, only the doubly resonant CC03 diagrams have a production cross-section sensitive to the W mass around the threshold energy. Hence one does not lose sensitivity in obtaining the W mass from the CC03 cross-section, rather than a four-fermion treatment.

In this study two approaches are taken to calculate the magnitude of the 'interference' effect: *(i)* using the production of simulation events separately for individual

[2]In fact their background contribution is small, never constituting more than 5% of the observed background in any channel.

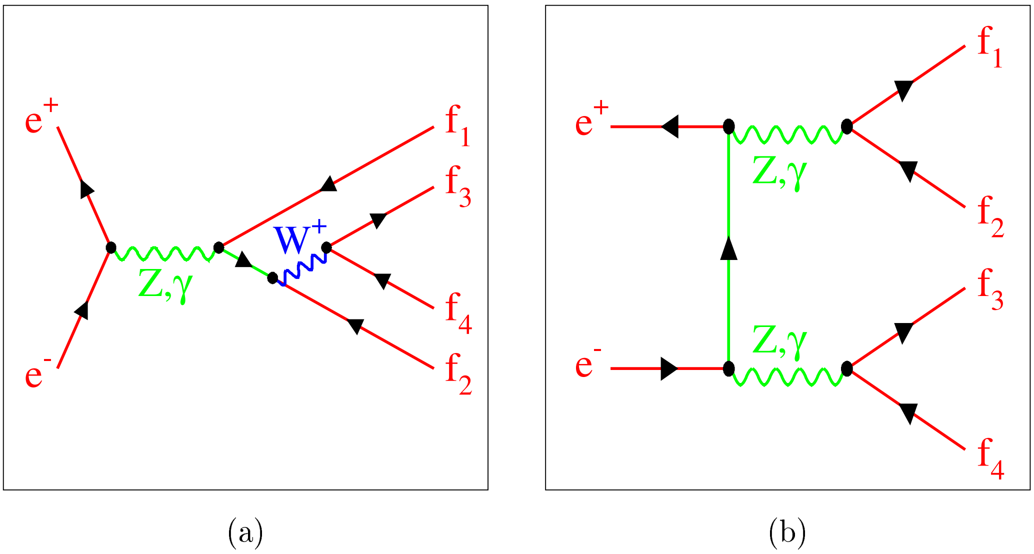

Figure 5.9: Feynman diagrams for (a) Singly resonant W production, (b) an example four-fermion neutral current process.

background processes, or *(ii)* using a full four-fermion generator treatment. In the first method we use the same background simulation processes as are used as in the DELPHI W Mass measurement [55]. The interference correction factors are calculated by comparing these background samples with an all diagram simulation from a four-fermion generator. Diagrams that have not been included explicitly in the simulation of the separate background processes are thus compensated for in the calculated correction factors. The second method assesses only the effect of the interference terms. The four-fermion generator is used to provide an all background diagram event simulation.

The W^+W^- analyses are aimed at selecting `CC03` diagram type events: hence the LEP experiments choose to interpret their results in terms of the `CC03` cross-section, rather than the full four-fermion cross-section. Furthermore, the full four-fermion cross-section calculation is divergent in several of the simulation event generators used in the analyses[3]. Although the `CC03` cross-section is not a strictly gauge invariant quantity (see [64] p8), in practice it is a well-defined variable which allows comparison between the measurements made by the experiments.

[3]Due to their massless fermion treatment.

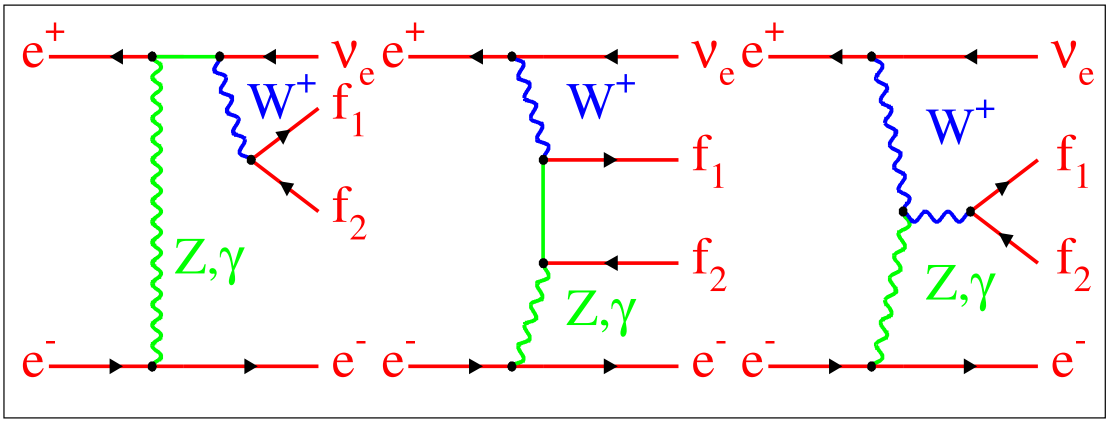

Figure 5.10: Example t-channel gauge boson Feynman graphs for the $\mathrm{e}\bar{\nu}_{\mathrm{e}}\mathrm{q}\bar{\mathrm{q}}'$decay channel.

The aim of the direct reconstruction study presented here is to assess whether the additional four-fermion diagrams significantly distort the reconstructed W mass distributions at 172 GeV. The comparison is simply made between the results of fitting the mass distribution from the `CC03` diagram events and the full four-fermion diagram event sample.

	$\bar{d}u$	$\bar{s}c$	$\bar{e}\nu_e$	$\bar{\mu}\nu_\mu$	$\bar{\tau}\nu_\tau$
$d\bar{u}$	43	11	20	10	10
$e\bar{\nu}_e$	20	20	56	18	18
$\mu\bar{\nu}_\mu$	10	10	18	19	9

Table 5.5: Number of lowest order Feynman graphs for the production of the given '`CC` type' final states.

5.7.2 Event Selection

`FASTSIM` Level Selection

The event selection used for the `FASTSIM` study presented here is based on that in [55]: this reference should be consulted for a full discussion and explanation. The tuning shown here is for 161 GeV; these cuts were also re-tuned for 172 GeV in line with the selection described in [67]. These event selections do not differ significantly from those described in Chapter 4.

Generator Level Selection

For brevity, the generator level cuts are not described here in full. The cuts made at the generator level were imposed at the level of the four fermions produced; they were a compromise between adopting cuts realistic to the analysis and obtaining efficiencies comparable to those obtained in the analysis. The most significant differences from a full DELSIM [59] treatment were expected to occur in the treatment of jets.

5.7.3 Method

Generators

The PYTHIA [60] Monte Carlo program was used to generate large samples of signal W-pair events and background events. The fragmentation parameters were tuned at LEP1[62]. The following PYTHIA processes are relevant:

$e^+e^- \to Z^0 + n\gamma$, **Process 1.** This process considers production of $f\bar{f}$ pairs via a Z^0 or γ^* plus extra photons generated via Initial State Radiation. It also includes multi-jet production via hard gluon emission e.g. $e^+e^- \to q\bar{q}g$.

$e^+e^- \to Z^0Z^0$, **Process 22.**

$e^+e^- \to W^+W^-$, **Process 25.** Includes only s-channel γ and Z^0 exchange and t-channel ν exchange, the CC03 diagrams.

$e^+e^- \to Z^0e^+e^-$, **Process 35.**

$e^+e^- \to We\nu$, **Process 36.**

These processes include only the dominant diagrams and they are taken as an incoherent sum, even when the same final state is produced by different processes.

The EXCALIBUR generator [61] [79] includes all tree-level diagrams for four-fermion production at LEP2. It therefore includes all interference effects and extra background diagrams not included in the PYTHIA samples generated with processes 22, 25, 35 and 36. The original program has been converted into an event generator by D. Charlton of OPAL and subsequently extended to include the Coulomb Correction [27] and the Naive QCD correction[64] [80]. The authors added the facility to generate the four-fermion background diagrams (i.e. the non-CC03 diagrams) alone; this provision was used extensively in this study.

Furthermore, the EXCALIBUR generation of $We\nu$ is believed to be more reliable than process 36 of PYTHIA, and was therefore used for this background in [55].

In this study, EXCALIBUR was used to calculate the four-fermion production cross-sections. The option of generating four-jet final states via gluon exchange was switched off in order to prevent double-counting with PYTHIA process 1. EXCALIBUR can be used to evaluate all diagrams or subsets, e.g. CC03 diagrams only, and this facility was used for this study.

The generators used in the first FASTSIM study were the same as those in [55], with one exception : the EXCALIBUR CC03 W^+W^- sample was used in place of the PYTHIA CC03 sample. Studies performed for [64] and subsequent work at DELPHI have shown these samples to be in excellent agreement.

Processes Used

EXCALIBUR four-fermion all diagram, CC03 diagram, and four-fermion background diagram (i.e. all - CC03 samples as discussed above) event samples were used in all channels. In addition to these the following four-fermion samples were used:

$q\bar{q}'\bar{q}q'$ Decay Channel	PYTHIA ZZ
$e\overline{\nu}_e q\bar{q}'$ Decay Channel	EXCALIBUR $We\nu$
$\mu\overline{\nu}_\mu q\bar{q}'$ Decay Channel	none
$l\overline{\nu}_l\bar{l}\nu_l$ Decay Channel	PYTHIA ZZ, Zee and EXCALIBUR $We\nu$

FASTSIM/GENERATOR

The generator level study uses only the four vectors of the produced four-fermions.

The FASTSIM [81] level study includes hadronization [60] and a basic model of the DELPHI detector geometry. The detector simulation is performed at the level of resolution smearing; the multiple scattering effect of the material in DELPHI is not explicitly simulated. The acceptance angles of the sub-detectors and effects caused by the mis-association of energy to charged tracks are simulated. The FASTSIM package is interfaced to WWANA [48] and full experimental cuts may be applied.

The performance of FASTSIM is illustrated in Figure 5.11, where four key variables are plotted for the $\mathrm{e}\overline{\nu}_{\mathrm{e}}\mathrm{q}\bar{\mathrm{q}}'$ decay channel after all the experimental cuts have been applied. The plots show the simulation of a CC03 sample with a full DELSIM treatment and with FASTSIM. The reconstructed W mass is shown after the application of a kinematic fit [82], in which the constraints of energy, momentum and equal masses for the two Ws have been applied. Clearly FASTSIM does not accurately reproduce the results of a full DELSIM treatment and hence care must be taken when interpreting the results.

Direct Reconstruction

Two studies were performed: the first at the generator level; and the second using the fast detector simulation. In both studies, the comparison was made between the CC03 and four-fermion EXCALIBUR samples. In the $\mathrm{q}\bar{\mathrm{q}}'\bar{\mathrm{q}}\mathrm{q}'$ and $\mu\overline{\nu}_{\mu}\mathrm{q}\bar{\mathrm{q}}'$ decay channels only the first study was performed. In producing these results a simplified event selection was applied at the generator level. However, for the $\mathrm{e}\overline{\nu}_{\mathrm{e}}\mathrm{q}\bar{\mathrm{q}}'$ channel both Generator level and FASTSIM studies were made. In this channel, the full event selection on the reconstructed tracks was applied in both the generator level and FASTSIM studies.

The first method uses the true generated W mass $\mathrm{M}_{\mathrm{gen}}$ for each selected event. $\mathrm{M}_{\mathrm{gen}}$ is calculated by appropriately pairing up the generated four final state fermions as if they came from W decays. Two invariant masses are then formed and the average is found. A fit is made to the distributions of $\mathrm{M}_{\mathrm{gen}}$ with a relativistic Breit Wigner over a range (78-82 GeV) which was chosen such that the χ^2/dof of the fit was close to 1.

The second study uses the full DELPHI W mass reconstruction techniques; this includes a two constrained kinematic fit [82, 67] in which the constraints of energy, momentum and equal masses for the two Ws have been applied. The fit is then performed to the reconstructed W mass distribution (see Figure 5.11(d)) over a range 75-85 GeV. The fitting function used is a convolution of three functions: a relativistic Breit-Wigner, a phase-space correction factor, and a Gaussian to describe detector resolution effects. The width of the Gaussian is obtained from the kinematic fit, and varies on an event by event basis. This technique is described in more detail in [67], and in Chapter 6.

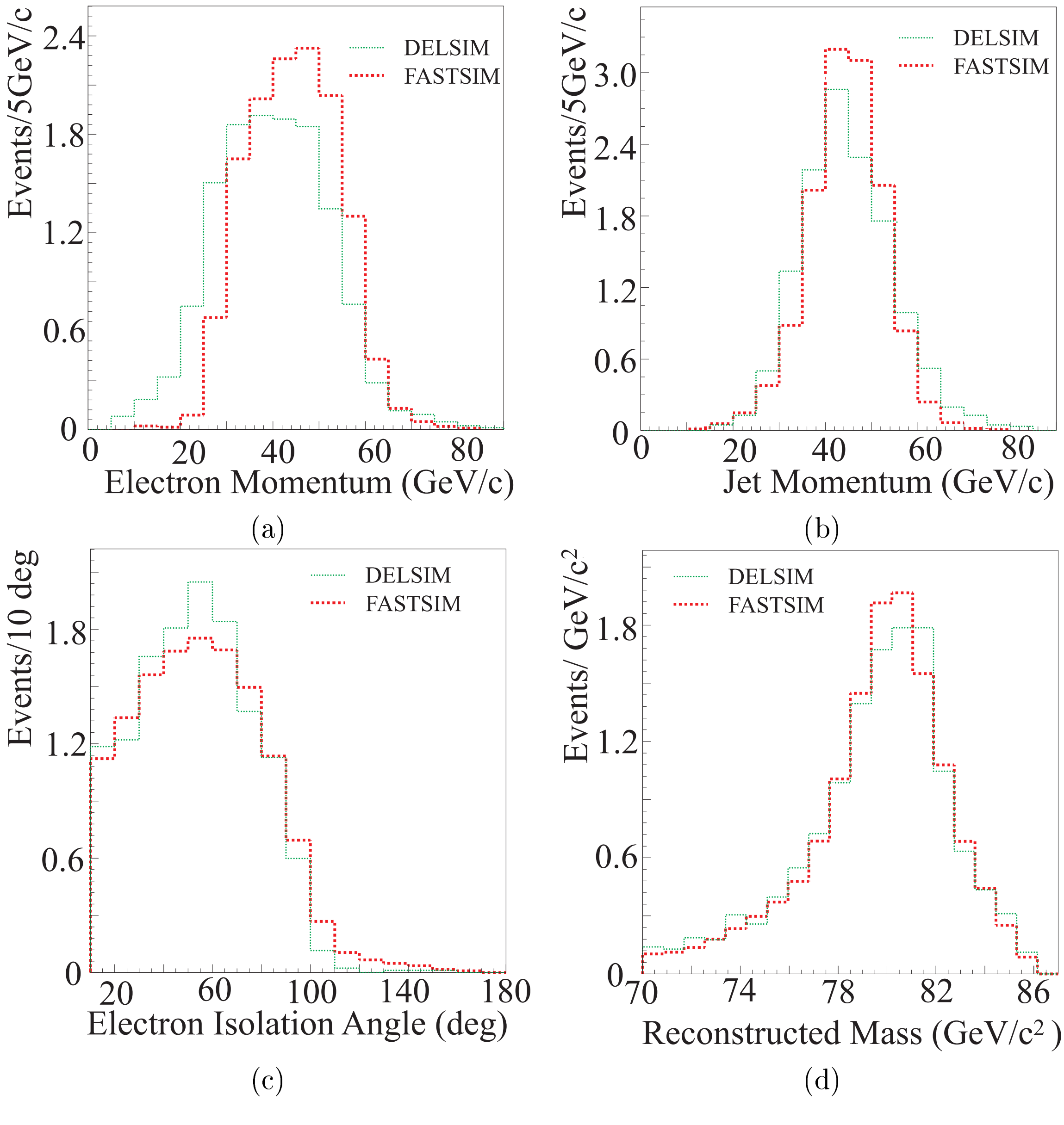

Figure 5.11: (a) electron momentum, (b) momentum of the highest momentum jet, (c) electron isolation angle and (d) reconstructed W mass, in the final state $e\overline{\nu}_e q\bar{q}'$ for `FASTSIM` and `DELSIM` `CC03` diagram simulation event samples at 172 GeV. The Figures are normalised to 10 pb^{-1}.

5.7.4 Results

Figure 5.12 illustrates the difference between the `CC03` diagram sample and an all diagram sample for the $e\overline{\nu}_e q\bar{q}'$ channel. The effect of the t-channel boson exchange processes of Figure 5.10 can be clearly seen: these processes predominantly produce events where an electron is deflected by only a small angle from the beam-pipe and lead to a tail of events at low invariant masses. In the central region of Figure 5.12(a), a small excess of `CC03` events over all diagram events can be seen. This excess (attributed to negative interference effects in the background diagrams) becomes more marked when experimental cuts are applied.

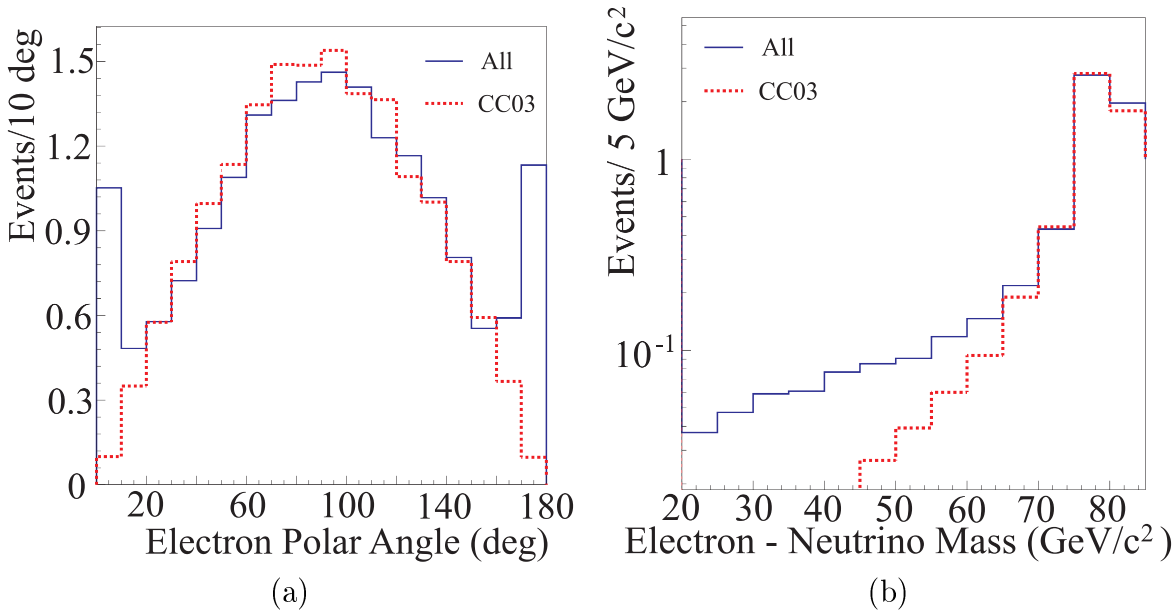

Figure 5.12: (a) polar angle of the final state electron and (b) invariant mass of the $e\ \nu_e$ system, in the final state $e\overline{\nu}_e q\bar{q}'$ for simulation events generated all diagrams and the `CC03` subset at 172 GeV. The Figures are normalised to 10 pb^{-1}.

Cross-Section

The full numerical results of the study at 161 and 172 GeV are shown in Table 5.6. The results marked 'generator' and '`FASTSIM`' were obtained by simulating event samples separately for each of the background diagrams that were considered. In the `FASTSIM` approach full experimental cuts were applied; the generator level procedure applies a selection on the four fermions produced in W^+W^- decays. Figures 5.13 to 5.16 show the results of the `FASTSIM` four-fermion approach (labelled as FASTSIM4f in Table 5.6) over the full energy range; in this approach the background diagrams were simulated using the `EXCALIBUR` all-`CC03` diagrams. The generated cross-sections are given in the lower section of these plots, a generator cut was imposed on the cosine of the polar angle of final state electrons and positrons to be less than 0.9999.

The 'incoherent' visible cross-section $\sigma_{incoh.}$ is obtained having applied the experimental cuts to the `CC03` sample and to each of the backgrounds discussed above: it is the sum of the visible cross-sections for all the processes relevant to the sample being analysed. The coherent visible cross-section (σ_{all}) is that obtained using the `EXCALIBUR` all diagram sample [4].

Channel	Method	161.3 GeV	172.3 GeV
$q\bar{q}'\bar{q}q'$	Generator	0.977 ± 0.006	0.978 ± 0.011
	`FASTSIM`	0.996 ± 0.013	
	`FASTSIM4f`	1.012 ± 0.013	0.980 ± 0.013
$e\overline{\nu}_e q\bar{q}'$	Generator	1.083 ± 0.010	1.008 ± 0.012
	`FASTSIM`	1.083 ± 0.016	
	`FASTSIM4f`	1.090 ± 0.012	1.019 ± 0.011
$\mu\overline{\nu}_\mu q\bar{q}'$	Generator	0.998 ± 0.012	1.021 ± 0.011
	`FASTSIM`	1.006 ± 0.016	
	`FASTSIM4f`	1.006 ± 0.016	0.996 ± 0.013
$l\overline{\nu}_l\bar{l}\nu_l$	Generator	1.035 ± 0.013	0.998 ± 0.014
	`FASTSIM`	1.045 ± 0.008	
	`FASTSIM4f`	1.088 ± 0.017	0.957 ± 0.018

Table 5.6: Results of the correction factor study. The correction factors are given in the form (see text) $\sigma_{incoh.}/\sigma_{all}$.

The quoted errors include the error on the cross-section of the produced samples combined with that on the selection efficiency. In addition, the systematic error was estimated on the `FASTSIM` sample. As the study has been performed using a fast simulation package, which does not reproduce the details of a full detector simulation, large variations in the cuts applied were tested: energy cuts were allowed to vary by up to $\pm 50\%$; polar angle cuts on leptons were applied, thus checking the sensitivity to modelling of the forward and barrel regions of the detector. The systematic uncertainty on the correction factors was demonstrated to be significantly

[4] The values given here differ slightly from those in [55] where they are quoted as correction factors in the form $\sigma_{cco3}/(\sigma_{all} - \sigma_{bck})$.

smaller than the statistical accuracy of this study and we ascribe to it a value of 0.5%.

Direct Reconstruction

The mass shifts observed between the CC03 and four-fermion samples are shown in Table 5.7. The generator level results for EXCALIBUR are confirmed by a further independent study in DELPHI [83], and by work on OPAL [29]. However, results from other generators [29] have shown somewhat smaller effects in the $\mathrm{e}\overline{\nu}_{\mathrm{e}}\mathrm{q}\bar{\mathrm{q}}'$ channel. Despite the large size of the generated samples (70,000 events) the statistical errors (given below) remain large.

channel	mass fitted	Generator shift MeV	FASTSIM study MeV
$\mathrm{q}\bar{\mathrm{q}}'\bar{\mathrm{q}}\mathrm{q}'$	average	$\lesssim 10$	
$\mathrm{e}\overline{\nu}_{\mathrm{e}}\mathrm{q}\bar{\mathrm{q}}'$	$q\bar{q}'$mass	$+30 \pm 9$	
	$e\overline{\nu}_e$mass	$+70 \pm 12$	
	'average'	$+50 \pm 10$	64 ± 20
$\mu\overline{\nu}_\mu\mathrm{q}\bar{\mathrm{q}}'$	average	$\lesssim 10$	

Table 5.7: Results of the direct reconstruction interference study. The difference in the fitted masses for the full four-fermion and for the CC03 samples ($M_{4f} - M_{\mathrm{CC03}}$) at 172 GeV.

Direct Reconstruction Addendum

This study has stimulated activity within the generator community on the issue of four-fermion biases in the direct reconstruction analysis. High statistic generator level results have been obtained with the EXCALIBUR [80] and WPHACT [84] generators: the results are in good agreement with those presented here.

5.7.5 Observations

$\mathrm{q}\bar{\mathrm{q}}'\bar{\mathrm{q}}\mathrm{q}'$ Decay Channel

Excellent agreement in the cross-section correction factor results is obtained between the Generator level study and the first FASTSIM study in all decay channels. In fact, the largest discrepancy is only 1.5 *s.d.*: this occurs in the fully-hadronic channel at 161 GeV. This is the channel in which one expects the generator level study to be least reliable (see 5.7.2).

In the $q\bar{q}'\bar{q}q'$ channel, no significant effect is observed over the full energy range; indeed, it is expected that the interference effect in this channel will be small [85]. Similarly, we did not find a significant mass shift in the direct reconstruction study.

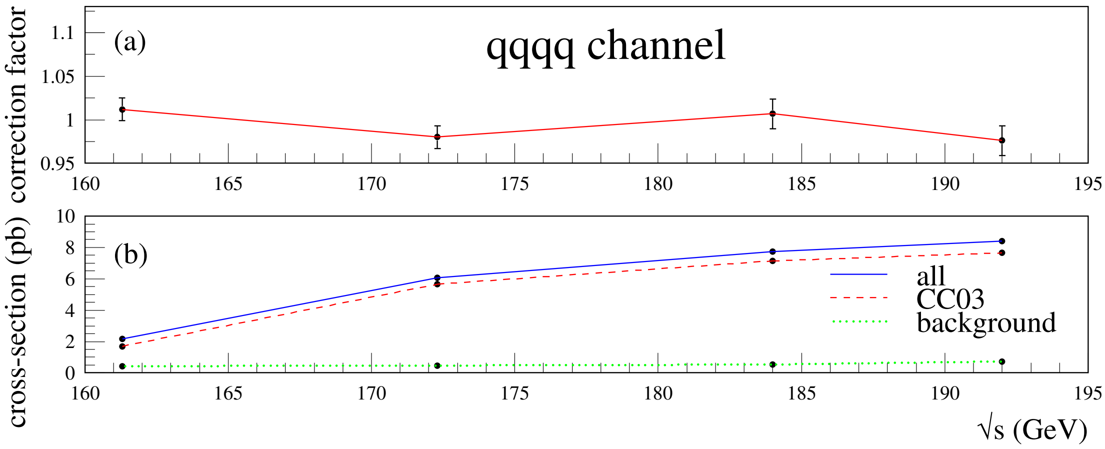

Figure 5.13: $q\bar{q}'\bar{q}q'$ decay channel: (a) interference correction factors and (b) cross-sections within generator cuts.

$\mu\overline{\nu}_\mu q\bar{q}'$ Decay Channel

The correction factor for the $\mu\overline{\nu}_\mu q\bar{q}'$ decay channel is compatible with unity at all energies, and no significant shift is observed in the direct reconstruction study. This result is to be expected as there are no significant four-fermion backgrounds to this channel (see the lower part of Figure 5.14). The W^+W^- decay channel $\tau\overline{\nu}_\tau q\bar{q}'$ proceeds through the same diagrams. As the result for $\mu\overline{\nu}_\mu q\bar{q}'$ is found to be relatively insensitive to the event selection, this result is expected to hold for the $\tau\overline{\nu}_\tau q\bar{q}'$ analysis also.

$e\overline{\nu}_e q\bar{q}'$ Decay Channel

A significant effect (8%) on the cross-section was obtained at 161 GeV which diminishes as the centre of mass energy increases[5]. The results at 184 and 192 GeV were compatible with unity. The generator level study showed good agreement with the FASTSIM study over the full LEP2 energy range.

[5]The generator level study was also conducted at an energy of 167 GeV where a value of 1.034 was obtained for the correction factor.

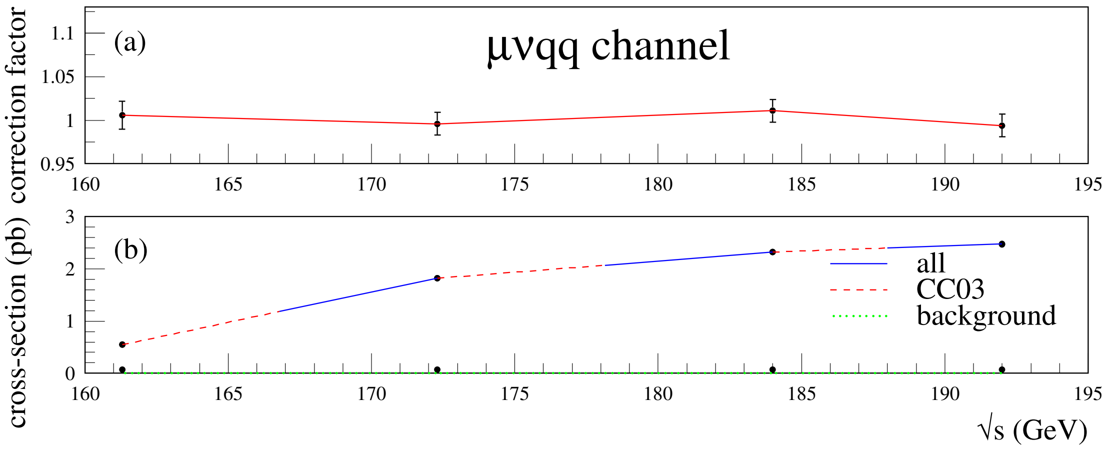

Figure 5.14: $\mu\overline{\nu}_\mu q\bar{q}'$ decay channel: (a) interference correction factors and (b) cross-sections within generator cuts.

The direct reconstruction study shows a significant shift in the average fitted mass at generator level. As can be seen in Table 5.7, this shift is due largely to the $e\overline{\nu}_e$ mass, rather than the $q\bar{q}'$ mass. This pattern agrees with one's naive expectation: in the additional diagrams shown in Figure 5.10, unlike the $e\overline{\nu}_e$ system, the $q\bar{q}'$ system is still the product of a W-decay. The study using `FASTSIM` is in good agreement with the generator level results. From the cross-section results, it is to be anticipated that a significantly larger effect occurs on the direct reconstruction of the threshold W mass, and that the effect is likely to decrease as $\sqrt{s}$ increases.

$l\overline{\nu}_l\bar{l}\nu_l$ Decay Channel

A significant effect was observed by the `FASTSIM` four-fermion approach at 161 GeV. At the other energies studied, the correction factor was compatible with unity.

The two approaches where the explicit backgrounds are considered individually show good agreement at 161 GeV. However, a significant difference is obtained with the `FASTSIM`4f approach and this difference is also observed at 172 GeV (see Table 5.6). A possible explanation of this discrepancy is that the background diagrams neglected in the explicit background approach are not negligible in this channel.

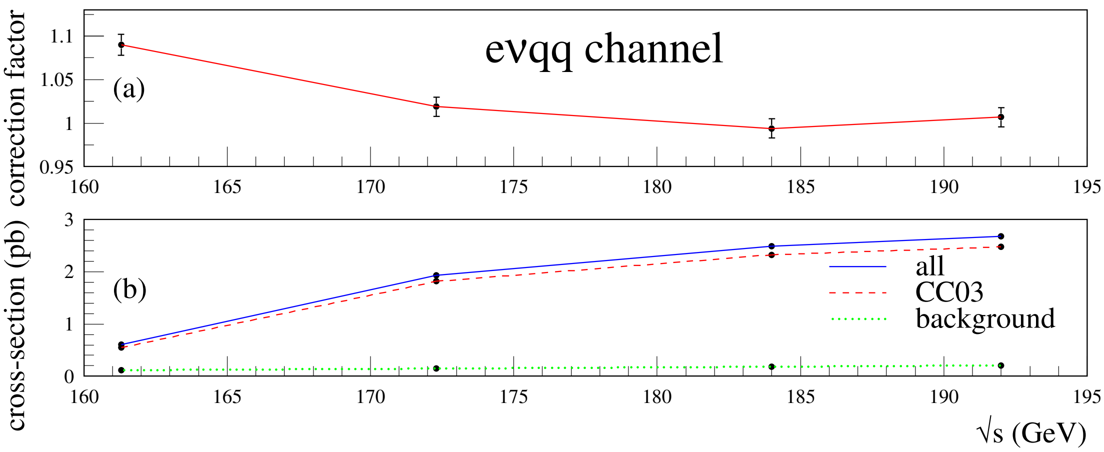

Figure 5.15: $e\overline{\nu}_e q\bar{q}'$ decay channel: (a) interference correction factors and (b) cross-sections within generator cuts.

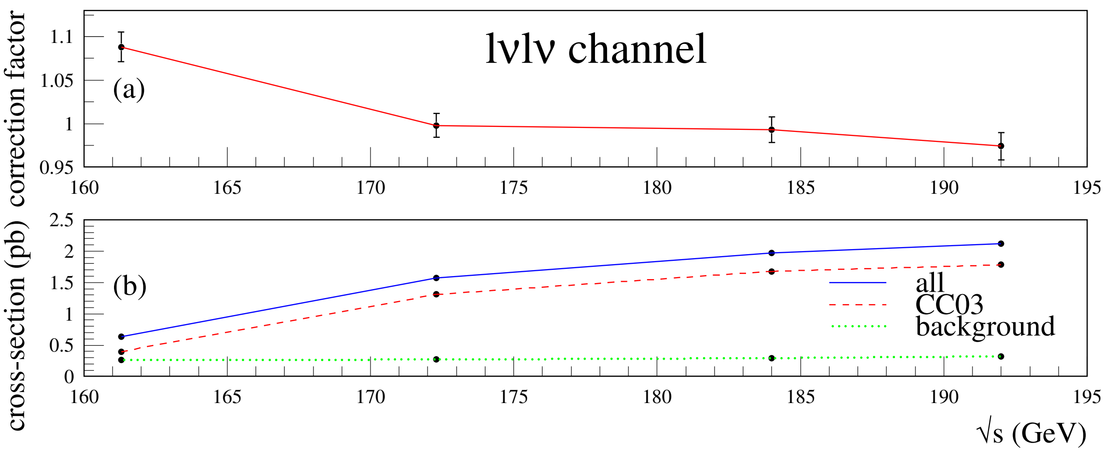

Figure 5.16: $l\overline{\nu}_l \bar{l}\nu_l$ decay channel: (a) interference correction factors and (b) cross-sections within generator cuts.

5.7.6 Conclusions

It is believed that the agreement between the generator level study and the FASTSIM study presented here demonstrates that the results are rather insensitive to the precise event selection. The results of varying the event selection cuts, as performed to estimate the systematic error on the cross-section results, further supports this view. Hence it is believed that the FASTSIM numbers provide a reliable estimate of the true effect for any event selection following the general pattern of cuts applied in this study.

Note that the observed effects in the semi-leptonic electron channel and fully-leptonic channel are in the sense of increasing the measured cross-section: thus it cannot be explained in terms of neglected backgrounds, but must be interpreted as due to the effect of interference terms.

Taking into account the observed effects in all channels gives an increase of 0.06 pb in the W^+W^- cross-section at 161 GeV, and thus a reduction of 30 MeV/c^2 in the measured W mass. The W mass obtained from the direct reconstruction of semi-leptonic CC03 events at 172 GeV would be 30 MeV too low.

Thus, interference terms *between* four-fermion final state processes can have a significant effect in W^+W^- physics. Hence it is the view of the authors that W^+W^- physics is best studied using four-fermion generators, and that future DELSIM production should be based on large statistic 'all' diagram samples from a four-fermion generator.

Chapter 6

Direct Reconstruction of the W Boson Mass

6.1 Introduction

In the previous chapter, we used the event selection described in Chapter 4 to extract the CC03 cross-section and from this we inferred the value of $\mathrm{M_W}$ within the Standard Model. The sensitivity of this approach (see Section 5.6) reduces as $\frac{d\sigma_{\mathrm{W^+W^-}}}{d\sqrt{s}}$ reduces: thus well above the W-pair production threshold this method does not provide an accurate determination of $\mathrm{M_W}$.

The method for extracting $\mathrm{M_W}$ described in this chapter relies upon the sharp peaking behaviour of the reconstructed invariant-mass distribution of the $\mathrm{W^\pm}$ bosons: this method is known as direct reconstruction. The statistical accuracy of this method depends on the number of $\mathrm{W^+W^-}$ events selected, and thus the accuracy of this measurement increases as $\sigma_{\mathrm{W^+W^-}}$ increases[1].

The method is sensitive only to the underlying physics function (that is, a distorted Breit Wigner - see below), which is not dependent upon the terms in the Lagrangian of the interaction: *i.e.* the charged TGC parameters. However, both the threshold and direct reconstruction methods also naturally have an additional loose dependence on the Standard Model due to the event selection. The efficiency and purity are extracted from simulation, and naturally these are sensitive to the TGC

[1] Assuming the event resolution remains constant, in fact the resolution worsens (but only slowly) with $\sqrt{s}$.

parameters: the dependence of the total cross-section and several angular distributions with anomalous couplings are shown in [23]. Consulting this reference will reassure the reader that the analysis presented here is essentially model independent.

Unless otherwise stated, the results quoted in the rest of this chapter are at 172 GeV. The samples marked 172 GeV in this chapter refer to the combined data sample collected around 170.3 and 172.3 GeV, the luminosity weighted average c.m. energy being 172.1 GeV.

The direct reconstruction method is not applied to the data collected at 161 GeV. The $\mathrm{W^+W^-}$ cross-section is over three times smaller than at 172 GeV, while the integrated luminosity collected at both energies is very similar. Furthermore, the reconstructed event mass distribution assumes a heavily distorted Breit-Wigner form (see Section 6.3.1) in the threshold region: this reduces the sensitivity of the direct reconstruction method to $\mathrm{M_W}$.

6.2 Chapter and Method Outline

In Figure 6.1, we show the reconstructed event mass distributions for the $\mathrm{q\bar{q}'\bar{q}q'}$ and the $\mathrm{l\overline{\nu}_l q\bar{q}'}$ decay channels in the data collected at 161 and 172 GeV. The aim of this chapter is to extract the value of $\mathrm{M_W}$ from the distributions at 172 GeV. It is clear from inspection of 6.1 that, in all four plots, $\mathrm{M_W}$ is in the region of 80 GeV.

The event selection used in this analysis is that described in Chapter 4. The event masses are reconstructed using a kinematic fit with five constraints; this technique is discussed in Section 6.4.

We defer the full discussion of the W mass fitting procedure until later in the chapter. The mass fitting uses a model of the probability of observing an event as a function of the event mass. This model is composed of a number of components which we will describe in turn in this chapter.

The components of the model are:

- The underlying physics function.
- Detector resolution effects.
- Background events.

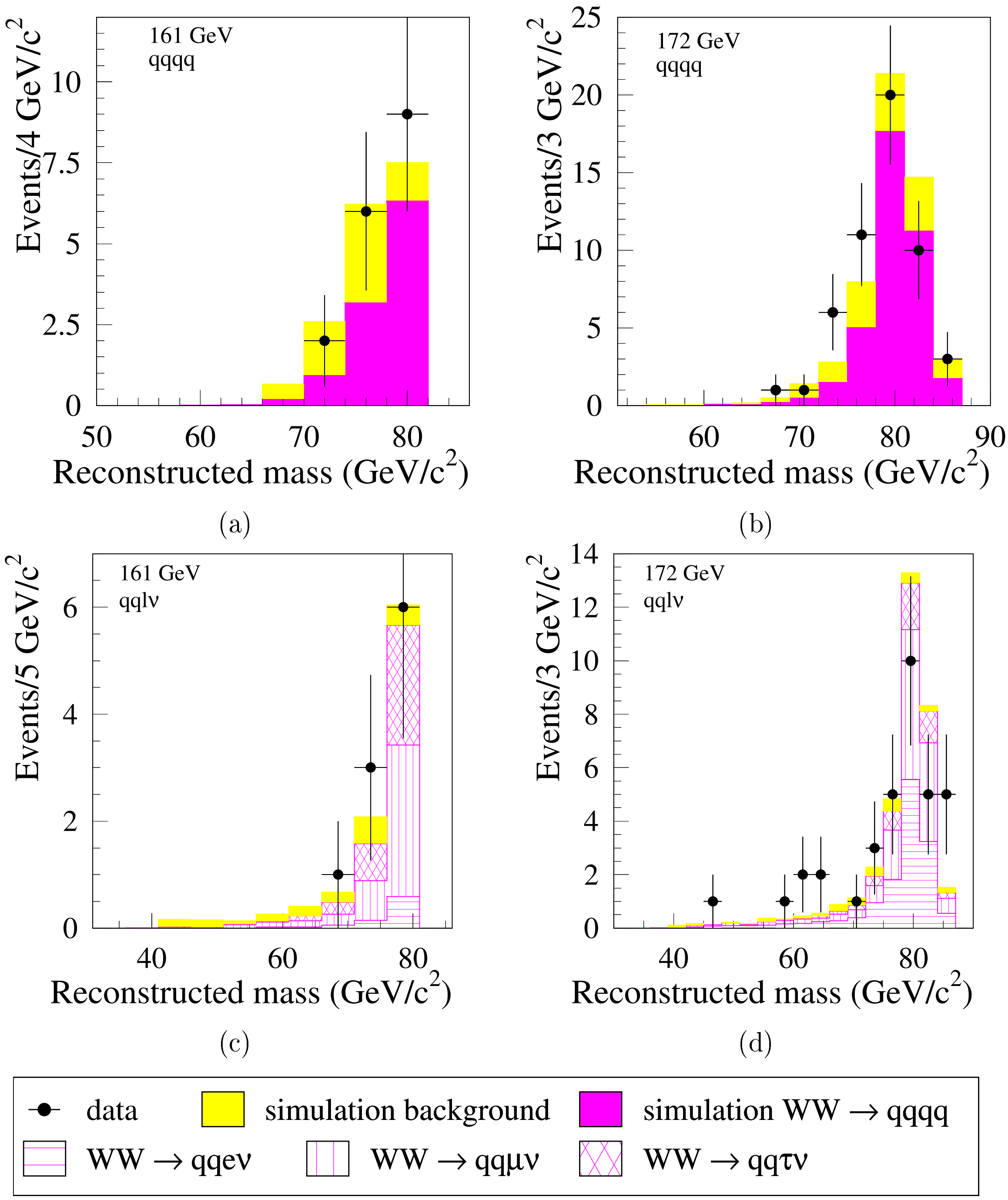

Figure 6.1: The reconstructed event mass (after a kinematic fit with five constraints) is shown for the combined $l\overline{\nu}_l q\bar{q}'$ channel and the $q\bar{q}'\bar{q}q'$ selected events at both 161 and 172 GeV. For each event in the $q\bar{q}'\bar{q}q'$ sample only the jet pairing which provides a mass closest to the world average M_W is used.

In the $q\bar{q}'\bar{q}q'$ decay channel we must also contend with:

- Selecting the correct pairing of the four reconstructed jets.
- The mass distribution of the wrong di-jet pairings.

The $q\bar{q}'\bar{q}q'$ decay channel mass distributions shown in Figure 6.1 (a) and (b), were produced by selecting the pairing of the jets which gives a mass closest to the world average value of M_W[8]. This is not the procedure used in the analysis described in this chapter, as this method would bias the result obtained.

Having discussed the modelling of these components, we describe their combination into an event probability model in Section 6.9. The results of applying this analysis to the selected data samples are then provided.

In this chapter we use the notation m_{W1} and m_{W2} for the masses of the two W bosons in an event. Their average is denoted $\bar{m}_W$. In the section below, we are concerned with describing the underlying physics function. Thus, we are interested in the true event masses before the resolution of these quantities is degraded by detector effects. In all other sections we are describing the reconstructed masses. The reconstructed event mass after a kinematic fit with five constraints is denoted m_{evt}. The physical parameter that we are attempting to estimate is labelled M_W. m is used for a generic mass.

6.3 Physics Function

6.3.1 Introduction

A free W boson mass resonance can be described by a relativistic Breit-Wigner with a mean value M_W (the pole mass) and a width Γ_W. However, a complication is introduced as the masses of the two W bosons produced in each W^+W^- event[2] (m_{W1},m_{W2}) are constrained by the centre of mass energy:

$$m_{W1} + m_{W2} \leq \sqrt{s}$$

Near the threshold production energy, when $\sqrt{s}$ is not much larger than 2 M_W, this is a significant constraint and causes the two W masses to be anti-correlated. The lineshape is distorted since $\sqrt{s} - 2M_W$ is the order of the W width Γ_W.

[2]That is the virtualities (q^2) of the internal W bosons.

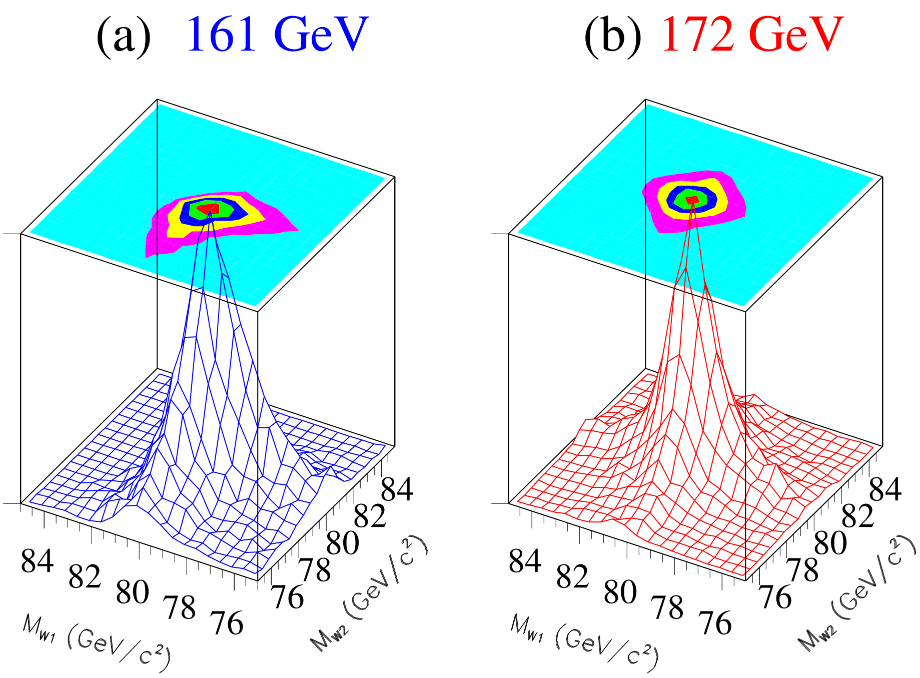

Figure 6.2: The two generated invariant masses (m_{W1},m_{W2}) in simulated W^+W^- events are plotted against each other, and contour plots are also given. Plot (a) is at a $\sqrt{s}$ of 161 GeV and (b) at 172 GeV.

Figure 6.2 shows the situation at $\sqrt{s}$ of 161 GeV and 172 GeV; correlation coefficients $\rho_{\sqrt{s}=161} = -0.199 \pm 0.009$ and $\rho_{\sqrt{s}=172} = -0.059 \pm 0.006$ between m_{W1} and m_{W2} were obtained for masses over the full generated range. In Figure (a) at 161 GeV the beam energy constraint is clearly visible; although the front faces show the characteristic Breit-Wigner form, the contour plot has the diagonal anti-correlation cut-off on the line:

$$m_{W1} + m_{W2} = \sqrt{s} \tag{6.1}$$

Each mass distribution is constrained to effectively be a 'half' Breit-Wigner, leading to the large correlation coefficient measured. In Figure (b), all four axial-'spines' of the Breit-Wigner can be seen, as the beam energy constraint is no longer as significant, and hence the correlation coefficient is now lower.

In principle, one can use a semi-analytical code such as `GENTLE` or a Monte-Carlo generator to describe the differential cross-section $\frac{d^2\sigma(s;M_W,\Gamma_W)}{dm_{W1}dm_{W2}}$, including radiative and Coulomb corrections, as a function of the centre of mass energy $\sqrt{s}$. The fit could then be performed on the mean event mass $\bar{m}_W$, or in two dimensions on m_{W1} and m_{W2}. However, in practice the implementation of this prescription would be CPU intensive, and excellent agreement is obtained using the approximations described below. The reader is advised that the following section is more detailed than that required for this analysis; results are derived applicable to the full expected LEP2 data samples as well as the current low statistic regime.

6.3.2 Simple Approximations

In the absence of the c.m. energy constraint we would describe each mass by a relativistic Breit-Wigner (see Section 1.4.3).

$$\rho_W(m; \mathrm{M_W}, \Gamma_\mathrm{W}) = \frac{1}{\pi}\frac{\Gamma_\mathrm{W}}{\mathrm{M_W}}\frac{m^2}{(m^2 - \mathrm{M_W}^2)^2 + m^4(\frac{\Gamma_\mathrm{W}}{\mathrm{M_W}})^2} \tag{6.2}$$

We use an s dependent width, where $s = m^2$:

$$\Gamma_\mathrm{W}(s) = \frac{s}{\mathrm{M_W}^2}\Gamma_\mathrm{W}(\mathrm{M_W}^2) \tag{6.3}$$

In Figure 6.3 (a) we show this formalism (labelled BW) applied to the mean event mass $\bar{m}_W$:

$$\bar{m}_W = \frac{1}{2}(m_{W1} + m_{W2})$$

Clearly this does not provide a good description of the right-hand tails of the distribution of the average mass: the observed cut-off is a consequence of Equation 6.1

The first extension of the Born-level on-shell `CC03` cross-section (σ_0) calculation discussed in Section 1.4.1 to off-shell Ws is given by

$$\begin{aligned} \sigma(\sqrt{s}; m_{W1}, m_{W2}) &= \int_0^{\sqrt{s}} dm_{W1}\ \rho_W(m_{W1}) \\ &\quad \int_0^{\sqrt{s}-m_{W1}} dm_{W2}\ \rho_W(m_{W2})\ \ \sigma_0(s; m_{W1}, m_{W2}) \end{aligned} \tag{6.4}$$

where $\rho_W(\mathrm{M_W})$ is given in Equation 6.2[3].

[3] We have obtained the total cross-section expression by setting the W branching ratios in Equation 1.5 to unity.

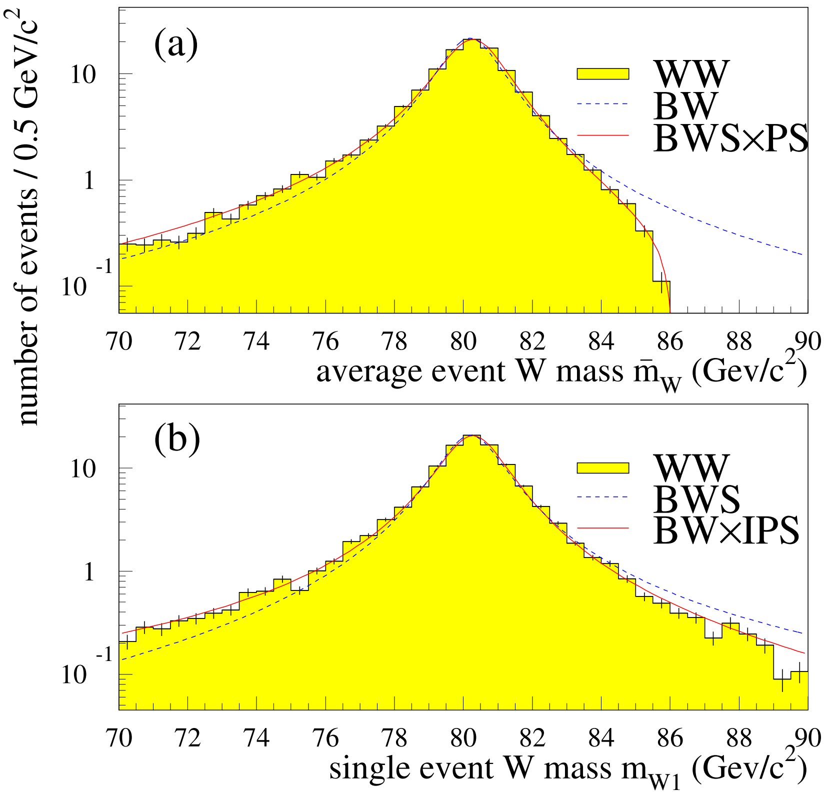

Figure 6.3: Results of fitting the generator information in a simulation sample of W^+W^- events with a range of functions. The functions used are a relativistic Breit-Wigner (BW) with an s-dependent width (BWS), and phase space factors (PS, IPS) (see text).

Although the full dependence of the Born-level cross-section on s is very complex, we can make a suitable approximation in the threshold region. Observing the form of the cross section [2] close to threshold, we find that the t-channel neutrino diagram (see Figure 5.8) dominates with a squared amplitude proportional to $\frac{s}{\mathrm{M_W}^2}$, and that the phase space factor is proportional to $\frac{\beta}{s}$, where β is the velocity of the $W^\pm$ bosons. Thus we find at threshold:

$$\begin{aligned}
\sigma_0(\sqrt{s};\mathrm{M_W}) &= \textit{phase space} \times |M|^2 \\
&\propto \frac{\beta}{s} \times \frac{s}{\mathrm{M_W}^2} \\
&\propto \frac{\beta}{\mathrm{M_W}^2} \equiv \sqrt{1-\left(\frac{2\mathrm{M_W}}{\sqrt{s}}\right)^2}/\mathrm{M_W}^2
\end{aligned}$$

A simple approximation that has been used at LEP2 [67] is to use β as a phase space factor, replacing $\mathrm{M_W}$ with the mean $\bar{\mathrm{m}}_\mathrm{W}$ in the event, that is:

$$\sigma_0(\sqrt{s};\mathrm{M_W}) \propto \beta \approx \beta_{av} \equiv \sqrt{1-\left(\frac{\mathrm{m_{W1}}+\mathrm{m_{W2}}}{\sqrt{s}}\right)^2} \tag{6.5}$$

However in the literature [86] we can find the full expression for the cross-section ($\sigma_0(s;\mathrm{m_{W1}},\mathrm{m_{W2}})$) in terms of Ws with different virtualities. Extracting the leading t-channel term, as previously, we find

$$\begin{aligned}\sigma_0(\sqrt{s};\mathrm{m_{W1}},\mathrm{m_{W2}}) \quad \propto \quad & \left[1-\left(\frac{\mathrm{m_{W1}}^2-\mathrm{m_{W2}}^2}{s}\right)^2 - 2\left(\frac{\mathrm{m_{W1}}^2+\mathrm{m_{W2}}^2}{s}\right)\right]^{\frac{1}{2}} \\ & \left(\frac{1}{\mathrm{m_{W1}}}+\frac{1}{\mathrm{m_{W2}}}\right)\end{aligned}$$

if we neglect terms in $(\mathrm{m_{W1}}-\mathrm{m_{W2}})$ this reduces to

$$\sigma_0(\sqrt{s};\mathrm{m_{W1}},\mathrm{m_{W2}}) \propto \frac{\beta_{av}}{\bar{\mathrm{m}}_\mathrm{W}^2} \tag{6.6}$$

thus further justifying the simple approximation of Equation 6.5.

In the kinematic fitting procedures used (see below), the two W masses are often set equal and, even when this is not imposed as a constraint, the method can introduce significant correlations between the measured masses which cannot easily be modelled. It is thus useful to be able to model the cross-section either as a function of a single event mass $\mathrm{m_{W1}}$, or the mean event mass $\bar{\mathrm{m}}_\mathrm{W}$.

We now refer to the approximations to σ_0 that we have described above as the phase space (PS) factor (Equation 6.5) and as the improved phase space (IPS) factor (Equation 6.6). Both approximations depend only on $\bar{\mathrm{m}}_\mathrm{W}$: this simplifies the algebra (see Section 6.13). For the average mass we obtain:

$$\frac{d\sigma(\bar{\mathrm{m}}_\mathrm{W})}{d\bar{\mathrm{m}}_\mathrm{W}} \propto \rho_W(\bar{\mathrm{m}}_\mathrm{W})\ PS(\bar{\mathrm{m}}_\mathrm{W}) \tag{6.7}$$

The results of a fit to the average generated mass for approximately 2 $\mathrm{fb}^{-1}$of $\mathrm{W^+W^-}$ simulation events is shown in Figure 6.3 (a) and results are given in Table 6.1. The phase space factor describes the event distribution in the neighbourhood of the c.m. energy cut-off well, but causes a small deviation to occur on the left of the plot. The addition of the s-dependent width reduces the effective Breit-Wigner width at the left and this improves the fit in this region, and hence the global χ^2. The IPS approximation is not used here as this worsens the fit on the left-hand side of the plot.

However, for a single mass distribution ($\mathrm{m_{W1}}$) from Equation 6.4 we find:

$$\frac{d\sigma(\mathrm{m_{W1}})}{d\mathrm{m_{W1}}} \propto \rho_W(\mathrm{m_{W1}}) \int_0^{\sqrt{s}-\mathrm{m_{W1}}} d\mathrm{m_{W2}}\ \rho_W(\mathrm{m_{W2}})\ PS(\mathrm{m_{W1}},\mathrm{m_{W2}})$$

the simplest approximation to the integral is to assume $\mathrm{m_{W2}}$ is on-shell, *i.e.* put

$$\rho_w(\mathrm{m_{W2}}) = \delta(\mathrm{m_{W2}},\mathrm{M_W})$$

thus,

$$\frac{d\sigma(\mathrm{m_{W1}})}{d\mathrm{m_{W1}}} \propto \rho_W(\mathrm{m_{W1}})\ PS(\mathrm{m_{W1}},\mathrm{M_W})$$

Figure 6.3 (b) and Table 6.1 show the results of a fit to the single event W mass $\mathrm{m_{W1}}$. Unlike graph (a), the description with an (s-dependent width) Breit-Wigner alone is acceptable. There is no longer an absolute cut-off in the mass; in Equation 6.1, a large $\mathrm{m_{W1}}$ is compensated for by a small $\mathrm{m_{W2}}$: thus, relative to a Breit-Wigner distribution, this constraint leads to a reduced number of events at large masses and an increased number at small masses. Inserting the improved phase space correction factor naturally improves the fit on the right-hand side; fortuitously it also improves the left-hand side as the $\frac{1}{\mathrm{m_W}}$ dependence boosts this region. The fit can be improved further by removing the s-dependence of the width, since this also has the effect of boosting the low mass region of the plot.

6.3.3 Summary

We fitted the mean event mass ($\mathrm{\bar{m}_W}$) with

$$Phys_{\mathrm{\bar{m}_W}} = \frac{1}{\pi}\frac{\Gamma_\mathrm{W}}{\mathrm{M_W}}\frac{\mathrm{\bar{m}_W^2}}{(\mathrm{\bar{m}_W^2}-\mathrm{M_W}^2)^2+\mathrm{\bar{m}_W^4}(\frac{\Gamma_\mathrm{W}}{\mathrm{M_W}})^2} \times \sqrt{1-\left(\frac{2\mathrm{\bar{m}_W}}{\sqrt{s}}\right)^2} \qquad (6.8)$$

where the W width is s-dependent according to Equation 6.3 and a single event mass with

$$Phys_{\mathrm{m_{W1}}} = \frac{1}{\pi}\frac{\Gamma_\mathrm{W}}{\mathrm{m_{W1}}}\frac{\mathrm{m_{W1}}^2}{(\mathrm{m_{W1}}^2-\mathrm{M_W}^2)^2+\mathrm{m_{W1}}^4(\frac{\Gamma_\mathrm{W}}{\mathrm{M_W}})^2} \times \frac{\sqrt{1-\left(\frac{\mathrm{m_{W1}}+\mathrm{M_W}}{\sqrt{s}}\right)^2}}{(\mathrm{m_{W1}}+\mathrm{M_W})^2}$$

where the W width is fixed

Good fits are obtained using these functions; the χ^2 are given in Table 6.1 for the fits of 2 fb^{-1} of W^+W^-simulation. This is sum of the integrated luminosity for all four LEP experiments that it is hoped will be obtained during the full LEP2 programme [87]. The χ^2 are dominated by events in the tails; these events carry less weighting in the mass fitting procedure. The shifts in the mass are below the final accuracy expected from the LEP M_W determination. Hence these simple approximations provide a suitable description of the underlying W^+W^- physics distribution not only for the limited data sample analysed in this thesis, but also for that expected from the complete LEP2 programme.

Function	Δ Mass (MeV/c^2)	Δ Width (MeV/c^2)	χ^2/dof
Mean Event Mass ($\bar{m}_W$)			
BW	-145 ± 10	-0.21 ± 0.02	26
BW × PS	$+13 \pm 6$	-0.11 ± 0.02	4.6
BWS × PS	0 ± 4	-0.04 ± 0.02	1.6
Single Event Mass (m_{W1})			
BWS	-112 ± 9	-0.16 ± 0.02	12.5
BW	-92 ± 9	-0.13 ± 0.02	5.9
BW × IPS	-42 ± 5	-0.12 ± 0.02	2.8

Table 6.1: Results of fitting a 2 fb^{-1} simulation sample of W^+W^- events with a range of functions. The difference Δ(fitted - generated) between the generated mass (80.35 GeV/c^2) and width (2.07 MeV/c^2) and the fitted values are given. The functions used are a relativistic Breit-Wigner (BW), with an s-dependent width (BWS), and phase space factors (PS,IPS) (see text).

6.4 Reconstruction Method

6.4.1 Constraints

The principle of direct reconstruction of the mass is simply to apply Einstein's equation:

$$m^2 = E^2 - p^2 \tag{6.9}$$

to the observed jets and leptons. We refer to this method below as the standard method.

Using the observed jets as a measure of the quark momentum, we can form the invariant mass of di-jet pairs and thus reconstruct the mass of hadronically decaying Ws. In the $q\bar{q}'\bar{q}q'$ channel, we must obtain the correct jet pairings for each W: this problem is discussed in Section 6.6.1 . In the study performed below, we extract the correct pairing from the simulation truth information by finding the jets which are closest in direction to the flight of the original quarks[4].

For a leptonic W decay we have a missing neutrino[5]: since we know the original $\sqrt{s}$, we can estimate the momentum of this particle from the missing momentum in the event (as in Equation 6.11). Clearly, this mechanism can only be applied to the $l\overline{\nu}_l q\bar{q}'$ decay channel: we cannot directly reconstruct events in the $l\overline{\nu}_l\bar{l}\nu_l$ decay channel as there are two missing neutrinos and thus the problem is under-constrained.

The method described in the previous two paragraphs does not make full use of our knowledge of the system. We can apply conservation of energy and momentum to both channels.

$$E_{f1} + E_{f2} + E_{f3} + E_{f4} = \sqrt{s} \tag{6.10}$$

$$\mathbf{p}_{f1} + \mathbf{p}_{f2} + \mathbf{p}_{f3} + \mathbf{p}_{f4} = 0 \tag{6.11}$$

where the f subscripts denote the four-fermions in the event[6]. However, these constraints are not absolute since significant ISR radiation occurs in these W^+W^- events. We cannot accurately determine the momentum of the ISR radiated photon in W^+W^- events (typically 1-2 GeV) as the resolution of the detector is insufficient. The ISR photon may cause a bias on our reconstructed mass. Any biases inherent in our reconstruction method are removed by calibrating the method with simulation samples (see Section 6.10).

In the limit that the observed mass distribution is dominated by the detector resolution function, one can treat the $W^\pm$ bosons in each event as on-shell. We can thus apply the additional constraint:

[4] This procedure was introduced in Section 4.5.3.

[5] The treatment of the tau lepton whose decay leads to a further neutrino is discussed in Appendix B.

[6] In this analysis we consider only the case of four reconstructed objects. Hard gluon emission from quarks can lead to further jets. The case of five jets in $q\bar{q}'\bar{q}q'$ events is considered in [67].

$$m_{W1} = m_{W2} \tag{6.12}$$

We then obtain only one mass per event, a mean mass $\bar{m}_W$ for the event.

Assuming equal masses for the W^+ and W^-, we can in fact reform Equation 6.9 in terms of the observed particle directions alone, not using the energies; this technique is discussed in [88]. We know the jet directions to a higher precision than their energies: hence this technique gives better precision than that of the standard method discussed above.

The mechanism adopted here which allows us to make use of all this information (Equations 6.10, 6.11 and 6.12) is to use a kinematic fit technique. The inputs to the fit are the four-vectors and their errors on each of the observed jets/leptons. The fit minimises a χ^2-like quantity, while applying the constraints using Lagrangian multipliers. For this analysis the `PUFITC+` package [82, 67] is used. The technical details of the package, specifically the form of the χ^2 and the error parameterisation used are discussed in Appendix B.

The $q\bar{q}'\bar{q}q'$ channel standard method of paragraph one is a 0 constrained fit: that is, it has only one solution. Applying the four constraints of Equations 6.10 and 6.11, we have four degrees of freedom and this is denoted as a four-constrained (4C) fit. Adding Equation 6.12 we have a 5C fit. In the case of the $l\overline{\nu}_l q\bar{q}'$ channel, we have lost three degrees of freedom due to the unobserved neutrino momentum and have either a 1C or a 2C fit.

It is clear from Figure 6.4 and the results presented in Table 6.2 that the kinematic fit improves the observed mass resolution. In the standard method we also find that the mean mass has a large shift: on average we miss 20% of the energy of a jet in the detector. The results in the $l\overline{\nu}_l q\bar{q}'$ channel follow the same pattern as those presented here for the $q\bar{q}'\bar{q}q'$ channel. After the 1C fit, the resolution on the $q\bar{q}'$ mass is 10% better than that on the $l\overline{\nu}_l$ mass. The mass resolutions in the $\mu\overline{\nu}_\mu q\bar{q}'$ channel are similarly improved (for both 1C and 2C fits) over the $e\overline{\nu}_e q\bar{q}'$ channel.

In general, the author favours the 4C fit over the 5C fit as the additional constraint is unphysical and hence will inevitably introduce a bias to the final result. However, it is clear from the results in Table 6.2 that the improvement obtained

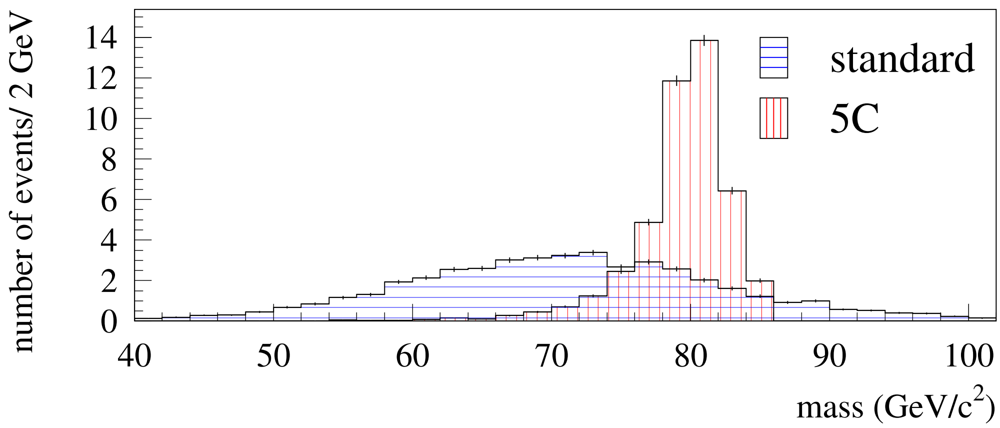

Figure 6.4: One of the reconstructed invariant masses ($\mathrm{m_{W1}}$) in the standard method, and the reconstructed W mass $\mathrm{m_W}$ after a 5C kinematic fit. The distributions are given for the $\mathrm{q\bar{q}'\bar{q}q'}$ decay channel. The plot is normalised to 10 pb^{-1}.

on the final result is significant. The two masses in the 4C fit are highly anti-correlated due to mis-measurement of jet energies: in the regime of low statistics, large correlations must be dealt with carefully as they can bias the final result [89].

A rescaling method which has a similar sharpening effect on the resolution function, but still provides two (albeit correlated) masses for each event, has been used by the ALEPH Collaboration for the $\mathrm{q\bar{q}'\bar{q}q'}$ channel [90]. This technique can be applied after the 4C fit has already improved the mass resolution. The procedure is:

$$\mathrm{m_{W1}}^{rescale} = \mathrm{m_{W1}} \times \frac{\frac{1}{2}\sqrt{s}}{E_1}$$

thus

$$E_1^{rescale} = \frac{1}{2}\sqrt{s}$$

$$\mathbf{p}_1^{rescale} = \mathbf{p}_1 \times \frac{\frac{1}{2}\sqrt{s}}{E_1}$$

This rescales the energy and momentum of the W such that its energy is equal to the beam energy. This introduces two highly unphysical characteristics: in general,

($m_{W1} \neq m_{W2}$) the momentum in the event will no longer balance after rescaling; each mass is now subject to the same cut-off

$$m_W{}^{rescale} \leq \frac{1}{2}\sqrt{s}$$

as the mean event mass of Figure 6.3 (a), rather than the single event mass of Figure (b). As stated in [29], the correlation is sensitively related to the applied cuts and reconstruction method. Furthermore, there is no evidence on DELPHI that this method reduces the error from that obtained in a 5C fit; a study by the OPAL Collaboration concluded similarly [29].

Invoking the Central Limit Theorem and Minimum Variance Bound, the limit on the resolution that can be obtained on each mass per event is simply the standard deviation: this limit will be reached for an unbiased and efficient estimator. Combining the results from both masses in an event, and taking account of their correlation, we obtain the results in the final column of Table 6.2

Method	Mean (GeV)	s.d. (GeV)	ρ	Δ M_W(GeV/ Event)
Generated	80.13 $\pm$ 0.01	2.11 $\pm$ 0.01	-0.059 $\pm$ 0.006	1.4
$q\bar{q}'\bar{q}q'$ Channel				
Standard	64.72 $\pm$ 0.10	12.18 $\pm$ 0.07	-0.161 $\pm$ 0.011	7.9
4C	78.63 $\pm$ 0.08	9.87 $\pm$ 0.06	-0.738 $\pm$ 0.005	3.6
4C Rescaled	79.89 $\pm$ 0.02	2.84 $\pm$ 0.02	+0.554 $\pm$ 0.008	2.5
5C	79.95 $\pm$ 0.03	2.54 $\pm$ 0.02		2.5

Table 6.2: Comparison of reconstructing the W mass on simulation W^+W^- events with a generated mass of 80.35 GeV, using several methods (see text). In order that the quoted standard deviation is not dominated by the distribution tails, the value was computed after removing the outlying 5% of events. In the 5C fit, only one mass is obtained per event; in the other methods two masses are obtained. The final column shows the best resolution on M_W that could be obtained per event.

6.4.2 Kinematic Fit Information

The kinematic fit is used to reconstruct the average W mass of the event by minimising a χ^2-like quantity. From the kinematic fit we may extract the event mass, its error, and the value of the χ^2. We have only discussed the use of the principal piece of information - the mass - in the previous section of this chapter; here we discuss the information content of these other two quantities.

The mass error reflects the level of detector resolution effects in that event[7]. Particular event topologies, and mis-measurement of energies, result in larger uncertainties on the reconstructed mass than in other W^+W^- events. For example, the energies and direction of the inferred neutrino are critical in obtaining an accurate event mass in the semi-leptonic events. A simple graphical demonstration of the value of the mass error information is given in Figure 6.5(a). The reconstructed mass resolution is formed from the reconstructed event mass and the average generated mass of the event ($m_{evt} - m_{av}$) for $\mathrm{l}\overline{\nu}_\mathrm{l}\mathrm{q}\bar{\mathrm{q}}'$ decay channel simulation events. The simulation events are divided into two samples: those with a kinematic fit error less than or greater than average. As expected, the events with smaller mass errors have a smaller width in the distribution.

The value of the χ^2 in the kinematic fit of an event is, naturally, an indication of the goodness of the fit. It is a measure of how much the measured momentum vectors must be changed by in order to obtain a mass which satisfies the constraints of the fit. In the kinematic fit, the errors on the energy and directions of the input vectors are assumed to be Gaussian. However, the reconstructed quantities will have significant non-Gaussian tails (see Figure 4.23). The result is that the χ^2 probability distribution has a large spike at low probabilities, as shown in Figure 6.5 (c): 20% of events have a χ^2 probability of less than 5% . In these events, the mass information is significantly degraded: the events lie in a much broader distribution around the true W mass. However, the Gaussian error assumption has caused the mass errors to be underestimated. Here we adopt a procedure, which is loosely based upon that in [25], to rescale the mass errors based on the kinematic fit χ^2.

If $\chi^2/\mathrm{dof} > 2$ then:

$$\sigma_{evt} = \sigma_{evt} \times \sqrt{\chi^2/\mathrm{dof}}$$

The property of this rescaling is such that, if we rescaled by this factor the errors on the four-vectors used in kinematic fit, then we would obtain a χ^2/dof of unity. The value of 2 for the rescaling procedure was chosen from studying the χ^2 probability distribution (see Figure 6.5(c)).

[7]We remind the reader that the mass error (which we extract from the kinematic fit error matrix) is equivalent to the value which the mass must be changed by to change the χ^2 by one unit.

An additional complication is introduced by the effect of the constraints applied in the kinematic fit Equations 6.10,6.11 and 6.12. The average event mass is forced to be less than the beam energy; it can be shown that this constraint also forces the event mass error to tend to zero at the kinematic limit. The following empirical parameterisation (the well known beta function) has been demonstrated to improve the error assessment.

$$\sigma_{evt} = \sigma_{evt} \times \frac{1}{\sqrt{1 - 4\mathrm{m_{evt}}^2/s}}$$

The mass error correction procedures adopted here are discussed in more depth in [91]. This procedure defines the relative mass errors of the events. The overall scale (a multiplicative factor) on the errors is tuned to obtain the required behaviour of the $\mathrm{M_W}$ likelihood fit (see Section 6.10).

We define the Pull

$$Pull = (m_{evt} - m_{av})/\sigma_{evt}$$

where σ_{evt} is the kinematic fit mass error. The pull distribution is shown in Figure 6.5(b): this should be a Gaussian distribution of unity width. The unit width Gaussian is shown on the plot; the pull distribution of the kinematic fit errors are observed to behave in an acceptable manner.

We provide here figures for the combined semi-leptonic channels, but note that the characteristics and the rescaling procedures described here are valid in all three semi-leptonic search channels and in the fully-hadronic channel. Plots for the fully-hadronic channel can be found in [91]. In Figure 6.6, we compare the mass error distribution observed in the data with that expected from the simulation in the $\mathrm{l\overline{\nu}_l q\bar{q}'}$ decay channel.

In summary, we find that the kinematic fit event mass errors are an estimate of the resolution in that event. We recognise two classes of events whose kinematic fit errors are lower than expected:*(i)* events with a bad fit χ^2 and *(ii)* events near the kinematic limit. We apply an error rescaling mechanism to increase the error on these data, thus reducing the impact of these events in the maximum likelihood fit. In Figure 6.5 (d), we show the pull distributions as a function of the reconstructed mass. Before the rescaling procedure is applied, we find that on the edges of the plot large pull values are observed in some events. The pull distribution of events on the right-hand edge is improved by the kinematic limit rescaling procedure and the distribution on the left-hand edge is improved by the χ^2 rescaling method. A comparative study shows that use of the kinematic fit mass errors, rather than fixed resolution errors, provides an improvement of approximately 15% on the statistical error of the analysis.

6.5 Signal Event Description

In Section 6.3, we obtained a suitable function to describe the W Boson mass distribution. Then, in Section 6.4, we showed how to reduce the measurement error on the reconstructed event mass by using a 5C kinematic fit. In the previous section we have shown that an estimate of the resolution error of an individual event can be obtained from the kinematic fit mass error. Here, we propose a method to combine these pieces of information and obtain a suitable functional form to describe the mass distribution of the reconstructed events.

Resolution Function

We assume that the Detector and Reconstruction effects can be represented by a simple Gaussian :

$$Res(m) = \frac{e^{\frac{-m^2}{2\sigma^2}}}{\sigma\sqrt{2\pi}} \tag{6.13}$$

Where the width σ represents the resolution. We use the kinematic fit mass error for each event as the σ of that event.

Combined Description

The probability density of observing a signal event with a mass m_{evt} we denote by Sig. We construct this probability from the Gaussian resolution function of Equation 6.13 and from the modified Breit-Wigner function of Equation 6.8.

We model the signal probability by the convolution integral of the resolution function Res and the physics function $Phys$:

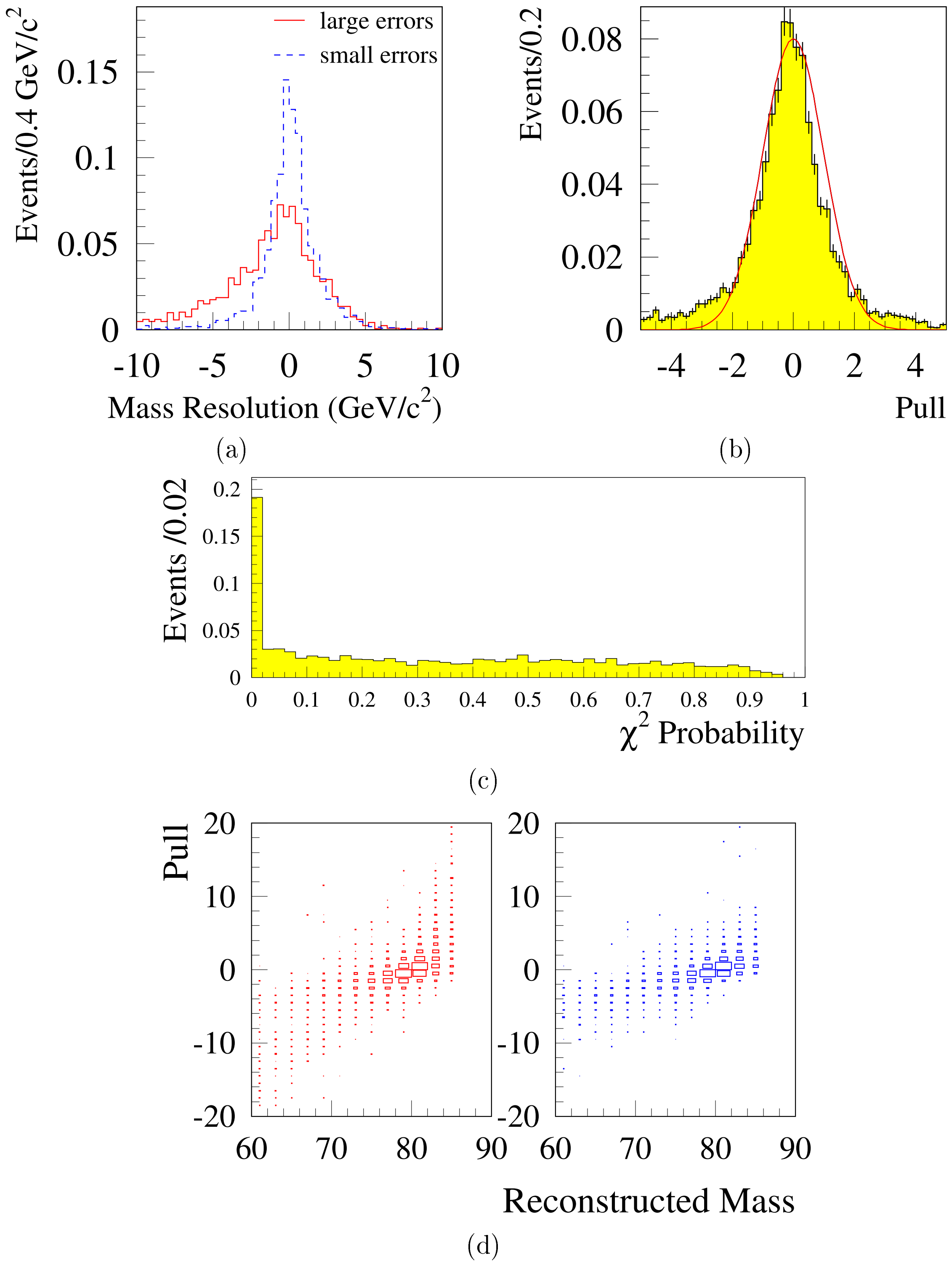

Figure 6.5: These plots illustrate the kinematic fit mass error. The mass resolution and pull are defined in the text. In plots (a) and (b) the rescaling procedures have already been applied. Figure (d) shows the pull distribution obtained before (left) and after (right) the rescaling procedures are applied. The plots are normalised to unity.

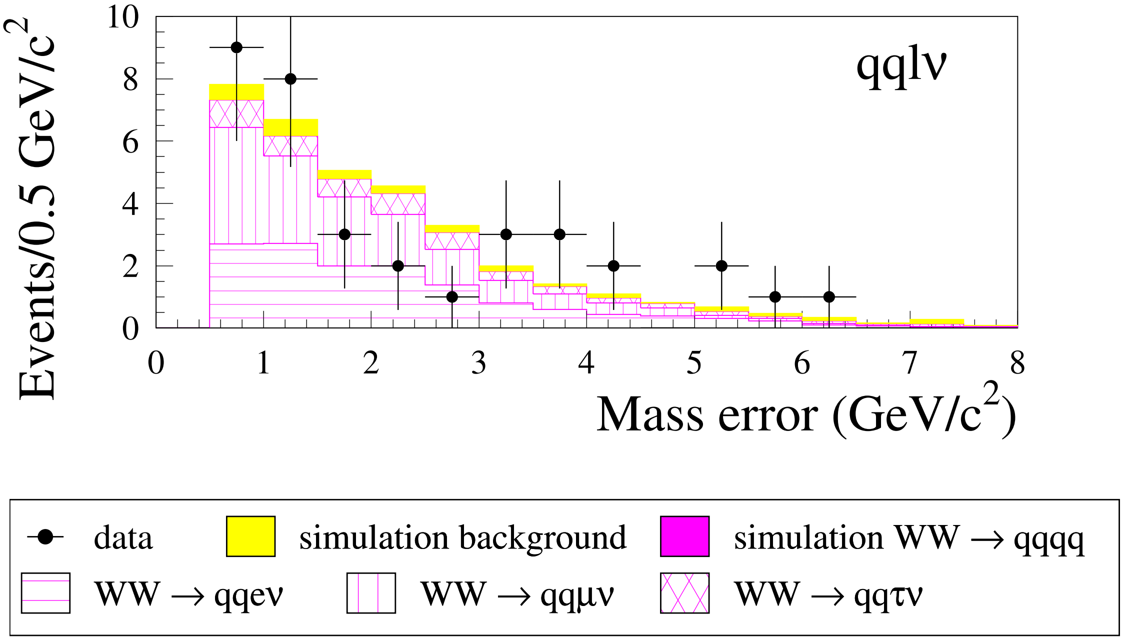

Figure 6.6: Kinematic fit mass error compared between data and simulation for the $l\overline{\nu}_l q\bar{q}'$ channel.

$$Sig = Res \otimes Phys = \int_0^{E_{beam}} Res(\mathrm{m_{evt}} - m', \sigma_{\mathrm{evt}}) \times Phys(\mathrm{M_W}; m')\ dm' \qquad (6.14)$$

Here, the dummy integration mass (m') plays the role of the average generated event mass (the quantity labelled $\bar{\mathrm{m}}_{\mathrm{W}}$ in Section 6.3).

The performance of this model is compared with a sample of simulated $\mathrm{W^+W^-}$ events in Figure 6.7. The solid line shows the number of expected events as a function of $\mathrm{m_{evt}}$. The number of expected events in each bin was calculated from the sum of repeated applications of Equation 6.14. The summing of repeated calculation is necessary as the value of the resolution function width σ used in our model must be extracted from the simulation events.

In Figure 6.7 (a), the function Sig is shown to be in good agreement with the simulation events for the semi-leptonic analysis. In Figure (b), the same plot is shown for the fully-hadronic analysis. However, in this analysis three event masses are obtained for each event, only one of which corresponds to the mass of a W. In producing Figure (b), we have extracted from the generator information of the

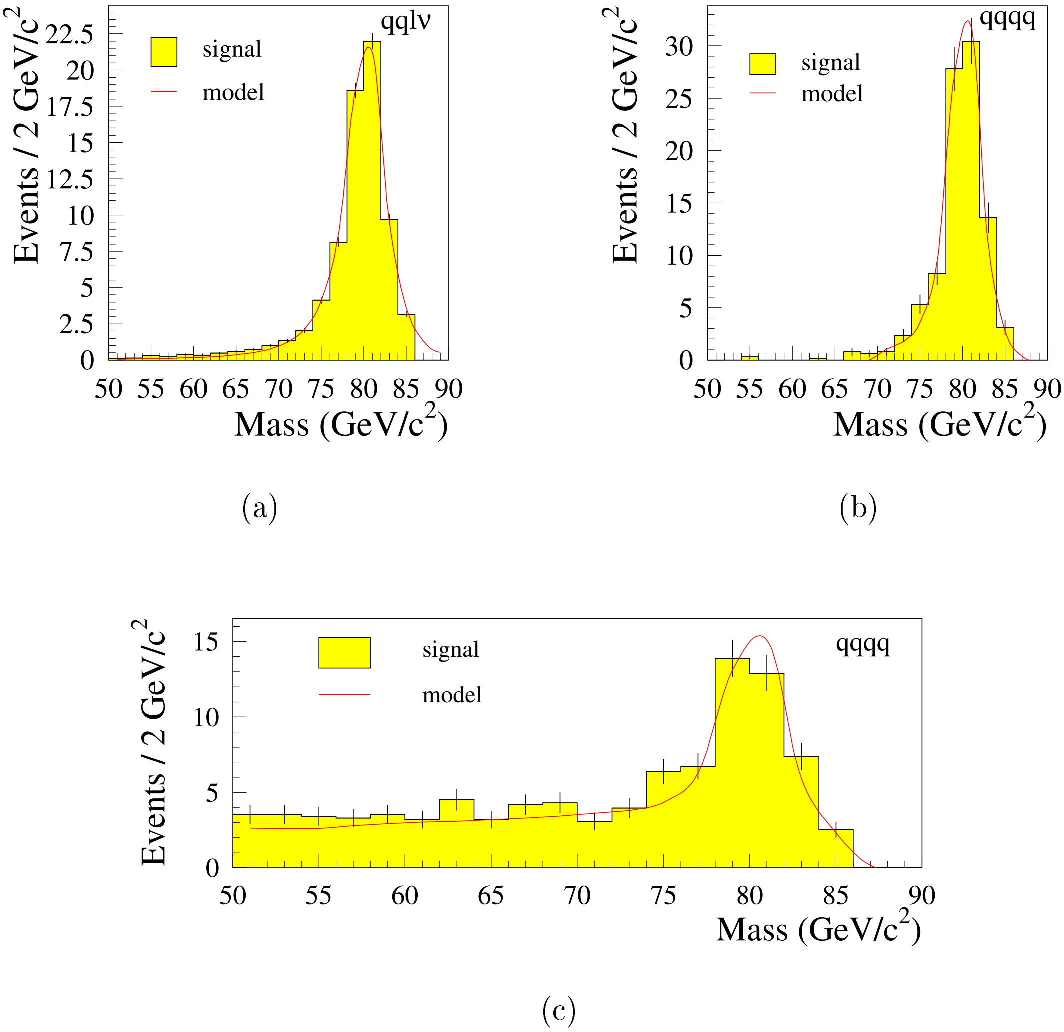

Figure 6.7: The model is compared to W^+W^- events in the $l\overline{\nu}_l q\bar{q}'$ channel (a), the true mass solution in the $q\bar{q}'\bar{q}q'$ channel (b), and a randomly chosen mass solution in the $q\bar{q}'\bar{q}q'$ channel (c).

simulation events knowledge of which are the correct jet pairings[8]. Figure (c) shows the same distribution where the mass solution shown has been chosen randomly. The mass distribution in Figure (c) is described by the sum of two components: the first describes the correct mass solution with Equation 6.14, and the second describes the wrong mass solutions. The wrong mass solution is extracted from simulation (see Section 6.8.2). The relative normalisation of the two components is discussed in Section 6.6.2.

[8]The correct mass solution was determined using the same procedure as in Section 4.5.3.

6.6 W $\rightarrow$q$\bar{\text{q}}'\bar{\text{q}}q'$ Assignment

6.6.1 How to Choose the Best Pairing

In the q$\bar{\text{q}}'\bar{\text{q}}q'$ final state, we reconstruct four hadronic jets. To form the invariant mass of the two W bosons, we must select a pairing of these jets from the three possible combinations[9]. For simulation events at 172 GeV we show in Figure 6.8, the distribution of the correct and incorrect mass combinations. Here we consider a range of methods for obtaining the correct jet pairings from the possible combinations (i). The mass values obtained after performing a 4C kinematic fit are denoted m_{i1}^{4C}, m_{i2}^{4C} and the mass from a 5C fit m_i^{5C}. In this study, the reference mass m_{ref} was taken as the generated value of $\mathrm{M_W}$ for the simulation events. The results of the study are provided in Table 6.3.

Name	Discriminant	Performance
Random	choose a random combination	33%
$\chi^2{}_{5C}$	minimum χ^2 from 5C kinematic fit	$68 \pm 0.5\%$
Mass Difference	minimum $\left\|m_{i1}^{4C} - m_{i2}^{4C}\right\|$	$52 \pm 0.6\%$
m_{ref}^{4C}	minimum $[(m_{i1}^{4C} - m_{ref})^2 - (m_{i1}^{4C} - m_{ref})^2]$	$80 \pm 0.4\%$
m_{ref}^{5C}	minimum $\left\|m_i^{5C} - m_{ref}\right\|$	$82 \pm 0.4\%$

Table 6.3: The results of a study on how best to select the correct jet-pairings combination in q$\bar{\text{q}}'\bar{\text{q}}q'$ events.

It is clear that the use of a (correct) reference mass can greatly improve the accuracy of the selection. Though it is vital to demonstrate that the use of a reference mass does not bias the final result of the fitting procedure, this can be achieved using an iterative procedure for the reference mass.

[9]Note that the three possible combinations are not independent. We take the idealised case where *(i)* the Energy and momentum of each jet is the same after each of the three solution kinematic fits and *(ii)* that the 5C fit mass squared is the average of the two 4C masses squared. The three 5C fit mass solutions we label m_1, m_2 and m_3. We find

$$2(m_1^2 + m_2^2 + m_3^2) = s$$

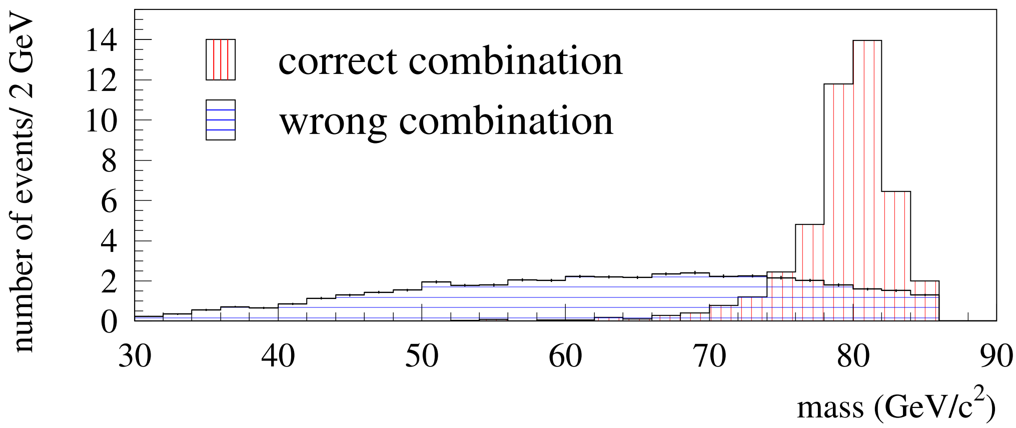

Figure 6.8: The reconstructed mass distribution after a 5C fit is shown for $W^+W^-\rightarrow q\bar{q}'\bar{q}q'$ simulation events. The distribution when the correct jet pairing has been chosen is contrasted with the distribution when one of the incorrect pairings is used. The plot is normalised to 10 pb^{-1}.

6.6.2 Choose All the Pairings

It is unnecessary to make a decision on the best pairing: an alternative approach is to take all three solutions. We could include all three solutions, ascribing to each a probability (C_i) of $\frac{1}{3}$. We are now sure to have included the correct combination, but at the cost of greatly increasing the background: for every true mass solution we have included two wrong solutions. A comparative study showed that this approach gives similar results to one in which only one solution is chosen with the χ^2 method.

In this analysis, we use a combination of these two approaches, which reduces the statistical error of the method by approximately 20%. We include all three solutions, but with different weights. One of the solutions must represent the correct jet combination: thus we require the sum of the weights to be unity:

$$C_1 + C_2 + C_3 = 1$$

The probability of each event as a function of mass is described in the signal event model. The normalisation procedure we apply to this signal event model (Equation 6.15) requires that the solution weight (C_i) is not a function of the mass. Consulting

Table 6.3, we choose to use the ${\chi^2}_{5C}$ measure in setting the solution weights. We set:

$$C_i = \frac{\chi^2\ Prob(m_i)}{\chi^2\ Prob(m_1) + \chi^2\ Prob(m_2) + \chi^2\ Prob(m_3)}$$

where $\chi^2\ Prob(m_i)$ is the χ^2 probability for the given mass solution, assuming that the fit has five degrees of freedom. From W^+W^- simulation events, we find that this procedure gives a weight of < 0.05 to only 12% of the correct mass solutions, compared with 64% of the wrong mass solutions. Using simulation $q\bar{q}$ events, we have checked that no correlation is observed between the weights obtained by this procedure and the reconstructed event mass.

6.7 Purity

Having applied the selection criteria in the $\mathrm{l}\overline{\nu}_\mathrm{l}\mathrm{q}\bar{\mathrm{q}}'$ analysis, we obtained samples of high purity. The purity is the probability of a selected event being a signal (*i.e.* $W^+W^- \rightarrow \mathrm{l}\overline{\nu}_\mathrm{l}\mathrm{q}\bar{\mathrm{q}}'$) event. In the range over which we fit the W mass (70 to 85 GeV/c^2), the purities are 94% for the electron search, 98% for the muon search and 82% for the tau search.

However, having applied all the selection criteria in the $\mathrm{q}\bar{\mathrm{q}}'\bar{\mathrm{q}}\mathrm{q}'$ analysis a purity of only 74% is obtained. Furthermore, it is clear from Figure 4.9 (c) that the purity of the selected events is a rapidly varying function of the D_{gluon} variable. Rather than imposing a constant purity for all the selected events, the purity distribution can be modelled as a function of D_{gluon}. Thus, on an individual event basis, we have a measure of the probability that a given event is a W^+W^- event. We could now include events that were not used in the Cross-Section analysis, giving these events lower weights. However, for consistency, we choose to apply the same event selection in this section of the analysis as has been used in previous chapters.

We choose to model the purity Pur_D with the simple functional form

$$Pur_D(x) = \frac{f(x)}{1 + f(x)}$$

where $f(x)$ is the third degree polynomial

$$f(x) = ax + bx^2 + cx^3$$

In Figure 6.9 we show the result of modelling the D_{gluon} distribution with this function.

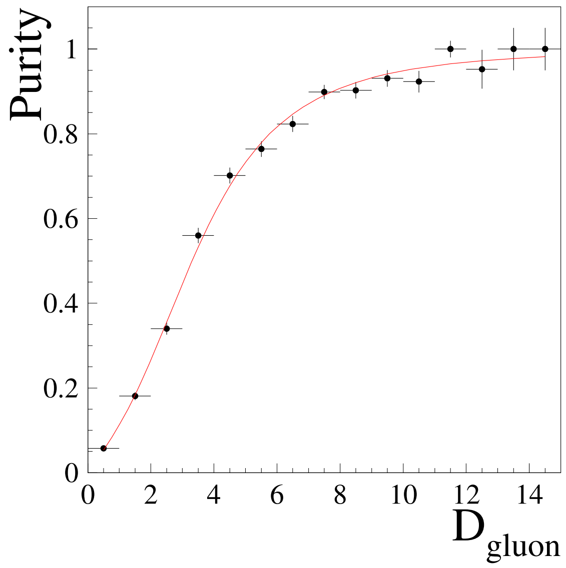

Figure 6.9: Purity of selected events in the $q\bar{q}'\bar{q}q'$ channel, as a function of the D_{gluon} variable in the $q\bar{q}'\bar{q}q'$ channel. The purity evaluated in simulation events is shown with points and statistical error bars, the solid line indicates the fitted function.

6.8 Background and Wrong Mass Solutions

6.8.1 Background

We attempted to describe the background distributions with a range of simple functions, but an accurate description of the background was not achieved. Instead, we choose to extract the background distributions from the simulation events. The background processes are discussed in Chapter 4; the dominant process in the fully-hadronic and semi-leptonic channels is $Z/\gamma \rightarrow q\bar{q}(\gamma)$ events, four-fermion final state diagrams also contribute.

Since the simulation statistics in the $l\overline{\nu}_l q\bar{q}'$ decay channel, after the full event selection has been applied, are not large we first apply a smoothing algorithm. The algorithm used is the HBOOK [92] smoothing algorithm QUAD which is based on multiquadratic radial basis functions. The results of this procedure are shown in Figure 6.10. The background event distribution shapes were found to be compatible within statistics for the three separate decay channels ($\mu\overline{\nu}_\mu q\bar{q}'$, $e\overline{\nu}_e q\bar{q}'$,$\tau\overline{\nu}_\tau q\bar{q}'$). The event selection process has biased the selected events towards high masses, the peak of the distribution lying at 72 GeV/c^2.

We apply the same procedure to the background events in the $q\bar{q}'\bar{q}q'$ event channel. Naturally, the event selection procedure has favoured the selection of events with high mass solutions.

6.8.2 Wrong Mass Solutions

When we select the incorrect jet-pairings in the $q\bar{q}'\bar{q}q'$ decay channel, we obtain a mass which is only very weakly dependent upon the W mass. We choose to extract this mass distribution from the simulation events. We use the generated information to identify the correct mass solutions. Again, we smooth the distribution when extracting it. The smoothing procedure helps prevent numerical instabilities occurring during the fitting procedure.

6.9 Probability Description

6.9.1 Maximum Likelihood Expression

Throughout this chapter, we have described the individual components of our event model. In the following sections, we describe how to combine this information to produce a probability density function $Prob_i$ for each event.

These probabilities are then combined using the maximum likelihood estimator. We form a likelihood probability of observing the data set:

$$L = \Pi_i Prob_i$$

and then maximise this likelihood in terms of the required parameter M_W. This expression assesses the likelihood of observing a set of event masses m_{evt}, given the parameter M_W.

Notes on the numerical implementation of this method are given at the end of this chapter in Section 6.14

6.9.2 $l\bar{\nu}_l q\bar{q}'$ Decay Channel Probability

Procedure

We wish to produce a probability density function *prob* which describes the likelihood of observing an event at a given m_{evt}. Treating M_W and the event resolution as constants, we choose to represent the probability density function (p.d.f.) by :

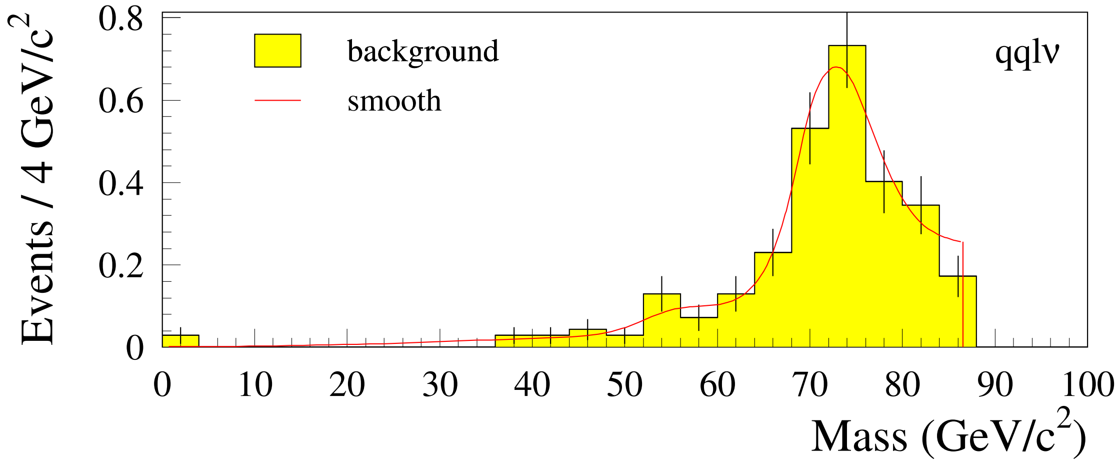

(a)

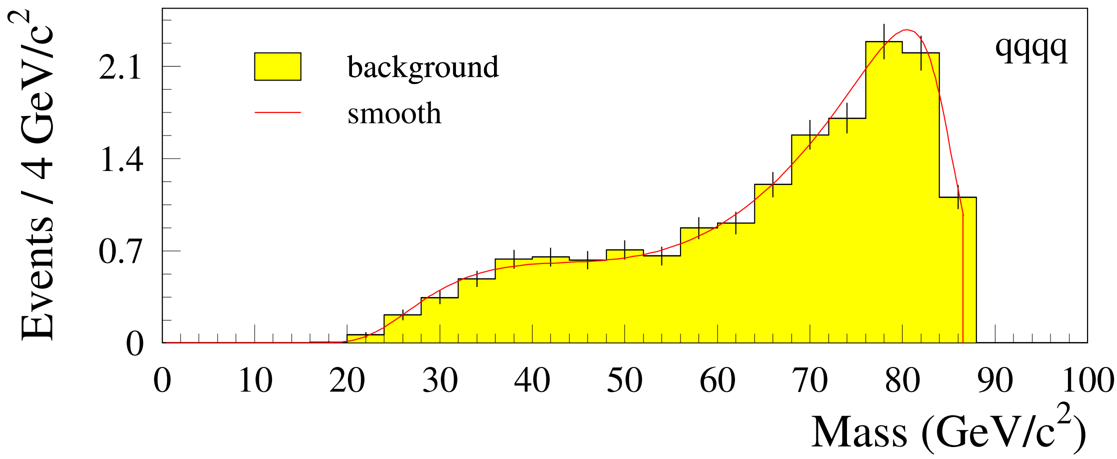

(b)

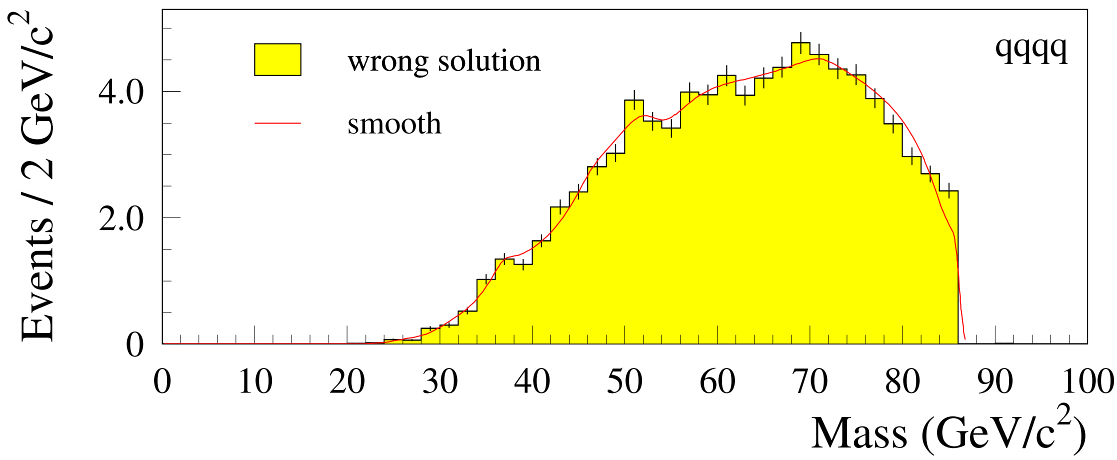

(c)

Figure 6.10: (a) and (b) show the reconstructed mass in simulation background events for the combined $l\overline{\nu}_l q\bar{q}'$ decay channel and for the $q\bar{q}'\bar{q}q'$ decay channel. (c) shows the reconstructed mass distribution for $W^+W^- \rightarrow q\bar{q}'\bar{q}q'$ simulation events when the wrong jet-pairings have been taken. The solid line indicates the distribution obtained when a smoothing algorithm is applied. The plots are normalised to 10 pb^{-1}.

$$Prob(\mathrm{m_{evt}}; \mathrm{M_W}, \sigma_{\mathrm{evt}}) = Pur \times Sig \ + \ (1 - Pur) \times \ Bck$$

- Pur: Global Event Purity (see Section 6.7). We use a constant value independent of $\mathrm{m_{evt}}$ or other event variables. For each semi-leptonic event it takes one of three discrete values, depending on whether the event was selected by the electron, muon or tau search analysis stream.

- $Bck(\mathrm{m_{evt}})$: Background Event Model (see Section 6.8.1). This is a probability density function with $\mathrm{m_{evt}}$ which is extracted from the simulation.

- $Sig(\mathrm{m_{evt}}; \mathrm{M_W}, \sigma_{\mathrm{evt}})$: Signal Event Model (see Section 6.5). This is a probability density function with $\mathrm{m_{evt}}$ for the expected distribution of signal ($\mathrm{W^+W^-}$) events. We choose to model the signal probability as the convolution of two functions:

$$Sig(\mathrm{m_{evt}}; \mathrm{M_W}, \sigma_{\mathrm{evt}}) = Res \otimes Phys$$

- $Res(\mathrm{m_{evt}} - m', \sigma_{\mathrm{evt}})$: Resolution Function (see Section 6.5). This describes detector and reconstruction effects. m' is a dummy integration variable. The resolution function also depends upon the rescaled kinematic fit mass error σ_{evt}.

- $Phys(m', \mathrm{M_W})$: Physics Function (see Section 6.3). This describes the underlying physics distribution for the true average event mass in $\mathrm{W^+W^-}$ events. It is through this function that the probability obtains its $\mathrm{M_W}$ dependence. m' is a dummy integration variable.

In order that we can identify $Prob$ as a p.d.f., we impose the normalisation condition :

$$\int_{Rng_{dn}}^{Rng_{up}} Prob(\mathrm{m_{evt}}; \mathrm{M_W}, \sigma_{\mathrm{evt}}) \ d\mathrm{m_{evt}}|_{\mathrm{M_W}, \sigma_{\mathrm{evt}}} = 1$$

i.e. the probability that the observed event mass lies within the integration range (Rng_{dn} to Rng_{up}) is unity. This condition must hold for any value of the parameter $\mathrm{M_W}$.

We achieve this by setting :

$$\int_{Rng_{dn}}^{Rng_{up}} Res \otimes Phys \; d\mathrm{m}_{\mathrm{evt}} \;|_{\mathrm{M_W},\sigma_{\mathrm{evt}}} = 1 \tag{6.15}$$

and define $Bck(\mathrm{m}_{\mathrm{evt}})$ by:

$$\int_{Rng_{dn}}^{Rng_{up}} Bck(\mathrm{m}_{\mathrm{evt}}) \; d\mathrm{m}_{\mathrm{evt}} = 1 \tag{6.16}$$

Description

The probability density function for a typical event is shown in Figure 6.11, the integral of the distribution is one. The model consists of two components *(i)* the background description and *(ii)* the signal description. The background model is a fixed component and is independent of $\mathrm{M_W}$. As $\mathrm{M_W}$ varies, the position of the peak in the signal component moves to reflect this variation. The signal component is described by the underlying physics function and a resolution function. In a typical event, the resolution function width is of similar size to that of the physics function.

We include in the $\mathrm{M_W}$ fit only events with masses lying in the range 70 GeV/c^2 to 85 GeV/c^2, and set the integration range (Rng_{dn} to Rng_{up}) accordingly. Events lying outside this range carry little information about the W mass. Restricting the mass range of the $\mathrm{M_W}$ fit helps reduce the biases and non-linearities in the method.

6.9.3 $\mathrm{q\bar{q}'\bar{q}q'}$ Decay Channel Probability

Procedure

For each event, we measure three mass solutions $\mathrm{m}_{\mathrm{evt}i}$ $(i = 1, 2, 3)$ and corresponding event resolutions σ_{evt}. In addition, we use the value of the D_{gluon} variable in our probability model. We form the event probability $Prob$ from the sum of separate p.d.f.s for the three mass solutions $Prob_i$.

$$Prob(\mathrm{m}_{\mathrm{evt1}}, \mathrm{m}_{\mathrm{evt2}}, \mathrm{m}_{\mathrm{evt3}}; \mathrm{M_W}, D_{gluon}, \sigma_{\mathrm{evt1}}, \sigma_{\mathrm{evt2}}, \sigma_{\mathrm{evt3}}, \chi^2_1, \chi^2_2, \chi^2_3)$$

$$= \frac{1}{3}(Prob_1 + Prob_2 + Prob_3)$$

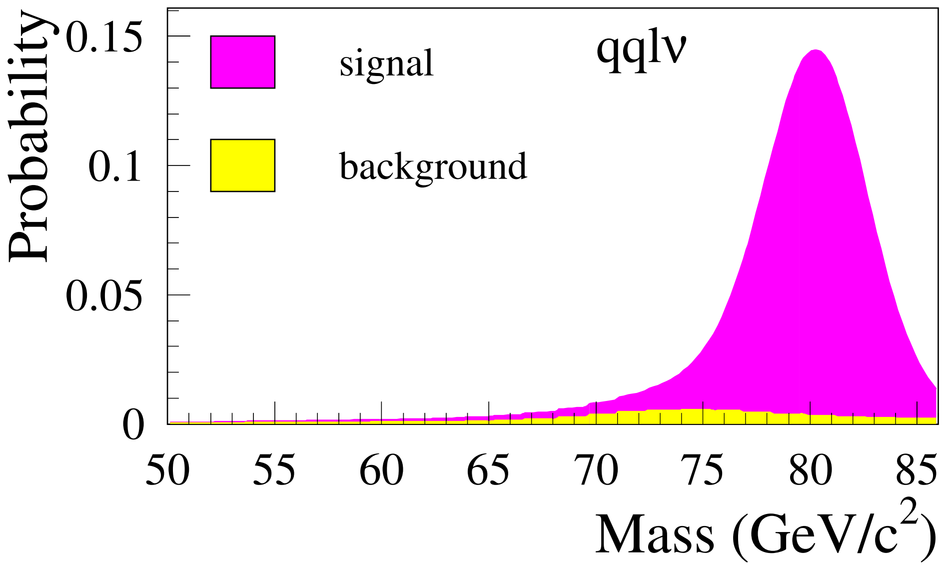

Figure 6.11: An example probability density function in the semi-leptonic channel. The plot shows the probability density of obtaining an event with a given mass. The integral of the plot is one.

We choose to model only one-dimensional mass distributions: that is, each of the probability models P_i is independent of the other two mass solutions. These p.d.f.s are each modelled by the same form as that used in the $\mathrm{l}\overline{\nu}_\mathrm{l}\mathrm{q}\bar{\mathrm{q}}'$ channel:

$$Prob_i(\mathrm{m}_{\mathrm{evt}(i)}; \mathrm{M_W}, \sigma_{\mathrm{evt}(i)}, D_{gluon}) = Pur_D \times Sig_i \; + \; (1 - Pur_D) \times \; Bck_i$$

However, the modelling of the individual terms in this expression have now changed.

- $Pur_D(D_{gluon})$: Event Purity (see Section 6.7). For the fully-hadronic events, it is a continuous variable and is a function of the D_{gluon} value of the event.

- $Bck_i(\mathrm{m}_{\mathrm{evt}(i)})$: Background Event Model (see Section 6.8.1). This is a probability density function with $\mathrm{m}_{\mathrm{evt}(i)}$ which is extracted from the simulation.

- $Sig_i(\mathrm{m}_{\mathrm{evt}(i)}; \mathrm{M_W}, \sigma_{\mathrm{evt}(i)})$: Signal Event Model (see Section 6.5). This is a probability density function with $\mathrm{m}_{\mathrm{evt}}$ for the expected distribution of signal events.

We build this probability from a normalisation factor and a description of the mass of the true jet pairings and those of the wrong combination solutions.

$$Sig_{(i)}(\mathrm{m}_{\mathrm{evt}(i)}; \mathrm{M_W}, \sigma_{\mathrm{evt}(i)}, \chi_1^2, \chi_2^2, \chi_3^2) = C_i \times Sig_{true\ sol} \ + \ (1 - C_i) \times Sig_{wrong\ sol}$$

- $C_i(\chi_1^2, \chi_2^2, \chi_3^2)$: $\mathrm{W^+W^-}$ true combination normalisation factor (see Section 6.6.2). This provides the only connection in our model between the three solutions. The solutions are connected through the constraint:

$$C_1 + C_2 + C_3 = 1$$

- $Sig_{wrong\ sol}(\mathrm{m}_{\mathrm{evt}(i)})$:Wrong Mass Solutions Model (see Section 6.8.2). This is a probability density function with $\mathrm{m}_{\mathrm{evt}(i)}$ which is extracted from the simulation.

- $Sig_{true\ sol}(\mathrm{m}_{\mathrm{evt}(i)}; \mathrm{M_W}, \sigma_{\mathrm{evt}(i)})$:Correct Mass Solutions Model (see Section 6.5). As in the $\mathrm{l}\overline{\nu}_\mathrm{l}\mathrm{q}\bar{\mathrm{q}}'$ channel, we choose to model this as the convolution of two functions:

$$Sig(\mathrm{m}_{\mathrm{evt}i}; \mathrm{M_W}, \sigma_{\mathrm{evt}i}) = Res \otimes Phys$$

- $Res(\mathrm{m}_{\mathrm{evt}(i)} - m', \sigma_{\mathrm{evt}(i)})$, $Phys(m', \mathrm{M_W})$: The resolution function and the $\mathrm{M_W}$ dependent Physics function. These terms are as defined in the $\mathrm{l}\overline{\nu}_\mathrm{l}\mathrm{q}\bar{\mathrm{q}}'$ description above.

We now identify $Prob$ as a three-dimensional probability density function and impose the normalisation condition:

$$\int_0^{E_{beam}} \int_0^{E_{beam}} \int_0^{E_{beam}} Prob \ d\mathrm{m}_{\mathrm{evt}1} d\mathrm{m}_{\mathrm{evt}2} d\mathrm{m}_{\mathrm{evt}3} = 1$$

We achieve this by setting the same constraints as above (Equations 6.15 and 6.16) for the true combination signal model and the background model. In addition we require:

$$\int_0^{E_{beam}} Sig_{wrong\ sol}(\mathrm{m}_{\mathrm{evt}(i)}) \ d\mathrm{m}_{\mathrm{evt}(i)} = 1$$

Description

In Figure 6.12, we illustrate the event probability model that we developed above. The upper plot presents the corresponding distribution for the $q\bar{q}'\bar{q}q'$ channel that we presented in Figure 6.11 for the $l\overline{\nu}_l q\bar{q}'$ decay channel. This plot (a) shows the probability density function ($Prob_i$) of only one of the three mass solutions. The correct mass solution component moves as M_W varies. There are now two fixed components due to: *(i)* the background events;*(ii)* the wrong mass solutions. For a typical event, the 'fixed' component is larger than in the $l\overline{\nu}_l q\bar{q}'$ channel. In the $q\bar{q}'\bar{q}q'$ channel, the purity of the expected events is lower than in the $l\overline{\nu}_l q\bar{q}'$ channel and hence the background component is larger. The wrong solution component is, of course, specific to the $q\bar{q}'\bar{q}q'$ channel.

The lower plot (b) shows how the full event probability ($Prob$) varies as a function of M_W. We have chosen an event in which the three mass solutions obtained are 20, 50 and 80 GeV/c^2. Three peaks are observed on the plot around the position of these event masses. As already noted, the background component of the description of each mass solution is independent of M_W. The background component gives rise to the flat tails observed for the three mass solutions.

In the $q\bar{q}'\bar{q}q'$ channel we do not restrict the allowed range of the three mass solutions. We do not wish to restrict the mass range of the incorrect jet-pairing solutions and since *a priori* we do not know which is the correct mass solution we choose to place no event mass restrictions. Accordingly, we set the integration range of the normalisation condition (see above) as 0 to E_{beam}.

6.10 Calibration

The semi-analytic mass fitting method described in this chapter must be calibrated with simulation samples. We produce event samples of simulation events comprised of the same number of events as observed in the data. The samples are comprised of a mixture of signal (W^+W^-) events and background ($Z\gamma \rightarrow q\bar{q}(\gamma)$) events. The relative proportions of these components are set by the purity values of the event selections as determined in Chapter 4. The number of background events in the samples is allowed to fluctuate in the appropriate statistical manner. Samples were

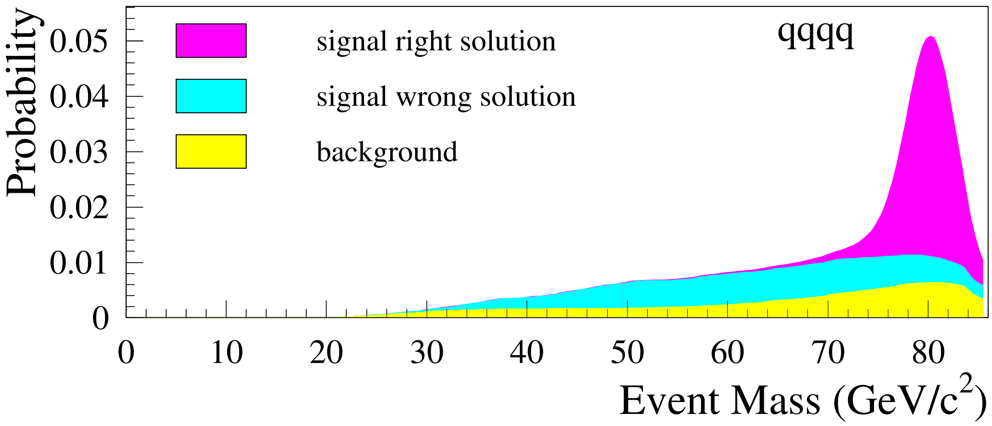

(a)

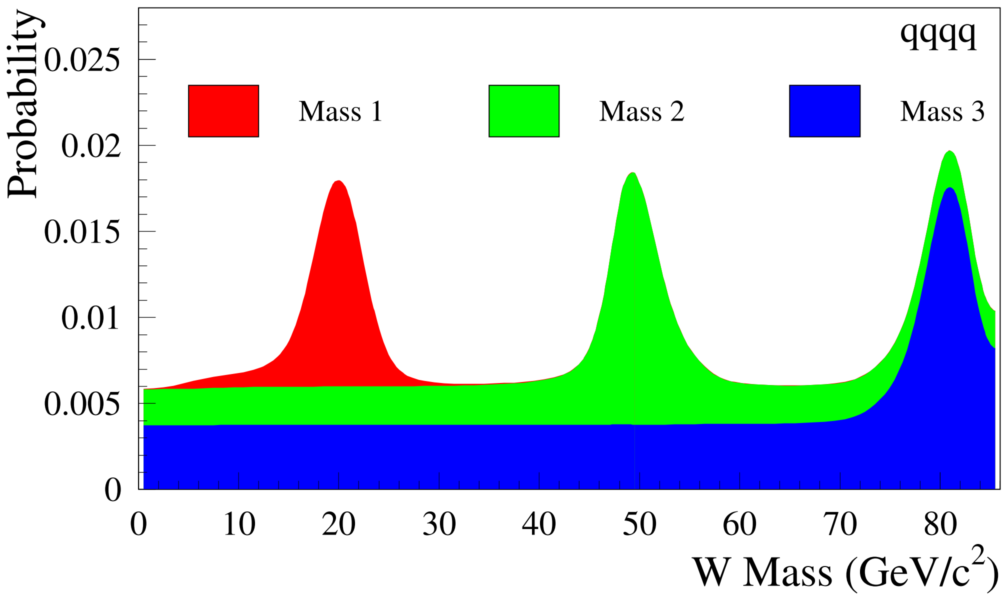

(b)

Figure 6.12: The plot (a) shows the single mass solution probability density function for obtaining an event with a given reconstructed mass in the $q\bar{q}'\bar{q}q'$ decay channel . The integral of the plot is unity. In Figure (b) the total $q\bar{q}'\bar{q}q'$ event probability is shown as M_W is varied. Three peaks are seen in the distribution corresponding to the three masses reconstructed in an example event.

produced where the W^+W^- component was generated with M_W varying in 250 MeV/c^2 steps from 78.35 to 82.35 GeV/c^2.

The absolute scale of the kinematic fit errors (see Section 6.4.2) was determined by tuning the fit on the simulation samples. We define a pull:

$$pull = \frac{M_{W_{fit}} - M_{W_{true}}}{\Delta_{fit}}$$

where $M_{W_{true}}$ is the generated value of the W mass in the simulation sample, $M_{W_{fit}}$[10] is the mass value returned by the fitting algorithm, and Δ_{fit} is the error on this mass returned by the fitting algorithm. In all channels of this analysis, the kinematic fit error scale was tuned such that a pull distribution r.m.s. of one, to an accuracy of $\pm 3\%$, was obtained. The pull distributions were found to be compatible with unit width Gaussians. The pull distribution r.m.s. was also checked as a function of the error obtained on the fitted samples. This distribution is shown for the combined semi-leptonic channel in Figure 6.14.

Any bias or non-linearity in the mass fitting method can also be removed using the simulation samples. In Figure 6.13, we show the results obtained from fitting the simulation samples for the combined semi-leptonic and the fully-hadronic analyses. The fitted W mass of the event samples is plotted against the true W mass and the best fit straight line through the points is indicated. In all channels, the fitted masses are found to be compatible with lying on a straight line. We fit the line using the χ^2 procedure. We parameterise the line as:

$$M_{W_{fit}} - 80.43 = b \times (M_{W_{true}} - 80.43) + C$$

The non-linearity and biases are due to inaccuracies in the probability model. The calibration curve is found to be sensitive to the form of the model used to describe the W^+W^- signal events and to the detector resolution error tuning in this model.

The calibration curve values are presented in Table 6.4. In the semi-leptonic channels, careful tuning of the fit has resulted in gradient values compatible with one, and relatively small bias values (c.f. [67]). However, in the $q\bar{q}'\bar{q}q'$ decay channel

[10] The calibration curve, as discussed in this section, is accounted for when calculating $M_{W_{fit}}$.

obtaining a precise model of the event probability is more difficult due to the presence of multiple mass solutions. We obtain linearities and biases compatible with those observed in [67].

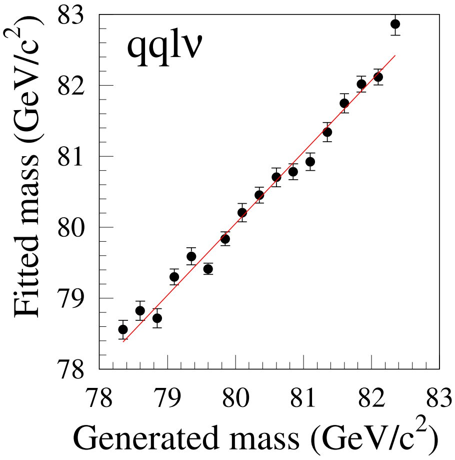

(a)

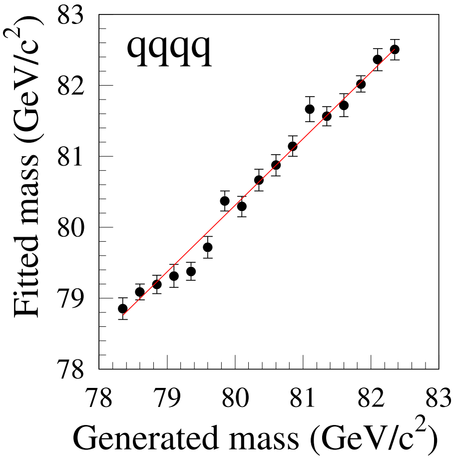

(b)

Figure 6.13: The fitted mass is shown against the generated W mass for simulation event samples in the combined semi-leptonic (a) and the fully-hadronic (b) decay channels.

	$\mathrm{e}\overline{\nu}_{\mathrm{e}}\mathrm{q}\bar{\mathrm{q}}'$	$\mu\overline{\nu}_{\mu}\mathrm{q}\bar{\mathrm{q}}'$	$\mathrm{l}\overline{\nu}_{\mathrm{l}}\mathrm{q}\bar{\mathrm{q}}'$	$\mathrm{q}\bar{\mathrm{q}}'\bar{\mathrm{q}}\mathrm{q}'$
linearity b	0.98 ± 0.03	1.03 ± 0.04	1.01 ± 0.02	0.94 ± 0.03
bias C	0.11 ± 0.04	0.05 ± 0.05	0.05 ± 0.03	0.28 ± 0.04

Table 6.4: Calibration procedure results in the different channels of the direct reconstruction analysis. The linearity b and bias C are defined in the text.

6.11 Systematic Errors

In this section, we discuss all the components of the systematic error that have been considered in the direct reconstruction analysis. The components of the error are summarised in Table 6.5.

In the fitting procedure described above, the signal contribution is modelled by an analytic function. However, the background distribution, the wrong $\mathrm{q}\bar{\mathrm{q}}'\bar{\mathrm{q}}\mathrm{q}'$ channel jet pairings solutions and the purity are all extracted from simulation. Furthermore, the method is calibrated with simulation samples. We must include in the systematic

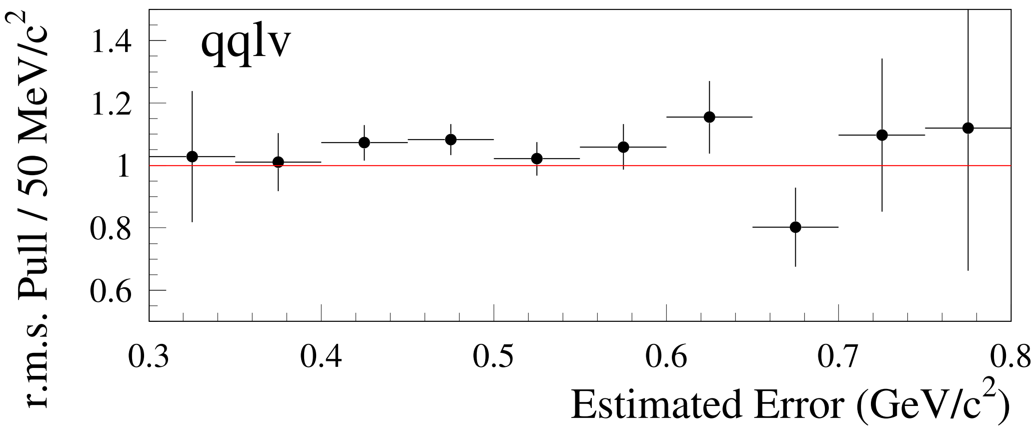

Figure 6.14: The r.m.s. of the pull of the M_W fit as a function of the fitted error. on a set of sample simulation samples in the $l\overline{\nu}_l q\bar{q}'$ channel.

error uncertainties to account for possible differences between the simulation and the data.

The uncertainties on the calibration correction procedure were calculated. These are due to the simulation statistics and are uncorrelated between channels.

The possible systematic error from the description of the response of the DELPHI detector to the hadronic system has been studied by my DELPHI collaborators [67]. Using the data collected at the Z resonance during 1996, discrepancies between the energy flow measurement in hadronic decays were evaluated and parameterised as a function of the polar angle. These discrepancies were then implemented in the simulation events. This leads to changes in the calibration correction of up to 30 MeV/c^2, which has been included in the systematic error. The effect is taken as 50% correlated between the semi-leptonic and fully-hadronic channels. This is due to the different impact of the jet energy measurement after the constrained fit.

This error was also evaluated in a complementary manner by the author. Event samples were generated where the charged energy of the jets was allowed to vary by $\pm 2\%$ and the neutral energy by $\pm 5\%$. Furthermore, the event selection and the track reconstruction efficiency were varied within their estimated errors.

The systematic uncertainty on the muon momentum and on the electron momentum were applied to the simulation events. The kinematic fit and mass fitting procedure were then applied to these events. The change in the fitted value of M_W is used as a systematic error.

The impact of an incorrect description in the simulation of the jet fragmentation was considered. This error was studied by comparing simulation samples generated with the `JETSET` and the `ARIADNE` parton shower description. This study was performed for both the signal and background events. For the W^+W^- events, we rely upon a `FASTSIM` study performed by my DELPHI collaborators [66].

The impact of the background on the semi-leptonic channel is very small; the result is insensitive to changes in both the level and shape of the background. Changing the number of background events in the $q\bar{q}'\bar{q}q'$ channel samples by $\pm10\%$ results in the error listed in Table 6.5.

The systematic error coming from the uncertainty of the simulation of initial state radiation was assigned to be 10 MeV/c^2 [27], fully correlated between the channels.

The effects of the interference between the `CC03` diagrams and the additional diagrams (See Section 5.7) on the reconstructed value of M_W was found to be small except in the $e\overline{\nu}_e q\bar{q}'$ channel. We ascribe a systematic error of 10 MeV/c^2 to the $\mu\overline{\nu}_\mu q\bar{q}'$ $\tau\overline{\nu}_\tau q\bar{q}'$ and the $q\bar{q}'\bar{q}q'$ decay channels. The electron channel is more affected due to interference with single W production.

The systematic uncertainty on the beam energy is 30 MeV/c^2, which corresponds to a systematic error on M_W of 30 MeV/c^2.

We choose to ascribe a 100 MeV/c^2 uncertainty to M_W in the $q\bar{q}'\bar{q}q'$ decay channel due to the Colour Reconnection and Bose Einstein interconnection phenomena (see Section 1.5). Again, we remind the reader that larger values cannot currently be excluded.

6.12 Results

The direct reconstruction analysis was performed on the 172 GeV data samples. Results are obtained for the $e\overline{\nu}_e q\bar{q}'$ search stream, the $\mu\overline{\nu}_\mu q\bar{q}'$ search stream, the $l\overline{\nu}_l q\bar{q}'$ combined semi-leptonic channel (including the $\tau\overline{\nu}_\tau q\bar{q}'$ search stream) and the $q\bar{q}'\bar{q}q'$ channel.

Error Source	$e\overline{\nu}_e q\bar{q}'$	$\mu\overline{\nu}_\mu q\bar{q}'$	$l\overline{\nu}_l q\bar{q}'$	$q\bar{q}'\bar{q}q'$	All
Calibration	50	60	60	50	40
Detector Jets	30	30	30	40	30
Lepton Energy	60	60	40	0	20
Fragmentation Signal	10	10	10	25	15
Fragmentation Background	0	0	0	10	5
Background Level	5	5	5	15	10
ISR	10	10	10	10	10
Four-Fermion Interference	50	10	25	10	15
TOTAL	99	92	83	72	60
Beam Energy	30	30	30	30	30
Interconnection Effects	0	0	0	100	45

Table 6.5: The components of the systematic error in the W mass direct reconstruction analysis in MeV/c^2. The components due to the DELPHI detector and simulation events are listed separately from the other components.

In each channel, we obtain two estimates of the statistical error: *(i)* that from the average expected error on the simulation samples, and *(ii)* that from fitting the observed data sample. The first is the error from a truly frequentist statistics approach, while the second is from a more Bayesian approach. Both the expected errors and the fit errors are reliable estimates of the W mass error. In Figure 6.15, we show the expected errors from the simulation and the fit errors on the data in the combined $l\overline{\nu}_l q\bar{q}'$ and the $q\bar{q}'\bar{q}q'$ decay channels; the errors are shown before applying the calibration procedure. The two values of the statistical errors for each of the four channels are provided in Table 6.6. In the results quoted below, we cautiously choose to use the larger of the two results for each decay channel.

The one standard deviation statistical errors are calculated in the conventional manner, from the parameter values which lead to a change in the log-likelihood of half a unit from its minimum value [93]. We plot the log-likelihood curves in a form which has comparable properties with the familiar χ^2 test. We define a $\Delta\chi^2$ value:

$$\Delta\chi^2(\mathrm{M_W}) = -\Sigma_k \; 2 \; ln \; L_k(\mathrm{M_W}) \; + \; \Sigma_k \; 2 \; ln \; L_k(\mathrm{M_{W\;\mathit{max}}})$$

where L is the likelihood and the sum runs over all the observed data events. $\mathrm{M_{W\;\mathit{max}}}$ is the value of $\mathrm{M_W}$ which maximises the likelihood of the data sample. This $\Delta\chi^2$ quantity is plotted in Figure 6.16 as a function of $\mathrm{M_W}$ for the combined $l\overline{\nu}_l q\bar{q}'$ decay channel (Figure (a)) and for the $q\bar{q}'\bar{q}q'$ decay channel (Figure (b)).

The final results of the direct reconstruction analysis are as follows. In addition to the statistical and DELPHI systematic errors, we give separately the statistical error due to the LEP beam energy determination (marked LEP) and the statistical error due to interconnection effects (marked int.).

$e\overline{\nu}_e q\bar{q}'$ Decay Channel

$$M_W = 80.31 \pm 1.08 \text{ (stat.)} \pm 0.10 \text{ (syst.)} \pm 0.03 \text{ (LEP) GeV/c}^2$$

$\mu\overline{\nu}_\mu q\bar{q}'$ Decay Channel

$$M_W = 80.39 \pm 0.72 \text{ (stat.)} \pm 0.09 \text{ (syst.)} \pm 0.03 \text{ (LEP) GeV/c}^2$$

$l\overline{\nu}_l q\bar{q}'$ Decay Channel

$$M_W = 80.59 \pm 0.58 \text{ (stat.)} \pm 0.08 \text{ (syst.)} \pm 0.03 \text{ (LEP) GeV/c}^2$$

$q\bar{q}'\bar{q}q'$ Decay Channel

$$M_W = 79.18 \pm 0.62 \text{ (stat.)} \pm 0.07 \text{ (syst.)} \pm 0.10 \text{ (int.)} \pm 0.03 \text{ (LEP) GeV/c}^2$$

This value is two standard deviations below the current world average W mass and one standard deviation below the published DELPHI result on this data sample [67].

All Channels Combined

This value is calculated from a weighted average of the $l\overline{\nu}_l q\bar{q}'$ and $q\bar{q}'\bar{q}q'$ decay channel results.

$$M_W = 79.93 \pm 0.42 \text{ (stat.)} \pm 0.06 \text{ (syst.)} \pm 0.05 \text{ (int.)} \pm 0.03 \text{ (LEP) GeV/c}^2$$

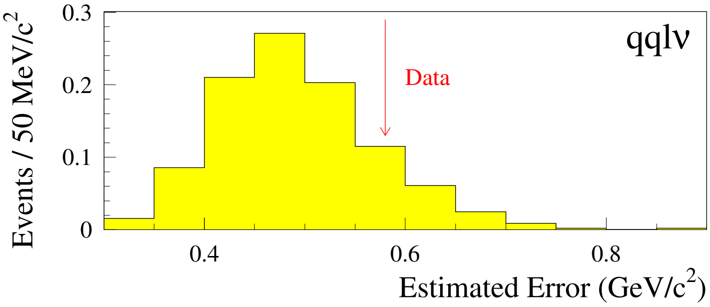

(a)

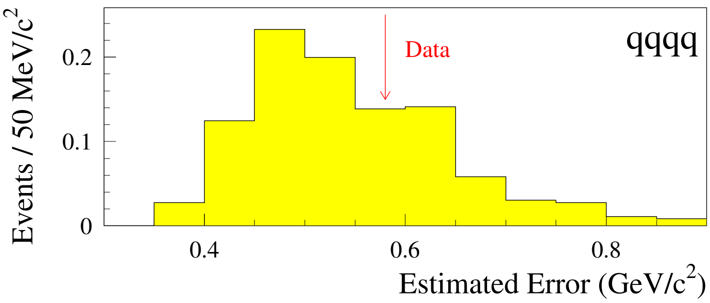

(b)

Figure 6.15: The expected error on M_W from fitting simulation samples is shown in (a) for the combined semi-leptonic channel, and (b) for the fully-hadronic channel. The error obtained on fitting the data is indicated.

	$e\overline{\nu}_e q\bar{q}'$	$\mu\overline{\nu}_\mu q\bar{q}'$	$l\overline{\nu}_l q\bar{q}'$	$q\bar{q}'\bar{q}q'$
Expected error on M_W (GeV/c^2)	0.98	0.72	0.49	0.59
Fitted error on M_W (GeV/c^2)	1.08	0.72	0.58	0.62

Table 6.6: Comparison between the average statistical error expected from simulation events and the error obtained when fitting the data sample.

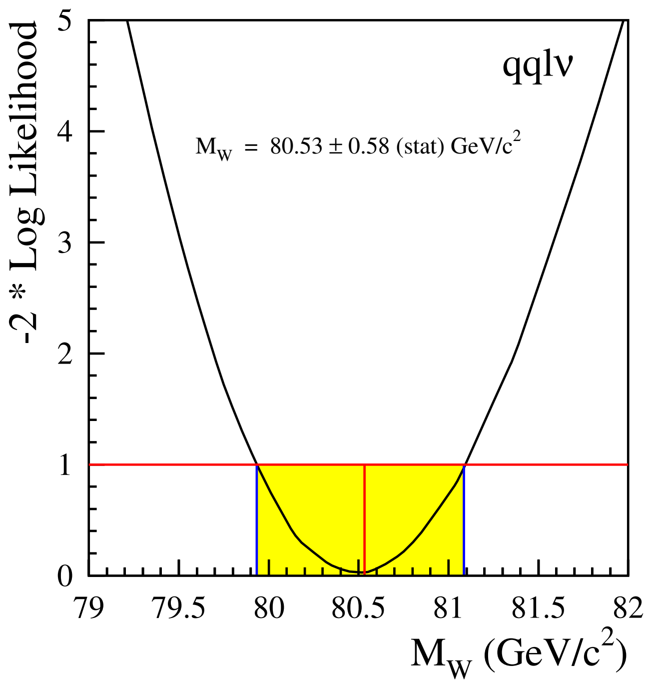

(a)

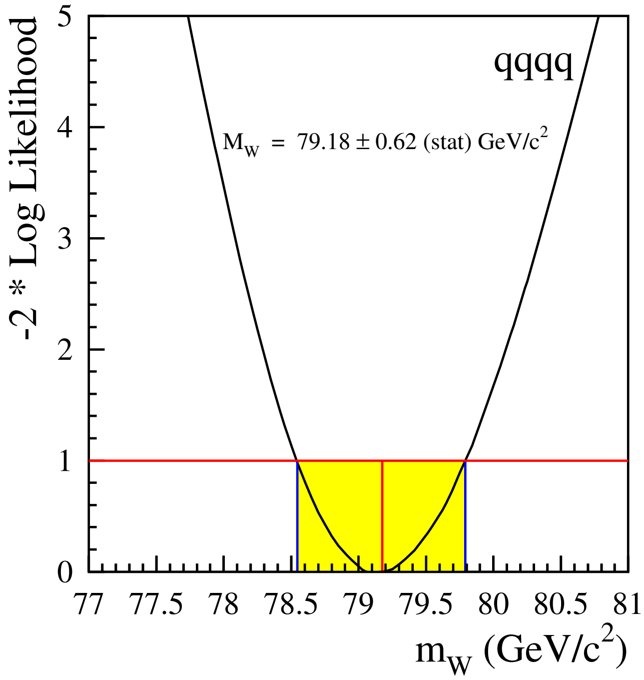

(b)

Figure 6.16: -2 × Log Likelihood of the data as a function of M_W. This quantity is equivalent to $\Delta\chi^2$(see text). The data is shown in (a) for the combined semi-leptonic decay channel and in (b) for the fully-hadronic channel.

6.13 Addendum - Average Mass

This section describes the derivation of results used earlier in this chapter when describing a kinematic fit where the W masses are constrained to be equal. In this case, the action of the kinematic fit is to produce an average W mass for the event. In general, the kinematic fit result will be a resolution weighted average, but, having imposed energy and momentum conservation, the resolution on the masses will be highly correlated. Hence, for simplicity, only the case of the simple mean is considered here. Note also that the effect of imposing the additional constraint in the kinematic fit is not simply to produce the average mass, but also to sharpen the resolution functions.

We define σ as the expected cross-section as a function of the masses of the two W's (true or reconstructed) (m_1, m_2) produced in the event.

If $\rho(m)$ is the probability density function for the mass m, then

$$\frac{d^2\sigma(m_1, m_2)}{dm_1 dm_2} = \rho(m_1)\rho(m_2)$$

defining the new variables $\overline{m} = \frac{m_1+m_2}{2}, \mu = \frac{m_1-m_2}{2}$

$$\begin{aligned}
\sigma(m_1, m_2) &= \int\int \rho(m_1)\rho(m_2)\ dm_1\ dm_2 \\
&= \int\int \rho(\overline{m}+\mu)\rho(\overline{m}-\mu)\ J\ d\mu\ d\overline{m} \\
&= 2\int\int \rho(\overline{m}+\mu)\rho(\overline{m}-\mu)\ d\mu\ d\overline{m}
\end{aligned}$$

where the Jacobian $J = \begin{vmatrix} \frac{\partial m_1}{\partial \mu} & \frac{\partial m_1}{\partial \overline{m}} \\ \frac{\partial m_2}{\partial \mu} & \frac{\partial m_2}{\partial \overline{m}} \end{vmatrix} = 2$

we can now rewrite this as:

$$\frac{d\sigma(\overline{m})}{d\overline{m}} = \int_{-\infty}^{\infty} \rho(\overline{m}+\mu)\rho(\overline{m}-\mu)\ d\mu \tag{6.17}$$

where the L.H.S. is the required p.d.f. as a function of the mean event mass ($\overline{m}$).

Resolution Dominated

If we use as our basis function a Gaussian:

$$\rho(m) = \frac{e^{\frac{-m^2}{2\sigma^2}}}{\sigma\sqrt{2\pi}} \tag{6.18}$$

applying Equation 6.17, it is simple to show that we obtain as expected

$$\frac{d\sigma(\overline{m})}{d\overline{m}} = \frac{e^{\frac{-\overline{m}^2}{2\sigma'^2}}}{\sigma'\sqrt{2\pi}}$$

where

$$\sigma' = \frac{\sigma}{\sqrt{2}}$$

that is, a Gaussian the width of which, compared with Equation 6.18, is reduced by $\sqrt{2}$.

This corresponds to the hypothetical case when the W invariant mass peak is dominated entirely by a Gaussian resolution function (and the two masses are uncorrelated). Neglecting other kinematic fit effects, the choice is then between fitting two mass distributions separately, or one sharper distribution (the average): both techniques will result in the same event mass resolution.

Physics Dominated

However, if we use a non-relativistic Breit Wigner,

$$\rho(m; \mathrm{M_W}, \Gamma_\mathrm{W}) = \frac{\Gamma_\mathrm{W}}{2\pi[(m - \mathrm{M_W})^2 + (\Gamma_\mathrm{W}/2)^2]}$$

it can be shown that

$$\frac{d\sigma(\overline{m})}{d\overline{m}} = \rho(\overline{m})$$

Hence, in the absence of detector resolution factors and the phase space correction, fitting the two individual mass distributions separately gives a factor 2 increase in the available statistics.

Consider now a relativistic Breit-Wigner (ρ_W) with Phase space correction factor (PS) (the formulae are given in Section 6.3). Then Equation 6.17 becomes

$$\frac{d\sigma(\overline{m})}{d\overline{m}} = \int \rho_\mathrm{W}(\overline{m} + \mu)\rho_\mathrm{W}(\overline{m} - \mu)\ PS(\overline{m}, \mu)\ d\mu \tag{6.19}$$

In the approximations of Equation 6.5 and 6.6 described earlier, PS is a function only of $\overline{m}$. Thus,

$$\frac{d\sigma(\overline{m})}{d\overline{m}} = PS(\overline{m})\ \rho_\mathrm{W}(\overline{m})$$

Thus we have obtained the result of Equation 6.7 that we used in fitting the generated mass distribution.

6.14 Numerical Implementation of Fit

The convolution integral (see Section 6.5), and its normalisation requirement are implemented numerically using the `CERNLIB` Gaussian adaptive Quadrature routines [94].

In order to render the convolution relatively flat as a function of the dummy mass, we use the following well known variable transformation [95].

To perform the convolution integral:

$$Res \otimes Phys = \int Res(m') \times Phys(m') dm'$$

we can write this as

$$Res \otimes Phys = \int \frac{Res(m') \times Phys(m')}{y(m')} y(m') dm'$$

put

$$y(m') = \frac{(\Gamma/2)}{(m' - \mathrm{m_{evt}})^2 + (\Gamma/2)^2}$$

then writing $d\beta = y(m)dm$

$$Res \otimes Phys = \int \frac{Res(\beta) \times Phys(\beta)}{y(\beta)} d\beta$$

where

$$\beta = \tan^{-1}\left(\frac{m' - \mathrm{m_{evt}}}{\Gamma/2}\right)$$

This transformation is illustrated in Figure 6.17. In the upper plot the sharply peaked signal event probability density function is shown against the dummy integration mass. In the lower plot, we show the same function against the new variable β. This transformation provides a smoother function for the integration routine, which increases the speed and accuracy of the calculation.

The final fit was implemented as a minimum log likelihood, the minimisation was performed using the `MINUIT` package [96].

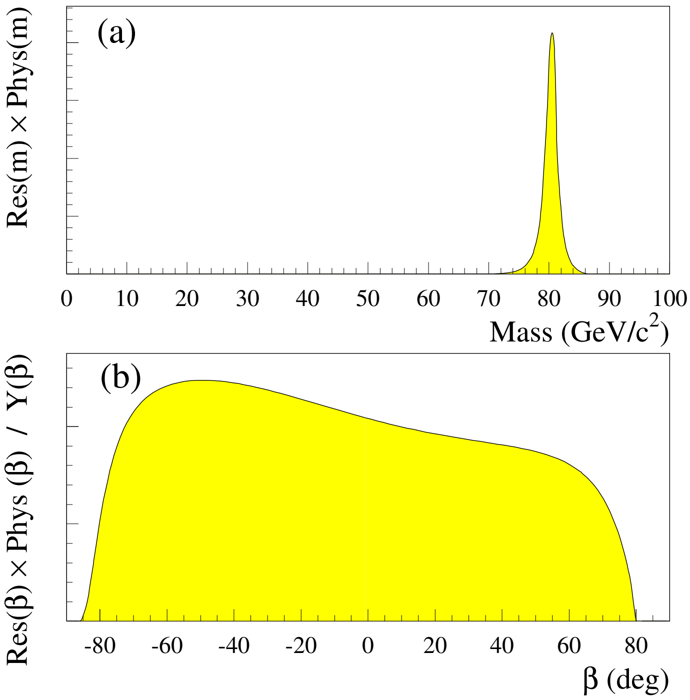

Figure 6.17: The plot shows the signal event probability function (for typical event values) as the dummy integration mass is varied. In the upper plot (a), we show the original signal probability against mass, in the lower plot we have transformed variables (see text) and perform an equivalent integration in β.

Chapter 7

Conclusions

7.1 Combination of M_W Results

In Chapter 4, we measured the total $e^+e^- \rightarrow W^+W^-$ cross-section at 161, 170 and 172 GeV. We interpreted this measurement, within the Standard Model, in terms of the W mass. We obtained the result:

$$M_W = 80.41 \pm 0.46 \text{ (stat.) } \pm 0.13 \text{(syst) } \pm 0.03 (\text{LEP}) \text{ GeV}/c^2$$

In Chapter 6, we applied the direct mass reconstruction method to events in the $l\overline{\nu}_l q\bar{q}'$ and $q\bar{q}'\bar{q}q'$ decay channels at 172 GeV. We obtained the result:

$$M_W = 79.93 \pm 0.42 \text{ (stat.) } \pm 0.06 \text{ (syst.) } \pm 0.05 \text{ (int.) } \pm 0.03 \text{ (LEP) GeV}/c^2$$

We now combine these two measurements, in a weighted average, to produce the final measurement of M_W from this analysis. The LEP beam energy error is taken as fully correlated; all other error components are assumed to be uncorrelated. We obtain the result:

$$M_W = 80.14 \pm 0.31 \text{ (stat.) } \pm 0.07 \text{ (syst.) } \pm 0.02 \text{ (int.) } \pm 0.03 \text{ (LEP) GeV}/c^2$$

Adding the error components in quadrature, we obtain the final result:

$$M_W = 80.14 \pm 0.32 \text{ GeV}/c^2$$

7.2 Comparison with Previous Measurements

The comparison of the principal measurements made in this thesis with those of previous experimental determinations are presented in Figure 7.1. In the following section, we list the most important results made in this analysis.

$e^+e^- \rightarrow$W$^+$W$^-$ **Cross-Section, at** $\sqrt{s}$ **of 161.31** $\pm$**0.06** GeV

$$\sigma_{\mathrm{W^+W^-}} = 3.82\ ^{+1.06}_{-0.93}\ \text{(stat.)}\ \pm 0.25\ \text{(syst.)}\ \text{pb}$$

This result is obtained from a fit in which lepton universality and the value of the W hadronic branching ratio are assumed. The combined LEP2 result shown in Figure 7.1 (a) is the LEP Electroweak Working Group Average [8].

$e^+e^- \rightarrow$W$^+$W$^-$ **Cross-Section, at** $\sqrt{s}$ **of 172.30** $\pm$**0.06** GeV

$$\sigma_{\mathrm{W^+W^-}} = 12.20\ ^{+1.66}_{-1.54}\ \text{(stat.)}\ \pm 0.50\ \text{(syst.)}\ \text{pb}$$

This result in is obtained from a fit in which lepton universality and the value of the W hadronic branching ratio are assumed. The combined LEP2 result shown in Figure 7.1 (b) is the LEP Electroweak Working Group Average [8].

W **Hadronic Branching Ratio**

$$BR_{\mathrm{W}\rightarrow \bar{q}q'} = 0.676\ ^{+0.039}_{-0.040}\ \text{(stat.)}\ \pm 0.013\ \text{(syst.)}$$

This result is obtained from a fit in which the values of the $e^+e^- \rightarrow$W$^+$W$^-$ cross-sections at $\sqrt{s}$ of 161.31, 172.0 and 172.3 GeV are assumed. The combined LEP2 result shown in Figure 7.1 (c) is the LEP Electroweak Working Group Average [8]. The TEVATRON branching ratio result is not included in the comparison since this is an indirect determination. At $p\bar{p}$ collider experiments, only charged leptons from W decays are identified.

W **Width**

$$\Gamma_{\mathrm{W}} = 2.09\ ^{+0.28}_{-0.23}\ \text{(stat.)}\ \pm 0.09\ \text{(syst.)}\ \text{GeV/c}^2$$

We include in the comparison shown in Figure 7.1 (d) only indirect determinations of the W Width. The results are obtained assuming the SM W $\rightarrow l\overline{\nu}_l$ partial width. The combined LEP2 result (marked †) has been produced by the author based on the LEP2 hadronic branching ratio determination. The combined TEVATRON result is taken from the report of the plenary talk at the EPS Conference 1997 [74]. In addition to the partial width assumption, the TEVATRON result also relies upon the Z $\rightarrow l^+l^-$ branching ratio and M_Z from LEP, and σ_w/σ_z from structure functions and the SM.

A measurement of Γ_W has been performed by the CDF Collaboration from the W boson transverse mass spectrum [97]. However, this determination still relies on significant SM assumptions [98]. Direct determinations of the W width from LEP on the 1996 data are of low accuracy [34, 99], though the LEP results should prove competitive in the future when larger data samples are analysed.

CKM Matrix Element $|V_{cs}|$

$$|V_{cs}| = 0.98 \pm 0.19 \text{ (stat.) } \pm 0.06 \text{ (syst.)}$$

The determinations shown in Figure 7.1 (e) are made without assuming CKM matrix unitarity. The combined LEP2 result (marked †) has been produced by the author based on the LEP2 hadronic branching ratio determination; this is the worlds best measurement of $|V_{cs}|$. The result of this thesis and the LEP2 result are obtained assuming the SM W $\rightarrow l\overline{\nu}_l$ partial width. The result marked 'DELPHI TAG' is obtained using charm and strange quark identification methods exploiting impact parameter tagging and the capabilities of the DELPHI RICH detectors [73]. The other results shown are from D meson decays (dominated by CLEO results) and neutrino charm production [25].

W Boson Mass

$$M_W = 80.14 \pm 0.31 \text{ (stat.) } \pm 0.07 \text{ (syst.) } \pm 0.02 \text{ (int.) } \pm 0.03 \text{ (LEP) GeV/c}^2$$

This result was obtained in the previous section. The value is obtained from the combination of the determination by the threshold cross-section method and the invariant mass direct reconstruction measurement. The combined LEP2 result shown in Figure 7.1 (f) is the LEP Electroweak Working Group Average [8]. The $p\bar{p}$ colliders result is the combination of the UA2, CDF, and D0 results [74]. The world average value is a combination of the LEP and $p\bar{p}$ collider results [8]. The final result shown in the comparison is an indirect measurement of $\mathrm{M_W}$ from a global electroweak fit to the LEP1 and SLD data within the Standard Model [8].

7.3 Conclusions

The first data on the process $e^+e^-\rightarrow \mathrm{W^+W^-}$ have been analysed in this thesis. Clear signatures were identified for all final states predicted by the Standard Model. We have successfully demonstrated the application of two complementary methods to the measurement of $\mathrm{M_W}$. Furthermore, these data have allowed the first direct determinations of the W boson hadronic branching ratio to be obtained.

All the principal results of this thesis are found to agree with the current world average and, where appropriate, the predictions of the Standard Model.

7.3.1 Future Prospects for $\mathrm{M_W}$

The most comprehensive predictions for the LEP2 $\mathrm{M_W}$ programme currently available were produced at the UK phenomenology workshop on LEP2 physics [29], to which the author was a contributor. Much of the following section and the predictions it contains are based on the conclusions of that workshop.

The statistical errors obtained in this thesis are compatible with those used in the workshop predictions. As the analyses develop further, the statistical accuracy of the $\mathrm{M_W}$ measurement per unit integrated luminosity is much more likely to improve than to worsen.

It is important to note that great effort has not yet been expended in reducing the systematic errors, since for the current integrated luminosity the statistical errors are completely dominant: indeed, currently the statistical errors from the number of simulation events produced can be a significant component of the systematic error. Collecting more data will assist in the reduction of the systematic errors:

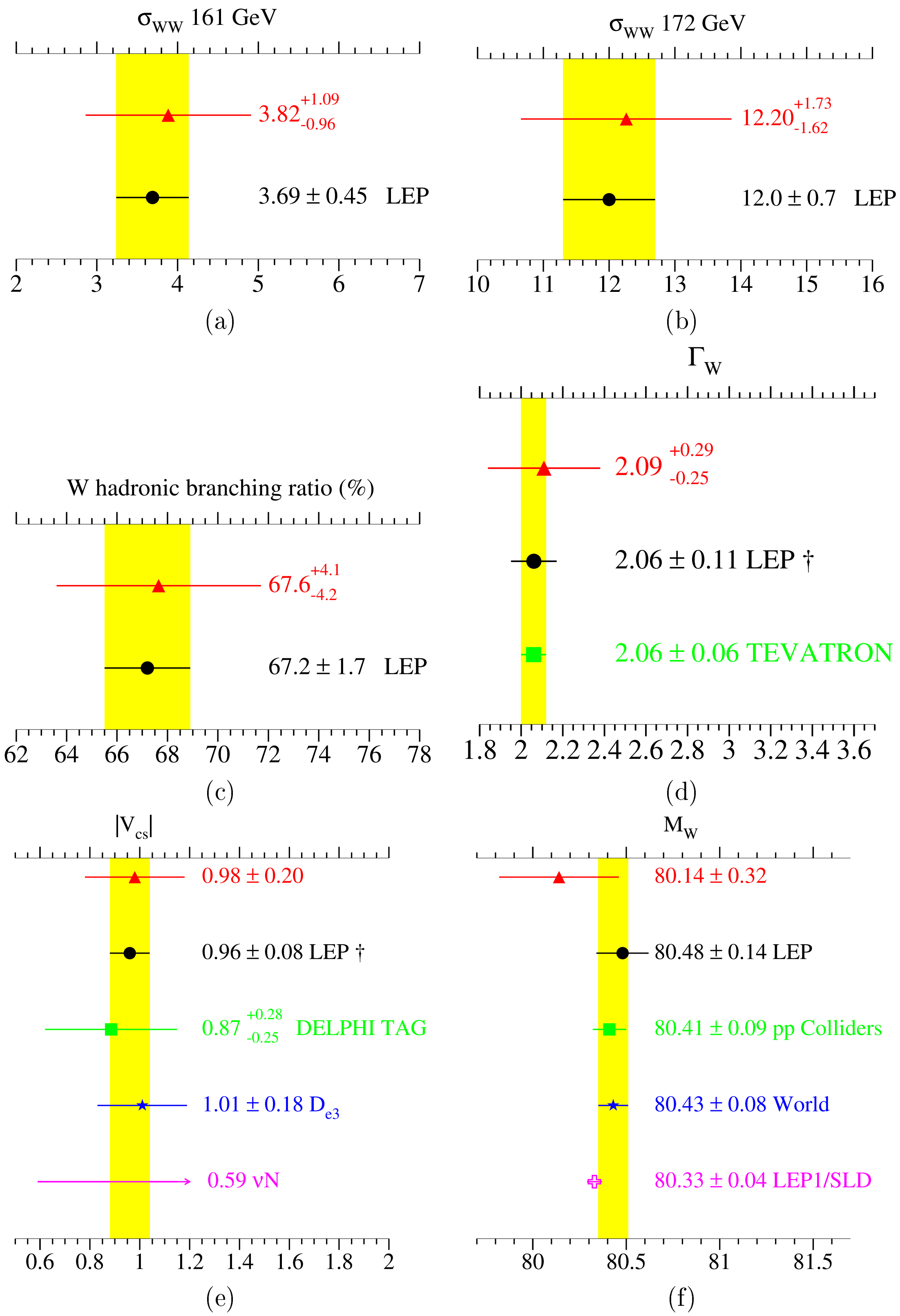

Figure 7.1: The principal measurements made in this analysis are compared with previous measurements of these quantities. The top point on each plot is that obtained in this thesis.

with increased statistics more meaningful comparisons of data and simulation can be performed.

The large background level in the fully-hadronic channel needs to be accurately assessed. This will require further studies of the simulation of the QCD processes $e^+e^- \to q\bar{q}$ with gluon emission.

For future high energy running, a LEP beam energy error of 15 MeV or better is desirable. In 1997, polarisation measurements were made in 6 fills at energies ranging from 40 to 55 GeV and the linearity of the extrapolation is being tested. Work is on-going, particularly on the development of a high precision magnetic spectrometer, but the target error still appears achievable.

Amongst particle accelerators which are currently operational, or under construction, the threshold method of determining $\mathrm{M_W}$ is unique to LEP2. In the long term, mass reconstruction methods on leptonic final states at the TEVATRON run II and the LHC may eventually obtain similar or better precision to the LEP2 determination of $\mathrm{M_W}$. However, the determination of $\mathrm{M_W}$ from the threshold method is unlikely to be performed outside LEP in the foreseeable future. A relatively modest integrated luminosity of 50 $\mathrm{pb^{-1}}$ per experiment at 161 GeV would probably result in an error on $\mathrm{M_W}$ comparable with that of the current world average.

The precision mass reconstruction of hadronic W final states is also only achievable at LEP2. However, use of the fully-hadronic final states in the eventual high luminosity $\mathrm{M_W}$ determination will require an accurate assessment of the interconnection effects. The predictions of models must be related to (non-$\mathrm{M_W}$ dependent) experimental quantities. There are on-going experimental and theoretical programmes.

An integrated luminosity of 500 $\mathrm{pb^{-1}}$ per experiment was considered achievable in [87], most of which will be delivered at energies above the threshold region. Assuming the interconnection effects are shown to be small, or can accurately be assessed, the direct reconstruction method may provide an accuracy of 35 $\mathrm{MeV/c^2}$. If the measurement is restricted to the semi-leptonic channel, the predicted error is 45 MeV.

In conclusion, an accuracy of 50 $\mathrm{MeV/c^2}$ or better on $\mathrm{M_W}$ from the LEP2 programme seems achievable.

In Figure 7.2 we show the W boson mass against the top quark mass. The desired 50 MeV/c^2 M_W accuracy is indicated as a dotted line. The comparison of such a high precision result with the indirect measurement of M_W will be a significant test of the Standard Model.

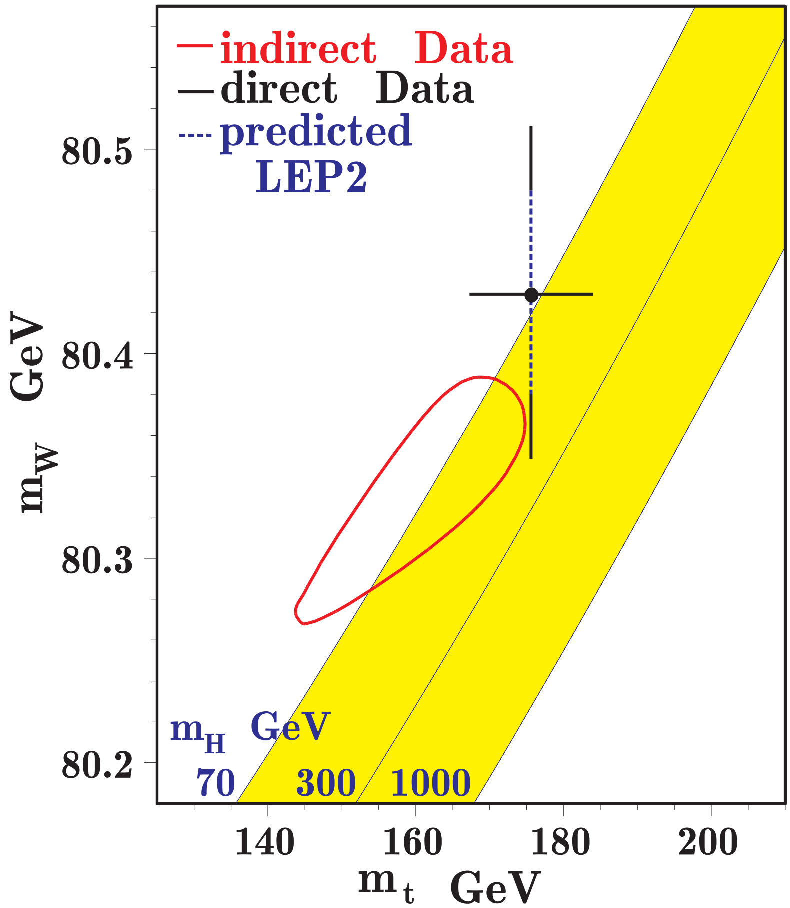

Figure 7.2: The W boson mass is plotted against the top quark mass. The current world average value of M_W, and m_t from direct determinations are indicated. The projected errors on M_W from the full LEP2 programme are shown (see text). The indirect determination of M_W and m_t from a global electroweak fit is included. The shaded bands show the Standard Model predictions as a function of the Higgs mass. This plot is a modified version of that in [8].

Appendix A

WWANA: A Standard Package for W Analysis

A.1 Introduction and Aims

`WWANA` is the standard analysis package for W physics in DELPHI: it aims to store all the quantities required for W mass, W^+W^- cross-section and charged TGC anlayses. Through direct access of the DST and extensive use of the `SKELANA` package [47], the required event parameters are obtained. However, `WWANA` does not simply provide an appropriately abridged version of the DST: the data is processed by the program into a form which is of more immediate use in an analysis.

This appendix is not intended as a manual for the operation of the `WWANA` package; for details on the general running procedure see [48]. An up-to-date guide of the available features is in [100]. The documentation provided here describes only the aims and main features of the program. All the analysis described in this thesis was produced using the `WWANA` package.

`WWANA` is a reliable studied package which will be a useful tool for all the analyses concerned with W production throughout the LEP200 program. The `WWANA` output format is flexible and easily modified by the user. The user also has control of all the selections applied inside the program and may attach additional code in a transparent way.

The extensive use of the `WWANA` program throughout the collaboration facilitates easier comparison of the results from analyses, and exchange of information among people who are interested in similar physics topics. It is anticipated that `WWANA` will continue to evolve to meet the needs of increasingly sophisticated physics analyses.

A.2 Structure

Figure A.1 shows a simplified flow chart illustrating the structure of the `WWANA` program. The package is constructed of 3 main types of routine: initialisation routines, processing routines and identification routines. The right hand column indicates which output block (see below) is filled by each stage in the program.

A.2.1 Initialisation

These routines prepare information that will be required in later stages of the program. Data such as the run and event number which uniquely identify the event are stored. A pre-selection of W^+W^- events can be performed using simple global variables, thus reducing the running time of the program. The selection of tracks used in the analysis is performed here; a system of flagging selected tracks[1] is implemented, rather than deleting unrequired tracks, thus preventing the loss of information. An accurate DELPHI beam energy for each data event can be obtained from an external file.

A.2.2 Processing

The analysis performed in these routines is of a general nature, and much of it is relevant in a wide range of physics analyses. Generator information[2] is extracted for simulation events: in particular on the four fermions from W^+W^-decay, but also other important features such as ISR and correspondence between generated and reconstructed leptons. The Event Analysis block produces global variables such as the charged or transverse energies and the missing momentum. The SPRIME package [65] is used to determine the value of the effective centre of mass energy. A natural jet clusterisation is performed and the thrust, sphericity, and jet charges are evaluated. Electron and muon identification is performed and, for the selected

[1] This was first proposed in the `SKELANA` program.

[2] Information is provided for all the generator programs currently used in DELPHI.

tracks, variables such as the isolation angle are calculated. Energy corrections for deposits in the electromagnetic calorimeters are included. As the background events in the analyses often contain ISR, information is provided on the neutral energy deposits detected in DELPHI.

A.2.3 Identification

`WWANA` contains identification routines that provide information on the three W^+W^- decay channels:

QQANA: $W^+W^-\to q\bar{q}'\bar{q}q'$ QLANA: $W^+W^-\to l\overline{\nu}_l q\bar{q}'$ FLANA: $W^+W^-\to l\overline{\nu}_l\bar{l}\nu_l$

• In QQANA the event is forced to be a four jet event and a constrained kinematic fit is performed [82].

• In QLANA a candidate lepton is selected and the remaining tracks are forced into two jets; a constrained kinematic fit is then performed. This block is subdivided into sections for different lepton identifications. The four sections are: electron search (QEANA); muon search(QMANA); unidentified single charged prong search (Q1ANA); and the narrow jet search (QTANA).

• In FLANA information is produced for events with two low multiplicity jets.

As the analysis described in this thesis relies on many of the variables produced in these routines, it is not necessary to repeat their description here.

A.2.4 Inputs

The user can control the flow of the program, apply some general cuts, and select the required output structure by setting a sequence of variables and logical words in the input file; for example the user can choose their preferred jet clusterisation algorithm, or focus only upon the $l\overline{\nu}_l\bar{l}\nu_l$ final state. The program thus requires a large amount of control data; however, the use of default settings and the extensive documentation allow the user to run the program immediately.

A.2.5 Outputs

The main output of the program is a Column Wise Ntuple [101]. By setting logical parameters, the user can choose which blocks of information to include in the ntuple.

This choice will depend on which analysis and which W decay channels the user is interested in studying. Some additional, less important, information is stored in common blocks.

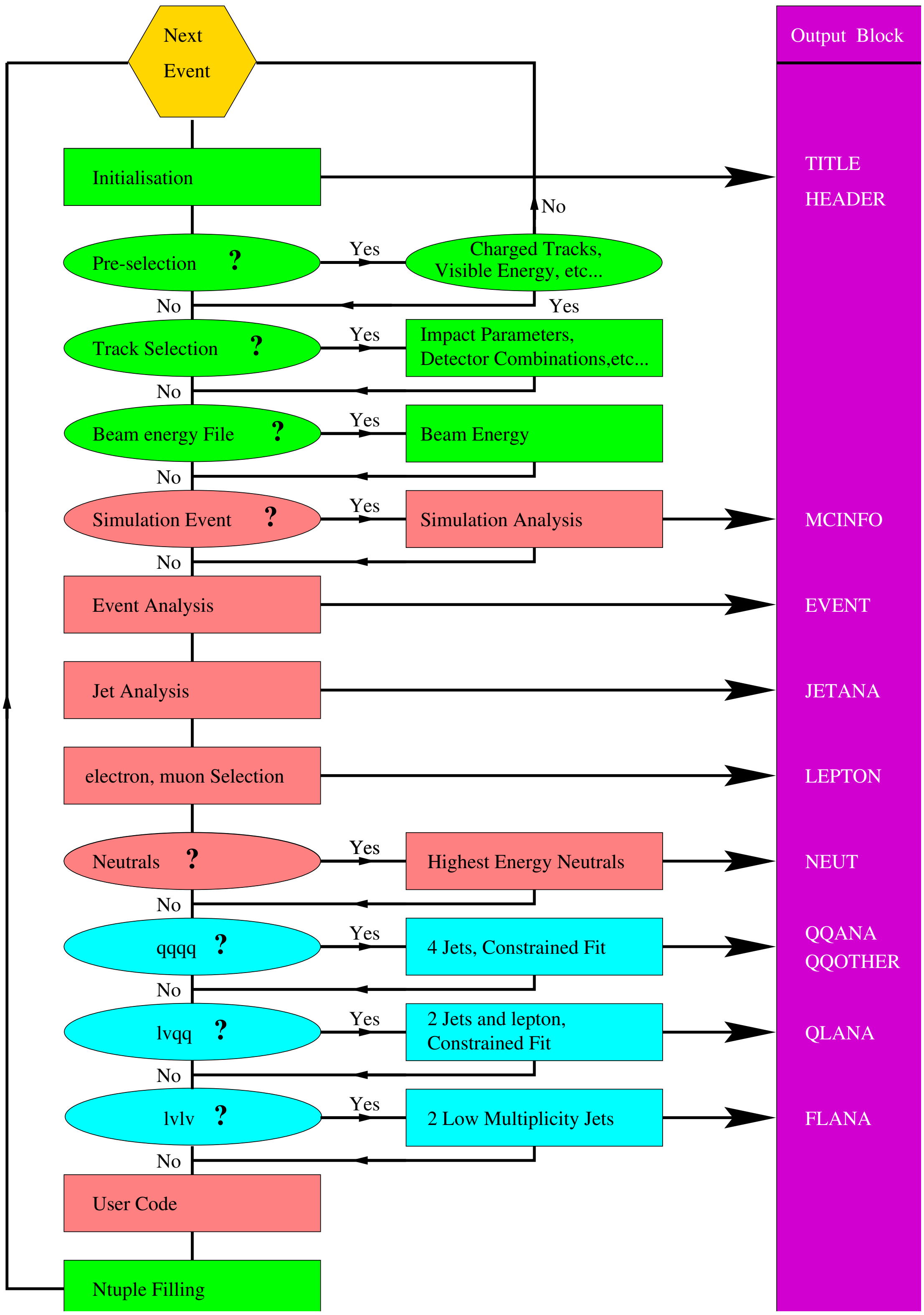

Figure A.1: Structure of the `WWANA` package.

Appendix B

PUFITC+: A Constrained Fitting Package

This section is based on references [82] and [67]. The `PUFITC+` program was written by Niels Kjær and Martijn Mulders.

The invariant mass direct reconstruction method for measuring M_W makes use of this constrained fitting package. The algorithm aims to improve the resolution on the reconstructed final state objects by applying a set of constraints. The constraints imposed are discussed in Section 6.4.

The inputs to the fit are the observed jets and charged leptons. Each element is described by three parameters.

The neutrino momentum vector is unobserved; this leads to a reduction of three in the number of degrees of freedom of the fit.

Muons are described by their measured momenta and their polar and azimuthal angles. The measurement errors are obtained directly for the track fit: only the momentum error is significant for the precision of the M_W determination.

Electrons are characterized by their measured energies in the electromagnetic calorimeters, and their angular positions determined from the tracking detectors. The energy errors were obtained from parameterisations of the response of the electromagnetic calorimeters. The angular errors were determined from the track fit.

Tau decays result in the emission of one or more neutrinos. As a result of this missing momentum, we treat them in a similar manner to the jets.

The fitted jet momentum, $\mathbf{p_i^{fit}}$, is projected onto a set of perpendicular axes with one component parallel to the measured jet momentum, $\mathbf{p_i^{meas}}$, and two transverse components $\mathbf{p_i^b}$ and $\mathbf{p_i^c}$.

$$\mathbf{p_i^{fit}} = exp(a_i)\mathbf{p_i^{meas}} + b_i\mathbf{p_i^b} + c_i\mathbf{p_i^c}$$

The parallel component is described by an exponential rescaling factor. The transverse momentum components are arbitrarily fixed to 1 GeV/c and their variation is described by a multiplicative parameter.

We form a χ^2:

$$\chi^2 = \Sigma_i \frac{(a_i - a_0)^2}{\sigma_{a_i}^2} \; + \; \frac{b_i^2}{\sigma_{b_i}^2} \; + \; \frac{c_i^2}{\sigma_{c_i}^2}$$

The measured jet momentum is typically lower than the true jet momentum due to the presence of unobserved particles in the detector. This is accounted for by introducing the expected energy loss parameter a_0. The σ quantities in this equation represent the expected errors on these parameters; the errors used are discussed below.

We introduce a set of constraints to the fit. In the direct reconstruction analysis, we use the conservation of energy and momentum, and equality of the two masses measured in an event. We denote the vector of constraints as $\mathbf{f}$ and require:

$$\mathbf{f}(\mathbf{p_1^{fit}}, \mathbf{p_2^{fit}}, \mathbf{p_3^{fit}}, \mathbf{p_4^{fit}}) = \mathbf{0}$$

where $\mathbf{p_1^{fit}}$ *etc.* are the momentum vectors of the four fitted fermions.

We introduce the Lagrangian multiplier vector λ, and define a function:

$$Q = \chi^2 - \lambda\mathbf{f}$$

We minimise this quantity w.r.t. the fitted momentum vectors, ensuring the constraints are imposed by using the Lagrangian multiplier method. In practice, the fit is minimised using an iterative procedure.

In the χ^2, we have assumed that the parameter errors are well described by a Gaussian function. In Section 6.4.2 we apply a rescaling procedure to take non-Gaussian resolution effects into account.

In both the fully-hadronic and the semi-leptonic channels, we parameterise the jet errors and the expected energy loss parameter as a function of the jet polar angle θ_i. The values and parameterisation were based on a study of simulated events.

$$a_0 = 0.15 \; + \; 0.4 \cos^4 \theta_i$$

$$\sigma_{a_i} = 0.27 \; + \; 0.72 \cos^4 \theta_i$$

$$\sigma_{b_i} = 1.5$$

$$\sigma_{c_i} = 1.5$$

Appendix C

DELPHI Collaboration

C.1 DELPHI Collaboration

P.Abreu[21], W.Adam[49], T.Adye[36], P.Adzic[11], G.D.Alekseev[16], R.Alemany[48], P.P.Allport[22], S.Almehed[24], U.Amaldi[9], S.Amato[46], P.Andersson[43], A.Andreazza[9], P.Antilogus[25], W-D.Apel[17], Y.Arnoud[14], B.Åsman[43], J-E.Augustin[25], A.Augustinus[9], P.Baillon[9], P.Bambade[19], F.Barao[21], R.Barbier[25], D.Y.Bardin[16], G.Barker[9], A.Baroncelli[39], O.Barring[24], M.J.Bates[36], M.Battaglia[15], M.Baubillier[23], J.Baudot[38], K-H.Becks[51], M.Begalli[6], P.Beilliere[8], Yu.Belokopytov[9,52], A.C.Benvenuti[5], C.Berat[14], M.Berggren[25], D.Bertini[25], D.Bertrand[2], M.Besancon[38], F.Bianchi[44], M.Bigi[44], M.S.Bilenky[16], P.Billoir[23], M-A.Bizouard[19], D.Bloch[10], M.Blume[51], M.Bonesini[27], W.Bonivento[27], M.Boonekamp[38], P.S.L.Booth[22], A.W.Borgland[4], G.Borisov[38], C.Bosio[39], O.Botner[47], E.Boudinov[30], B.Bouquet[19], C.Bourdarios[19], T.J.V.Bowcock[22], I.Bozovic[11], M.Bozzo[13], P.Branchini[39], K.D.Brand[35], T.Brenke[51], R.A.Brenner[47], R.Brown[9], P.Bruckman[35], J-M.Brunet[8], L.Bugge[32], T.Buran[32], T.Burgsmueller[51], P.Buschmann[51], S.Cabrera[48], M.Caccia[27], M.Calvi[27], A.J.Camacho Rozas[40], T.Camporesi[9], V.Canale[37], M.Canepa[13], F.Carena[9], L.Carroll[22], C.Caso[13], M.V.Castillo Gimenez[48], A.Cattai[9], F.R.Cavallo[5], Ch.Cerruti[10], V.Chabaud[9], N.Chalanda[41], Ph.Charpentier[9], L.Chaussard[25], P.Checchia[35], G.A.Chelkov[16], M.Chen[2], R.Chierici[44], P.Chliapnikov[41], P.Chochula[7], V.Chorowicz[25], J.Chudoba[29], V.Cindro[42], P.Collins[9], M.Colomer[48], R.Contri[13], E.Cortina[48], G.Cosme[19], F.Cossutti[45], J-H.Cowell[22], H.B.Crawley[1], D.Crennell[36], G.Crosetti[13], J.Cuevas Maestro[33], S.Czellar[15], B.Dalmagne[19], G.Damgaard[28], P.D.Dauncey[36], M.Davenport[9], W.Da Silva[23], A.Deghorain[2], G.Della Ricca[45], P.Delpierre[26], N.Demaria[34], A.De Angelis[9], W.De Boer[17], S.De Brabandere[2], C.De Clercq[2], C.De La Vaissiere[23], B.De Lotto[45], A.De Min[35], L.De Paula[46], H.Dijkstra[9], L.Di Ciaccio[37], A.Di Diodato[37], A.Djannati[8], J.Dolbeau[8], K.Doroba[50], M.Dracos[10], J.Drees[51], K.-A.Drees[51], M.Dris[31], A.Duperrin[25], J-D.Durand[25,9], D.Edsall[1], R.Ehret[17], G.Eigen[4], T.Ekelof[47], G.Ekspong[43], M.Ellert[47], M.Elsing[9], J-P.Engel[10], B.Erzen[42], M.Espirito Santo[21], E.Falk[24], G.Fanourakis[11], D.Fassouliotis[45], J.Fayot[23], M.Feindt[17], A.Fenyuk[41], P.Ferrari[27], A.Ferrer[48], S.Fichet[23], A.Firestone[1], P.-A.Fischer[9], U.Flagmeyer[51], H.Foeth[9], E.Fokitis[31], F.Fontanelli[13], F.Formenti[9], B.Franek[36], A.G.Frodesen[4], R.Fruhwirth[49], F.Fulda-Quenzer[19], J.Fuster[48], A.Galloni[22], D.Gamba[44], M.Gandelman[46], C.Garcia[48], J.Garcia[40], C.Gaspar[9], M.Gaspar[46], U.Gasparini[35], Ph.Gavillet[9], E.N.Gazis[31], D.Gele[10], J-P.Gerber[10], L.Gerdyukov[41], N.Ghodbane[25], F.Glege[51], R.Gokieli[50], B.Golob[42], P.Goncalves[21], G.Gopal[36], L.Gorn[1,53], M.Gorski[50], Yu.Gouz[41], V.Gracco[13], J.Grahl[1], E.Graziani[39], C.Green[22], A.Grefrath[51], P.Gris[38], G.Grosdidier[19], K.Grzelak[50], M.Gunther[47], J.Guy[36], F.Hahn[9], S.Hahn[51], S.Haider[9], Z.Hajduk[18], A.Hallgren[47], K.Hamacher[51], F.J.Harris[34], V.Hedberg[24], S.Heising[17], R.Henriques[21], J.J.Hernandez[48], P.Herquet[2], H.Herr[9], T.L.Hessing[34], J.-M.Heuser[51], E.Higon[48], S-O.Holmgren[43], P.J.Holt[34], D.Holthuizen[30], S.Hoorelbeke[2], M.Houlden[22], J.Hrubec[49], K.Huet[2], K.Hultqvist[43], J.N.Jackson[22], R.Jacobsson[43], P.Jalocha[9], R.Janik[7], Ch.Jarlskog[24], G.Jarlskog[24], P.Jarry[38], B.Jean-Marie[19], E.K.Johansson[43], L.Jonsson[24], P.Jonsson[24], C.Joram[9], P.Juillot[10], M.Kaiser[17], F.Kapusta[23], K.Karafasoulis[11], S.Katsanevas[25], E.C.Katsoufis[31], R.Keranen[4], B.A.Khomenko[16], N.N.Khovanski[16], B.King[22], N.J.Kjaer[30], O.Klapp[51], H.Klein[9], P.Kluit[30], D.Knoblauch[17], P.Kokkinias[11], M.Koratzinos[9], K.Korcyl[18], V.Kostioukhine[41], C.Kourkoumelis[3], O.Kouznetsov[16], M.Krammer[49], C.Kreuter[9], I.Kronkvist[24], Z.Krumstein[16], P.Kubinec[7], W.Kucewicz[18], K.Kurvinen[15], C.Lacasta[9], J.W.Lamsa[1], L.Lanceri[45], D.W.Lane[1], P.Langefeld[51], V.Lapin[41], J-P.Laugier[38], R.Lauhakangas[15], G.Leder[49], F.Ledroit[14], V.Lefebure[2], C.K.Legan[1], A.Leisos[11], R.Leitner[29], J.Lemonne[2], G.Lenzen[51], V.Lepeltier[19], T.Lesiak[18], M.Lethuillier[38], J.Libby[34], D.Liko[9], A.Lipniacka[43], I.Lippi[35], B.Loerstad[24], J.G.Loken[34], J.H.Lopes[46], J.M.Lopez[40], D.Loukas[11], P.Lutz[38], L.Lyons[34], J.MacNaughton[49], J.R.Mahon[6], A.Maio[21], A.Malek[51], T.G.M.Malmgren[43], V.Malychev[16], F.Mandl[49], J.Marco[40], R.Marco[40], B.Marechal[46], M.Margoni[35], J-C.Marin[9], C.Mariotti[9], A.Markou[11], C.Martinez-Rivero[33], F.Martinez-Vidal[48], S.Marti i Garcia[22], F.Matorras[40], C.Matteuzzi[27], G.Matthiae[37], M.Mazzucato[35], M.Mc Cubbin[22], R.Mc Kay[1], R.Mc Nulty[9], G.Mc Pherson[22], J.Medbo[47], C.Meroni[27], W.T.Meyer[1], M.Michelotto[35], E.Migliore[44], L.Mirabito[25], W.A.Mitaroff[49], U.Mjoernmark[24], T.Moa[43], R.Moeller[28], K.Moenig[9], M.R.Monge[13], X.Moreau[23], P.Morettini[13], K.Muenich[51], M.Mulders[30], L.M.Mundim[6], W.J.Murray[36], B.Muryn[14,18], G.Myatt[34], T.Myklebust[32], F.Naraghi[14], F.L.Navarria[5], S.Navas[48], K.Nawrocki[50], P.Negri[27], S.Nemecek[12], N.Neufeld[9], W.Neumann[51], N.Neumeister[49], R.Nicolaidou[14], B.S.Nielsen[28], M.Nieuwenhuizen[30], V.Nikolaenko[10], M.Nikolenko[10,16], P.Niss[43], A.Nomerotski[35], A.Normand[22], A.Nygren[24], W.Oberschulte-Beckmann[17], V.Obraztsov[41], A.G.Olshevski[16], A.Onofre[21], R.Orava[15], G.Orazi[10], S.Ortuno[48], K.Osterberg[15], A.Ouraou[38], P.Paganini[19], M.Paganoni[27], S.Paiano[5], R.Pain[23], R.Paiva[21], H.Palka[18], Th.D.Papadopoulou[31], K.Papageorgiou[11], L.Pape[9], C.Parkes[34], F.Parodi[13], U.Parzefall[22], A.Passeri[39], M.Pegoraro[35], L.Peralta[21], H.Pernegger[49], M.Pernicka[49], A.Perrotta[5], C.Petridou[45], A.Petrolini[13], H.T.Phillips[36], G.Piana[13], F.Pierre[38], M.Pimenta[21], E.Piotto[35], T.Podobnik[34], O.Podobrin[9], M.E.Pol[6], G.Polok[18], P.Poropat[45], V.Pozdniakov[16], P.Privitera[37], N.Pukhaeva[16], A.Pullia[27], D.Radojicic[34], S.Ragazzi[27], H.Rahmani[31], J.Rames[12], P.N.Ratoff[20], A.L.Read[32], P.Rebecchi[9], N.G.Redaelli[27], M.Regler[49], D.Reid[9], R.Reinhardt[51], P.B.Renton[34], L.K.Resvanis[3], F.Richard[19], J.Ridky[12], G.Rinaudo[44], O.Rohne[32], A.Romero[44], P.Ronchese[35], E.I.Rosenberg[1], P.Rosinsky[7], P.Roudeau[19], T.Rovelli[5], V.Ruhlmann-Kleider[38], A.Ruiz[40], H.Saarikko[15], Y.Sacquin[38], A.Sadovsky[16], G.Sajot[14], J.Salt[48], D.Sampsonidis[11], M.Sannino[13], H.Schneider[17], U.Schwickerath[17], M.A.E.Schyns[51], F.Scuri[45], P.Seager[20], Y.Sedykh[16], A.M.Segar[34], A.Seitz[17], R.Sekulin[36], V.Senko[41], R.C.Shellard[6], A.Sheridan[22], P.Siegrist[9,38], R.Silvestre[38], F.Simonetto[35], A.N.Sisakian[16], T.B.Skaali[32], G.Smadja[25], N.Smirnov[41], O.Smirnova[24], G.R.Smith[36], O.Solovianov[41], R.Sosnowski[50], D.Souza-Santos[6], T.Spassov[21], E.Spiriti[39], P.Sponholz[51], S.Squarcia[13], D.Stampfer[9], C.Stanescu[39], S.Stanic[42], S.Stapnes[32], I.Stavitski[35], K.Stevenson[34], A.Stocchi[19], J.Strauss[49], R.Strub[10], B.Stugu[4], M.Szczekowski[50], M.Szeptycka[50], T.Tabarelli[27], O.Tchikilev[41], F.Tegenfeldt[47], F.Terranova[27], J.Thomas[34], A.Tilquin[26], J.Timmermans[30], L.G.Tkatchev[16], T.Todorov[10], S.Todorova[10], D.Z.Toet[30], A.Tomaradze[2], B.Tome[21], A.Tonazzo[27], L.Tortora[39], G.Transtromer[24], D.Treille[9], G.Tristram[8], A.Trombini[19], C.Troncon[27], A.Tsirou[9], M-L.Turluer[38], I.A.Tyapkin[16], M.Tyndel[36], S.Tzamarias[11], B.Ueberschaer[51], O.Ullaland[9], V.Uvarov[41], G.Valenti[5], E.Vallazza[45], C.Vander Velde[2], G.W.Van Apeldoorn[30], P.Van Dam[30], W.K.Van Doninck[2], J.Van Eldik[30], A.Van Lysebetten[2], I.Van Vulpen[30], N.Vassilopoulos[34], G.Vegni[27], L.Ventura[35], W.Venus[36], F.Verbeure[2], M.Verlato[35], L.S.Vertogradov[16], V.Verzi[37], D.Vilanova[38], P.Vincent[23], N.Vishnevsky[41], L.Vitale[45], E.Vlasov[41], A.S.Vodopyanov[16], V.Vrba[12], H.Wahlen[51], C.Walck[43], F.Waldner[45], C.Weiser[17], A.M.Wetherell[9], D.Wicke[51], J.H.Wickens[2], G.R.Wilkinson[9], W.S.C.Williams[34], M.Winter[10], M.Witek[18], T.Wlodek[19], G.Wolf[9], J.Yi[1], A.Zalewska[18], P.Zalewski[50], D.Zavrtanik[42], E.Zevgolatakos[11], N.I.Zimin[16], G.C.Zucchelli[43], G.Zumerle[35]

C.2 DELPHI W^+W^- Cross-Section and W Mass Team

P.Buschmann[51], M.Bigi[44], M.Calvi[27], V.Canale[37], R.Chierici[44], D.Fassouliotis[45], P.Jarry[38], N.J.Kjaer[30], G.Matthiae[37], R.Moeller[28], K.Moenig[9], M.Mulders[30], G.Orazi[10], A.Ouraou[38], M.Paganoni[27], C.Parkes[34], P.Privitera[37], P.B.Renton[34], J.Thomas[34], M-L.Turluer[38], J.Timmermans[30], A.Tonazzo[27], V.Verzi[37], H.Wahlen[51], G.R.Wilkinson[9]

[1] Department of Physics and Astronomy, Iowa State University, Ames IA 50011-3160, USA

[2] Physics Department, Univ. Instelling Antwerpen, Universiteitsplein 1, BE-2610 Wilrijk, Belgium, and IIHE, ULB-VUB, Pleinlaan 2, BE-1050 Brussels, Belgium, and Faculté des Sciences, Univ. de l'Etat Mons, Av. Maistriau 19, BE-7000 Mons, Belgium

[3] Physics Laboratory, University of Athens, Solonos Str. 104, GR-10680 Athens, Greece

[4] Department of Physics, University of Bergen, Allégaten 55, NO-5007 Bergen, Norway

[5] Dipartimento di Fisica, Università di Bologna and INFN, Via Irnerio 46, IT-40126 Bologna, Italy

[6] Centro Brasileiro de Pesquisas Físicas, rua Xavier Sigaud 150, BR-22290 Rio de Janeiro, Brazil, and Depto. de Física, Pont. Univ. Católica, C.P. 38071 BR-22453 Rio de Janeiro, Brazil, and Inst. de Física, Univ. Estadual do Rio de Janeiro, rua São Francisco Xavier 524, Rio de Janeiro, Brazil

[7] Comenius University, Faculty of Mathematics and Physics, Mlynska Dolina, SK-84215 Bratislava, Slovakia

[8] Collège de France, Lab. de Physique Corpusculaire, IN2P3-CNRS, FR-75231 Paris Cedex 05, France

[9] CERN, CH-1211 Geneva 23, Switzerland

[10] Institut de Recherches Subatomiques, IN2P3 - CNRS/ULP - BP20, FR-67037 Strasbourg Cedex, France

[11] Institute of Nuclear Physics, N.C.S.R. Demokritos, P.O. Box 60228, GR-15310 Athens, Greece

[12] FZU, Inst. of Phys. of the C.A.S. High Energy Physics Division, Na Slovance 2, CZ-180 40, Praha 8, Czech Republic

[13] Dipartimento di Fisica, Università di Genova and INFN, Via Dodecaneso 33, IT-16146 Genova, Italy

[14] Institut des Sciences Nucléaires, IN2P3-CNRS, Université de Grenoble 1, FR-38026 Grenoble Cedex, France

[15] Helsinki Institute of Physics, HIP, P.O. Box 9, FI-00014 Helsinki, Finland

[16] Joint Institute for Nuclear Research, Dubna, Head Post Office, P.O. Box 79, RU-101 000 Moscow, Russian Federation

[17] Institut für Experimentelle Kernphysik, Universität Karlsruhe, Postfach 6980, DE-76128 Karlsruhe, Germany

[18] Institute of Nuclear Physics and University of Mining and Metalurgy, Ul. Kawiory 26a, PL-30055 Krakow, Poland

[19] Université de Paris-Sud, Lab. de l'Accélérateur Linéaire, IN2P3-CNRS, Bât. 200, FR-91405 Orsay Cedex, France

[20] School of Physics and Chemistry, University of Lancaster, Lancaster LA1 4YB, UK

[21] LIP, IST, FCUL - Av. Elias Garcia, 14-1^o, PT-1000 Lisboa Codex, Portugal

[22] Department of Physics, University of Liverpool, P.O. Box 147, Liverpool L69 3BX, UK

[23] LPNHE, IN2P3-CNRS, Univ. Paris VI et VII, Tour 33 (RdC), 4 place Jussieu, FR-75252 Paris Cedex 05, France

[24] Department of Physics, University of Lund, Sölvegatan 14, SE-223 63 Lund, Sweden

[25] Université Claude Bernard de Lyon, IPNL, IN2P3-CNRS, FR-69622 Villeurbanne Cedex, France

[26] Univ. d'Aix - Marseille II - CPP, IN2P3-CNRS, FR-13288 Marseille Cedex 09, France

[27] Dipartimento di Fisica, Università di Milano and INFN, Via Celoria 16, IT-20133 Milan, Italy

[28] Niels Bohr Institute, Blegdamsvej 17, DK-2100 Copenhagen Ø, Denmark

[29] NC, Nuclear Centre of MFF, Charles University, Areal MFF, V Holesovickach 2, CZ-180 00, Praha 8, Czech Republic

[30] NIKHEF, Postbus 41882, NL-1009 DB Amsterdam, The Netherlands

[31] National Technical University, Physics Department, Zografou Campus, GR-15773 Athens, Greece

[32] Physics Department, University of Oslo, Blindern, NO-1000 Oslo 3, Norway

[33] Dpto. Fisica, Univ. Oviedo, Avda. Calvo Sotelo s/n, ES-33007 Oviedo, Spain, (CICYT-AEN96-1681)

[34] Department of Physics, University of Oxford, Keble Road, Oxford OX1 3RH, UK

[35] Dipartimento di Fisica, Università di Padova and INFN, Via Marzolo 8, IT-35131 Padua, Italy

[36] Rutherford Appleton Laboratory, Chilton, Didcot OX11 OQX, UK

[37] Dipartimento di Fisica, Università di Roma II and INFN, Tor Vergata, IT-00173 Rome, Italy

[38] DAPNIA/Service de Physique des Particules, CEA-Saclay, FR-91191 Gif-sur-Yvette Cedex, France

[39] Istituto Superiore di Sanità, Ist. Naz. di Fisica Nucl. (INFN), Viale Regina Elena 299, IT-00161 Rome, Italy

[40] Instituto de Fisica de Cantabria (CSIC-UC), Avda. los Castros s/n, ES-39006 Santander, Spain,
(CICYT-AEN96-1681)

[41] Inst. for High Energy Physics, Serpukov P.O. Box 35, Protvino, (Moscow Region), Russian Federation

[42] J. Stefan Institute, Jamova 39, SI-1000 Ljubljana, Slovenia, and Department of Astroparticle Physics, School of Environmental Sciences, Kostanjeviska 16a, Nova Gorica, SI-5000 Slovenia, and Department of Physics, University of Ljubljana, SI-1000 Ljubljana, Slovenia

[43] Fysikum, Stockholm University, Box 6730, SE-113 85 Stockholm, Sweden

[44] Dipartimento di Fisica Sperimentale, Università di Torino and INFN, Via P. Giuria 1, IT-10125 Turin, Italy

[45] Dipartimento di Fisica, Università di Trieste and INFN, Via A. Valerio 2, IT-34127 Trieste, Italy, and Istituto di Fisica, Università di Udine, IT-33100 Udine, Italy

[46] Univ. Federal do Rio de Janeiro, C.P. 68528 Cidade Univ., Ilha do Fundão BR-21945-970 Rio de Janeiro, Brazil

[47] Department of Radiation Sciences, University of Uppsala, P.O. Box 535, SE-751 21 Uppsala, Sweden

[48] IFIC, Valencia-CSIC, and D.F.A.M.N., U. de Valencia, Avda. Dr. Moliner 50, ES-46100 Burjassot (Valencia), Spain

[49] Institut für Hochenergiephysik, Österr. Akad. d. Wissensch., Nikolsdorfergasse 18, AT-1050 Vienna, Austria

[50] Inst. Nuclear Studies and University of Warsaw, Ul. Hoza 69, PL-00681 Warsaw, Poland

[51] Fachbereich Physik, University of Wuppertal, Postfach 100 127, DE-42097 Wuppertal, Germany

[52] On leave of absence from IHEP Serpukhov

[53] Now at University of Florida

References

[1] C. Parkes. First $e^+e^- \rightarrow$ W$^+$W$^-$ Event. In T. Ferbel, editor, *Techniques and Concepts of High-Energy Physics: Proceedings of a NATO Advanced Study Institute held July* 11^{th}-22^{nd} *1996*. Plenum Press, *(1997)*.

[2] P.B. Renton. *Electroweak Interactions.* C.U.P., *(1990)*.

[3] D. Perkins. *Introduction to High Energy Physics.* Addison-Wesley, *(1987)*.

[4] G. Wilkinson. *A Study of* $B^0\overline{B^0}$ *Oscillations at the* Z *Resonance.* PhD thesis, University of Oxford *(1993)*.

[5] P. J. Holt. *An Investigation of Radiative Interference in* $e^+e^-\rightarrow\mu^+\mu^-$ *at the* Z *Resonance and a Search for Contact Interactions Between Leptons at* $\sqrt{s}$ *= 130 - 140* GeV. PhD thesis, University of Oxford *(1996)*.

[6] T. Todorov. *Détermination des Paramètres du Modèle Standard et Tests de sa Validité dans les Désintégrations Hadroniques du* Z^0. PhD thesis, Louis Pasteur University, Strasbourg *(1993)*.

[7] Delphi Collaboration (P. Aarnio *et al*). The Delphi Detector at Lep. *Nucl. Instr. and Meth. in Phys. Res.* **A303** *233-276 (1991)*.

[8] The Lep Collaborations, the Lep Electroweak Working Group and the Sld Heavy Flavour Group. A Combination of Preliminary Electroweak Measurements and Constraints on the Standard Model. *CERN-PPE/97-154 (1997)*.

[9] G. 't Hooft. Renormalization of Massless Yang-Mills Fields. *Nucl. Phys.* **B33** *173 (1971)*.

[10] G. 't Hooft. Renormalizable Lagrangians for Massive Yang-Mills Fields. *Nucl. Phys.* **B35** *167 (1971)*.

[11] P.W. Higgs. Broken Symmetries, Massless Particles and Gauge Fields. *Phys.Lett.* **12** *132 (1964).*

[12] P.W. Higgs. Spontaneous Symmetry Breakdown without Massless Bosons. *Phys. Rev.* **145** *1156 (1966).*

[13] E. Fermi. An Attempt of a Theory of Beta Radiation. 1. *Z. Phys.* **88** *161 (1934).*

[14] H. Yukawa. On the Interaction of Elementary Particles. *Proc. Phys. Math. Soc. Japan* **17** *48-57 (1935).*

[15] S.L. Glashow. Partial-Symmetries of Weak Interactions. *Nuc. Phys.* **22B** *579 (1961).*

[16] A. Salam, J.C. Ward. Electromagnetic and Weak Interactions. *Phys. Lett.* **13** *168 (1964).*

[17] S. Weinberg. A Model of Leptons. *Phys. Rev. Lett.* **19** *1264 (1967).*

[18] UA1 Collaboration (G. Arnison *et al*). Experimental Observation of Isolated Large Transverse Energy Electrons with Associated Missing Energy at $\sqrt{s}$ = 540 GeV. *Phys. Lett.* **122B** *103 (1983).*

[19] UA2 Collaboration (M. Banner *et al*). Observation of Single Isolated Electrons of High Transverse Momentum in Events with Missing Transverse Energy at the CERN $\bar{p}p$ Collider. *Phys. Lett.* **122B** *476 (1983).*

[20] CDF Collaboration (F. Abe *et al*). Limits on WWZ and WWγ Couplings from W^+W^- and WZ Production in $p\overline{p}$ Collisions at $\sqrt{s} = 1.8$ TeV. *Phys. Rev. Lett.* **75** *1017 (1995).*

[21] D0 Collaboration (B. Abbott *et al*). Limits on WWZ and WWγ Couplings from $p\bar{p} \rightarrow$e Neutrino Jet Jet X Events at $\sqrt{s} = 1.8$ TeV. *Phys. Rev. Lett.* **79** *1441 (1997).*

[22] L3 Collaboration (M. Acciarri *et al*). Production of Single W Bosons at LEP. *Phys. Lett.* **B403** *168-176 (1997).*

[23] K. Hagiwara *et al* . Probing the Weak Boson Sector in $e^+e^- \rightarrow W^+W^-$. *Nuc. Phys.* **B282** *253 (1987).*

[24] M. Bilenky *et al* . Trilinear Couplings among the Electroweak Vector Bosons and their Determination at LEP2. *Nuc. Phys.* **B409** *22 (1993).*

[25] R.M. Barnett *et al* . Review of Particle Physics . *Phys. Rev.* **D54** *1 (1996).*

[26] Conveners: Z. Kunst, W.J. Stirling Editors: G. Altarelli, T. Sjöstrand, F. Zwirner. Physics at LEP2 Vol. 1, Determination of the mass of the W Boson. Technical report, CERN, *(1996)*.

[27] Conveners: W. Beenakker, F.A. Berends Editors: G. Altarelli, T. Sjöstrand, F. Zwirner. Physics at LEP2 Vol. 1, W^+W^- Cross-Sections and Distributions. Technical report, CERN, *(1996)*.

[28] B. R. Webber. Colour Reconnection and Bose-Einstein Effects. *HEP-PH/9708463 (1997)*.

[29] Workshop Participants. Proceedings of the UK Phenomenology Workshop on LEP2 Physics, Oxford, 14-18 April 1997. *Journal of Physics G* **Vol 24**, *Special Issue No. 2 271-482 (1998)*.

[30] J. Ellis, K. Geiger. Space, Time and Color in Hadron Production via $e^+e^-\to$Z and $e^+e^-\to W^+W^-$. *Phys. Rev.* **D54** *1967 (1996)*.

[31] J. Ellis, K. Geiger. Signatures of Parton Exogamy in $e^+e^-\to W^+W^-\to$ Hadrons. *Phys. Lett.* **B404** *230-237 (1997)*.

[32] CDF Collaboration (M. W. Bailey *et al*). Charmonium and Bottomonium Production in p anti-p Collisions at CDF. *FERMILAB-CONF-96-235-E (1996)*.

[33] DELPHI Collaboration (P. Abreu *et al*). Charged Particle Multiplicity in $e^+e^- \to q\overline{q}$ Events at 161 and 172 GeV and from the Decay of the W Boson. *CERN-PPE-97-113 (1997)*.

[34] OPAL Collaboration (K. Ackerstaff *et al*). Measurement of the W Boson Mass and W^+W^- Production and Decay Properties in e^+e^-Collisons st $\sqrt{s} = 172$ GeV. *CERN-PPE-97-116 (1997)*.

[35] DELPHI Collaboration (P. Abreu *et al*). Bose-Einstein Correlations in the Hadronic Decays of the Z. *Phys. Lett.* **281B** *383 (1992)*.

[36] L. Lönnblad, T. Sjöstrand. Modelling Bose-Einstein Correlations at LEP2. *HEP-PH/9711460 (1997)*.

[37] DELPHI Collaboration (P. Abreu *et al*). Measurement of Correlations between Pions from Different W's in $e^+e^- \to W^+W^-$ Events. *Phys. Lett.* **B401** *181 (1997)*.

[38] ALEPH Collaboration (R. Barate *et al*). Bose-Einstein Correlations in W- pair Decays. *CONF 97 HEP97 paper 590 (1997)*.

[39] DELPHI Collaboration (P. Abreu *et al*). Performance of the DELPHI Detector. *Nucl. Instr. and Meth. in Phys. Res.* **A378** *57-100 (1996).*

[40] LEP Design Report. *CERN-LEP/84-01 Vol. I and II (1984).*

[41] S. Myers. The LEP Collider, from Design to Approval and Commissioning. *CERN/91-08 (1991).*

[42] P. Chochula *et al* . The DELPHI Silicon Tracker at LEP2 . *CERN-PPE/97-155.*

[43] DELPHI Collaboration. DELPHI Data Analysis Program `DELANA` User's Guide. *DELPHI 89-44 PROG 137 (1989).*

[44] S. Navas, P. Rebecchi, A. Trombini. `DAFNE`: `DAFNE` Program Description. *DELPHI 96-46 PROG 215 (1996).*

[45] R. Brun, J. Zoll. `ZEBRA`: Data Structure Management System. CERN *Program Library Long Writeups Q100.*

[46] V. Perevozchikov, N. Smirnov. `PHDST` Package Description V.3 VZD - Viewer of Zebra Data for DELPHI User's Manual. *DELPHI 92-118 PROG 189 (1994).*

[47] T. Spassoff, N. Smirnov. `SKELANA`: Skeleton Analysis Program. *DELPHI note in preparation (1998).*

[48] R. Chierici, C. Parkes, A. Tonazzo. `WWANA` A Standard Package for W Analysis. *DELPHI 96-128 PROG 218 (1996).*

[49] DELPHI Collaboration (P. Abreu *et al*). Improved Measurements of Cross Sections and Asymmetries at the Z Resonance. *Nucl. Phys.* **B418** *403-430 (1994).*

[50] DELPHI Collaboration (P. Abreu *et al*). Measurement of Fermion-Pair Production at LEP energies from 130 to 172 GeV. *HEP97 paper 464, DELPHI 97-132 CONF 110 (1997).*

[51] P. Billoir. Track Fitting with Multiple Scattering. *Nucl. Inst. and Meth.* **225** *352 (1984).*

[52] D. Johnson, D. Reid, W. Trischuk. A Beamspot Database for Lifetime Measurements. *DELPHI 92-36 PHYS 168 (1992).*

[53] M. Blume, G. Sciolla, M. Caccia. Study of a Combined ID-VD Pattern Recognition. *DELPHI 95-18 PROG 212 (1995).*

[54] P. Antilogus. Private Communication.

[55] DELPHI Collaboration (P. Abreu *et al*). Measurement and Interpretation of the W pair Cross-Section in e^+e^- Interactions at 161 GeV. *Phys. Lett.* **B397** *158-170 (1997).*

[56] Convenors: S. Jadach, O. Nicrosini Editors: G. Altarelli, T. Sjöstrand, F. Zwirner. Physics at LEP2 Vol. 2, Event generators for Bhabha Scattering. Technical report, CERN, *(1996).*

[57] LEP Energy Working Group. LEP Energy Calibration in 1996. *LEP Energy Group/97-01 (1997).*

[58] M. Calvi. Measurement of $\mathrm{W^+W^-} \rightarrow l\overline{\nu}_l\bar{l}\nu_l$ Cross-Section at $\sqrt{s} = 170 - 172$ GeV . *DELPHI 97-164 PHYS 741 (1996).*

[59] DELPHI Collaboration (P. Abreu *et al*). `DELSIM` User's Guide. DELPHI *89-67 PROG 142 (1989).*

[60] T. Sjöstrand. `PYTHIA` 5.7 and `JETSET` 7.4 Physics and Manual . *CERN-TH 7112 (1993).*

[61] F.A. Berends, R. Kleiss, R. Pittau. `EXCALIBUR`: A Monte Carlo Program to Evaluate all Four Fermion Processes at LEP-200 and Beyond. *Comput. Phys. Commun.* **85** *437-452 (1995).*

[62] DELPHI Collaboration (P.Abreu *et al*). Tuning and Test of Fragmentation models Based on Identified Particles and Precision Event Shape Data. *Zeit. Phys.* **C73** *11-60 (1996).*

[63] L. Lönnblad. `ARIADNE` version 4: A program for Simulation of QCD Cascades implementing the Color Dipole Model . *Comput. Phys. Commun.* **71** *15-31 (1992).*

[64] Convenors: D. Bardin, R. Kleiss Editors: G. Altarelli, T. Sjöstrand, F. Zwirner. Physics at LEP2 Vol. 2, Event generators for $\mathrm{W^+W^-}$ Physics. Technical report, CERN, *(1996).*

[65] P. Abreu *et al* . SPRIME - A Package for Estimating the Effective $\sqrt{s'}$ Centre of Mass Energy in $q\bar{q}\gamma$ Events. *DELPHI 96-124 PHYS 632 (1996).*

[66] P. Buschmann. Private Communication.

[67] DELPHI Collaboration (P. Abreu *et al*). Measurement of the W-pair Cross-Section and of the W Mass in e^+e^- Interactions at 172 GeV. *CERN-PPE-97-160 (1997).*

[68] M.Calvi, M.Margoni. Private Communication.

[69] D. Fassouliotis. Private Communication.

[70] S. Bethke *et al* . New Jet Cluster Algorithms: next-to-leading order QCD and Hadronization Corrections. *Nucl. Phys.* **B370** *310-334 (1992).*

[71] Yu.L. Dokshitzer *et al* . Better Jet Clustering Algorithms . *Cavendish-HEP-97/06 (1997).*

[72] A. Normand. *A Measurement of the Ratio of Partial Decay Widths* R_b°. PhD thesis, University of Oxford *(1996).*

[73] M. Battaglia *et al* . Measurement of the $|V_{cs}|$ using W- Decays at LEP2. *DELPHI 97-114 CONF 97, HEP97 paper 535 (1997).*

[74] D. Ward. Tests of the Standard Model: W mass and WWZ Couplings. *Plenary Talk at the International Conference on High Energy Physics, Jerusalem,19-26 August 1997, HEP- PH/9711515 (1997).*

[75] W.J. Stirling. The Measurement of $\mathrm{M_W}$ from the $\mathrm{W^+W^-}$ Threshold Cross-Section at LEP2. *Nucl. Phys.* **B456** *3 (1995).*

[76] D. Bardin *et al* . GENTLE/4fan v2.0 A Program for the Semi-Analytic Calculation of Predictions for the Process $e^+e^-\to 4f$. *DESY 96-233, HEP-PH/9612409 (1996).*

[77] P.B. Renton. Private Communication.

[78] C.J. Parkes, P.B. Renton, H.T. Phillips. A Study of Four Fermion Final State Interference relevant to the Measurement of the $\mathrm{W^+W^-}$ Cross-Section and the W Mass. *DELPHI 97-96 PHYS 718 (1997).*

[79] H. Phillips. EXFF : The DELPHI-Customised Version of EXCALIBUR. *DELPHI 96-156 PHYS 648 (1996).*

[80] R. Pittau. Private Communication.

[81] C. Green, T. Bowcock. FASTSIM Manual, DELPHI WWW Pages http://wwwcn.cern.ch/~greenc/fsimguide/fsimguide.html.

[82] N. Kjær, R. Möller. Reconstruction of Invariant Masses in Multi-Jet Events. *DELPHI 91-17 PHYS 88 (1991).*

[83] K. Mönig. Private Communication.

[84] A. Ballestrero, R. Chierici. Reconstruction and Approximation Effects on W mass Distributions at LEP2. *HEP-PH/9710282 (1997).*

[85] W.J. Stirling. Private Communication.

[86] T. Muta, R. Najima, S. Wakaizumi. Effects of the W Boson Width in $e^+e^- \rightarrow W^+W^-$ Reactions. *Mod. Phys. Lett.* **A1** *No.3 203 (1986).*

[87] Conveners: S. Myers, C. Wyss Editors: G. Altarelli, T. Sjöstrand, F. Zwirner. Physics at LEP2 Vol. 1, Prospects for Energy and Luminosity at LEP2. Technical report, CERN, *(1996).*

[88] V. Canale et al. Measurement of M_W with the Jet Direction Method in the Hadronic Channel. *DELPHI 97-29 PHYS 682 (1997).*

[89] N. Kjær, I.B. van Vulpen . Combination of Analyses with Low Statistics. *Internal Note for Direct W Mass Reconstruction (1997).*

[90] ALEPH Collaboration (R. Barate *et al*). Measurement of the W Mass by Direct Reconstruction in e^+e^- Collisions at 172 GeV. *CERN-PPE-97-164 (1997).*

[91] M. Bigi, R. Chierici. Remarks on Mass Errors in Constrained Fitting Methods near to a Kinematical Limit. *DELPHI 97-152 PHYS 731 (1997).*

[92] HBOOK Reference Manual. CERN *Program Library Long Writeups Y250.*

[93] R.J. Barlow. *Statistics - a guide to the Use of Statistical Methods in the Physical Sciences.* John Wiley and Sons, *(1989).*

[94] CERNLIB Short Writeups. CERN *Program Library Short Writeups.*

[95] L. Lyons. *Statistics for Nuclear and Particle Physicists.* C.U.P., *(1986).*

[96] MINUIT Function Minimization and Error Analysis. CERN *Program Library Long Writeups D506.*

[97] CDF Collaboration (F. Abe *et al*). A Direct Measurement of the W Boson Width Gamma (W) . *Phys. Rev. Lett.* **74** *341-345 (1995).*

[98] I.F. Ginzburg, K. Melnikov. About the Modern Experimental Value of W Boson Width. *HEP-PH/9503256 (1995).*

[99] L3 Collaboration (M. Acciarri *et al*). Measurements of Mass, Width and Gauge Couplings of the W Boson at LEP. *Phys. Lett.* **B413** *176-190 (1997).*

[100] A. Tonazzo R. Chierici, C. Parkes. `WWANA` Manual Current Version. */afs/cern.ch/delphi/tasks/lep200/wphysics/wwana/wwana.manual (1998).*

[101] R. Brun *et al* . `PAW` - The Complete Reference. CERN *program Library Long Writeups Q121.*